1290

UNIVERSIDADE Ð COIMBRA

Sérgio Rafael Alves Gomes

DYNAMICS OF THE URANIAN SYSTEM

Tese no âmbito do Doutoramento em Física, Astrofísica orientada pelo Professor Doutor Alexandre Carlos Morgado Correia e apresentada ao Departamento de Física da Faculdade de Ciências e Tecnologia da Universidade de Coimbra.

Novembro de 2023

Sérgio Rafael Alves Gomes

DYNAMICS OF THE URANIAN SYSTEM

Tese no âmbito do Doutoramento em Física, Astrofísica orientada pelo Professor Doutor Alexandre Carlos Morgado Correia e apresentada ao Departamento de Física da Faculdade de Ciências e Tecnologia da Universidade de Coimbra.

Novembro de 2023

Preface

The present manuscript is the result of research carried out under the supervision of Professor Doctor Alexandre Correia, at the Centre for Physics of the University of Coimbra. The original contributions that resulted from this research work are partially contained in this thesis and gave origin to several scientific publications:

- **Gomes, S. R. A. and Correia, A. C. M. (2023a)**.
  Effect of the inclination in the passage through the 5/3 mean motion resonance between Ariel and Umbriel. Astronomy and Astrophysics, 674:A111. DOI: 10.1051/0004-6361/202346101.

- **Gomes, S. R. A. and Correia, A. C. M. (2023b)**.
  Stability maps for the 5/3 mean motion resonance between Ariel and Umbriel with inclination. arXiv e-prints, page arXiv:2309.04786. DOI: 10.48550/arXiv.2309.04786.
  Accepted for publication in the International Astronomical Union Proceedings Series.

- **Maire et al. (2023)**.
  Workshop Summary: Exoplanet Orbits and Dynamics. Publications of the Astronomical Society of the Pacific, 135(1052):106001. DOI: 10.1088/1538-3873/acff88.

This work was also presented in the form of the following talks:

- *Estratégias de mitigação de detritos espaciais.*
  Dia do Asteróide 2020, July 30, 2020, Portugal and Angola
  (`https://asteroidday.org/event/dia-do-asteroide-2020-portugal-angola/`);

- *The passage through the 5:3 resonance between Ariel and Umbriel with inclination.*
  Complex Planetary Systems II – Kavli-IAU Symposium 382 – July 3-7, 2023, Namur, Belgium
  (`https://cpsii.unamur.be`);

- *The passage through the 5:3 resonance between Ariel and Umbriel with inclination.*
  Journal club, June 27, 2023, Coimbra, Portugal;

- *The passage through the 5/3 resonance between Ariel and Umbriel: effect of the inclination.*
  XXXIII ENAA, September 7-9, 2023, Coimbra, Portugal (`https://www.uc.pt/events/enaa2023/`);

and in the form of the following posters:

- *Tidal evolution of the Uranian satellites and how to escape the 5:3 Ariel-Umbriel MMR.*
  Research day, April 27, 2022, Coimbra, Portugal;

- *Tidal evolution of the Uranian satellites and how to escape the 5:3 Ariel-Umbriel MMR.*
  Habitability in the Solar System and beyond, November 28 to December 2, 2022, Nantes, France
  (`https://geoplanet-sp.eu/en/activities`);

- *The passage through the 5/3 resonance between Ariel and Umbriel: effect of the inclination.*
  Research day, March 8, 2023, Coimbra, Portugal.

Abstract

The planet Uranus and its satellites form one of the most mysterious systems in our Solar System. Geological traces of global resurfacing of the main satellites and the abnormally relatively high values of some of their orbital elements suggest a rich dynamical evolution. The orbits are expected to slowly drift away owing to tides raised on the planet. As a result, several mean motion resonances (MMR) between the satellites were likely encountered in the past. In this work, we address the dynamical and tidal evolution of the five major satellites of Uranus, namely, Miranda, Ariel, Umbriel, Titania, and Oberon.

Resorting to an N-body model that takes into account the tidal evolution of the orbits and the spins of all bodies, we re-estimated the interval of the specific dissipation factor of Uranus to be $5\,800 < Q_0 < 11\,500$. We determined that, at present, there are no spin-orbit resonances within the Uranian satellites, invalidating them as a mechanism to decrease the inclinations of the satellites, as proposed in previous studies. We confirmed that the current eccentricities of the satellites are not forced, and estimated the tidal damping timescales of the satellites' eccentricities and inclinations. By simulating the system from just after their formation, 4.5 Gyr ago, until the present days, we observed that it could have crossed a large number of MMR during the orbital evolution, deviating the final orbits from the currently observed. By adopting a *step-by-step* approach, we reconstructed the orbital evolution of the main satellites just after the 5/3 Ariel-Umbriel MMR, and have shown that the system has not been much disturbed since then. We also confirmed that, during capture within the 5/3 Ariel-Umbriel MMR, the orbits of the five satellites are strongly excited. Consequently, the 5/3 MMR must be shortly skipped.

To study in detail the passage through the 5/3 Ariel-Umbriel MMR, we developed a secular two-satellite model, where we adopt the weak friction tidal model, using complex Cartesian coordinates. With the consideration of the conservation of the total angular momentum, we only need to perform one average over one fast angle. We also portray the chaotic nature of the system with Poincaré surface sections and stability maps.

By performing a large number of numerical simulations, we studied the passage through the 5/3 Ariel-Umbriel in the circular, planar, and eccentric-inclined cases. We have shown that the eccentricity of Ariel is the key variable to evade the 5/3 MMR. Moreover, if $\sqrt{e_1^2 + e_2^2} < 0.007$, long term capture within the resonance is certain. We determined that, with $e_1 > 0.015$ and $e_2 < 0.01$, the system avoids capture in at least 60% of the cases. We have also shown that, to replicate the currently observed inclinations of Ariel and Umbriel ($I_1 = 0.0167°, I_2 = 0.0796°$), the initial inclinations of both satellites must be $I_1 \leq 0.05°$ and $I_2 \approx 0.082°$. These initial inclination values are similar to the currently observed.

The results from the secular two-satellite body were finally confirmed with the N-body model, that includes all the five main satellites.

Resumo

O planeta Úrano e os seus satélites formam um dos sistemas mais misteriosos do nosso Sistema Solar. Vestígios geológicos observados nas superfícies das maiores luas de Úrano e os valores relativamente altos de alguns dos seus elementos orbitais, sugerem uma evolução dinâmica complexa. Prevê-se que as órbitas estejam a afastar-se lentamente devido às marés geradas no planeta. Como resultado, várias ressonâncias de movimento médio (MMR) entre os satélites provavelmente ocorreram no passado. Neste trabalho, estudou-se a evolução dinâmica e de marés dos cinco satélites principais de Úrano, nomeadamente, Miranda, Ariel, Umbriel, Titânia e Oberon.

Através de um modelo de N-corpos, que considera a evolução das órbitas e das rotações de todos os corpos, estimou-se o intervalo do fator de dissipação específica de Úrano como estando compreendido entre $5\,800 < Q_0 < 11\,500$. Foi possível determinar que atualmente não existem ressonâncias spin-órbita entre os satélites uranianos, invalidando-as assim como sendo um mecanismo para diminuir as inclinações dos satélites, conforme proposto em estudos anteriores. Confirmou-se que as excentricidades livres atuais dos satélites não são forçadas e calcularam-se os tempos de amortecimento por maré das excentricidades e inclinações dos satélites. Simulando o sistema desde após a sua formação, há 4,5 mil milhões de anos atrás, até ao presente, constatou-se que o sistema provavelmente cruzou um grande número de MMRs durante a sua evolução orbital, desviando as órbitas finais das observadas atualmente. Ao adotar uma abordagem *etapa-a-etapa*, reconstruiu-se a evolução orbital dos principais satélites logo após a MMR 5/3 entre Ariel e Umbriel e mostrou-se que o sistema não foi muito perturbado desde então. Confirmou-se também que, durante a captura na MMR 5/3 entre Ariel e Umbriel, as órbitas dos cinco satélites são fortemente excitadas. Consequentemente, o sistema deve escapar rapidamente da MMR 5/3.

Para estudar detalhadamente a passagem pela MMR 5/3 entre Ariel e Umbriel, desenvolveu-se um modelo secular de dois-satélites, onde se adotou o modelo linear de maré e coordenadas Cartesianas complexas. Tendo em conta a conservação do momento angular total, apenas foi necessário realizar uma média sobre um dos ângulos rápidos. Estudou-se também a natureza caótica do sistema através de secções de superfícies de Poincaré e de mapas de estabilidade.

Realizando um grande número de simulações numéricas, estudou-se a passagem pela MMR 5/3 entre Ariel e Umbriel nos casos circular, planar e excêntrico-inclinado. Foi possível mostrar que a excentricidade de Ariel é fundamental para escapar à MMR 5/3. Além disso, se $\sqrt{e_1^2 + e_2^2} < 0.007$, a captura de longo prazo na ressonância 5/3 é garantida. Determinou-se ainda que, com $e_1 > 0.015$ e $e_2 < 0.01$, o sistema evita a captura em pelo menos 60% dos casos. Mostrou-se igualmente que, para replicar as inclinações de Ariel e Umbriel atualmente observadas ($I_1 = 0.0167°, I_2 = 0.0796°$), as inclinações iniciais de ambos os satélites devem ser $I_1 \leq 0.05°$ e $I_2 \approx 0.082°$. Estes valores iniciais de inclinação são semelhantes às observações atuais.

Os resultados do modelo secular de dois-satélites foram por fim confirmados com o modelo de N-corpos, que inclui os cinco principais satélites.

Acknowledgements

Nomenclature

Notation	Definition	Notation	Definition
bold	Vector	$\vert \; \vert$	Vector module
$\bar{}$	Complex conjugate	i	$\sqrt{-1}$
$\langle \; \rangle$	Average	$\cdot$	Time derivative
t	Time	MMR	**M**ean **M**otion **R**esonance
$\mathcal{G}$	Gravitational constant ($\mathcal{G} = 4\pi^2\,\mathrm{au}^3\mathrm{M}_\odot^{-1}\mathrm{yr}^{-2}$)	m	Mass
μ_k	$\mathcal{G}(m_0 + m_k)$	β_k	Reduced mass ($m_0 m_k/(m_0 + m_k)$)
R	Radius	C	Moment of inertia
J_2	Second order gravity field (Eq. (2.20))	k_2	Second Love number
V	Gravitational potential	U	Gravitational potential energy
S	Generating function	$\mathcal{P}$	Legendre polynomials
$b_s^{(j)}$	Laplace coefficients		
$\mathbf{R}\,,\mathbf{r}$	Position vectors	$\mathbf{P}\,,\mathbf{p}$	Linear momentum vectors
$\mathbf{L}$	Angular momentum vector	$\boldsymbol{\Gamma}$	Torque ($\boldsymbol{\Gamma} = \dot{\mathbf{L}}$)
Q	Specific dissipation factor (Eq. (2.69))	τ	Tidal time lag
$\tau_{\mathrm{ecc}}\,,\tau_{\mathrm{inc}}$	Damping timescales (Sects. 2.4.4 and 4.4)	$g\,,s$	Secular modes (Sect.2.4.2)
$\mathcal{H}$	Hamiltonian	$\tilde{\mathcal{H}}$	Averaged Hamiltonian ($\langle\mathcal{H}\rangle_\gamma$)
a	Semi-major axis	M	Mean anomaly
e	Eccentricity	ϖ	Longitude of the pericentre
I	Inclination	Ω	Longitude of the ascending node
		ω	Argument of the pericentre
ν	True anomaly	n	Mean motion
$\boldsymbol{\omega}$	Angular velocity vector	ϵ	Obliquity
$\Lambda_k, \lambda_k,$ $\Sigma_k, -\varpi_k,$ $\Phi_k, -\Omega_k$	Poincaré variables (Eqs. (3.26), (3.27), and (3.28))	Θ_k, θ_k	Andoyer variables for rotation (Eq. (3.25))
Σ	Total angular momentum (Eq. (3.36))	Γ, γ	Eq. (3.39)
σ	Resonant angle (Eq. (3.32))	σ_k, ϕ_k	Resonant angles (Eqs. (3.40), (3.41), (3.42), and (3.43))
ϑ_k	Eqs. (3.44), (3.45), and (3.46)		
$\boldsymbol{x_k}, \overline{\boldsymbol{x}}_k,$ $\boldsymbol{y_k}, \overline{\boldsymbol{y}}_k$	Complex rectangular coordinates (Eqs. (3.92) and (3.93))	$\Gamma_1\,,\Gamma_2$	Eqs. (3.49) and (3.50)

Contents

Chapter 1

Introduction

Uranus, together with its satellites, is one of the least studied planets in the Solar System. Records suggest that the earliest observations of this not so distant planet remount to the 2nd century BC, by the famous Greek astronomer Hipparchus (Bourtembourg 2013). Often confused with a star by several astronomers throughout the years (Wright 1987), its discovery is attributed to William Hershel on 13 March 1781, but not before it was mistakenly confused with a comet (Herschel and Watson 1781). Latter observations, (on 11 January 1787, i.e., about six years later) led to the discovery of the two largest satellites of Uranus, Titania, and Oberon (Herschel 1787). Ariel and Umbriel, the two other large moons, innermost to Titania's orbit, were discovered in 1851 by William Lassell (Mozel 1986).

In Greek mythology, Uranus was the personification of the sky. Together with Gaia, whose Roman name is Earth, they were the parents of the first generation of Titans, which includes Cronus (Saturn in Roman mythology). Later, Cronus, together with his sister Rhea, gave birth to the first generation of Olympians. Between them, there were Zeus, Poseidon and Hades, that is, Jupiter, Neptune, and Pluto in Roman mythology. Ergo, according to mythology, the moons of Uranus were supposed to be named after their children or grandchildren. To avoid mythological incongruities, William Hershel requested to name the Uranian satellites as a tribute to famous English writers. Being Uranus the god of sky, Oberon and Titania are the king and queen of the fairies in Shakespeare's "Midsummer Night's Dream", while Ariel is a sylph, and Umbriel a gnome in Pope's "Rape of the Lock" (Barton 1946; Kuiper 1949). More recently, Miranda, the innermost and smallest of the major Uranian satellites, was first photographed on February 16, 1948, by Kuiper (1949), and was named once more as a Shakespeare character. Since then, the number of known satellites has increased to twenty-seven, although due to the large distance of Uranus from the Earth and the lack of spacecraft missions on the planet, the real number of satellites is possibly higher than the currently known.

Voyager 2 was the only spacecraft to have visited Uranus so far, with a flyby mission early in 1986. The large number of high-resolution images acquired by the spacecraft's instruments allowed many developments in the comprehension of this mysterious planet, making the following years after this flyby some of the most impelling of the study of Uranus. Since then, the interest in Uranus has decreased, as can be seen by the decreasing number of published articles on the subject Uranus (see Fig. 1.1). However, new ground based observations (e.g. Jacobson 2014), together with improved theoretical models and the will to launch a new spacecraft mission to the Uranian system (Bocanegra-Bahamón et al. 2015; Cartwright et al. 2021; Xavier et al. 2022), have clearly made this system a hot topic again.

1.1 Uranus

Together with Neptune, Uranus is one of the outermost planets in the Solar system. They display a significant number of similar key quantities, such as mass, radius, surface temperature, and atmospheric composition. They represent a unique planetary class, the ice giants (Schubert 2015; Scheibe et al. 2021), with numerous discovered exoplanets with similar mass and radius (Helled and Bodenheimer 2014; Helled and Fortney 2020). Consequently, these two planets can be seen as a laboratory to understand
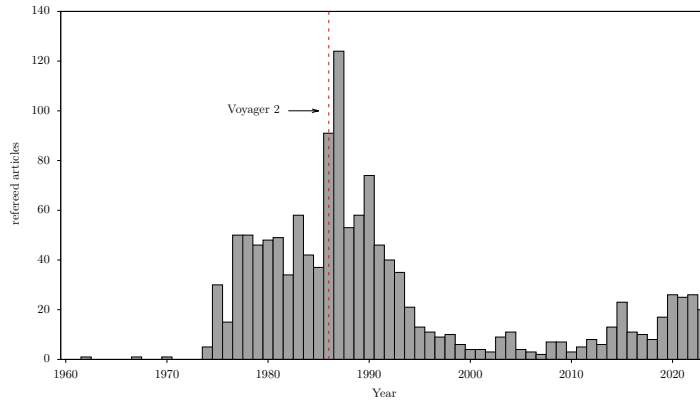
Figure 1.1: Number of refereed articles per year on Uranus and its satellites in the last 63 years. Data from ADS database (`https://ui.adsabs.harvard.edu`, accessed on October 30, 2023).

a unique set of formation processes, evolution, and stability of planetary systems. Contrarily to gas giants Jupiter and Saturn, which are thought to have very low mass cores with massive gas envelopes, measurements from Voyager 2 indicate that Uranus and Neptune have more massive cores, composed of heavier elements and surrounded by icy mantles, allowing better constraints for the interior models and gravitational properties than those for the gas giants (Helled et al. 2011; Nettelmann et al. 2016).

The most striking difference between the two ice giants is the extreme 98° tilt of the rotation axis of Uranus relatively to the orbital plane, known as the obliquity. The origin of the large obliquity of Uranus remains elusive. Two scenarios have been proposed: an impulsive tilt due to a collision with one or multiple bodies (Safronov 1966; Morbidelli et al. 2012; Kurosaki and Inutsuka 2019) or a slow tilt due to a resonance between the precession rates of the spin-axis and of the orbit of a migrating satellite (Kubo-Oka and Nakazawa 1995; Saillenfest et al. 2022) or the theoretical planet nine (Lu and Laughlin 2022). More details and implications of the two distinct hypotheses will be later discussed in Sect. 1.2.

The rotation period of Uranus is usually accepted to be 17.24 hours. However, Helled et al. (2010) suggests that winds within the atmosphere of Uranus could result in misleading models of the rotation of the planet. The authors state that the rotation period of Uranus is in fact faster than the widely accepted, imposing an uncertainty on this value. More recently, using observations taken by the Very Large Array Telescope, Akins et al. (2023) found evidence of a cyclonic polar vortex on Uranus, similar to the structures observed on Saturn's and Neptune's poles. This is yet another indicator of the scientific richness and how little knowledge we have of this cold giant and its complexity. The physical properties of Uranus are summarized in Table 1.1.

Mass [a]	$4.365628821047407 \times 10^{-5} M_\odot$	Obliquity [a]	98°
Radius [a]	25 559 km	J_2 [a]	3.51068×10^{-6}
Density [b]	$1.270 \pm 0.001 \mathrm{g.cm^{-3}}$	k_2 [d]	0.104
Rotation period [c]	17.24 ± 0.01 hour	Moment of inertia [e]	0.2296

Table 1.1: Physical properties of Uranus. [a] Jacobson (2014); [b] Helled and Fortney (2020); [c] Desch et al. (1986), [d] Gavrilov and Zharkov (1977); [e] estimated using the Darwin-Radau relation (e.g. Correia and Rodríguez 2013).

1.2   Formation of the satellites

Natural satellites are believed to be formed in a protoplanetary disk around the host planet (e.g. Peale 1999), or to be "free bodies" that were captured by the host planet (e.g. Singer 1968; Agnor and Hamilton 2006; Jewitt and Haghighipour 2007). Data from Voyager 2 shows that the distribution of mass between

the satellites and Uranus and their chemical composition are consistent with these bodies having been condensed from a concentric disk, withstanding the idea that the regular moons of Uranus formed in an accretion disk around the planet (Prentice 1986; Pollack et al. 1991). However, the peculiar 98° obliquity of Uranus, which places it in a nearly horizontal configuration, poses many unknowns about the origin of the accretion disk.

One hypothesis proposes that a late giant impact with Uranus created a large debris disk, a mechanism already proposed for the formation of the Moon (e.g. Canup and Asphaug 2001; Canup 2012; Asphaug 2014) and Charon (e.g. Canup 2005; Kenyon and Bromley 2021). This is a compiling scenario, since some studies suggests that a collision could drive the extreme tilt of the Uranus (Harris and Ward 1982; Korycansky et al. 1990; Slattery et al. 1992; Brunini 1995; Parisi and Brunini 1997; Brunini et al. 2002; Parisi et al. 2008; Morbidelli et al. 2012; Kegerreis et al. 2018; Kurosaki and Inutsuka 2019; Ida et al. 2020; Rogoszinski and Hamilton 2021; Woo et al. 2022). One strong evidence of this possibility is the fact that the orbits of the regular moons of Uranus are equally tilted, suggesting that they were formed after the tilt of the spin-axis of the planet (Ida et al. 2020). Mosqueira and Estrada (2003) state that a collision could not create a debris disk capable of originating the satellites, and such disk would have to be retrograde, but recent results show that a collision is indeed compatible with the present value of the angular moment of Uranus and the satellite system, as well as the masses of the regular satellites (Kegerreis et al. 2018; Kurosaki and Inutsuka 2019; Salmon and Canup 2022). Considering that only one impact drove obliquity to the observed value, an impactor with a mass larger than 1 $M_\oplus$ is required. Yet, the probability of an encounter with such a large mass is very low (Rogoszinski and Hamilton 2021). Morbidelli et al. (2012) have shown that to achieve the current high obliquity of Uranus simultaneously with a prograde orbit of the regular satellites through an impact with a massive body, the planet must have an initial non-negligible tilt prior to the event. This leads to the more likely hypothesis of multiple impacts with smaller masses. In addition, such a massive collision could significantly alter the planet's primordial rotation period. Since the rotation periods of Uranus and Neptune are similar (T_U = 17.24h, T_N = 16.10h), it is difficult to conciliate that one planet suffered multiple impacts and the other did not. Furthermore, to achieve the necessary debris disk mass and size to form the satellites is very difficult, with simulations generating disks of at least one order of magnitude more massive and smaller than required to form the Uranian satellites (Rogoszinski and Hamilton 2021).

More recently, a collisionless scenario based on the increase of the precession rate of the spin-axis of Uranus due to the presence of its satellites has been proposed by Boué and Laskar (2010). A similar mechanism was previously proposed to explain Saturn's 26.7° obliquity, through a commensurability between the precession period of Saturn's spin-axis and the precession period of Neptune's orbital plane (Ward and Hamilton 2004; Hamilton and Ward 2004). In the case of Uranus, a spin-orbit resonance between the planet and an ancient moon, larger than any of the current moons, is invoked to increase the obliquity. The main difficulty of this process is the missing satellite, especially because it needs a minimum mass of $0.006M_\oplus$ (Saillenfest et al. 2022), larger than the mass of any current Uranian satellites. Resorting to the close encounters during the giant planet outward migration proposed by the Nice Model (Tsiganis et al. 2005), it is possible to eject the satellite. However, a moon with this dimension should leave traces of its existence. Yet, no such evidences were found so far. Alternatively, Rogoszinski and Hamilton (2021) suggests a spin-orbit resonance not with a moon, but instead with a circumplanetary disk in the final stages of its formation, the same disk that originated the current satellite system. Nonetheless, the timescales of this process are either too short or near the age of the Solar system. In addition, unless unrealistic masses of the ancient moon or the circumplanetary disk are taken into account, none of the proposals successfully achieve the 98° obliquity of Uranus (Rogoszinski and Hamilton 2021).

Even so, Laskar and Robutel (1993) showed that the present obliquity of Uranus is stable and should be considered primordial. Moreover, the regular satellites are immune to the migration effects of the giant planets of the solar system (Deienno et al. 2011). Thus, the study of the satellite system can be conducted as an isolated system, regardless if the spin-axis of Uranus was tilted by a collision or a spin-orbit resonance.

1.3   Satellites surfaces and interiors

We can divide the five regular Uranian moons into three groups of mass and radius. Titania and Oberon are the largest satellites of Uranus, with very similar radius and masses (Table 1.2). However, Titania is slightly bigger and more massive than Oberon. Ariel and Umbriel have almost a third of the mass of Titania and Oberon, and radius of about $\sim$ 600 km. This places these moons with roughly the same mean densities, suggesting similar bulk compositions. Miranda, is the smallest of the largest satellites, with just $\sim$ 2% of the mass of Titania and a third of its radius, resulting in the lowest mean density of the system.

The lack of observational constraints makes studies of the internal composition of the satellites very challenging. Current models predict that all the satellites are differentiated, with rocky cores surrounded by icy layers (Canup and Ward 2006; Kirchoff et al. 2022). However, the lower density of Miranda indicates a higher percentage of ice than on the remaining satellites. A more tantalizing idea suggests that Titania and Oberon can hold thick subsurface oceans (Hussmann et al. 2006; Cochrane et al. 2021; Bierson and Nimmo 2022), placing the Uranian system as a candidate for search for life conditions in the Solar system (Cartwright et al. 2021).

The images captured by the Voyager 2 flyby (Fig.1.2) display evidences of extreme to moderated resurfacing of some Uranian moons (Smith et al. 1986). The surfaces of Umbriel and Oberon do not show tectonic structures and are dominated by craters, dating to a period where the cratering rate was significantly higher (Plescia 1987). Furthermore, there is a high degree of saturation, that is, multiple overlapping of the craters. This indicates that the surfaces of both satellites are ancient, possible dating to their formation (Strom 1987; Zahnle et al. 2003). On the contrary, the surfaces of Miranda, Ariel, and Titania present complex geological structures and a much smaller density and size of craters. This is an indicator of intensive melting of the surfaces at some point during their history, erasing the first population of larger craters and reshaping the primordial surface (Smith et al. 1986; Thomas 1988; Avramchuk et al. 2007). Miranda presents the largest amount of geological features, where the most distinguished are the three large resurfaced regions, known as "coronae", surrounded by heavily cratered regions (Plescia 1988; Beddingfield and Cartwright 2020). Measurements of the fault system within these features revealed that a heat flux of $31 - 112$ mW m^{-2} is required to resurface these regions (Beddingfield et al. 2015). Ariel's and Titania's surfaces display similar geological features, with large cratered regions, overlapped by long rifts [1] and ridges [2]. For Ariel, depending on the surface composition, heat fluxes ranging between $1 - 98$ mW m^{-2} are necessary to create such structures (Peterson et al. 2015; Beddingfield et al. 2022). The low image resolution of the surface of Titania do not allow resolving the tectonic structures. Thus, estimates of the heat flux have not yet been performed (Prockter et al. 2010).

Analysing the crater densities, sizes, and depths allow us to estimate the ages of the features on the surfaces of the satellites. However, the cratering rates of the Solar system are still under debate, posing high uncertainties on these estimations (Zahnle et al. 2003; Kirchoff et al. 2022). Umbriel and Oberon present the oldest surfaces and are possibly primordial. The surface of Miranda is believed to be the youngest between the regular moons of the Uranian system, with studies pointing to regions with only 0.1-1 Gyr and the other with 2-3.5 Gyr. The crater density on Ariel and the rift system suggests that some features have $\sim$ 1 Gyr. As for Titania, Zahnle et al. (2003) indicate that some features are 2 Gyr old, while Kirchoff et al. (2022) states that resurfacing occurred just after their formation.

Gravitational interactions depend on the distance between two masses by a factor of $1/r^2$. Therefore, taking into account the volume of two bodies, the gravitational force will be different throughout the volume. If the bodies are not fully stiff, the masses will deform under the differential field. Furthermore, if we consider that the relative position of the infinitesimal masses of both bodies are constantly changing, e.g., if a satellite's orbital period is different from the rotational period of the planet, the gravitational field on which both masses lay is constantly changing, and the internal structures will be constantly

---

[1]Rifts are longitudinal faults along the surface. They are created by opposing forces acting on a region of the tectonic plane, which divide the surface.

[2]Ridges are elevations on the surface, created by upward forces from the melted interior. It is common to find rifts along these structures.
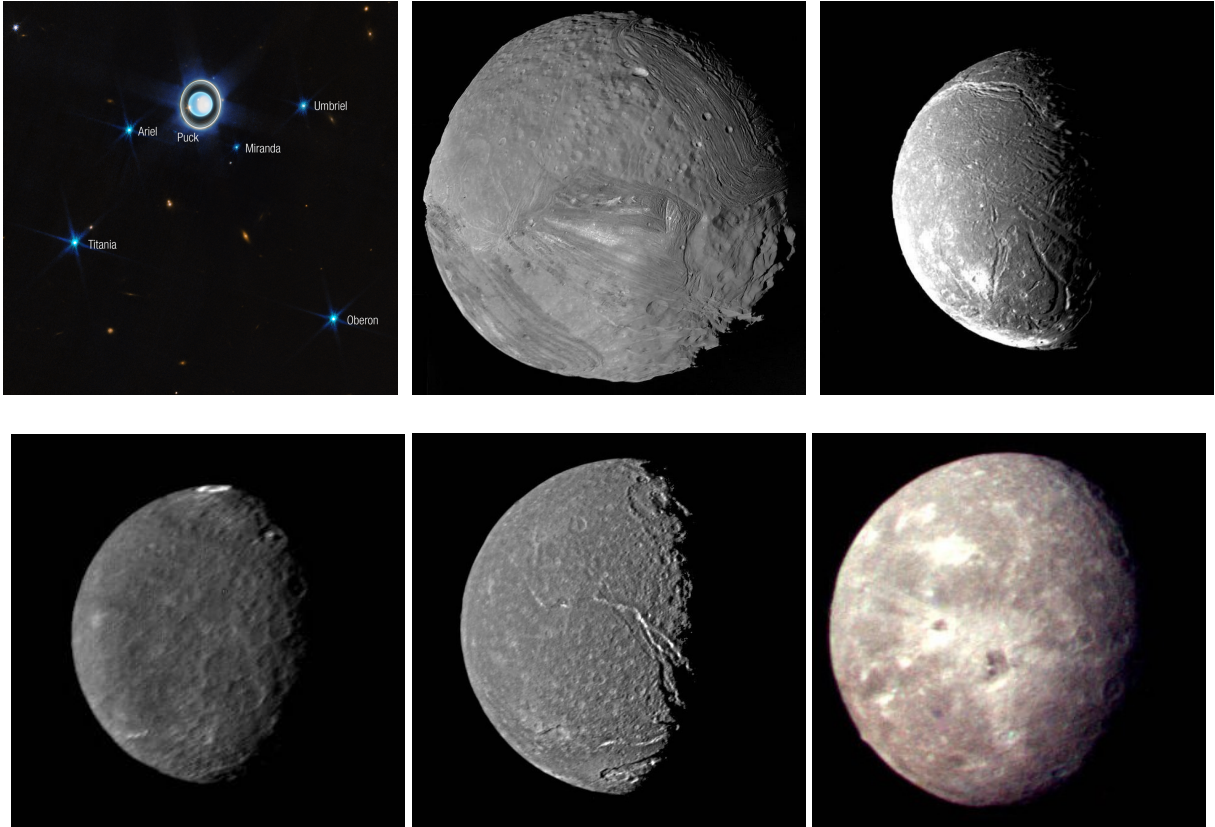
Figure 1.2: Top left: Image from James Web Space Telescope from Uranus and the six largest Uranian satellites (Credits: NASA, ESA, CSA, STScI, with image processing by Joseph DePasquale (STScI)). Closest images of the five largest satellites of Uranus, taken by Voyager 2: top centre: Miranda; top right: Ariel; bottom left: Umbriel; bottom centre: Titania; bottom right: Oberon (Credits: NASA).

rearranging. This process leads to friction within the internal layers of the bodies, and, consequently, energy dissipation through heat. This process is known as tidal friction, and over large periods of time can produce a significant impact on the dynamical and geological evolution of the bodies.

Radiogenic heating and primordial heat from the formation cannot solely explain the geological features observed in Miranda, Ariel, and Titania (Peale 1988; Castillo-Rogez et al. 2023). Therefore, tidal friction provides the best explanation to the energy dissipation. It could explain the fact that Miranda and Ariel, the closest moons to the planet, present the youngest surfaces, respectively, and Umbriel and Oberon, which are further from Uranus, have older surfaces. Though, with the current configuration of the system, tidal dissipation cannot easily explain why Titania, which lays between Umbriel and Oberon, also has a younger surface than its neighbours.

Thus, an intricate evolution of the system should have occurred in the past, and some dynamical process, such as resonance capture (see Chap. 2), could explain a prolonged dissipation of energy of Titania that did not take place in Umbriel and Oberon (Peale 1988).

1.4 Orbits of the Uranian system

The orbits of the five largest moons of Uranus pose many queries. Their proximity with the host body and the short orbital periods make them a very compact system, similar to many exoplanetary systems (Zhu et al. 2018) such as Trappist-1 (Barstow and Irwin 2016; Grimm et al. 2018), Kepler-11 (Lissauer et al. 2011), TOI-178 (Leleu et al. 2021) or TOI-1136 (Dai et al. 2023). As can be seen in Fig.1.3, the ratio between the mass of Uranus and the satellites is comparable to the ratio between the mass of the

Satellite	Miranda	Ariel	Umbriel	Titania	Oberon
Mass ($\times 10^{10}$ M$_\odot$)	0.323997	6.291561	6.412118	17.096471	15.468953
Radius (km)	235.8	578.9	584.7	788.4	761.2
Period (day)	1.413480	2.520381	4.144176	8.705883	13.463254
a (R$_0$)	5.080715	7.470167	10.406589	17.069604	22.827536
e ($\times 10^{-3}$)	1.35	1.22	3.94	1.23	1.40
I ($^\circ$)	4.4072	0.0167	0.0796	0.1129	0.1478
J_2	6.10×10^{-3}	1.39×10^{-3}	6.13×10^{-4}	1.13×10^{-4}	1.48×10^{-5}

Table 1.2: Physical and orbital mean parameters of the five largest Uranian satellites. The masses, orbital periods, semi-major axis (a), eccentricities (e), and inclinations (I) are from Jacobson (2014), the radius from Thomas (1988), and the second order gravity field (J_2) from Chen et al. (2014).

host star and their planets. The same applies for the ratio between the orbital period of the innermost orbiting body and the remaining satellites. This places the Uranian system as a perfect laboratory to study a large set of multi-planetary compact systems.

Tides enable exchanges between the satellite's orbital angular momentum and the rotational angular momentum of the planet. If the satellite's orbital period is higher than the planet's rotational period, the satellite moves away from the planet, while the planet's rotation rate slows down. If the satellite's orbital period is lower than the planet's rotational period, the reverse situation occurs. From Tables 1.1 and 1.2, we can state that all the Uranian satellites are drifting away from Uranus, and a migration motion of the satellites is undergoing, driven by energy dissipation within the planet due to tidal friction, mainly between the moons and Uranus.

Tides are also very effective on damping the eccentricities, with a strong tendency to circularize orbits over short periods of time. Despite small when compared with other bodies of the Solar System, the eccentricities of the Uranian satellites are surprisingly large when tidal friction is taken into account (e.g. Squyres et al. 1985), indicating that some dynamical process must have excited the system's eccentricities in a not very distant past. The inclinations of the regular moons of Uranus are also intriguing. The regular satellites have very small, close to zero inclinations, except for Miranda, which has a value around 4.4° (Table 1.2). If the moons were formed by one of the processes discussed in Sect. 1.2, the inclination of Miranda should have been smaller, like the remaining moons in the system. Thus, Miranda's orbit must have undergone through some process of excitation, leading to the present value (e.g. Tittemore and Wisdom 1989, 1990; Ćuk et al. 2020).

Due to the proximity of the satellites to the planet, the migration rate is differential (Goldreich 1965). The strength of the tidal forces decreases with distance, and so the migration rate is likely higher for the innermost moons. As the inner satellites closes to the outer ones, simple numerical commensurabilities between their orbital periods can be encountered, called mean motion resonances (MMRs). The present orbits of the satellites are quasi-periodic, and the mutual perturbations cancel in the long-term. However, if a MMR is reached, the perturbations no longer cancel and mutual gravitational interactions between the bodies are enhanced, leading to the excitation of the eccentricities and the inclinations, as well as a change in their migration rates (e.g. Murray and Dermott 1999). At present, there are no resonant pairs in the Uranian system. Yet, considering the tidal induced drift on each individual moon, it is possible to conclude that the satellites of Uranus may have crossed in the past several MMRs (Peale 1988). During the evolution of the orbits, only Miranda, Ariel, and Umbriel can cross low order resonances, as can be seen in Fig. 1.4, where the latest one was the 5/3 MMR between Ariel and Umbriel. The effects of MMR resonances in the evolution of the Uranian satellite system were already studied in the late 1980s by Tittemore and Wisdom, in a series of three papers encompassing the four most recent low-order MMR possibly encountered, with a two-body analytical secular model (that only considers long-term effects on the system). They found that, disregarding the effects of the inclination during the 5/3 Ariel-Umbriel MMR passage, in other words, assuming that both satellites orbit on the equatorial
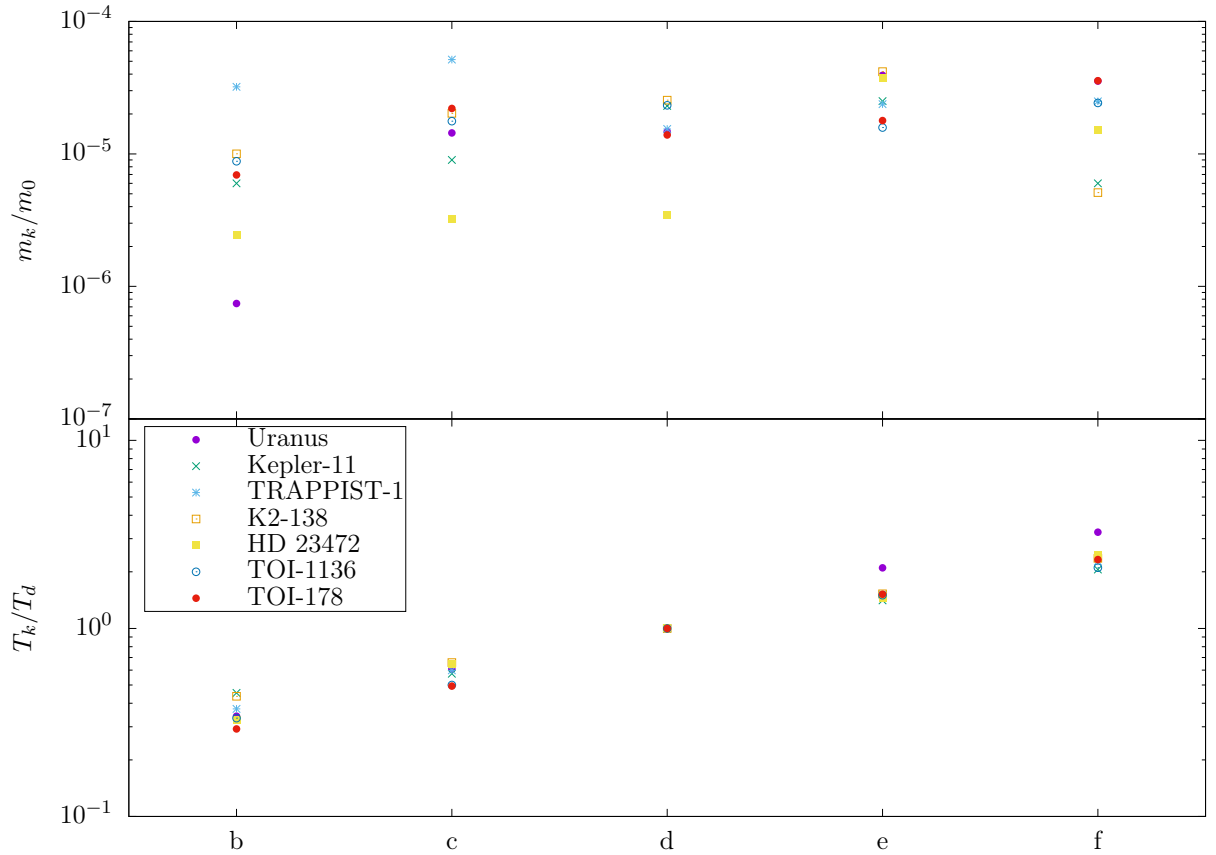
Figure 1.3: Comparison between the masses (top) and orbital periods (bottom) between the Uranian satellites, and the exoplanetary system Kepler-11, TRAPPIST-1, K2-138, HD 23472, TOI-1136 and TOI-178 . m_0 is the mass of the central massive body, m_k is the mass of the satellite or exoplanet, and T_d is the orbital period of the body subbed as d. Starting from the letter b, the satellites/exoplanets are ordered in alphabetical order by the distance to the central body (subbed as a).

plane of Uranus, chaotic motion can increase the eccentricities to values $2 \sim 3$ times higher than the values before the resonance encounter (Tittemore and Wisdom 1988). Currently, we do not observe any commensurability within Ariel and Umbriel. Thus, the satellites must have escaped the MMR. Tittemore and Wisdom (1988) results point that this is only possible if, at the resonance encounter, the eccentricities of the satellites are much higher than the current ones. This would require some previous mechanism to increase the eccentricities, which the authors could not explain. In addition, the increase of the eccentricities is most likely not sufficient to melt the surface of Ariel. The impact of MMR passage is much more striking for the 3/1 Miranda-Umbriel MMR. Assuming the circular approximation, that is, considering both eccentricities null,Tittemore and Wisdom (1989) have shown that Miranda can escape from the resonance with a high orbital inclination, providing a convincing explanation for the currently observed 4.4° value. The 5/3 Miranda-Ariel MMR, could also have increased this value, not being however as important as the 3/1 MMR (Tittemore and Wisdom 1990).

When analysing more distant MMR with a more complete analytical model that studies the effect of eccentricity and inclination simultaneously, Tittemore and Wisdom (1990) concluded that, if the system had encountered the 2/1 MMR, it would be most likely trapped on it until the present days. This is an important result, since it imposes a threshold to the maximum tidal migration rate of the satellites.

In a recent work, Ćuk et al. (2020) revisited the passage through the 5/3 MMR using a N-body symplectic numerical integrator, which includes the five main satellites, non-planar orbits, and spin evolution. They started their simulations with the current eccentricities and adopted nearly zero inclination for all satellites ($< 0.1°$), and confirmed that low initial eccentricities translate into capture in resonance,
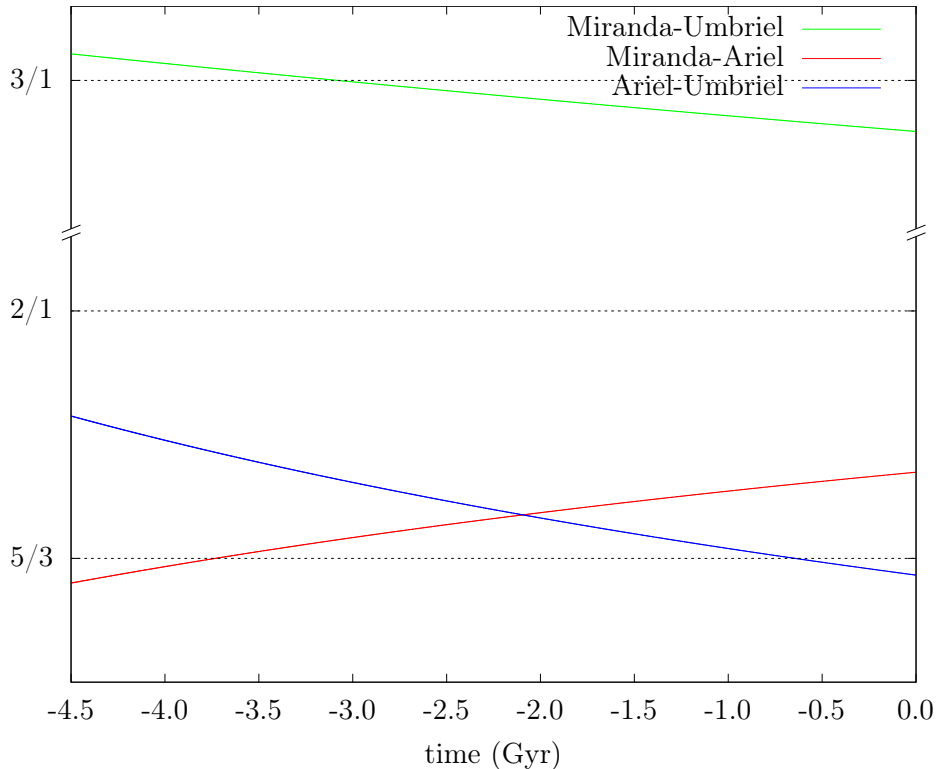
Figure 1.4: Mean motion ratio evolution between Miranda, Ariel, and Umbriel, assuming tidal induced migration without MMR capture.

which can nevertheless be broken after some time due to some chaotic excitation of the eccentricities. Furthermore, they suggested that the high inclination of Miranda can be explained not with the 3/1 Miranda-Ariel MMR, as proposed by Tittemore and Wisdom (1989), but as a consequence of the more recent 5/3 Ariel-Umbriel MMR. This is a surprising result, since Miranda is not involved in the 5/3 MMR. However, the simulations also show that during the resonance passage, the inclination of all satellites are severely affected. At the time of the resonance break, the satellites present relatively high inclinations, with Ariel and Umbriel escaping resonance with inclinations of $\sim 0.1°$. To decrease the inclinations to the currently observed values, the authors resort to a series of secular resonances among the moon's secular modes. These secular resonances transfer eccentricity and inclination from the orbits of Ariel, Titania, and Oberon to that of Umbriel. Although Ćuk et al. (2020) took a purely numerical approach with a more robust method, the authors fail to reproduce the current orbital architecture.

1.5   Objectives and manuscript outline

Tittemore and Wisdom (1988, 1989) and Ćuk et al. (2020) present contradictory conclusions. Neither of these studies present a final result capable of explaining the full dynamical history of the Uranian system. Despite using a more complete model, Ćuk et al. (2020) did not explore the system analytically, not providing physical explanation for the dynamical evolution during the resonance crossing. On the other hand, Tittemore and Wisdom (1988), using the planar approximation, did not fully capture the richness of the dynamics of Uranian moons. Besides, more than three decades passed, and the current computational capabilities far exceed what the authors had at their disposal at the time. Therefore, in this work we pursue the Tittemore and Wisdom (1988, 1989, 1990) methodology, and engage in a complete study of the dynamical evolution of the Uranian system.

We begin in Chapter 2 by describing the N-body problem with tides and spin, similar to Ćuk et al. (2020). Using this model, we analyse the evolution of the Uranian satellites shortly after the dissipation of the accretion disk, 4.5 Gyr ago. Applying the N-body problem, we have undergone in a series of nu-

merical simulations and described the dynamical events that could have shaped the orbital architecture of the satellites. In Chapter 3, we introduce a conservative secular two-satellite model with low eccentricities and inclinations using complex Cartesian coordinates. Next, in Chapter 4, we added dissipative tidal effects to the conservative model, and investigated the morphology of the passage through the 5/3 MMR between Ariel and Umbriel in the coplanar approximation and in the circular approximation. In Chapter 5, we performed massive numerical simulations to estimate the individual effects of eccentricity and the inclination for the outcome of the passage through the resonance. Afterwards, the same methodology was used to ascertain the passage with both inclination and eccentricity simultaneously. Finally, we used the insights gained to simulate the five regular satellites with the N-body model.

Chapter 2

N-body problem

The classic N-body problem consists of some initial configuration of N bodies, represented as point-mass particles, under the action of Newton's law of gravitation. By taking into account extended bodies, a wide range of physical effects can be added to the model, such as their spin and oblateness, as well as tidal effects. However, the N-body problem it is not integrable and numerical methods are generally used.

In this chapter, we begin by describing the N-body problem in the approximation of point-mass particles (Sect. 2.1). Then, the contribution from rotation of the central mass (Sect. 2.2) and deformations from mutual gravitational interactions are developed (Sect. 2.3). Finally, in Sect. 2.4, we use a numerical integrator to study different stages of the dynamical evolution of the Uranus' satellites and constrain some properties of the system.

2.1 Point-mass particles

Consider a system with $N+1$ bodies, with masses m_k, where $m_0 \gg m_{k \neq 0}$. The Hamiltonian of the system is given by (e.g. Meyer and Hall 1992)

$$\mathcal{H} = \sum_{k=0}^{N} \frac{\mathbf{P}_k^2}{2m_k} - \sum_{k=0}^{N} \sum_{j>k}^{N} \frac{\mathcal{G}m_j m_k}{|\mathbf{R}_k - \mathbf{R}_j|} , \tag{2.1}$$

where $\mathcal{G}$ is the gravitational constant, $\mathbf{R}_k$ the position vector of m_k relatively to an inertial frame centred at O (see Fig.2.1) and the linear momentum $\mathbf{P}_k = m_k \dot{\mathbf{R}}_k$ is the conjugated momenta of $\mathbf{R}_k$. The first term of $\mathcal{H}$ is the total orbital kinetic energy and the second term is the gravitational potential energy.
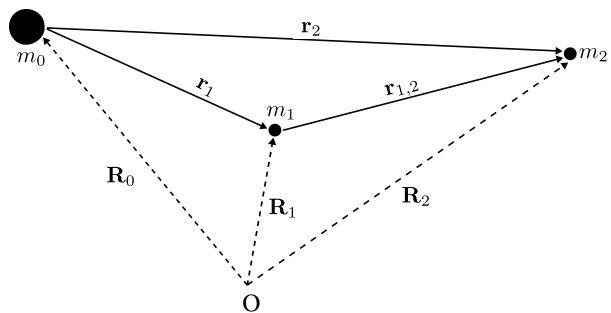
Figure 2.1: Schematic representation of a three-body system, with a massive central body, m_0, and two smaller masses, m_1 and m_2. The capital letters represent the position vector of each mass in an inertial reference frame, centred at O. The lower case letters represent the position vectors of each mass with respect to the centre of mass of m_0, with $r_1 < r_2$.

We now introduce a new set of canonical coordinates. We let (Laskar and Robutel 1993)

$$\mathbf{p}_0 = \mathbf{P}_{\mathrm{CM}} = \sum_{k=0}^{N} \mathbf{P}_k \quad \text{and} \quad \mathbf{p}_k = \mathbf{P}_k \quad (k \neq 0), \tag{2.2}$$

where $\mathbf{p}_0$ is the total linear momentum of the system. Using a type 2 generating function (S_2):

$$S_2 = \mathbf{P}_0 \cdot \mathbf{R}_0 + \sum_{k=1}^{N} \mathbf{P}_k \cdot \mathbf{R}_k = \left(\mathbf{p}_0 - \sum_{k=1}^{N} \mathbf{p}_k \right) \cdot \mathbf{R}_0 + \sum_{k=1}^{N} \mathbf{p}_k \cdot \mathbf{R}_k, \tag{2.3}$$

the canonical conjugates of $\mathbf{p}_0$ and $\mathbf{p}_k$ are obtained by $\mathbf{r}_0 = \partial S_2 / \partial \mathbf{p}_0$ and $\mathbf{r}_k = \partial S_2 / \partial \mathbf{p}_k$, yielding to

$$\mathbf{p}_0, \qquad \mathbf{r}_0 = \mathbf{R}_0, \tag{2.4}$$

$$\mathbf{p}_k, \qquad \mathbf{r}_k = \mathbf{R}_0 - \mathbf{R}_k. \tag{2.5}$$

We note that $\dot{\mathbf{P}}_{\mathrm{CM}} = 0$, thus, $\mathbf{p}_0 = $ constant. For simplicity, we can adopt $\mathbf{p}_0 = 0$. Substituting the new set of canonical coordinates into the Hamiltonian (2.1), we get

$$\mathcal{H} = \sum_{k=1}^{N} \left(\frac{\mathbf{p}_k^2}{2\beta_k} - \frac{\beta_k \mu_k}{r_k} \right) + \sum_{k=1}^{N} \sum_{j>k}^{N} \left(\frac{\mathbf{p}_j \cdot \mathbf{p}_k}{m_0} - \frac{\mathcal{G} m_j m_k}{|\mathbf{r}_k - \mathbf{r}_j|} \right), \tag{2.6}$$

where $\mu_k = \mathcal{G}(m_0 + m_k)$, $\beta_k = \frac{m_0 m_k}{m_0 + m_k}$ is the reduced mass, and $r_k = |\mathbf{r}_k|$.

The equations of motion are simply obtained using the Hamiltonian formalism by

$$\dot{\mathbf{r}}_k = \frac{\partial \mathcal{H}}{\partial \mathbf{p}_k} \quad \text{and} \quad \dot{\mathbf{p}}_k = -\frac{\partial \mathcal{H}}{\partial \mathbf{r}_k}, \tag{2.7}$$

yielding to

$$\dot{\mathbf{r}}_k = \frac{\mathbf{p}_k}{\beta_k} + \sum_{j \neq k}^{N} \frac{\mathbf{p}_j}{m_0}, \tag{2.8}$$

and

$$\dot{\mathbf{p}}_k = -\beta_k \mu_k \frac{\mathbf{r}_k}{r_k^3} - \sum_{j \neq k} \mathcal{G} m_j m_k \frac{\mathbf{r}_k - \mathbf{r}_j}{|\mathbf{r}_k - \mathbf{r}_j|^3}. \tag{2.9}$$

2.2   Permanent quadrupole moment

The mass of a real body is not constrained to a single adimensional point, but is distributed over some volume, $\mathcal{V}_0$. We thus now consider the gravitational potential energy of an extended body with mass m_0, acting on an external mass m, from any distance from its centre of mass.

The potential energy at an arbitrary position $\mathbf{R}$ outside m_0 is given by

$$U(\mathbf{R}) = -\int_{\mathcal{V}_0} \frac{\mathcal{G} m}{|\mathbf{R} - \mathbf{R}'|} dm', \tag{2.10}$$

where m is an arbitrary mass at $\mathbf{R}$ and $\mathbf{R}'$ is the position vector relatively to the origin of the referential (O) of the mass element dm' (Fig.2.2), with $m_0 = \int dm'$.

It is convenient to express the potential energy in a referential fixed in the centre of mass of m_0, located at $\mathbf{R}_0$. We let $\mathbf{r} = \mathbf{R} - \mathbf{R}_0$ and $\mathbf{r}' = \mathbf{R}' - \mathbf{R}_0$. Then the denominator of Eq. (2.10) becomes

$$\frac{1}{|\mathbf{R} - \mathbf{R}'|} = \frac{1}{|\mathbf{r} - \mathbf{r}'|} = \frac{1}{\sqrt{r^2 + r'^2 - 2\,\mathbf{r} \cdot \mathbf{r}'}}. \tag{2.11}$$
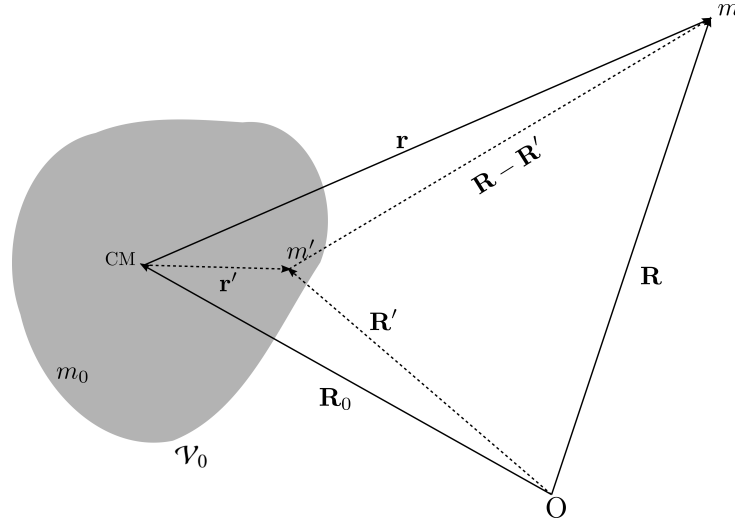
Figure 2.2: Scheme of the position vectors of an arbitrary mass m on the vicinity of an extended body m_0 with volume $\mathcal{V}_0$. The capital letters are the position vectors on an inertial reference frame, centred at O. The lower case vectors are the position vectors on the reference frame of the centre of mass (CM) of m_0.

Let θ be the angle between the vectors $\mathbf{r}'$ and $\mathbf{r}$, and consider that $r' \ll r$. Expanding Eq. (2.11) in Taylor series up to $(r'/r)^3$, yields to (quadrupolar approximation)

$$\frac{1}{r}\left[1 + \left(\frac{r'}{r}\right)^2 - \frac{r'}{r}\cos\theta\right]^{-1} = \frac{1}{r}\left[1 + \frac{r'}{r}\cos\theta + \left(\frac{3}{2}\cos^2\theta - \frac{1}{2}\right)\left(\frac{r'}{r}\right)^2\right] + O\left(\frac{r'}{r}\right)^3. \tag{2.12}$$

Substituting the Eq. (2.12) on (2.10), we obtain a more convenient expression for the potential energy

$$U(\mathbf{r}) = -\frac{Gm}{r}\left(\int dm' - \frac{1}{r}\int r'\cos\theta\, dm' + \frac{1}{2r^2}\int r'^2\, dm' - \frac{3}{2r^2}\int r'^2\cos^2\theta\, dm'\right) + O\left(\frac{r'}{r}\right)^3. \tag{2.13}$$

Let us analyse each term of the equation individually. The first integral is simply the total mass, $\int dm' = m_0$. Since we set the centre of mass of m_0 as the origin of the referential, $\mathbf{r}_{\mathrm{CM}} = 0$, the second integral becomes

$$\int r'\cos\theta\, dm' = \frac{1}{r}\int \mathbf{r}' \cdot \mathbf{r}\, dm' = m_0 \frac{\mathbf{r}_{\mathrm{CM}} \cdot \mathbf{r}}{r} = 0. \tag{2.14}$$

To compute the remaining terms of Eq. (2.13), we can introduce the principal moments of inertia, $\mathcal{A}$, $\mathcal{B}$, and $\mathcal{C}$, defined as

$$\mathcal{A} = \int (y^2 + z^2)\, dm', \quad \mathcal{B} = \int (z^2 + x^2)\, dm' \quad \text{and} \quad \mathcal{C} = \int (x^2 + y^2)\, dm', \tag{2.15}$$

with $\mathbf{r}' = x\,\mathbf{e}_x + y\,\mathbf{e}_y + z\,\mathbf{e}_z$, where $(\mathbf{e}_x, \mathbf{e}_y, \mathbf{e}_z)$ are the axes of symmetry of m_0 (see Fig. 2.3), and $\mathbf{e_z}$ is the axis of rotation. We can replace the principal moments of inertia in the third term of Eq. (2.13), leading to

$$\int r'^2\, dm' = \int (x^2 + y^2 + z^2)\, dm' = \frac{\mathcal{A} + \mathcal{B} + \mathcal{C}}{2}. \tag{2.16}$$

Analogously, the fourth term of the potential energy equation can be written in terms of the principal moments of inertia as

$$\int r'^2 \cos^2\theta\, dm' = \frac{1}{r^2}\int (\mathbf{r}' \cdot \mathbf{r})^2 dm'$$
$$= \frac{1}{r^2}\left(\frac{-\mathcal{A} + \mathcal{B} + \mathcal{C}}{2}r^2 - (\mathcal{B} - \mathcal{A})(\mathbf{r} \cdot \mathbf{e}_y)^2 - (\mathcal{C} - \mathcal{A})(\mathbf{r} \cdot \mathbf{e}_z)^2\right). \tag{2.17}$$
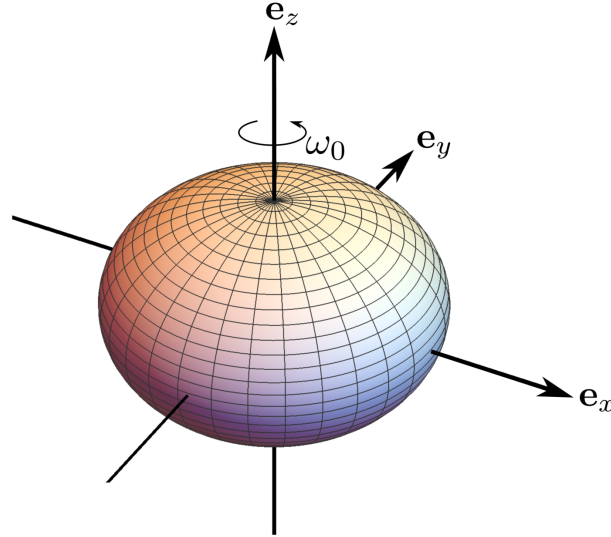
Figure 2.3: Rotational deformation of a body rotating around the $\mathbf{e}_z$ axis. Adapted from Murray and Dermott (1999).

Thus, the potential of an extended body to the quadrupolar order (Eq. (2.13)) can then be written as

$$U(\mathbf{r}) = -\frac{\mathcal{G}m_0 m}{r} - \frac{\mathcal{G}m}{2r^3}\left[(\mathcal{B}-\mathcal{A})\left(1 - 3\frac{(\mathbf{r}\cdot\mathbf{e}_y)^2}{r^2}\right) + (\mathcal{C}-\mathcal{A})\left(1 - 3\frac{(\mathbf{r}\cdot\mathbf{e}_z)^2}{r^2}\right)\right] + O\left(\frac{r'}{r}\right)^3 . \qquad (2.18)$$

A body rotating around the $\mathbf{e}_z$ axis undergoes more intense centrifugal forces in the equatorial region than in the poles. This induces a flattening of the body, where the polar radius decreases, while the equatorial radius increases evenly (see Fig.2.3). Therefore, the rotational flattening maintains the symmetry between $\mathbf{e}_x$ and $\mathbf{e}_y$. Within this regime, from Eq. (2.15) we can conclude that $\mathcal{A} \approx \mathcal{B}$, and Eq. (2.18) takes the simpler form

$$U(\mathbf{r}) \approx -\frac{\mathcal{G}m_0 m}{r} - \frac{\mathcal{G}m(\mathcal{C}-\mathcal{A})}{2r^3}\left(1 - 3\frac{(\mathbf{r}\cdot\mathbf{e_z})^2}{r^2}\right) . \qquad (2.19)$$

The difference between the principal moments of inertia $(\mathcal{C}-\mathcal{A})$ gives us a measure for the rotational flattening of the body. This quantity can be related to the second order gravity field coefficient,

$$J_2 = \frac{\mathcal{C}-\mathcal{A}}{mR^2} . \qquad (2.20)$$

It depends on the angular velocity, ω, the radius, R, and the susceptibility of the body to deform.

Substituting the principal moments of inertia by Eq. (2.20), the potential energy can be finally rewritten as

$$U(\mathbf{r}) \approx -\frac{\mathcal{G}m_0 m}{r} - \frac{\mathcal{G}m_0 m R_0^2}{2r^3}J_{2_0}\left(1 - 3\frac{(\mathbf{r}\cdot\boldsymbol{\omega}_0)^2}{r^2\omega_0^2}\right) . \qquad (2.21)$$

The first term of Eq. (2.21) corresponds to the potential energy of a point-like mass body (Eq. (2.1)). The second term is the potential energy due to the rotation of a rigid body (U_{cent}). The rotational kinetic energy is given by (e.g. Goldstein et al. 2002)

$$T_{\text{rot}} = \frac{1}{2}\boldsymbol{\omega}_0 \cdot \mathbf{L}_0 , \qquad (2.22)$$

where $\mathbf{L}_0 = C_0\,\boldsymbol{\omega}_0$ is the rotational angular momentum of m_0 and $\boldsymbol{\omega}_0 = \omega_0\,\mathbf{e_z}$ is the angular velocity vector.

The additional Hamiltonian contribution of the rotational deformation is then the sum of the rotation potential energy and the rotational kinetic energy of m_0, that is, $\mathcal{H}_{\text{rot}} = U_{\text{cent}} + T_{\text{rot}}$. Using the Hamiltonian formulation, from Eqs. (2.21) and (2.22) we can obtain the variation of linear momentum of m,

$$\dot{\mathbf{p}} = \frac{\partial \mathcal{H}}{\partial \mathbf{r}} = -3 \mathcal{G} m_0 m R_0^2 J_{2_0} \left[2 \frac{\mathbf{r} \cdot \mathbf{e}_z}{r^5} \mathbf{e}_z - \left(\frac{1}{r^5} + 5 \frac{(\mathbf{r} \cdot \mathbf{e}_z)^2}{r^7} \right) \mathbf{r} \right] . \tag{2.23}$$

The variation of the angular momentum, that is, the torque ($\boldsymbol{\Gamma}$), is obtained by

$$\dot{\mathbf{L}}_{\text{orb}} = \boldsymbol{\Gamma}_{\text{orb}} = \mathbf{R}_0 \times \dot{\mathbf{P}}_0 + \mathbf{R} \times \dot{\mathbf{P}} . \tag{2.24}$$

However, the total linear momentum is conserved. This means that $\dot{\mathbf{P}}_0 = -\dot{\mathbf{P}}$, and Eq. (2.24) can be written as

$$\boldsymbol{\Gamma}_{\text{orb}} = \mathbf{r} \times \dot{\mathbf{p}} , \tag{2.25}$$

leading to (Eq. (2.23)),

$$\boldsymbol{\Gamma}_{\text{orb}} = -6 \mathcal{G} m_0 m R_0^2 J_{2_0} \frac{\mathbf{r} \cdot \mathbf{e}_z}{r^5} (\mathbf{r} \times \mathbf{e}_z) . \tag{2.26}$$

Since the total angular momentum is conserved, that is, $\dot{\mathbf{L}}_{\text{orb}} + \dot{\mathbf{L}}_{\text{rot}} = 0$, the rotational angular momentum variation is simply obtained by $\boldsymbol{\Gamma}_{\text{rot}} = -\boldsymbol{\Gamma}_{\text{orb}}$, that is,

$$\dot{\mathbf{L}}_{\text{rot}} = \boldsymbol{\Gamma}_{\text{rot}} = 6 \mathcal{G} m_0 m R_0^2 J_{2_0} \frac{\mathbf{r} \cdot \mathbf{e}_z}{r^5} (\mathbf{r} \times \mathbf{e}_z) . \tag{2.27}$$

2.3 Tidal deformation

In the previous section, we considered the effect of the rotational deformation of a body. Here, we consider another kind of perturbation to the gravitational potential energy due to the presence of an external body, known as tidal effects. Tides arise from differential and inelastic deformations of an extended body owing to the gravitational effect of a perturbing mass. The resulting distortion gives rise to a tidal bulge, which modifies the gravitational potential of the extended body (see Fig. 2.5).

Let us consider the configuration of Fig. 2.4, where m_1 is orbiting m_0. The gravitational potential raised by m_1 at an arbitrary point $\mathbf{r}'$ of the extended body m_0 in the frame of the centre of mass is

$$\begin{aligned} V(\mathbf{r}', \mathbf{r}_1) &= -\mathcal{G} \frac{m_1}{|\mathbf{r}_1 - \mathbf{r}'|} = \mathcal{G} \frac{m_1}{r_1} \left(1 - \left(\frac{r'}{r_1} \right) \cos \theta + \left(\frac{r'}{r_1} \right)^2 \right)^{-\frac{1}{2}} \\ &= -\mathcal{G} \frac{m_1}{r_1} \sum_{l=0}^{\infty} \left(\frac{r'}{r_1} \right)^l \mathcal{P}_l(\cos \theta) , \end{aligned} \tag{2.28}$$

where $\mathcal{P}_l(\cos \theta)$ are the Legendre polynomials. We have (e.g. Goldstein et al. 2002),

$$\mathcal{P}_0(x) = 1 , \quad \mathcal{P}_1(x) = x , \quad \mathcal{P}_2(x) = \frac{3}{2} x^2 - \frac{1}{2} . \tag{2.29}$$

The first term ($l = 0$) corresponds to the potential at the centre of mass of m_0 (Eq. (2.1)). Since we describe the problem in the frame of the centre of mass, the second term ($l = 1$), by Eq. (2.14), disappears from the Hamiltonian. The third term, with the second-degree Legendre polynomial (Eq. (2.29)), corresponds to the influence of the external body differential gravitational potential on m_0. Assuming $r_1 \gg r'$, the differential gravitational potential (Eq. (2.28)) can be approximated only by the second order of the Legendre polynomial (quadrupolar approximation),

$$V(\mathbf{r}', \mathbf{r}_1) = -\frac{\mathcal{G} m_1}{2 r_1^2 r'} \left(\frac{r'}{r_1} \right)^2 (3 \mathbf{r}_1 \cdot \mathbf{r}' - 2 r_1 r') + O\left(\frac{r'}{r_1} \right)^3 . \tag{2.30}$$
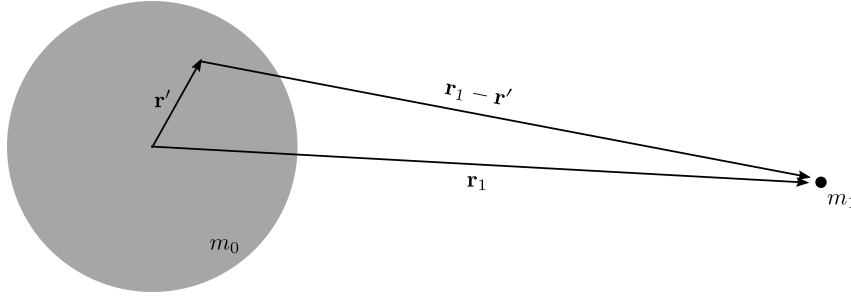
Figure 2.4: Scheme of the position vectors of a perturber, m_1, on the vicinity of m_0.

So far, we have only taken into account the influence of m_1 on m_0. However, the self-gravity of m_0 and its composition induces an opposition to the differential deformation. The response of the internal mass distribution of a body to a gravitational disturbance can be expressed in terms of Love numbers (e.g. Kellermann et al. 2018). At the surface of m_0, i.e., when $r' = R_0$, the tidal potential then becomes (Mignard 1979)

$$V(\mathbf{R}_0, \mathbf{r}_1) = -\frac{\mathcal{G}m_1 k_{2_0}}{2r_1^5} \left(3(\mathbf{R}_0 \cdot \mathbf{r}_1)^2 - R_0^2\, r_1^2 \right), \tag{2.31}$$

where k_{2_0} is the second Love number of m_0. The tidal potential generated by the deformed body at a generic point $\mathbf{r}$ from its centre of mass can be obtained through the Laplace equation

$$\nabla^2 V_t(\mathbf{r}) = 0. \tag{2.32}$$

The boundary conditions of the equation are the potential at the surface and the potential at very distant points. At the surface, the tidal potential is given by Eq. (2.31), while at infinity the tidal potential simply vanishes, that is, $V_t(|\mathbf{r}| \to \infty) = 0$. Applying these boundary conditions to the solution of the Laplace equation (Eq. (2.32)), we obtain a unique solution of the tidal potential of m_0 at a distance $\mathbf{r}$ from the centre of mass

$$V_t(\mathbf{r}, \mathbf{r_1}) = -\frac{\mathcal{G}m_1 k_{2_0} R_0^5}{2r_1^5\, r^5} \left(3(\mathbf{r} \cdot \mathbf{r}_1)^2 - r^2\, r_1^2 \right). \tag{2.33}$$

The response of the extended body to an external potential, although very fast, is not instantaneous. In general, the perturbing body m_1 is moving with respect to m_0, which rotates with an angular velocity of $\boldsymbol{\omega}_0$ (see Fig. 2.5). Therefore, we have to impose a correction to $\mathbf{r}_1$. Let us consider that m_0 takes a time τ_0 to respond to the perturbing potential. Then, the corrected $\mathbf{r}_1'(t)$ is $\mathbf{r}_1'(t) = \mathbf{r}_1(t - \tau_0)$. Taking the weak friction model (e.g. Singer 1968; Alexander 1973), which assumes a constant and small τ, we can assume the linear approximation (e.g. Mignard 1979), that is,

$$\mathbf{r}_1' \approx \mathbf{r}_1 + \tau_0(\boldsymbol{\omega}_0 \times \mathbf{r}_1 - \dot{\mathbf{r}}_1). \tag{2.34}$$

Substituting $\mathbf{r}_1'$ in Eq. (2.33), and retaining only the first order terms in τ_0, we get for the tidal potential

$$\begin{aligned}
V_t(\mathbf{r}, \mathbf{r}_1) = &-\frac{\mathcal{G}m_1\, k_{2_0} R_0^5}{2\, r_1^5\, r^5} \left(3(\mathbf{r} \cdot \mathbf{r}_1)^2 - r^2\, r_1^2 \right) \\
&-\frac{3\mathcal{G}m_1\, k_{2_0}\, R_0^5}{r_1^5\, r^5} \tau_0 \bigg((\mathbf{r} \cdot \mathbf{r}_1) \left[\mathbf{r}_1 \cdot (\boldsymbol{\omega}_0 \times \mathbf{r}) + \mathbf{r} \cdot \dot{\mathbf{r}}_1 \right] - \frac{\mathbf{r}_1 \cdot \dot{\mathbf{r}}_1}{2r_1^2} \left[5(\mathbf{r} \cdot \mathbf{r}_1)^2 - r^2\, r_1^2 \right] \bigg).
\end{aligned} \tag{2.35}$$

For a body with mass m at $\mathbf{r}$ interacting with the tidal potential, we compute the tidal potential energy simply as $U_t(\mathbf{r}, \mathbf{r}_1) = mV_t(\mathbf{r}, \mathbf{r}_1)$. Using Eq. (2.7), the variation of linear momentum of the interacting

body with mass m with respect to m_0 is given by

$$
\begin{aligned}
\dot{\mathbf{p}}(\mathbf{r}, \mathbf{r}_1) = & -\frac{\mathcal{G}m\,m_1\,k_{2_0}R_0^5}{2\,r_1^5\,r^5}\left(6(\mathbf{r}\cdot\mathbf{r}_1) - 15\left(\frac{\mathbf{r}\cdot\mathbf{r}_1}{r}\right)^2 + 3\,r_1^2\right)\mathbf{r} \\
& -\frac{3\mathcal{G}m\,m_1\,k_{2_0}R_0^5}{r_1^5\,r^7}\tau_0\left(-5(\mathbf{r}\cdot\mathbf{r}_1)\left[\mathbf{r}_1\cdot\boldsymbol{\omega}_0\times\mathbf{r}+\mathbf{r}\cdot\dot{\mathbf{r}}_1\right] + 5\frac{\mathbf{r}_1\cdot\dot{\mathbf{r}}_1}{2\,r_1^2}\left[5(\mathbf{r}\cdot\mathbf{r}_1)^2 - r^2\,r_1^2\right]\right)\mathbf{r} \\
& -\frac{3\mathcal{G}m\,m_1\,k_{2_0}R_0^5}{r_1^5\,r^5}\tau_0\left(\left[\mathbf{r}_1\cdot\boldsymbol{\omega}_0\times\mathbf{r}+\mathbf{r}\cdot\dot{\mathbf{r}}_1\right]\mathbf{r}_1 + (\mathbf{r}\cdot\mathbf{r}_1)\left[\mathbf{r}_1\times\boldsymbol{\omega}_0+\dot{\mathbf{r}}_1\right]\right. \\
& \left. -\frac{\mathbf{r}_1\cdot\dot{\mathbf{r}}_1}{r_1^2}\left[5(\mathbf{r}\cdot\mathbf{r}_1)\mathbf{r}_1 - r_1^2\,\mathbf{r}\right]\right).
\end{aligned}
\tag{2.36}
$$

When the interacting body is the same as the perturbing body, we can replace $\mathbf{r} = \mathbf{r}_1$ and $m = m_1$, and obtain the variation of linear momentum of m_1,

$$
\dot{\mathbf{p}}_1 = \frac{3\mathcal{G}m_1^2 k_{2_0}R_0^5}{r_1^8}\mathbf{r}_1 - \frac{3\mathcal{G}m_1^2 k_{2_0}R_0^5}{r_1^8}\tau_0\left(2\frac{\mathbf{r}_1\cdot\dot{\mathbf{r}}_1}{r_1^2}\mathbf{r}_1 + \mathbf{r}_1\times\boldsymbol{\omega}_0 + \dot{\mathbf{r}}_1\right).
\tag{2.37}
$$

The variation of orbital angular momentum of m_0 can be obtained using Eq. (2.25),

$$
\boldsymbol{\Gamma}_{\text{orb}} = -\frac{3\mathcal{G}m_1^2 k_{2_0}R_0^5}{r_1^8}\tau_0\left((\mathbf{r}_1\cdot\boldsymbol{\omega}_0)\mathbf{r}_1 - r_1^2\boldsymbol{\omega}_0 + \mathbf{r}_1\times\dot{\mathbf{r}}_1\right).
\tag{2.38}
$$

The variation of rotational angular momentum is given using the same arguments used in Eq. (2.27), that is, $\dot{\mathbf{L}}_{\text{orb}} + \dot{\mathbf{L}}_{\text{rot}} = 0 \rightarrow \boldsymbol{\Gamma}_{\text{rot}} = -\boldsymbol{\Gamma}_{\text{orb}}$, resulting in

$$
\boldsymbol{\Gamma}_{\text{rot}} = \frac{3\mathcal{G}m_1^2 k_{2_0}R_0^5}{r_1^8}\tau_0\left((\mathbf{r}_1\cdot\boldsymbol{\omega}_0)\mathbf{r}_1 - r_1^2\boldsymbol{\omega}_0 + \mathbf{r}_1\times\dot{\mathbf{r}}_1\right).
\tag{2.39}
$$

2.3.1 Specific dissipation factor

Tidal forces dissipate energy due to inelastic deformations inside the extended body. To measure the strength of the tidal dissipation, we introduce the specific dissipation factor, Q, which is a measure of the fraction of energy dissipated over one tidal cycle. It can be calculated using

$$
Q = \frac{2\pi E_0}{\Delta E},
\tag{2.40}
$$

where ΔE is the energy dissipated over one cycle and E_0 is the peak energy stored over one cycle (Murray and Dermott 1999). The lower is Q, the greater is the energy dissipated by tides.

Due to the periodic nature of the tidal effects, the response is often compared to a forced harmonic oscillator, which can be described by

$$
\ddot{x} = -\omega_0^2 x - \frac{1}{\tau}\dot{x} + \frac{F}{m}\cos(\omega t),
\tag{2.41}
$$

where x is the position of the tidal bulge, ω_0 is the natural frequency of the oscillator, τ is the damping timescale, F/m is the amplitude of the external force and ω the frequency of the external force. Using the trial function $x = A\cos(\omega t - \delta)$ in Eq. (2.41) we get (Murray and Dermott 1999)

$$
A = \frac{F}{m}\left[(\omega_0^2 - \omega^2)^2 + \left(\frac{\omega}{\tau}\right)^2\right]^{-1/2} \quad \text{and} \quad \sin\delta = \frac{\omega}{\tau}\left[(\omega_0^2 - \omega^2)^2 + \left(\frac{\omega}{\tau}\right)^2\right]^{-1/2}.
\tag{2.42}
$$

This comparison allow us to calculate both energies present on Eq. (2.40). The energy dissipated over one cycle (ΔE) is equivalent to the work done by the drag force, that is,

$$
\Delta E = \int_0^{\frac{2\pi}{\omega}} -\frac{m}{\tau}\dot{x}dx = -\frac{m}{\tau}\int_0^{\frac{2\pi}{\omega}}\ddot{x}xdt = -\frac{A^2 m\pi\omega}{\tau},
\tag{2.43}
$$
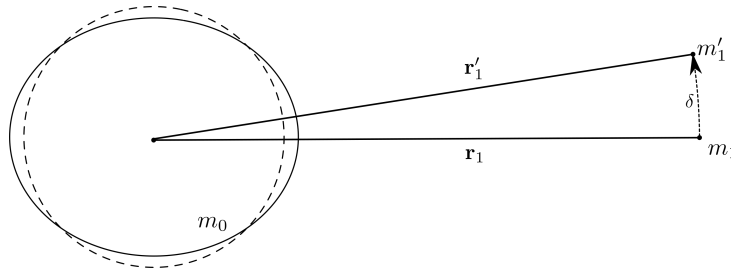
Figure 2.5: Phase shift of the tidal lag. The dashed lines of m_0 correspond to the volume shape of the body without a gravitational interaction. The solid line correspond to tidally elongated shape due to perturbation of m_1. The primed quantities represent the position of m_1 at the time m_0 reaches maximum elongation.

while the energy stored during the cycle (E_0) is the work done by the restoring force, i.e., the elastic force on our comparison, described as

$$E_0 = \int_0^A -m\omega_0^2 x\, dx = -\frac{1}{2}m\omega_0^2 A^2 \,. \tag{2.44}$$

If $\omega_0 \gg \omega$, the system is not close to any resonance and, from Eq. (2.42), we conclude that

$$Q = \frac{1}{\sin \delta} \,, \tag{2.45}$$

where δ is the phase lag between the position of the perturber at the time of the interaction and the position of the perturber at the moment of maximum tidal elongation (Fig. 2.5). The specific dissipation function is then related to the phase shift between the perturbing potential and the maximum deformation of the body. This means that if there is no displacement between the perturbing potential and the tidal bulge, there is no tidal energy dissipation.

2.3.2 Tidal evolution equations

Tidal effects can modify the long-term evolution of the orbit and spin. It is thus important to understand the consequences of these effects. Consider the system composed by m_0 and m_1 (Fig. 2.4). The total angular momentum of the system (assuming zero inclinations and zero obliquities), is given by (e.g. Murray and Dermott 1999),

$$L = \mathbf{L} \cdot \mathbf{e_z} = C_0\omega_0 + \frac{m_1 m_0}{m_1 + m_0}a_1^2 n_1 \,, \tag{2.46}$$

where ω_0 and C_0 are the angular velocity and moment of inertia of m_0, respectively, and a_1 and n_1 are the semi-major axis and mean motion (Eq. (A.22)) of m_1. Since $\mathbf{L}$ is conserved ($\dot{\mathbf{L}} = 0$),

$$C_0\dot{\omega}_0 = -\frac{m_1 m_0}{2(m_1 + m_0)}n_1 a_1 \dot{a}_1 \,. \tag{2.47}$$

We note that, $C_0\dot{\omega}_0 = \mathbf{\Gamma}_{\text{rot}} \cdot \mathbf{e_z}$. Assuming circular orbits, we have that $r_1 = a_1$, which yields to (Eq. (2.39))

$$\dot{\omega}_0 = -\frac{3\mathcal{G}m_1^2}{C_0 a_1}\left(\frac{R_0}{a_1}\right)^5 (\omega_0 - n_1)\, k_{2_0}\tau_0 \,. \tag{2.48}$$

Due to the conservation of $\mathbf{L}$ (Eq. (2.47)), we also have that

$$\dot{a}_1 = -\frac{2(m_1 + m_0)}{m_1 m_0 n_1 a_1}C_0\dot{\omega}_0 = 6\frac{m_1}{m_0}\left(\frac{R_0}{a_1}\right)^5 (\omega_0 - n_1)\, k_{2_0}\tau_0\, n_1 a_1 \,. \tag{2.49}$$

The total energy, considering circular orbits, is given by the rotational energy of m_0 plus the orbital energy of m_1,

$$E = \frac{C_0 \omega_0^2}{2} - \mathcal{G}\frac{m_1 m_0}{2a_1} \,. \tag{2.50}$$

The variation of the energy is then given by

$$\dot{E} = C_0 \omega_0 \dot{\omega}_0 + \frac{m_1 m_0}{2(m_1 + m_0)}n_1^2 a_1 \dot{a}_1 \,. \tag{2.51}$$

Replacing Eqs. (2.48) and (2.49) in Eq. (2.51) leads to

$$\dot{E} = -\frac{3\mathcal{G}m_1}{a_1}\left(\frac{R_0}{a_1}\right)^5 (\omega_0 - n_1)^2\, k_{2_0}\tau_0 < 0 \,. \tag{2.52}$$

That is, for $\omega_0 \neq n_1$, the energy of the system always decreases due to the tidal dissipation.

The results obtained in this section show that tidal forces are responsible for the migration of the orbits. At the same time, due to the conservation of the total angular momentum, the rotation rate of the extended body also varies. In other words, the system transfers angular momentum from the spin of m_0 to the orbit of m_1. The direction of the migration is determined by the sign of the difference between the rotation rate of m_0 and the mean motion of m_1. If the mean motion is smaller than the rotation rate ($\omega_0 > n_1$), the system evolves with an outward movement of m_1, while the rotation rate decreases. In the opposite situation, where the mean motion is higher than the rotation rate ($\omega_0 < n_1$), m_1 migrates inwards, while the rotation rate increases. This transfer of angular momentum occurs until the synchronous state is reached, where $\omega_0 = n_1$, and the dissipation of energy becomes null (Eq. (2.52)).

In a more realistic situation, the rotation rate of m_1 changes as well. In a similar way, performing the calculations for m_1, the variation of the spin rate is (Eq. (2.48))

$$\dot{\omega}_1 = -\frac{3\mathcal{G}m_0^2}{C_1 a_1}\left(\frac{R_1}{a_1}\right)^5 (\omega_1 - n_1)\, k_{2_1}\tau_1 \,. \tag{2.53}$$

Thus, if a system has sufficient time, tidal evolution changes the rotation rates and the mean motion until synchronization. This is, for instance, the case of the Moon, where the spin rate of the moon is synchronous with its own mean motion. The same is believed to occur for the five largest moons of Uranus. Indeed, the passage of Voyager 2 was too fast, so not enough data was collected to give a definite conclusion on the spin states of the moons. However, since the system most likely formed with Uranus or shortly after, the synchronous state is therefore often assumed (Smith et al. 1986).

2.4 Numerical applications

We now numerically integrate the set of N-body Eqs. (2.8), (2.9), (2.27), (2.37), and (2.39) to simulate the evolution of the Uranian system. For that purpose, we use the numerical code `spins` (Correia 2018). We take into account the spin of Uranus and the orbits of the main five satellites: Miranda, Ariel, Umbriel, Titania, and Oberon. In some simulations, we also consider the presence of the Sun (as an additional "satellite").

2.4.1 The present system

Jacobson (2014) provides the best precise estimation to date of the position and velocity vectors of the satellite's orbits, expressed on the Earth's equatorial frame (Table 2.1). From these values, we computed the corresponding elliptical elements ($a, e, I, M, \omega, \Omega$) (Appendix A), expressed in the Uranus equatorial frame (Table 2.2), as follows.

Satellite	Position (km) (X, Y, Z)	Velocity (km.s^{-1}) $(\dot{X}, \dot{Y}, \dot{Z})$
Miranda	−127430.9607930668	−0.422514450329333
	23792.64617013941	−1.271890082631948
	−3464.554580724168	6.552338419694388
Ariel	−185785.2177189803	−0.384730129923274
	42477.81018746200	−1.393752472818678
	−2109.273462727150	5.325004225204424
Umbriel	−176566.9475784755	−3.350588413391897
	89016.12833946147	−0.153568184837806
	−3.350588413391897	3.273855499527411
Titania	−221240.1941919138	−3.049048602775958
	145452.9878060127	0.138409610142017
	−346697.1461249496	1.991437563896877
Oberon	−155108.4287158760	−2.962407899779837
	181606.6634411168	0.385864135361727
	−532879.3651011410	0.993694238058708

Table 2.1: Instantaneous position and velocity vectors at 1 August 1985 on the Earth equatorial frame of the five main satellites of Uranus (Jacobson 2014).

Departing from the position vector $\mathbf{R} = (X, Y, Z)$ and the velocity vector $\dot{\mathbf{R}} = (\dot{X}, \dot{Y}, \dot{Z})$, we can compute the corresponding elliptical elements by first calculating the specific energy,

$$\mathcal{E} = \frac{\dot{\mathbf{R}}^2}{2} - \frac{\mu}{\mathrm{R}}, \tag{2.54}$$

which allows us to compute the semi-major axis , a,

$$a = -\frac{\mu}{2\mathcal{E}}. \tag{2.55}$$

The eccentricity, e, inclination, I, and longitude of the ascending node, Ω, can be obtained using the specific angular momentum vector, $\mathbf{h} = (\mathrm{h}_x, \mathrm{h}_y, \mathrm{h}_z)$ (Eq. (A.4)), by

$$e = \sqrt{1 - \frac{\mathrm{h}^2}{a\mu}}, \tag{2.56}$$

$$I = \texttt{arccos}\left(\frac{\mathrm{h}_z}{\mathrm{h}}\right), \qquad \text{and} \tag{2.57}$$

$$\Omega = \texttt{arctan}\left(-\frac{\mathrm{h}_x}{\mathrm{h}_y}\right). \tag{2.58}$$

We then compute the true anomaly, ν, using

$$\nu = \texttt{arctan}\left(\sqrt{\frac{a(1 - e^2)}{\mu}} \frac{\mathbf{R} \cdot \dot{\mathbf{R}}}{a(1 - e^2) - \mathrm{R}}\right), \tag{2.59}$$

which yields the eccentric anomaly, E^*,

$$\mathrm{E}^* = 2\texttt{arctan}\left(\sqrt{\frac{1 - e}{1 + e}} \tan\left(\frac{\nu}{2}\right)\right), \tag{2.60}$$

Figure 2.6: Scheme of the spherical trigonometric relation between Earth's and Uranus's equatorial frame, and a satellite orbit frame, and their respective angles. For further details, see Smart and Green (1977).

and the argument of the pericentre, ω,

$$\omega = \texttt{arctan}\left(\frac{Z}{(X\cos\Omega + Y\sin\Omega)\,\sin I}\right) - \nu. \tag{2.61}$$

Finally, the mean anomaly, M, is obtained from Kepler's equation (Kepler 1609)

$$M = \mathrm{E}^* - e\,\sin\left(\mathrm{E}^*\right). \tag{2.62}$$

These elliptical elements are also given in the Earth equatorial frame, but we want to express them in the Uranian equatorial reference frame. We start from the Uranus' pole orientation angles at 1 August 1985, $\alpha = 77.31003302401596°$ and $\delta = 15.172593631449473°$, obtained from the Appendix B of Jacobson (2014). Then, we calculate the obliquity and the longitude of the Uranus' equator, $\epsilon = 74.82740636855053°$ and $\psi = 167.31003302401598°$, respectively, by solving (see Fig. 2.6)

$$\cos\epsilon = \sin\delta \tag{2.63}$$

and

$$\cos\psi = -\frac{\cos\delta\sin\alpha}{\sin\epsilon}. \tag{2.64}$$

Finally, the elliptical angles expressed in the Uranian equatorial reference frame are obtained by solving (see also Fig. 2.6)

$$\cos I = \cos\epsilon\cos I' + \sin\epsilon\sin I'\cos(\Omega' - \psi), \tag{2.65}$$

$$\cos(\omega' - \omega) = \frac{\cos\epsilon - \cos I'\cos I}{\sin I'\sin I}, \qquad \text{and} \tag{2.66}$$

$$\cos\Omega = \cos\Omega'\cos(\omega' - \omega) - \sin(\Omega' - \psi)\sin(\omega' - \omega)\cos I', \tag{2.67}$$

yielding the elliptical elements presented in Table 2.2.

2.4.2 Secular modes

As the Uranian satellites orbit the central planet, mutual gravitational interactions between them lead to small oscillations in the eccentricities and inclinations over broad periods of time, known as secular variations. Through semi-analytical simplified models, it is possible to estimate the oscillation frequency associated to the eccentricity and inclination for each satellite, known as the secular modes (e.g. Dermott and Nicholson 1986). These frequencies were estimated by Laskar (1986); Laskar and Jacobson (1987) using an analytical model, called GUST (General Uranian satellite theory). Later, Malhotra et al. (1989)

Satellite	$a\,(\times 10^{-3})$ (au)	$e\,(\times 10^{-3})$	$I\,(°)$
Miranda	0.867 829 806 096 133 50	1.514 384 267 990 232 1	4.409 022 644 189 928 3
Ariel	1.275 948 662 323 624 6	1.805 443 506 830 879 5	0.016 291 682 978 667 430
Umbriel	1.777 460 690 547 404 9	4.191 314 031 279 796 3	0.063 682 350 178 256 561
Titania	2.915 953 942 255 327 8	2.691 429 331 439 770 1	0.121 328 358 382 614 83
Oberon	3.899 495 282 248 682 5	1.021 848 548 198 646 7	0.158 417 224 439 574 40

	$M\,(°)$	$\omega\,(°)$	$\Omega\,(°)$
Miranda	41.942 408 881 076 503	284.305 780 158 769 44	32.632 119 491 654 876
Ariel	33.218 135 927 489 953	63.302 552 850 506 800	262.704 359 532 296 85
Umbriel	13.588 624 937 743 543	55.213 489 878 652 354	247.494 695 744 495 12
Titania	90.650 344 474 884 832	220.392 997 600 391 08	353.260 064 668 545 00
Oberon	178.449 591 026 891 74	58.951 246 213 571 956	51.710 122 333 743 321

Table 2.2: Instantaneous elliptical elements of the five main Uranian satellites on the Uranus' equatorial frame.

revisited the results obtained with GUST, incorporating the effects of near first order mean motion resonances, as a part of the LONGSTOP program (Carpino et al. 1987; Milani et al. 1987). Since then, the estimations of the satellite masses were updated, as well as the orbital parameters (Jacobson 2014), thus, a recalculation of these frequencies is required.

Departing from the orbital solution from Table 2.2 and the physical properties from Tables 1.1 and 1.2, we integrated the system composed by Uranus, Miranda, Ariel, Umbriel, Titania, and Oberon over 100 000 years, disregarding the tidal perturbations. Through the software TRIP (Gastineau and Laskar 2011), we performed a frequency analysis of the orbits (Laskar 1990, 1993) to determine the fundamental frequencies of the eccentricities (g_k) and inclinations (s_k) of the major Uranian satellites. The results are presented in Table 2.3, alongside the results obtained by Laskar and Jacobson (1987) and Malhotra et al. (1989). The subscripts are ordered in ascending order of the semi-axis of the satellites.

The good agreement between the values in Table 2.3, allow us to conclude that the secular modes are not very sensitive to the improvements of the physical parameters of the system performed by Jacobson (2014).

	GUST (deg/yr)	LONGSTOP (deg/yr)	N-body integrator (deg/yr)		GUST (deg/yr)	LONGSTOP (deg/yr)	N-body integrator (deg/yr)
g_1	20.082	20.117	20.0417	s_1	−20.309	−20.340	−20.2408
g_2	6.217	6.186	6.2271	s_2	−6.287	−6.239	−6.2363
g_3	2.865	2.848	2.8506	s_3	−2.836	−2.790	−2.7674
g_4	2.079	2.086	2.1652	s_4	−1.843	−1.839	−1.8309
g_5	0.386	0.410	0.4063	s_5	−0.259	−0.269	−0.2677

Table 2.3: Secular modes of Miranda (g_1, s_1), Ariel (g_2, s_2), Umbriel (g_3, s_3), Titania (g_4, s_4), and Oberon (g_5, s_5).

2.4.3   Tidal evolution

Tittemore and Wisdom (1988, 1989, 1990) performed a series of studies encompassing the most important low order commensurabilities of the Uranian system. One of their observations states that if the system has crossed the 2/1 MMR between Ariel and Umbriel, escape is not likely and the system should probably remain trapped until the present days. Since Ariel and Umbriel are not presently trapped in this MMR, the system most likely never crossed it. Furthermore, their results show that the 3/1 Miranda-Umbriel MMR could be the mechanism responsible to excite the inclination of Miranda to the current

~ 4.4° value. Using these statements, the authors constrained the Q-factor (Sect. 2.3.1) to be between 11 000 and 39 000. With this interval, passage through the 2/1 Ariel-Umbriel MMR cannot occur, while forcing the passage through the 3/1 Miranda-Umbriel MMR. However, since then, the physical properties and the orbital parameters estimations of the Uranian moons were updated (Jacobson 2014; Chen et al. 2014). In addition, tidal models were also improved, and more realistic models are now available. Thus, using the same statements as Tittemore and Wisdom (1990), we re-estimated the minimum and maximum values of Q.

Neglecting the effect of the eccentricity, inclination, and obliquity, the tidal evolution of the satellites is given by Eq. (2.49), which can be generalized as

$$\frac{\dot{a}_k}{a_k} \approx \frac{6\mathcal{G}m_k^2 R_0^5}{\beta_k a_k^8} k_{2_0} \tau_0 \left(\frac{\omega_0}{n_k} - 1 \right). \tag{2.68}$$

We numerically integrated Eq. (2.68) backwards, until 4.5 Gyr ago, neglecting any resonant interactions. To account for the variation of the angular velocity of Uranus's spin-axis, we calculated the current total angular momentum of the system, $\Sigma = 9.446\,070 \times 10^{-10}\,\mathrm{M}_\odot\,\mathrm{au}^2\,\mathrm{yr}^{-1}$ (see Sect. 3.3). Taking the rotation period of the satellites synchronous with the orbital period ($\omega_k/n_k = 1$), the rotation rate of Uranus, ω_0, is constantly adjusted so that Σ remains always constant.

Integrating Eq. (2.68) using a wide range of reasonable τ_0 values, we note that for $\tau_0 > 0.855$ s, the system crosses the 2/1 Ariel-Umbriel MMR (Fig. 2.7a), thus imposing an upper limit on τ_0. On the other hand, if $\tau_0 < 0.429$ s, the system does not pass through the 3/1 Miranda-Umbriel MMR (Fig. 2.7b). In light of these results, we took $\tau_0 = 0.617$ s as a suitable mean value to accommodate our assumptions (Fig. 1.4) and constrained $0.429\,\mathrm{s} < \tau_0 < 0.855\,\mathrm{s}$. This places the latest commensurability, the 5/3 Ariel-Umbriel MMR, ~ 640 Myr in the past.

The phase lag δ (Eq. (2.45)) can be related to the tidal time delay, τ, leading to (e.g. Correia and Valente 2022),

$$Q_0 = \frac{1}{2\omega_0 \tau_0} \qquad \text{and} \qquad Q_k = \frac{1}{n_k \tau_k}, \tag{2.69}$$

where Q_0 and Q_k are the specific dissipation factors for the central planet and for the satellites, respectively. Note that there is a correction factor of 1/2 between the two values, that arises from the semi-diurnal tides at m_0. From these expressions, the limits on τ_0 are translated as $5800 < Q_0 < 11500$ (see Fig. 2.7), and the adopted mean τ_0 as $Q_0 = 8000$. With $k_{2_0} = 0.104$ (Table 1.1) and $\tau_0 = 0.617$ s,
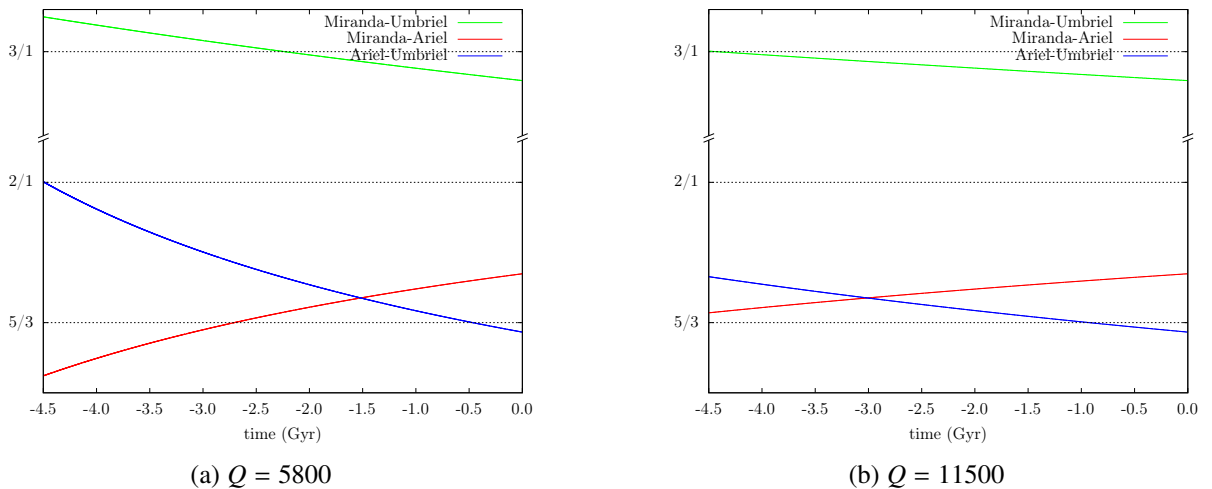

Figure 2.7: Evolution of the ratio between the mean motions of Miranda and Umbriel (green), Miranda and Ariel (red), and Ariel and Umbriel (blue) for $Q = 5800$ (left) and $Q = 11500$ (right). The dashed lines mark the positions of the lowest second order nominal resonances.

this leads to

$$k_{2_0}\tau_0 = 0.064\text{s} \quad \Leftrightarrow \quad \frac{k_{2_0}}{Q_0} = 1.3 \times 10^{-5}\,. \tag{2.70}$$

The corresponding semi-major axes of the regular satellite's 4.5 Gyr ago are then

$$\begin{aligned}
a_1 &= 4.9032\,R_0\,, \\
a_2 &= 6.7260\,R_0\,, \\
a_3 &= 10.2992\,R_0\,, \\
a_4 &= 17.0475\,R_0\,, \\
a_5 &= 22.8202\,R_0\,.
\end{aligned} \tag{2.71}$$

As for Uranus, the specific dissipation factor for the satellites is poorly constrained and precise measurements are not currently available. Thus, we start by setting $Q_S = 100$, a common choice for small bodies (Murray and Dermott 1999). Using the Love numbers obtained by Chen et al. (2014), we computed $k_{2_k}\tau_k$ and k_{2_k}/Q_S, presented in Table 2.4. We also present the same amounts for $Q_S = 500$, which will be used later in this work.

Satellite	k_{2_k}	$Q_S = 100$			$Q_S = 500$		
		τ_k (s)	$k_{2_k}\tau_k$ (s)	k_{2_k}/Q_S	τ_k (s)	$k_{2_k}\tau_k$ (s)	k_{2_k}/Q_S
Miranda	8.84×10^{-4}	194.3	0.171	8.84×10^{-6}	38.9	0.034	1.77×10^{-6}
Ariel	1.02×10^{-2}	346.5	3.534	1.02×10^{-4}	69.3	0.707	2.04×10^{-5}
Umbriel	7.35×10^{-3}	569.6	4.187	7.35×10^{-5}	113.9	0.8374	1.47×10^{-5}
Titania	1.99×10^{-2}	1196.9	23.819	1.99×10^{-4}	239.4	4.764	3.98×10^{-5}
Oberon	1.68×10^{-2}	1851.0	31.096	1.99×10^{-4}	370.2	6.219	3.36×10^{-5}

Table 2.4: Second Love number k_{2_k} and tidal lag τ_k of the main Uranian satellites. The second Love numbers are from Chen et al. (2014) and τ_k were calculated through Eq. (2.69).

2.4.4   Free and forced orbital elements

Without tidal friction, the secular oscillations of the eccentricity and inclination are conservative and constrained within a given range, known as free oscillations. As tidal friction damps the eccentricities and the inclinations of the satellites (Sect. 2.3.2), the system evolves into an equilibrium state uniquily dominated by its secular modes (Table 2.3), known as forced oscillations (e.g. Murray and Dermott 1999).

To estimate the average free orbital elements, we disabled tidal effects and integrate the current configuration of the Uranian system (Table 2.2) over 50 000 years. Furthermore, in addition to the five regular satellites, we performed one integration which also included the Sun and another without it. The results are presented in Table 2.5. We note that there are no significant differences between the results with and without the gravitational effect from the Sun, despite the high obliquity of Uranus. Such happens because Uranus is one of the outermost planets of the Solar System, and perturbations from the Sun are three orders of magnitude smaller than those from the satellites. These results confirm that the Uranian system can thus be analysed as an isolated system within our Solar System.

To evaluate the forced orbital elements, we integrated the system departing from the same configuration as for the free orbital elements. However, now we consider the tidal dissipation within the satellites, that is, $\tau_k \neq 0$. We do not need to include the tidal dissipation within Uranus ($\tau_0 = 0$), such that the semi-major axes do not increase (Eq. (2.68)). To ensure that the eccentricities converge to the equilibrium value, we need to integrate the system over a very long time span, which is computationally expensive. One solution to decrease the computation time, is to enhance the tidal strength by increasing τ_k and

Without the Sun						
Satellite	e_{min}	e_{mean}	e_{max}	I_{min} (°)	I_{mean} (°)	I_{max} (°)
Miranda	8.62×10^{-4}	1.31×10^{-3}	1.76×10^{-3}	4.404	4.409	4.414
Ariel	5.77×10^{-5}	1.29×10^{-3}	2.25×10^{-3}	7.92×10^{-4}	2.51×10^{-2}	5.90×10^{-2}
Umbriel	2.20×10^{-3}	3.67×10^{-3}	5.06×10^{-3}	2.41×10^{-3}	7.55×10^{-2}	1.36×10^{-1}
Titania	2.43×10^{-5}	1.64×10^{-3}	3.48×10^{-3}	2.48×10^{-2}	1.22×10^{-1}	1.93×10^{-1}
Oberon	3.64×10^{-5}	1.75×10^{-3}	3.46×10^{-3}	6.62×10^{-2}	1.39×10^{-1}	1.96×10^{-1}
With the Sun						
Miranda	8.44×10^{-4}	1.31×10^{-3}	1.76×10^{-3}	4.373	4.409	4.445
Ariel	5.27×10^{-5}	1.29×10^{-3}	2.31×10^{-3}	8.70×10^{-5}	2.72×10^{-2}	8.50×10^{-2}
Umbriel	2.21×10^{-3}	3.53×10^{-3}	5.18×10^{-3}	5.09×10^{-4}	7.35×10^{-2}	1.67×10^{-1}
Titania	1.95×10^{-5}	1.64×10^{-3}	3.50×10^{-3}	1.58×10^{-2}	1.32×10^{-1}	2.59×10^{-1}
Oberon	2.96×10^{-5}	1.82×10^{-3}	3.44×10^{-3}	4.55×10^{-2}	1.72×10^{-1}	2.74×10^{-1}

Table 2.5: Free orbital elements of the regular Uranus satellites with and without the influence of the Sun.

rescale the evolution time by the same factor. This is possible because the tidal equations of motion are proportional to τ_k (Eqs. (2.27) and (2.37)).

We start by comparing the results from different tidal multiplication factors, ×10, ×100, and ×1000. In Fig. 2.8, we superimposed the eccentricity and the inclination of Miranda of an integration over 20 Myrs, 2 Myrs and 0.2 Myrs, where, for each simulation, we re-scaled the time axis by the respective multiplication factor. It is noticeable that the general evolution of the orbital elements is insensitive to the enhancement of the tidal strength. Therefore, we can speed up at least 1000 times the computation time without compromising the results. We note that, contrarily to the eccentricity, tides are not very efficient to damp the inclinations. After 200 Myr of evolution, the inclinations of all the satellites remain virtually unchanged (Fig. 2.8). It is not feasible to determine the forced inclinations through this method, and we then only focus on the eccentricities.

With a multiplication factor of ×100, we integrated the system over 2 Gyr departing from the current orbital configuration (Table 2.2). As can be seen in Fig. 2.9, the eccentricities of Miranda, Ariel, and Umbriel are quickly damped in less than 500 Myr to values at least three times smaller than the initial ones (Table 2.6). The eccentricity damping timescale of Ariel, ~ 50 Myr, is significantly smaller than that for Miranda, ~ 150 Myr, and Umbriel ~ 330 Myr, indicating that tidal effects are stronger for Ariel. For Titania and Oberon, the decrease in eccentricity over 2 Gyr is small when compared with the other innermost moons. We also note that the forced eccentricities of Miranda, Ariel, and Umbriel (Table 2.6) are one order of magnitude smaller than the currently observed values (Table 1.2). As a consequence, we conclude that some mechanism must have excited the eccentricities of the three innermost Uranian satellites in a not so distant past.

Satellite	$\langle e_f \rangle$	τ_{ecc}
Miranda	2.2×10^{-4}	150 Myr
Ariel	1.6×10^{-4}	50 Myr
Umbriel	6.0×10^{-4}	330 Myr
Titania	$< 1.3 \times 10^{-3}$	> 2000 Myr
Oberon	$< 1.4 \times 10^{-3}$	> 2000 Myr

Table 2.6: Forced eccentricities for the major Uranian satellites. The values were numerically obtained by integrating the current system for 2 Gyr and disregarding tidal effects from Uranus (Fig. 2.9).
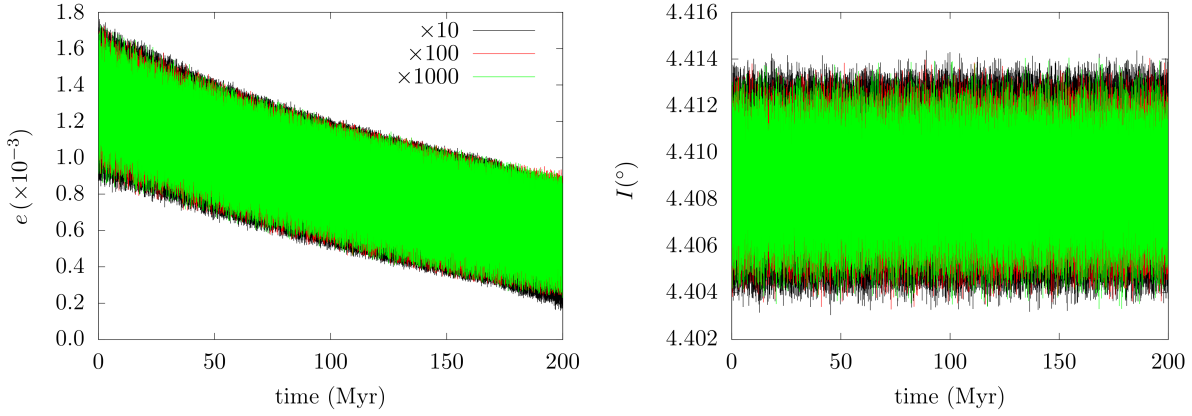
Figure 2.8: Comparison of the evolution of the eccentricity (left) and inclination (right) of Miranda between three distinct time lags τ'_k. In black, $\tau'_k = \tau_k \times 10$, in red, $\tau'_k = \tau_k \times 100$, and in green $\tau'_k = \tau_k \times 1000$, where τ_k are the values from Table 2.4 for $Q_S = 100$.

2.4.5 Spin-orbit resonances

Tidal effects drive the obliquity of the satellites to zero (Hut 1980), unless an additional perturbation maintains a non-zero obliquity, such as a spin-orbit resonance (e.g. Fabrycky et al. 2007; Correia 2009). Such a resonance is established if the spin precession period of the satellite and its orbital nodal precession are nearly equal (Ward and Hamilton 2004; Levrard et al. 2007), that is

$$\alpha_k \cos \epsilon_k \approx |s_k|, \tag{2.72}$$

where ϵ_k is the angle between the spin vector and the vector normal to the orbital plane, know as obliquity, s_k the inclination secular mode (Sect. 2.4.2) and α_k is the spin-axis precession constant, given by (Millholland and Laughlin 2019)

$$\alpha_k = \frac{1}{2} \frac{m_0}{m_k} \left(\frac{R_k}{a_k} \right)^3 \frac{k_f}{C'_k} \omega_k, \tag{2.73}$$

where C'_k is the normalized moment of inertia (Jeffreys 1976),

$$C' = \frac{C}{mR^2} = \frac{2}{3} \left(1 - \frac{2}{5} \sqrt{\frac{5}{k_f + 1} - 1} \right), \tag{2.74}$$

and k_f is the potential Love number. The potential Love number of the satellites can be related with the second order gravity field by (e.g. Correia and Rodríguez 2013)

$$J_2 = \frac{4}{3} k_f \frac{\omega^2 R^3}{\mathcal{G}m}. \tag{2.75}$$

Using the values from Table 1.2, we obtain

$$
\begin{aligned}
C'_1 &= 0.3270081029518477, \\
C'_2 &= 0.3204444545209566, \\
C'_3 &= 0.3422604068886157, \\
C'_4 &= 0.3259712648677198, \\
C'_5 &= 0.3096258001542771.
\end{aligned}
$$

Adopting the present semi-major axes of the satellites (Table 1.2) and taking their rotation rates synchronous with the orbital mean motion (Eq. (2.73)), we obtain the α_k values listed in Table 2.7.
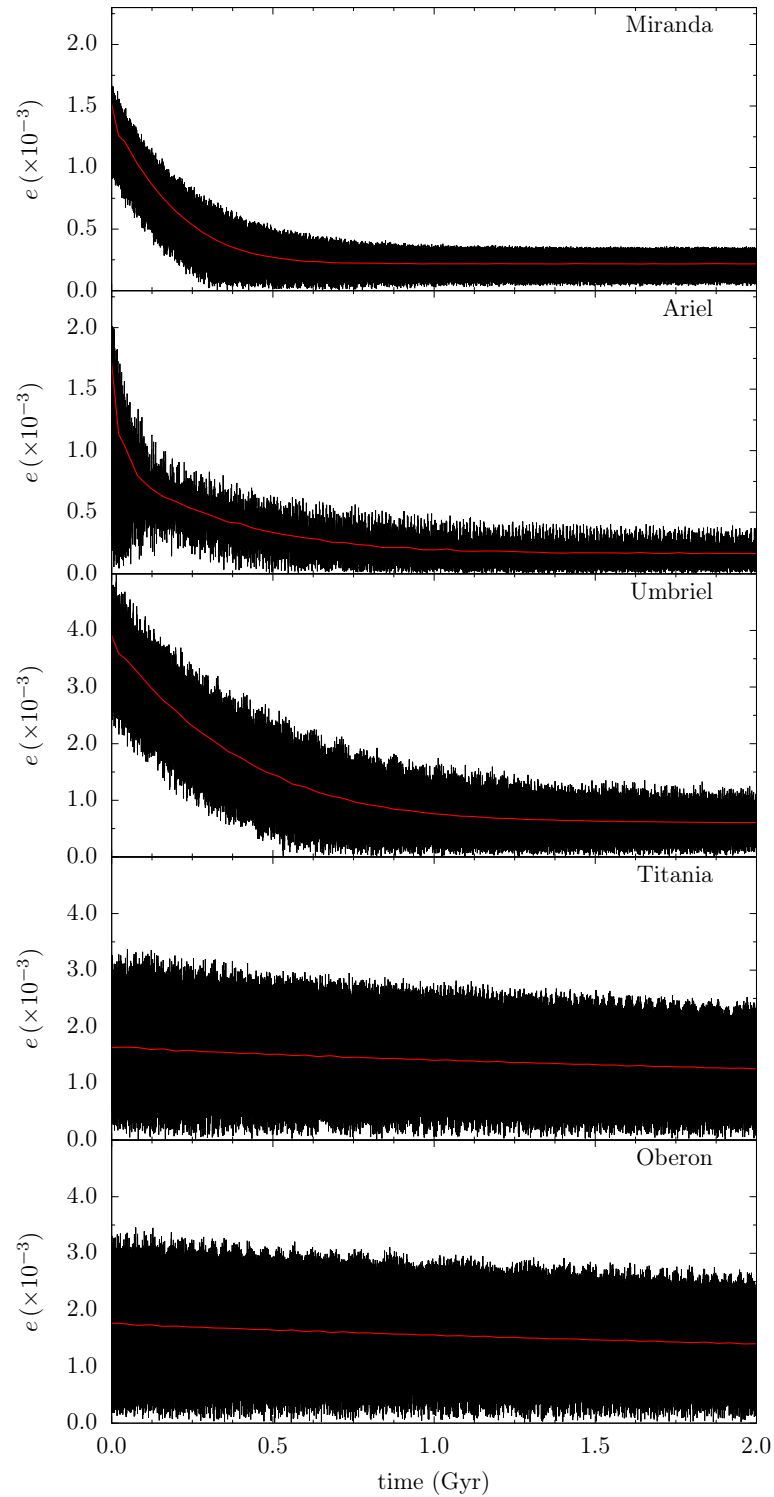
Figure 2.9: Forced eccentricities of the major Uranian satellites. The average values of the eccentricities are represented as a red line.

Satellite	Analytical (deg/yr)	Numerical (deg/yr)
Miranda	4164.7182	4078.5164
Ariel	542.6365	540.3787
Umbriel	136.4137	136.1541
Titania	12.5519	12.5696
Oberon	3.3546	3.1287

Table 2.7: Comparison between the computed analytical spin-axis precession constant (α) and the numerically estimated.

Using the same method performed to estimate the secular modes (Sect. 2.4.2), the α_k can also be obtained using a frequency analysis of the precession of the spin-axis of each satellite. From the results of the integration of the Uranian system obtained in Sect. 2.4.2, we used `TRIP` to analyse the precession frequency of the satellites. The numerical results are also shown in Table 2.7.

Ćuk et al. (2020) suggest a commensurability between the spin-axis precession of Oberon, α_5, and the inclination normal mode of Umbriel, s_3, as a mechanism to decrease the relatively high inclinations resulting from their numerical simulations. However, by comparing the obtained spin-axis precession constants (Table 2.7) with the inclination secular modes from Table 2.3, it is possible to verify that, at present, there are no commensurabilities between the precession of the spins and the nodes of the main satellites if we consider that the obliquities of the satellites are very small.

The commensurability suggested by Ćuk et al. (2020) can nevertheless be achieved if the obliquity of Oberon is $\sim 28°$ (Eq. (2.72)). Although the spins of the satellites are expected to be tidally evolved, non-zero obliquities can be maintained by an equilibrium state, called Cassini state (see Ward and Hamilton 2004, for a detailed description). The forced obliquity from a Cassini state can be estimated by (Levrard et al. 2007)

$$\epsilon_k = \sqrt{\frac{1}{\frac{2\alpha_k}{|s_k|} - 1}} \, . \tag{2.76}$$

Eq. (2.76) leads to $\epsilon_1 = 87°$, $\epsilon_2 = 86°$, $\epsilon_3 = 84°$, $\epsilon_4 = 74°$, and $\epsilon_5 = 78°$. Replacing the forced obliquities into Eq. (2.72), we obtain that $\alpha_1 \cos \epsilon_1 = 213.5$ deg/yr, $\alpha_2 \cos \epsilon_2 = 37.7$ deg/yr, $\alpha_3 \cos \epsilon_3 = 14.2$ deg/yr, $\alpha_4 \cos \epsilon_4 = 3.46$ deg/yr, and $\alpha_5 \cos \epsilon_5 = 0.6$ deg/yr. Comparing these values with the inclination normal modes from Table 2.3, we observe that there are no possible spin-orbit resonances within the Uranian satellites at present, even if we consider Cassini-state obliquities. Therefore, the mechanism proposed by Ćuk et al. (2020) does not seem suitable to decrease the inclinations of the satellites after the 5/3 Ariel-Umbriel MMR.

2.4.6 Long-term evolution

Using the tentative initial semi-major axes obtained with Eq. (2.71), we performed a series of numerical integrations with the five satellites using the full set of N-body equations of motion with tides (Eqs. (2.8), (2.9), (2.27), (2.37), and (2.39)). As initial conditions, we chose very low initial eccentricities ($e_k = 2 \times 10^{-3}$) and the current mean inclinations, except for Miranda, which was lowered to $I_1 = 0.1°$, as this is the expected outcome of a satellite system formed in a circumplanetary disc (e.g. Prentice 1986; Canup and Ward 2006; Szulágyi et al. 2018; Salmon and Canup 2022). The spin-axis rotation periods of the satellites were adjusted so that the satellites were synchronous with their respective orbital period. We set $Q_0 = 8000$, $Q_S = 100$, and the corresponding dissipation parameters from Table 2.4. Since we expect that the system is chaotic (Tittemore and Wisdom 1988, 1989, 1990; Ćuk et al. 2020), we integrated five sets of initial conditions, where, for each run, we changed the mean longitude, $\lambda_k = \varpi_k + \Omega_k$, of the satellites to capture different evolution outcomes.

In Fig. 2.10, we display one representative example of the above mentioned simulations. Initially, all the satellites drift outwards, while tidal friction quickly damps the initial eccentricities. As expected, for the inclinations the tidal damping is much weaker, almost imperceptible. As the different migration rates
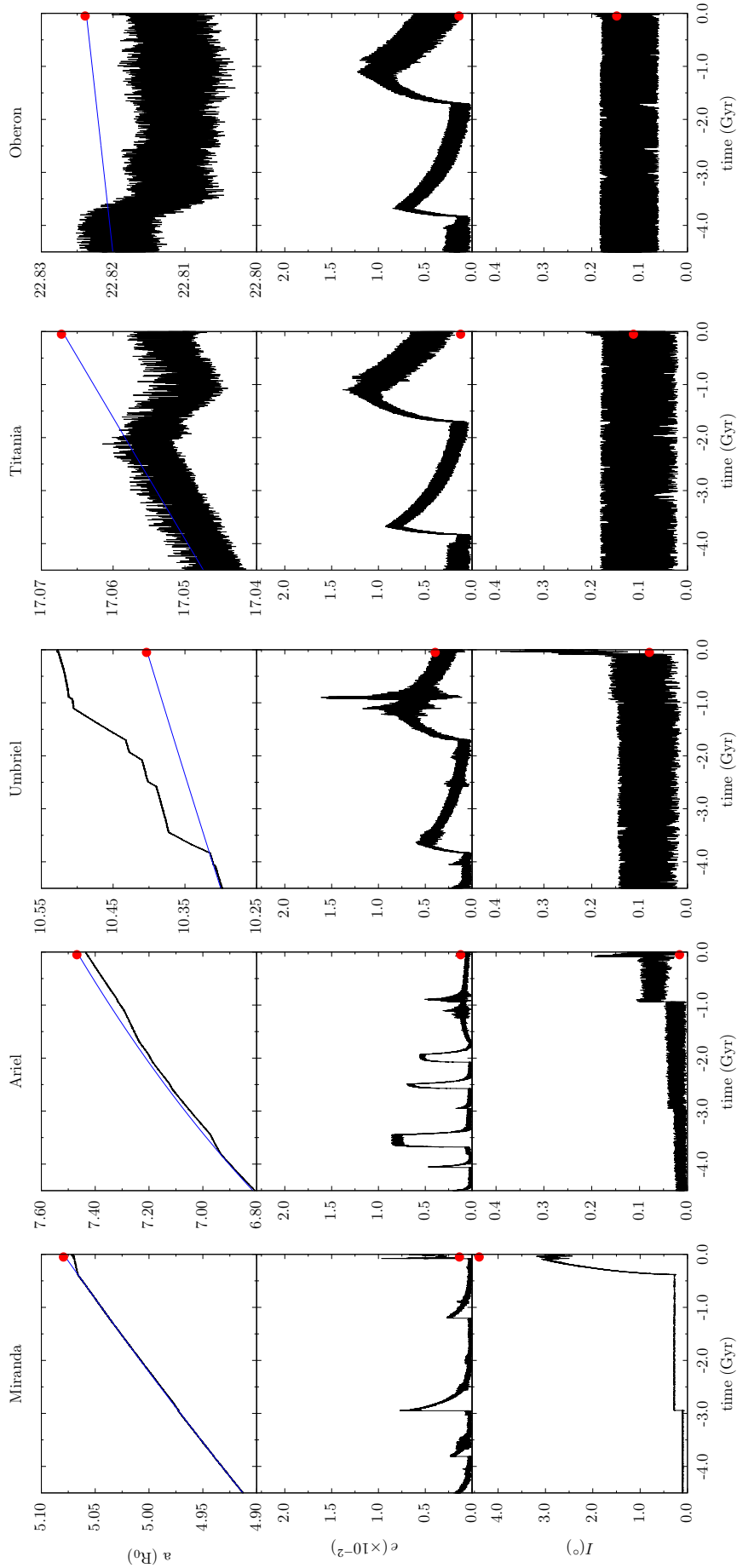
Figure 2.10: Numerical integration where the semi-major axis were extrapolated using Eq. (2.68) (given in Eq. (2.71)). The eccentricities were initially set to $e = 2 \times 10^{-3}$ and the inclinations to the current mean value, except for Miranda, with $I = 0.1°$. The first row gives the semi-major axes of the five satellites, the middle row shows the eccentricities, and the bottom one gives the inclinations. The current orbital mean properties were superimposed as red circles and the asymptotic semi-major axes evolution as a blue line.

change the relative distances between the satellites, several orbital commensurabilities induce dramatic changes on the orbital parameters. The first event takes place at $t \approx -3.84$ Gyrs, with a capture in a first order three-body MMR involving Ariel, Umbriel, and Oberon, $-2n_2 + 4n_3 - n_5 \approx 0$. During capture, the eccentricities of all satellites are excited. The migration rate of Ariel slows down, Umbriel's speeds up, and Oberon starts migrating inwards. This is a typical signature of a three-body MMR with dissipation (e.g. Petit 2021). After 400 Myr of entrapment, the resonance is broken and the semi-major axes start once again to migrate solely due to the tidal friction. At $t \approx -2.95$ Gyr, Miranda and Ariel reach the 5/3 MMR. Although the satellites were not trapped into the resonance, an increase in the eccentricity of Miranda is observed, together with the inclination rising to a value three times larger than the initial one. Then, a series of three-body MMR are again observed. Between $t \approx -2.57$ Gyr and $t \approx -2.49$ Gyr there is another first order three-body commensurability between Ariel, Umbriel, and Oberon, $-3n_A + 6n_U - 2n_O \approx 0$, which increases the eccentricity of Ariel, while not significantly exciting the remaining moons. Following, at $t \approx -2.08$ Gyr, Ariel, Umbriel, and Titania were captured in the $-4n_A + 9n_U - 4n_T \approx 0$ MMR. After 150 Myr of entrapment, the moons escaped the resonance, only to be later captured once more on a lower index[1] three-body resonance, $-2n_A + 4n_U - n_T \approx 0$. Both captures induced an inward migration of Titania, sped up the outward migration of Umbriel and slowed down that of Ariel. However, the higher index commensurability did not excite the eccentricities and the inclinations of the satellites. On the contrary, the lower index commensurability increased more the eccentricities of Umbriel and Titania than the remaining commensurabilities. Interestingly, we note that low index three-body resonances involving either Titania or Oberon excite the eccentricities of both satellites, even if one of them is not involved. This behaviour was observed for the $-2n_A + 4n_U - n_O \approx 0$ and the $-2n_A + 4n_U - n_T \approx 0$ MMR. Later on, at $t \approx -0.94$ Gyr, there was an increase of Ariel's inclination due to a brief 50 Myr capture in the two-body 7/4 MMR between Ariel and Umbriel. This is a third order resonance, ergo, should not affect the system as much as a second or first order MMR. Nevertheless, this capture suggests that such commensurabilities can also play an important role in the evolution of the Uranian moons. Finally, Miranda and Umbriel reach the 3/1 MMR at $t \approx -0.4$ Gyr. Right from the moment of capture, a sharp increase of Miranda's inclination up to 3° confirm Tittemore and Wisdom (1989) result that this resonance could explain the current high inclination of Miranda. Capture within the resonance occurred at the late stages of the 4.5 Gyr integration, and at the end of the simulation, the system remained trapped. Furthermore, although the eccentricities of the five satellites and the inclinations of Titania and Umbriel are compatible with the currently observed values (Table 1.2), the semi-major axes and the inclinations of the three innermost satellites are largely off setted. After 4.5 Gyr of integration, there is a clear misalignment between the final orbits of the satellites, and the currently observed values (Table 1.2), marked with a red dot. This is not a surprising outcome since the initial semi-major axes were obtained considering evolution solely due to tidal effects, assuming non interacting circular orbits in the equatorial plane (Eq. (2.71)). Therefore, this estimation does not take into account the effects of multiple resonance crossings, resulting in the observed deviation between the evolution of the semi-major axes and the asymptotic evolution (blue line).

Attempting to replicate the current architecture observed, we integrated the system once more, but readjusting the initial semi-major axes, so that they agree with the current semi-major axes. This adjustment modifies the initial mean motion ratios between the satellites. Thus, the resonant configurations observed in the previous integrations, either occurred at different evolutionary stages or were not achieved, and different orbital resonances shaped the outcome of the integration.

In Fig. 2.11, we provide an example of the evolution of a system for which we increased the initial semi-major axes of Miranda and Ariel, and decreased the semi-major axis of Umbriel, relatively to the values from Eq. (2.71), while keeping the same semi-major axes for Titania and Oberon. Once more, we were not able to attain the current configuration of the satellites. A series of additional iterations with different initial semi-major axis were conducted, where, at each iteration, the semi-major axes were slightly changed accordingly to the results from the previous integrations. Throughout the different

---

[1]The index of a three-body resonance is the sum of the absolute values of the integers, that is, $|k_1| + |k_2| + |k_3|$, where k_1, k_2, and k_3 are the integers associated to n_1, n_2, and n_3, respectively (Petit 2021).

iterations, capture in three-body MMR often divert the migration of the satellites from the expected "path". This clearly suggests that this type of resonances may have played an important role in the dynamical history of Uranus.

Some initial conditions, for which the initial semi-major axes of Ariel and Umbriel were carefully placed in such a way that the passage of both 3/1 Miranda-Umbriel and 5/3 Ariel-Umbriel MMRs is observed, show an intricate evolution of Miranda's inclination. In Fig. 2.12, we show one of the simulations where both MMRs were crossed. First, capture in the 3/1 MMR excites the initially low inclination of Miranda up to $\sim 5°$. This once more replicates the result obtained by Tittemore and Wisdom (1989), and was observed in most simulations where the 3/1 MMR was crossed. Later, capture in the 5/3 MMR between Ariel and Umbriel induces an additional large increase on Miranda's inclinations, as reported by Ćuk et al. (2020). After leaving the 3/1 MMR, the inclination is already at $\sim 10°$, two times the current value. In addition, Ariel and Umbriel leave the resonance with considerably higher inclination values than the presently observed, also verifying the results from Ćuk et al. (2020). Therefore, we confirm that both MMRs are able to reproduce the high inclination of Miranda. However, an evolution path with long-term capture in both commensurabilities does not seem likely, since it can over inflate the inclination of Miranda. Since the 3/1 MMR between Miranda and Umbriel reproduce Miranda's inclination without perturbing the remaining inclination of the satellites, we conclude that this commensurability provides a simpler explanation for this observation, without needing to resort to further mechanisms to damp the inclinations of the remaining moons.

Figure 2.11: Numerical integration where the semi-major axis were extrapolated using Eq. (2.68), with small changes on the asymptotic initial values of Miranda, Ariel, and Umbriel, so that the final semi-major axes in Fig. 2.10 match those currently observed (Table 1.2). The eccentricities were initially set to $e = 2 \times 10^{-3}$ and the inclinations to the current mean value, except for Miranda, with $I = 0.1°$. The first row gives the semi-major axes of the five satellites, the middle row shows the eccentricities, and the bottom one gives the inclinations. The current orbital mean properties were superimposed as red circles and the asymptotic semi-major axes evolution as a blue line.
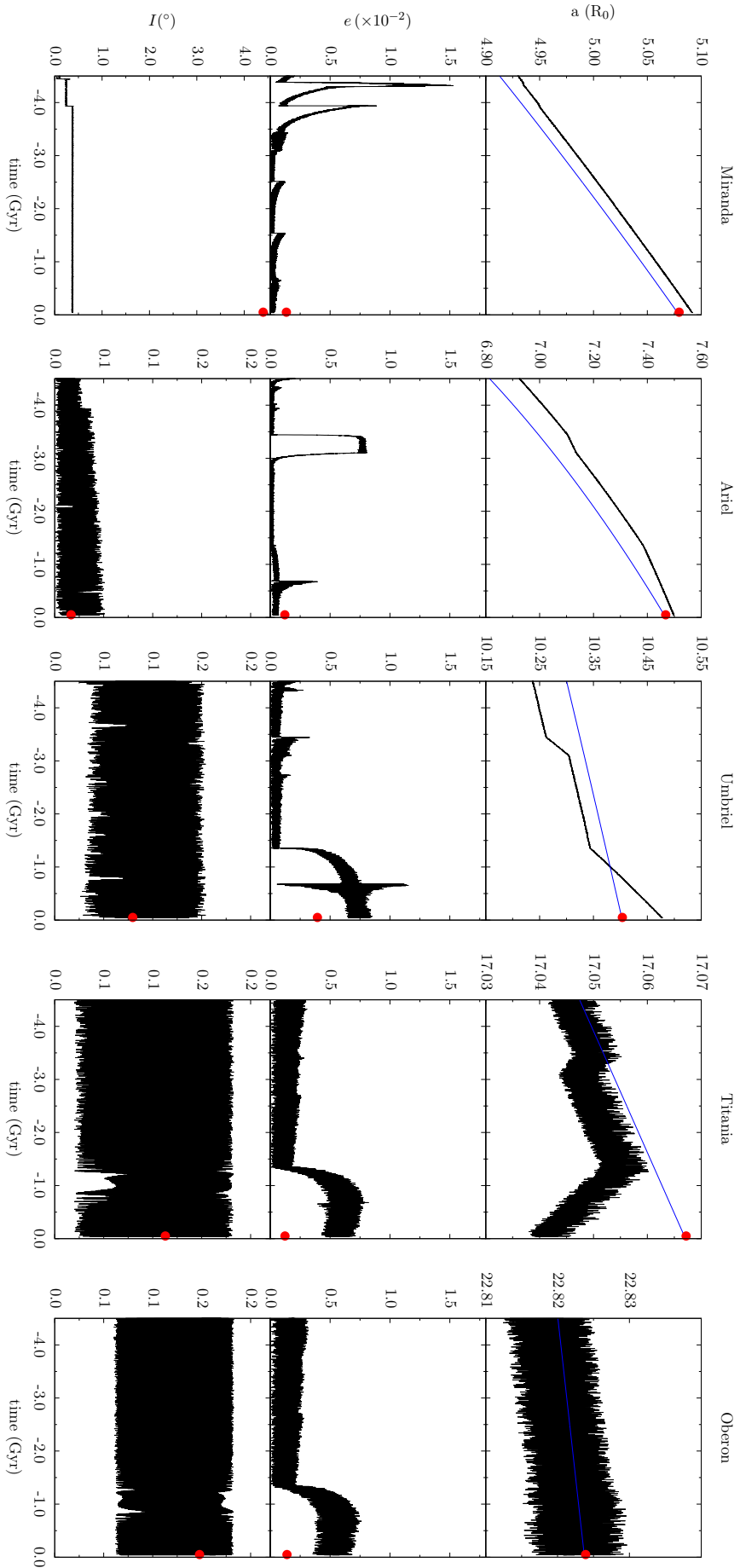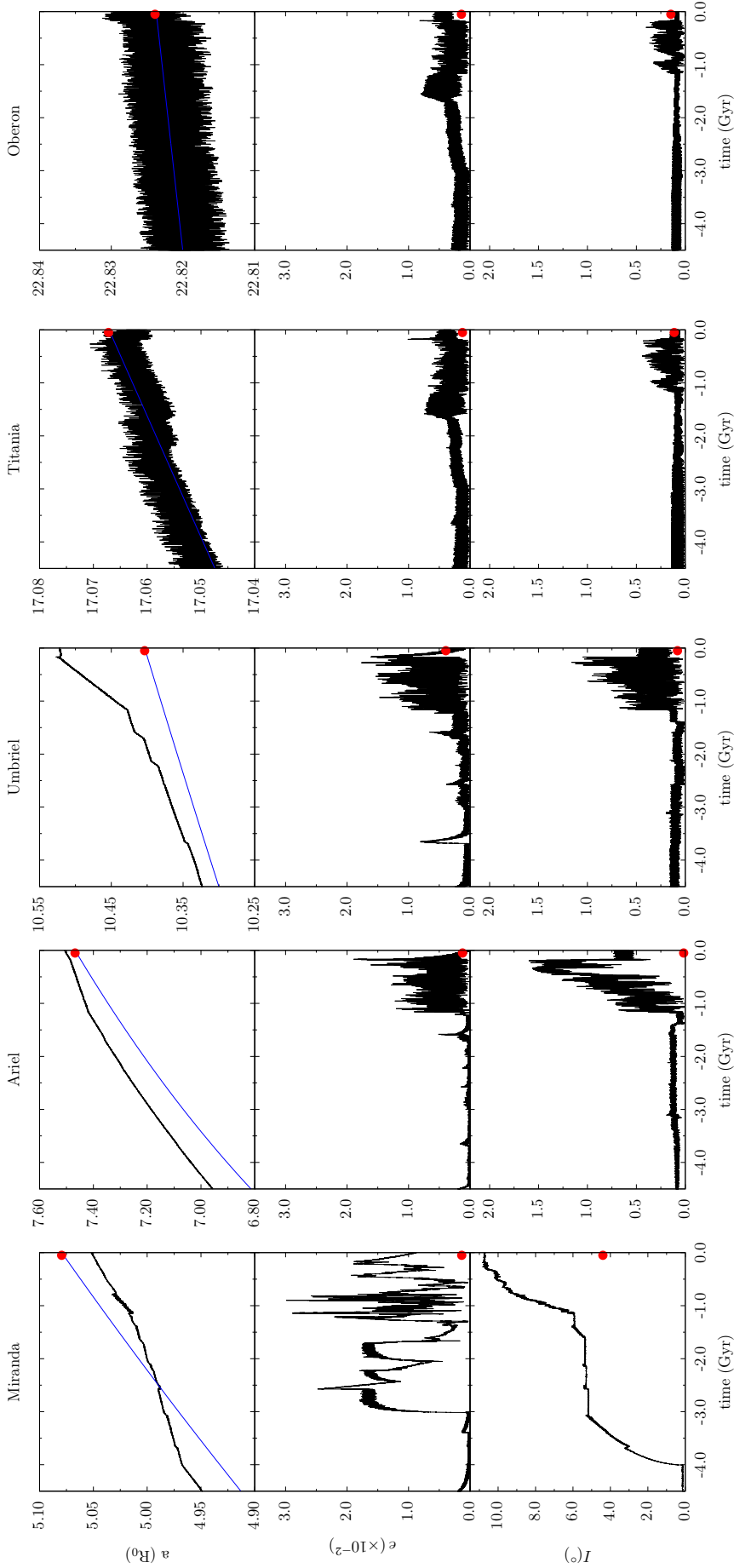
Figure 2.12: Numerical integration where the semi-major axes were extrapolated using Eq. (2.68), with small changes on the asymptotic initial values for Miranda, Ariel, and Umbriel, so that the 3/1 Miranda-Umbriel MMR and the 5/3 Ariel-Umbriel MMR are crossed. The eccentricities were initially set to $e = 2 \times 10^{-3}$ and the inclinations to the current mean value, except for Miranda, with $I = 0.1°$. The first row gives the semi-major axes of the five satellites, the middle row shows the eccentricities, and the bottom one gives the inclinations. The current orbital mean properties were superimposed as red circles and the asymptotic semi-major axes evolution as a blue line.

2.4.7   Backwards evolution

We were not able to achieve the current architecture of the Uranian system (not even close) in none of the trial initial configurations. The inward migration of the largest satellites Titania and Oberon, together with the changes on the semi-major axes migration rates, pose many uncertainties on the exact evolutionary path of the satellites, and tuning the initial conditions proved to be very difficult and time expensive. A more suitable approach consists in dividing the integration interval into smaller time slices, and then study each dynamical event individually.

Accordingly to Eq. (2.68) and choosing $Q_0 = 8000$, the latest commensurability encountered was the 5/3 MMR between Ariel and Umbriel, about 640 Myr ago (see also Fig.1.4). We extrapolated the semi-major axes of the satellites just after the MMR passage, using the same assumptions previously considered, leading to

$$
\begin{aligned}
a_1 &= 5.0570\,R_0\,, \\
a_2 &= 7.3910\,R_0\,, \\
a_3 &= 10.3892\,R_0\,, \\
a_4 &= 17.0644\,R_0\,, \\
a_5 &= 22.8234\,R_0\,.
\end{aligned}
\tag{2.77}
$$

The initial eccentricities were set to

$$
\begin{aligned}
e_1 &= 7.0 \times 10^{-3}\,, \\
e_2 &= 8.5 \times 10^{-3}\,, \\
e_3 &= 1.1 \times 10^{-2}\,, \\
e_4 &= 2.0 \times 10^{-3}\,, \\
e_5 &= 2.0 \times 10^{-3}\,,
\end{aligned}
\tag{2.78}
$$

and the initial inclinations were set to the presently observed values (Table 1.2), except for Miranda's inclination, which was slightly increased to 4.41° to match the current inclination at the end of the simulation. We then performed 20 simulations, where, for each run, we changed the mean longitude λ_k of the satellites.

In Fig. 2.13, we display the evolution of the semi-major axes, eccentricities and inclinations, resulting from the integration of one of these initial conditions. As expected, no two-body MMR was crossed. Furthermore, no three-body resonant interactions were observed either, and the migration rates are in excellent agreement with the asymptotical predictions (Fig. 2.13). The final eccentricity closely match the currently observed eccentricities, and the inclinations are in perfect agreement with the currently observed values. Therefore, we conclude that, after the passage through the 5/3 MMR between Ariel and Umbriel, the evolution of the system is mostly peaceful and dominated by tidal friction induced on Uranus by the satellites.

The next step consists in studying in detail the passage through the 5/3 MMR between Ariel and Umbriel. When a resonance is crossed, we cannot perform a backwards integration, because we have a stochastic evolution. As a result, we need to place the system slightly before the resonance encounter and then integrate it forwards. We also need to explore a large range of initial conditions and the role of the eccentricity and the inclination to the outcome of the resonance crossing. In order to do that, we cannot rely on slow N-body numerical integrations, which are time expensive. Therefore, in the next chapters, we develop a simplified two-satellite secular averaged model, that we use to quickly cover a large spectrum of configurations of Uranus, Ariel, and Umbriel before the resonant encounter, that otherwise would not be possible to attain. Later, using the results from the simplified model, we will once more resort to the N-body problem (Sect. 5.4), but now in a more efficient way, exploring only the more interesting results from the simplified model.

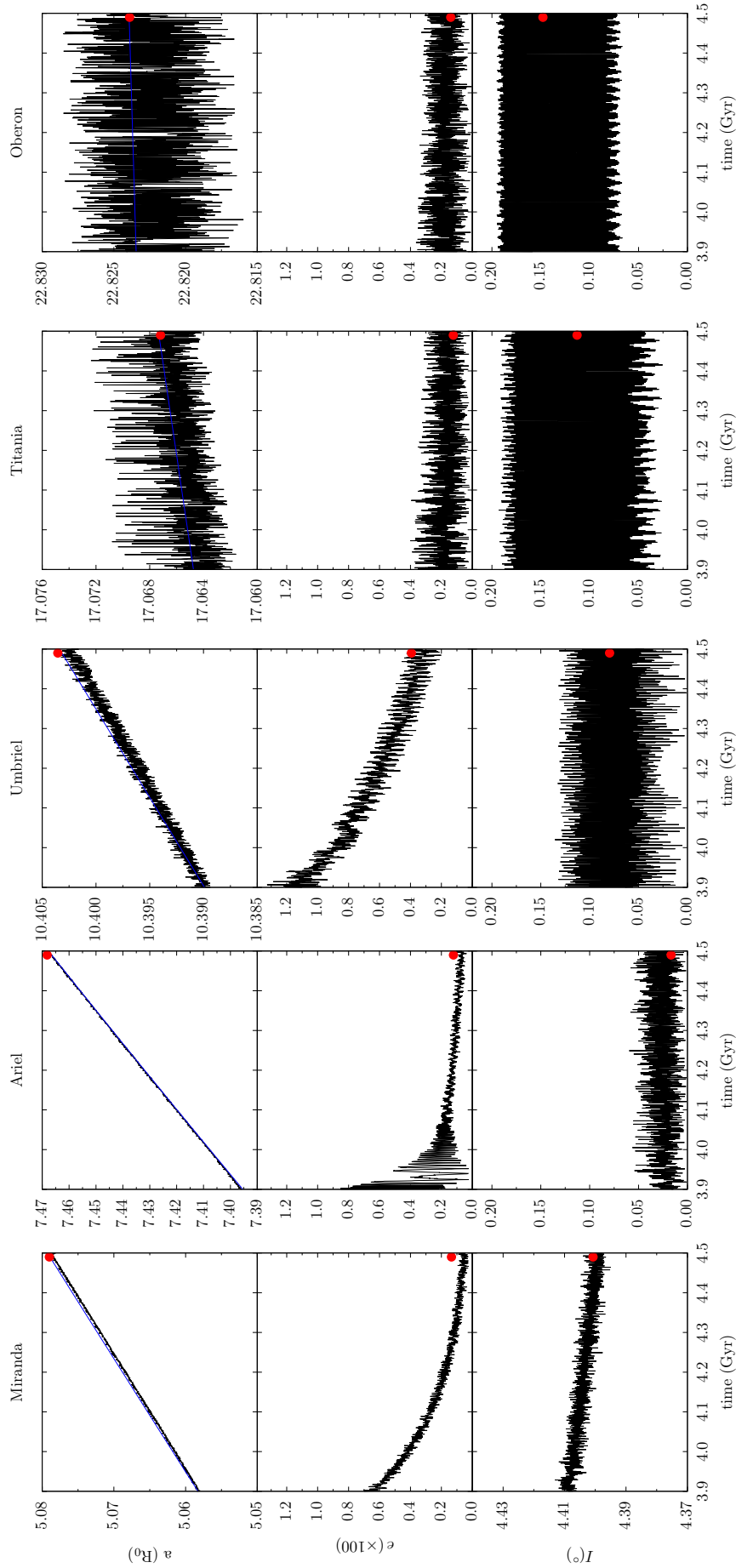Figure 2.13: Evolution of the orbits of the Uranian satellites from 640 Myr ago to the present. The blue line is the asymptotic evolution of the semi-major axes, obtained by Eq. (2.68). The first row gives the semi-major axes of the five satellites, the middle row shows the eccentricities, and the bottom one gives the inclinations. The current orbital mean properties were superimposed as red circles.

Chapter 3

Secular conservative motion

The three-body problem is not integrable and the large number of degrees of freedom limit the analytical analysis of the problem. For quasi-periodic motion, the mutual gravitational interactions between two satellites in the system can be decomposed into infinity series of the fundamental frequencies of the problem (e.g. Murray and Dermott 1999). High frequency terms are relevant for the short-period variations and osculating orbital elements. Yet, at long-term, these interactions average out and do not reflect the general evolution of the system. By considering only the long period interactions within the system, the secular perturbations, together with some other considerations, we are able to decrease the number of degrees of freedom of the problem and use a simplified model to describe the long-term evolution. In this chapter, we develop a general two-satellite secular model to study the passage through second order MMR.

Let us consider two masses, m_1 and m_2, orbiting around a central more massive mass, m_0, such that, $m_1, m_2 \ll m_0$. Taking an arbitrary inertial frame, $\mathbf{R}_0$, $\mathbf{R}_1$, and $\mathbf{R}_2$ are the positions of m_0, m_1, and m_2, respectively (Fig. 2.1), whereas $\mathbf{r}_1 = \mathbf{R}_1 - \mathbf{R}_0$, $\mathbf{r}_2 = \mathbf{R}_2 - \mathbf{R}_0$ are the positions of the satellites relative to m_0, where $r_k = \|\mathbf{r}_k\|$, $r_1 < r_2$, and $\mathbf{r}_{1,2} = \mathbf{R}_2 - \mathbf{R}_1$ is the relative position between m_1 and m_2. The Hamiltonian of the system is then given by Eq. (2.1), which can be rewritten as

$$\mathcal{H} = \left(\frac{\mathbf{p}_1^2}{2\beta_1} - \frac{\mu_1 \beta_1}{r_1} \right) + \left(\frac{\mathbf{p}_2^2}{2\beta_2} - \frac{\mu_2 \beta_2}{r_2} \right) + \left(\frac{\mathbf{p_1} \cdot \mathbf{p_2}}{m_0} - \frac{\mathcal{G} m_1 m_2}{r_{1,2}} \right). \tag{3.1}$$

The first two terms correspond to the Keplerian orbits of m_1 and m_2, and can be expressed in elliptical elements as

$$\mathcal{H}_K = \mathcal{H}_{K_1} + \mathcal{H}_{K_2} = -\frac{\beta_1 \mu_1}{2a_1} - \frac{\beta_2 \mu_2}{2a_2}. \tag{3.2}$$

The last terms of Eq. (3.1) arise from the mutual interactions between m_1 and m_2, dubbed by perturbative function.

3.1 Perturbative Hamiltonian

The perturbative component of the Hamiltonian (3.1) is given by

$$\mathcal{H}_P = \frac{\mathbf{p_1} \cdot \mathbf{p_2}}{m_0} - \frac{\mathcal{G} m_1 m_2}{r_{1,2}}, \tag{3.3}$$

where we name the first term as the indirect contribution ($\mathcal{H}_I$) and the second term as the direct contribution ($\mathcal{H}_D$). Similarly to the Keplerian contributions, the direct and indirect terms can be expressed in elliptical elements by expanding the relative position and the conjugated momenta.

We start by developing the direct term $\mathcal{H}_D$, given by:

$$\mathcal{H}_D = -\frac{\mathcal{G} m_1 m_2}{r_{1,2}}. \tag{3.4}$$

Expanding $1/r_{1,2}$ in elliptical elements[1] and truncating to the first order in the mass ratios, m_k/m_0, and second order in the eccentricities, e_k, and the inclinations, I_k (with respect to the equatorial plane of the central body), $\mathcal{H}_D$ is given by

$$
\begin{aligned}
\mathcal{H}_D = \sum_{s=0} \Big[&A_s \cos[s(\lambda_1 - \lambda_2)] \\
&+ B_s \cos[s(\lambda_1 - \lambda_2) + \varpi_1 - \varpi_2] + C_s \cos[s(\lambda_1 - \lambda_2) + \Omega_1 - \Omega_2] \\
&+ D_s \cos[(1-s)\lambda_1 + s\lambda_2 - \varpi_1] + E_s \cos[(1-s)\lambda_1 + s\lambda_2 - \varpi_2] \\
&+ F_s \cos[(2-s)\lambda_1 + s\lambda_2 - 2\varpi_1] + G_s \cos[(2-s)\lambda_1 + s\lambda_2 - 2\varpi_2] \\
&+ I_s \cos[(2-s)\lambda_1 + s\lambda_2 - \varpi_1 - \varpi_2] \\
&+ L_s \cos[(2-s)\lambda_1 + s\lambda_2 - 2\Omega_1] + N_s \cos[(2-s)\lambda_1 + s\lambda_2 - 2\Omega_2] \\
&+ P_s \cos[(2-s)\lambda_1 + s\lambda_2 - \Omega_1 - \Omega_2] \Big],
\end{aligned}
\tag{3.5}
$$

with

$$
\begin{aligned}
A_s = -\mathcal{G}\frac{m_1 m_2}{a_2} \bigg(&\frac{1}{2} b_{\frac{1}{2}}^{(s)} + \frac{1}{8}(e_1^2 + e_2^2)\Big[-4s^2 + 2\alpha D + \alpha^2 D^2 \Big] b_{\frac{1}{2}}^{(s)}(\alpha) \\
&+ \frac{1}{4}(I_1^2 + I_2^2)\Big(-\alpha b_{\frac{3}{2}}^{(s-1)}(\alpha) - \alpha b_{\frac{3}{2}}^{(s+1)}(\alpha) \Big) \bigg),
\end{aligned}
\tag{3.6}
$$

$$
B_s = -\mathcal{G}\frac{m_1 m_2}{a_2}\frac{1}{4}e_1 e_2 \Big[2 + 6s + 4s^2 - 2\alpha D - \alpha^2 D^2 \Big] b_{\frac{1}{2}}^{(s+1)}(\alpha),
\tag{3.7}
$$

$$
C_s = -\mathcal{G}\frac{m_1 m_2}{a_2} I_1 I_2 \alpha b_{\frac{3}{2}}^{(s+1)}(\alpha),
\tag{3.8}
$$

$$
D_s = -\mathcal{G}\frac{m_1 m_2}{a_2}\frac{1}{2}e_1 \Big[-2s - \alpha D \Big] b_{\frac{1}{2}}^{(s)}(\alpha),
\tag{3.9}
$$

$$
E_s = -\mathcal{G}\frac{m_1 m_2}{a_2}\frac{1}{2}e_2 \Big[-1 + 2s + \alpha D \Big] b_{\frac{1}{2}}^{(s-1)}(\alpha),
\tag{3.10}
$$

$$
F_s = -\mathcal{G}\frac{m_1 m_2}{a_2}\frac{1}{8}e_1^2 \Big[-5s + 4s^2 - 2\alpha D + 4s\alpha D + \alpha^2 D^2 \Big] b_{\frac{1}{2}}^{(s)}(\alpha),
\tag{3.11}
$$

$$
G_s = -\mathcal{G}\frac{m_1 m_2}{a_2}\frac{1}{8}e_2^2 \Big[2 - 7s + 4s^2 - 2\alpha D + 4s\alpha D + \alpha^2 D^2 \Big] b_{\frac{1}{2}}^{(s-2)}(\alpha),
\tag{3.12}
$$

$$
I_s = -\mathcal{G}\frac{m_1 m_2}{a_2}\frac{1}{4}e_1 e_2 \Big[-2 + 6s - 4s^2 + 2\alpha D - 4s\alpha D - \alpha^2 D^2 \Big] b_{\frac{1}{2}}^{(s-1)}(\alpha),
\tag{3.13}
$$

$$
L_s = -\mathcal{G}\frac{m_1 m_2}{a_2}\frac{1}{2}I_1^2 \alpha b_{\frac{3}{2}}^{(s-1)}(\alpha),
\tag{3.14}
$$

$$
N_s = -\mathcal{G}\frac{m_1 m_2}{a_2}\frac{1}{2}I_2^2 \alpha b_{\frac{3}{2}}^{(s-1)}(\alpha),
\tag{3.15}
$$

$$
P_s = -\mathcal{G}\frac{m_1 m_2}{a_2} I_2 I_1 [-\alpha] b_{\frac{3}{2}}^{(s-1)}(\alpha),
\tag{3.16}
$$

where λ_k is the mean longitude, ϖ_k is the longitude of pericentre, Ω_k is the longitude of ascending node (see Appendix A), $\alpha = a_1/a_2$, $D = \partial/\partial\alpha$, and $b_s^{(j)}$ are Laplace coefficients (e.g. Murray and Dermott 1999).

For the indirect term,

$$
\mathcal{H}_I = \frac{\mathbf{p_1} \cdot \mathbf{p_2}}{m_0},
\tag{3.17}
$$

the linear momenta can be expressed as (Laskar and Robutel 1995)

$$
\mathbf{p}_k = \beta_k \dot{\mathbf{r}}_k = \frac{\beta_k n_k a_k}{\sqrt{1-e_k^2}} \mathcal{R}_3(\Omega_k)\,\mathcal{R}_1(I_k)\,\mathcal{R}_3(\omega_k) \begin{bmatrix} -\sin\nu_k \\ e_k + \cos\nu_k \\ 0 \end{bmatrix},
\tag{3.18}
$$

---

[1]We used the algebric manipulator Maxima (Maxima 2020) to perform these kind of calculations throughout this manuscript.

where ω_k is the argument of the pericentre and ν_k is the true anomaly (see Appendix A). The linear momenta $\mathbf{p}_1$ and $\mathbf{p}_2$ are then replaced into Eq. (3.17) and also expanded to the second order in the eccentricities and the inclinations, leading to

$$
\begin{aligned}
\mathcal{H}_I = \frac{\beta_1 \beta_2 n_1 n_2 a_1 a_2}{8 m_0} \Big(& (8 - 4e_1^2 - 4e_2^2 - 2I_1^2 - 2I_2^2) \cos (\lambda_1 - \lambda_2) \\
& + 8e_1 \cos (2\lambda_1 - \lambda_2 - \varpi_1) + 8e_2 \cos (\lambda_1 - 2\lambda_2 + \varpi_2) \\
& + e_1^2 (9 \cos (3\lambda_1 - \lambda_2 - 2\varpi_1) - \cos (\lambda_1 + \lambda_2 - 2\varpi_1)) \\
& + e_2^2 (9 \cos (\lambda_1 - 3\lambda_2 + 2\varpi_2) - \cos (\lambda_1 + \lambda_2 - 2\varpi_2)) \\
& + 8e_1 e_2 \cos (2\lambda_1 - 2\lambda_2 - \varpi_1 + \varpi_2) \\
& - 2I_1^2 \cos (\lambda_1 + \lambda_2 - 2\Omega_1) - 2I_2^2 \cos (\lambda_1 + \lambda_2 - 2\Omega_2) \\
& + 4I_1 I_2 \cos (\lambda_1 + \lambda_2 - \Omega_1 - \Omega_2) + 4I_1 I_2 \cos (\lambda_1 - \lambda_2 - \Omega_1 + \Omega_2) \Big).
\end{aligned}
\tag{3.19}
$$

3.2 Planet oblateness

In Sect. 2.2 we developed the potential energy arising from a rotationally deformed body, given by

$$
U(\mathbf{r}_k) \approx -\frac{k_{2_0} m_k \omega_0^2 R_0^5}{6 r_k^3} \left(1 - 3 \frac{(\mathbf{r}_k \cdot \omega_0)^2}{r_k^2 \omega_0^2} \right).
\tag{3.20}
$$

Thus, the total contribution of the rotational deformation from the host planet to the Hamiltonian (3.1) can be written as

$$
\mathcal{H}_O = \sum_{k=1}^{2} \frac{G m_0 m_k R_0^2 J_{2_0}}{r_k^3} \mathcal{P}_2 (\hat{\mathbf{r}}_k \cdot \hat{\omega}_0),
\tag{3.21}
$$

where J_{2_0} is the second order gravity field of the central body (Eq. (2.20)) and $\hat{\mathbf{r}}_k \cdot \hat{\omega}_0 = \sin I_k \sin (\omega_k + \nu_k)$ (Eq. (A.27)). Expanding ν_k and r_k in orbital elements and truncating up to the second order in the eccentricities and the inclinations (see Appendix A), $\mathcal{H}_O$ can be written as

$$
\begin{aligned}
\mathcal{H}_O = -\sum_{k=1}^{2} \frac{G m_0 m_k}{2 a_k} J_{2_0} \left(\frac{R_0}{a_k} \right)^2 \Big(& 1 + 3e_k \cos (\lambda_k - \varpi_k) + \frac{3}{2} e_k^2 (1 + 3 \cos (2\lambda_k - 2\varpi_k)) \\
& - \frac{3}{2} I_k^2 (1 - \cos (2\lambda_k - 2\Omega_k)) \Big).
\end{aligned}
\tag{3.22}
$$

We note that $J_{2_0} R_0^2 \gg J_{2_k} R_k^2$ (Tables 1.1 and 1.2), and so we neglected the contribution arising from the rotational deformation of the satellites.

The Hamiltonian in elliptical elements to the first order in the mass ratios, m_k/m_0, second order in the eccentricities and the inclinations, with respect to the equatorial plane of the central oblate body and with rotation then finally writes as

$$
\mathcal{H} = \mathcal{H}_K + \mathcal{H}_O + \mathcal{H}_D + \mathcal{H}_I + \mathcal{H}_\Theta,
\tag{3.23}
$$

where

$$
\mathcal{H}_\Theta = \sum_{k=0}^{2} \frac{\Theta_k^2}{2 C_k}
\tag{3.24}
$$

is the total rotational kinetic energy, C_k is the principal moment of inertia of m_k (Eq. (2.15)) and

$$
\Theta_k = C_k \omega_k,
\tag{3.25}
$$

which corresponds to the rotational angular momentum, where $\omega_k = \dot{\theta}_k$ is the angular velocity and θ_k is the rotation angle (we assume zero obliquity for all bodies). In the conservative case, the rotational kinetic energy is constant and could be dropped from the Hamiltonian. Nevertheless, when we include tidal dissipation (Chap. 4), there are angular momentum exchanges between the spins and the orbits, and this term cannot be neglected.

3.3 Action-angle resonant variables

Although very useful and practical to use with a simple geometrical interpretation, the elliptical elements are not canonical. Therefore, they do not allow to use the advantages of the Hamiltonian formulation. For this reason, we introduce a set of widely used canonical variables $(\Lambda_k, \lambda_k, \Sigma_k, -\varphi_k, \Phi_k, -\Omega_k)$, known as Poincaré variables (e.g. Murray and Dermott 1999), related with the elliptical elements by the following expressions:

$$\Lambda_k = \beta_k \sqrt{\mu_k a_k}, \qquad\qquad\qquad \lambda_k = M_k + \varpi_k, \qquad (3.26)$$

$$\Sigma_k = \Lambda_k \left(1 - \sqrt{1 - e_k^2} \right), \qquad\qquad -\varpi_k, \qquad (3.27)$$

$$\Phi_k = (\Lambda_k - \Sigma_k)(1 - \cos I_k), \qquad\qquad -\Omega_k. \qquad (3.28)$$

Expanded up to second order in the eccentricities and the inclinations, the semi-major axes, the eccentricities, and the inclinations can be expressed using Poincaré variables using Eqs. (3.26)-(3.28) as:

$$a_k = \frac{\Lambda_k^2}{\beta_k^2 \mu_k}, \qquad (3.29)$$

$$e_k \approx \sqrt{\frac{2\Sigma_k}{\Lambda_k}}, \qquad (3.30)$$

$$I_k \approx \sqrt{\frac{2\Phi_k}{\Lambda_k}}. \qquad (3.31)$$

We also adopt the canonical Andoyer variables (Andoyer 1915, 1923) for the rotation (Θ, θ), previously used in the definition of angular momentum of rotation (Eq. (3.25)).

Suppose that the system is near a mean-motion commensurability of the form $(p + q)/p$, that is, $(p + q)\dot{M}_2 - p\dot{M}_1 \approx 0$, where p and q are positive integers, and q is the resonance order. We may then introduce the resonance angle of the $(p + q)/p$ MMR:

$$\sigma = \left(1 + \frac{p}{q} \right)\lambda_2 - \frac{p}{q}\lambda_1. \qquad (3.32)$$

Substituting $\lambda_1 = \left(1 + \frac{q}{p} \right)\lambda_2 - \frac{q}{p}\sigma$, we now introduce a new set of canonical coordinates, that we dubbed *resonant variables*, which are obtained from the Poincaré canonical variables using a type 3 generating function (S_3), given by (Eqs. (3.26)-(3.28))

$$
\begin{aligned}
S_3 &= - \left[\Lambda_1 \lambda_1 + \Lambda_2 \lambda_2 - \Sigma_1 \varpi_1 - \Sigma_2 \varpi_2 - \Phi_1 \Omega_1 - \Phi_2 \Omega_2 + \Theta_0 \theta_0 + \Theta_1 \theta_1 + \Theta_2 \theta_2 \right] \\
&= - \left[-\frac{q}{p}\Lambda_1 \sigma + \left(\left(1 + \frac{q}{p} \right)\Lambda_1 + \Lambda_2 \right)\lambda_2 - \Sigma_1 \varpi_1 - \Sigma_2 \varpi_2 - \Phi_1 \Omega_1 - \Phi_2 \Omega_2 + \Theta_0 \theta_0 + \Theta_1 \theta_1 + \Theta_2 \theta_2 \right].
\end{aligned}
$$
$$(3.33)$$

The new canonical momenta are simply obtained by $\boldsymbol{P} = -\partial S_3/\partial \boldsymbol{Q}$, where $\boldsymbol{P} = (P_\sigma, \Gamma, \Sigma_k, \Phi_k, \Theta_k)$ are

the new canonical momenta and $\mathbf{Q} = (\sigma, \lambda_2, -\varpi_k, -\Omega_k, \theta_k)$ are the new canonical angles, yielding to

$$P_\sigma = -\frac{q}{p}\Lambda_1\,, \qquad\qquad\qquad\qquad \sigma\,, \qquad\qquad (3.34)$$

$$\Gamma = \left(1 + \frac{q}{p}\right)\Lambda_1 + \Lambda_2\,, \qquad\qquad\qquad \lambda_2\,, \qquad\qquad (3.35)$$

$$\Sigma_k\,, \qquad\qquad\qquad\qquad -\varpi_k\,,$$

$$\Phi_k\,, \qquad\qquad\qquad\qquad -\Omega_k\,,$$

$$\Theta_k\,, \qquad\qquad\qquad\qquad \theta_k\,.$$

We can also take advantage of the conservation of the total angular momentum of the system $\mathbf{L}_{\text{tot}}$, that is, the sum of the orbital angular momentum of m_1 and m_2, with the sum of the rotational angular momenta of all the bodies of the system. Projecting $\mathbf{L}_{\text{tot}}$ along the direction of $\mathbf{e}_z$, we have

$$\begin{aligned}
\Sigma &= \mathbf{L}_{\text{tot}} \cdot \mathbf{e}_z \\
&= (\Lambda_1 - \Sigma_1 - \Phi_1) + (\Lambda_2 - \Sigma_2 - \Phi_2) + \Theta_0 + \Theta_1 + \Theta_2 \\
&= \beta_1\sqrt{\mu_1 a_1(1 - e_1^2)}\cos I_1 + \beta_2\sqrt{\mu_2 a_2(1 - e_2^2)}\cos I_2 + C_0\omega_0 + C_1\omega_1 + C_2\omega_2\,.
\end{aligned} \qquad (3.36)$$

Using a type 4 generating function (S_4), which depends on the new and the old canonical moments, we can obtain a new set of canonical variables, where we replaced $\Lambda_1 = \Sigma - \Lambda_2 + \Sigma_1 + \Sigma_2 + \Phi_1 + \Phi_2 - \Theta_0 - \Theta_1 - \Theta_2$, that is,

$$\begin{aligned}
S_4 = {}& -\frac{q}{p}\Lambda_1\,\sigma + \Gamma\,\lambda_2 - \Sigma_1\,\varpi_1 - \Sigma_2\,\varpi_2 - \Phi_1\,\Omega_1 - \Phi_2\,\Omega_2 + \Theta_0\,\theta_0 + \Theta_1\,\theta_1 + \Theta_2\,\theta_2 \\
={}& \Sigma\,\sigma + \Gamma\,(\lambda_2 - \sigma) + \Sigma_1\,(\sigma - \varpi_1) + \Sigma_2\,(\sigma - \varpi_2) + \Phi_1\,(\sigma - \Omega_1) + \Phi_2\,(\sigma - \Omega_2) \\
& + \Theta_0(\theta_0 - \sigma) + \Theta_1(\theta_1 - \sigma) + \Theta_2(\theta_2 - \sigma)\,.
\end{aligned} \qquad (3.37)$$

The new resonant canonical coordinates are simply obtained by $\mathbf{Q} = \partial S_4/\partial \mathbf{P}$, giving

$$\Sigma\,, \qquad \sigma = \left(1 + \frac{p}{q}\right)\lambda_2 - \frac{p}{q}\lambda_1\,, \qquad\qquad (3.38)$$

$$\Gamma\,, \qquad \gamma = \lambda_2 - \sigma\,, \qquad\qquad (3.39)$$

$$\tilde{\Sigma}_1 = \Sigma_1\,, \qquad \sigma_1 = \sigma - \varpi_1\,, \qquad\qquad (3.40)$$

$$\tilde{\Sigma}_2 = \Sigma_2\,, \qquad \sigma_2 = \sigma - \varpi_2\,, \qquad\qquad (3.41)$$

$$\tilde{\Phi}_1 = \Phi_1\,, \qquad \varphi_1 = \sigma - \Omega_1\,, \qquad\qquad (3.42)$$

$$\tilde{\Phi}_2 = \Phi_2\,, \qquad \varphi_2 = \sigma - \Omega_2\,, \qquad\qquad (3.43)$$

$$\tilde{\Theta}_0 = \Theta_0\,, \qquad \vartheta_0 = \theta_0 - \sigma\,, \qquad\qquad (3.44)$$

$$\tilde{\Theta}_1 = \Theta_1\,, \qquad \vartheta_1 = \theta_1 - \sigma\,, \qquad\qquad (3.45)$$

$$\tilde{\Theta}_2 = \Theta_2\,, \qquad \vartheta_2 = \theta_2 - \sigma\,, \qquad\qquad (3.46)$$

where the angles σ_1, σ_2, φ_1, and φ_2 are the resonance angles associated with e_1, e_2, I_1, and I_2, respectively.

It is important to note that Λ_1 and Λ_2 are no longer actions of the resonant variables, but can be obtained as

$$\Lambda_1 = \Gamma_1 - \frac{p}{q}(\Sigma_1 + \Sigma_2 + \Phi_1 + \Phi_2)\,, \qquad\qquad (3.47)$$

$$\Lambda_2 = \Gamma_2 + \left(1 + \frac{p}{q}\right)(\Sigma_1 + \Sigma_2 + \Phi_1 + \Phi_2)\,, \qquad\qquad (3.48)$$

with

$$\Gamma_1 = \frac{p}{q}\Gamma\,(1 - \Delta)\,, \qquad\qquad (3.49)$$

$$\Gamma_2 = -\frac{p}{q}\Gamma\left(1 - \left(1 + \frac{q}{p}\right)\Delta\right) , \tag{3.50}$$

$$\Delta = (\Sigma - \Theta)/\Gamma , \tag{3.51}$$

and

$$\Theta = \Theta_0 + \Theta_1 + \Theta_2 . \tag{3.52}$$

In the approximation of small eccentricities and small inclinations, we have that $\Sigma_k \ll \Lambda_k$ and $\Phi_k \ll \Lambda_k$. As a consequence, we also have that $\Sigma_k \ll \Gamma_k$ and $\Phi_k \ll \Gamma_k$ (Eqs. (3.47) and (3.48)), which allows us to obtain:

$$\Lambda_1^\alpha \approx \Gamma_1^\alpha \left[1 - \alpha \frac{p}{q} \frac{\Sigma_1 + \Sigma_2 + \Phi_1 + \Phi_2}{\Gamma_1}\right] , \tag{3.53}$$

$$\Lambda_2^\alpha \approx \Gamma_2^\alpha \left[1 + \alpha \left(1 + \frac{p}{q}\right) \frac{\Sigma_1 + \Sigma_2 + \Phi_1 + \Phi_2}{\Gamma_2}\right] , \tag{3.54}$$

and

$$e_k \approx \sqrt{\frac{2\Sigma_k}{\Gamma_k}} , \tag{3.55}$$

$$I_k \approx \sqrt{\frac{2\Phi_k}{\Gamma_k}} . \tag{3.56}$$

Substituting the resonant angles σ_k and φ_k in $\mathcal{H}_D$ (Eq. (3.5)), the direct part becomes

$$\begin{aligned}
\mathcal{H}_D = \sum_{s=0} \Bigg[&A_s \cos\left(s\frac{q}{p}\gamma\right) + B_s \cos\left(s\frac{q}{p}\gamma + \sigma_2 - \sigma_1\right) + C_s \cos\left(s\frac{q}{p}\gamma + \varphi_2 - \varphi_1\right) \\
&+ D_s \cos\left(\left(1 + (1-s)\frac{q}{p}\right)\gamma + \sigma_1\right) + E_s \cos\left(\left(1 + (1-s)\frac{q}{p}\right)\gamma + \sigma_2\right) \\
&+ F_s \cos\left(\left(2 + (2-s)\frac{q}{p}\right)\gamma + 2\sigma_1\right) + G_s \cos\left(\left(2 + (2-s)\frac{q}{p}\right)\gamma + 2\sigma_2\right) \\
&+ I_s \cos\left(\left(2 + (2-s)\frac{q}{p}\right)\gamma + \sigma_1 + \sigma_2\right) \\
&+ L_s \cos\left(\left(2 + (2-s)\frac{q}{p}\right)\gamma + 2\varphi_1\right) + N_s \cos\left(\left(2 + (2-s)\frac{q}{p}\right)\gamma + 2\varphi_2\right) \\
&+ P_s \cos\left(\left(2 + (2-s)\frac{q}{p}\right)\gamma + \varphi_1 + \varphi_2\right) \Bigg] ,
\end{aligned} \tag{3.57}$$

the indirect part $\mathcal{H}_I$ (Eq. (3.19)) becomes

$$\begin{aligned}
\mathcal{H}_I = \frac{\beta_1\beta_2 n_1 n_2 a_1 a_2}{8m_0} \Bigg[&\left(8 - 4e_1^2 - 4e_2^2 - 2I_1^2 - 2I_2^2\right)\cos\left(\frac{q}{p}\gamma\right) \\
&+ 8e_1 \cos\left(\gamma\left(1 + \frac{2q}{p}\right) + \sigma_1\right) + 8e_2 \cos\left(\gamma\left(1 - \frac{q}{p}\right) + \sigma_2\right) \\
&+ e_1^2\left(9\cos\left(\gamma\left(2 + \frac{3q}{p}\right) + 2\sigma_1\right) - \cos\left(\gamma\left(2 + \frac{q}{p}\right) + 2\sigma_1\right)\right) \\
&+ e_2^2\left(9\cos\left(\gamma\left(2 - \frac{q}{p}\right) + 2\sigma_2\right) - \cos\left(\gamma\left(2 + \frac{q}{p}\right) + 2\sigma_2\right)\right) \\
&+ 8e_1 e_2 \cos\left(\gamma\frac{2q}{p} + \sigma_1 - \sigma_2\right) - 2I_1^2 \cos\left(\gamma\left(2 + \frac{q}{p}\right) + \varphi_1\right) - 2I_2^2 \cos\left(\gamma\left(2 + \frac{q}{p}\right) + \varphi_2\right) \\
&+ 4I_1 I_2 \cos\left(\gamma\frac{q}{p} + \varphi_1 - \varphi_2\right) + 4I_1 I_2 \cos\left(\gamma\left(2 + \frac{q}{p}\right) + \varphi_1 + \varphi_2\right) \Bigg] ,
\end{aligned}$$

$$\tag{3.58}$$

and the oblateness part $\mathcal{H}_O$ (Eq. (3.22)) becomes

$$
\begin{aligned}
\mathcal{H}_O = &-\frac{\mathcal{G}m_0 m_1}{2a_1} J_{2_0} \left(\frac{R_0}{a_1}\right)^2 \left(1 + 3e_1 \cos\left[\left(1 + \frac{q}{p}\right)\gamma + \sigma_1\right] + \frac{3}{2}e_1^2\left(1 + 3\cos\left[2\left(1 + \frac{q}{p}\right)\gamma + 2\sigma_1\right]\right)\right.\\
&\left. - \frac{3}{2}I_1^2\left(1 - \cos\left[2\left(1 + \frac{q}{p}\right)\gamma + 2\varphi_1\right]\right)\right)\\
&-\frac{\mathcal{G}m_0 m_2}{2a_2} J_{2_0} \left(\frac{R_0}{a_2}\right)^2 \left(1 + 3e_2 \cos\left[\gamma + \sigma_2\right] + \frac{3}{2}e_2^2(1 + 3\cos 2\left[2\gamma + 2\sigma_2\right])\right.\\
&\left. - \frac{3}{2}I_2^2(1 - \cos 2\left[2\gamma + 2\varphi_2\right])\right).
\end{aligned}
\tag{3.59}
$$

We note that none of the angles θ_k appear in the expression of the Hamiltonian, and so, ϑ_k do not appear as well. Consequently, ϑ_k are cyclic coordinates in the conservative approximation, and the Θ_k are constants of motion. According to the d'Alembert rule (conservation of the angular momentum), the remaining angles must be combined as

$$
\cos\left(k_1\lambda_1 + k_2\lambda_2 + k_3\varpi_1 + k_4\varpi_2 + k_5\Omega_1 - (k_1 + k_2 + k_3 + k_4 + k_5)\Omega_2\right), \quad k_j \in \mathbb{Z}.
\tag{3.60}
$$

where $\sum_j k_j = 0$. Using the resonance angles (Eqs. (3.38)-(3.43)) the relation becomes

$$
\cos\left[\left(\left(1 + \frac{2}{p}\right)k_1 + k_2\right)\gamma - k_3\sigma_1 - k_4\sigma_2 - k_5\varphi_1 + (k_1 + k_2 + k_3 + k_4 + k_5)\varphi_2\right].
\tag{3.61}
$$

Hence, the angle σ does not appear in the Hamiltonian, and, consequently, its conjugated action, Σ, is another constant of motion, as expected.

3.4 Average

Near the commensurability, the resonance angles σ_k and φ_k vary much slower than γ, i.e., $\dot{\sigma}_k \ll \dot{\gamma}$ and $\dot{\phi}_k \ll \dot{\gamma}$. Therefore, we can construct the resonant secular normal form of the Hamiltonian (to the first order in m_k/m_0) by averaging over γ:

$$
\tilde{\mathcal{H}} = \langle \mathcal{H} \rangle_\gamma = \frac{1}{2p\pi} \int_0^{2p\pi} \mathcal{H}\, d\gamma.
\tag{3.62}
$$

The Keplerian terms, $\mathcal{H}_K$ (Eq. (3.1)), do not have a dependency on γ, and remain unchanged by the average. For the oblateness contribution, $\mathcal{H}_O$ (Eq. (3.59)), all the terms with cosines are removed. For $\mathcal{H}_D$ (Eq. (3.57)), if $s = 0$, only the terms with coefficients A_0 (Eq. (3.6)), B_0 (Eq. (3.7)), and C_0 (Eq. (3.8)) do not depend on γ and are not avereged out. The resulting terms are known as the *secular terms*, and, as the Keplerian and oblateness contributions, they remain for any order MMR.

The lowest order MMRs that possibly recently occurred in the Uranian system are second order commensurabilities (Fig. 1.4), that is, $q = 2$. Thus, from now on, our study will be restricted to this particular case. Then, only when $s = p + 2$ the terms of $\mathcal{H}_D$ (Eq. (3.57)) associated to the coefficients F_2 (Eq. (3.11)), G_2 (Eq. (3.12)), I_2 (Eq. (3.13)), L_2 (Eq. (3.14)), N_2 (Eq. (3.15)), and P_2 (Eq. (3.16)) do not vanish by averaging over γ. Furthermore, in the particular case where $s = p + 2$ and $p = 1$, that is, for the 3/1 MMR, the term with $\cos\left[\gamma(2 - \frac{q}{p}) + 2\sigma_2\right]$ of the indirect Hamiltonian (Eq. (3.58)) does not depend on γ and is preserved. However, note that this term is only valid for the but for 3/1 MMR, since, if $p \neq 1$, this term also vanishes. We name these terms as the *resonant terms* for the second order MMR. All the remaining terms are removed by averaging the Hamiltonian over γ.

The average Hamiltonian expressed with the resonant angles is then given by

$$
\tilde{\mathcal{H}} = \mathcal{H}_K + \tilde{\mathcal{H}}_O + \tilde{\mathcal{H}}_S + \tilde{\mathcal{H}}_R + \tilde{\mathcal{H}}_I + \mathcal{H}_\Theta,
\tag{3.63}
$$

where $\mathcal{H}_K$ (Eq. (3.2)) is the Keplerian part,

$$\tilde{\mathcal{H}}_O = -\sum_{k=1}^{2} \frac{\mathcal{G}m_0 m_k}{2a_k} J_{2_0} \left(\frac{R_0}{a_k}\right)^2 \left(1 + \frac{3}{2}e_k^2 - \frac{3}{2}I_k^2\right) \tag{3.64}$$

is the contribution from the oblateness of the planet,

$$\begin{aligned}
\tilde{\mathcal{H}}_S = -\frac{\mathcal{G}m_1 m_2}{8a_2} \Big[&4b_{\frac{1}{2}}^{(0)}(\alpha) + \left(e_1^2 + e_2^2\right)\left(2\alpha D + \alpha^2 D^2\right) b_{\frac{1}{2}}^{(0)}(\alpha) \\
&+ 2e_1 e_2 \cos(\sigma_2 - \sigma_1)\left(2 - 2\alpha - \alpha^2\right) b_{\frac{1}{2}}^{(1)}(\alpha) \\
&- \left(I_1^2 + I_2^2 - 2I_1 I_2 \cos(\varphi_2 - \varphi_1)\right) \alpha\, b_{\frac{3}{2}}^{(1)}(\alpha) \Big]
\end{aligned} \tag{3.65}$$

is the secular part, and

$$\begin{aligned}
\tilde{\mathcal{H}}_R = -\frac{\mathcal{G}m_1 m_2}{8a_2} \Big[&e_1^2 \left(4p^2 + 11p + 6 + (4p+6)\alpha D \alpha^2 D^2\right) b_{\frac{1}{2}}^{(p+2)}(\alpha) \cos(2\sigma_1) \\
&+ e_2^2 \left(4p^2 + 9p + 4 + (4p+6)\alpha D + \alpha^2 D^2\right) b_{\frac{1}{2}}^{(p)}(\alpha) \cos(2\sigma_2) \\
&- 2e_1 e_2 \left(4p^2 + 10p + 6 + (4p+6)\alpha D + \alpha^2 D^2\right) b_{\frac{1}{2}}^{(p+1)}(\alpha) \cos(\sigma_1 + \sigma_2) \\
&+ \left(I_1^2 \cos(2\varphi_1) + I_2^2 \cos(2\varphi_2) - 2I_1 I_2 \cos(\varphi_1 + \varphi_2)\right) \alpha b_{\frac{3}{2}}^{(p+1)}(\alpha) \Big]
\end{aligned} \tag{3.66}$$

and

$$\tilde{\mathcal{H}}_I = \frac{9}{8} \frac{\sqrt{\mu_1 \mu_2}\,\beta_1 \beta_2}{m_0\, a_1^{5/2} a_2^{5/2}} e_2^2 \cos(2\sigma_2^*) \tag{3.67}$$

are the contributions from the second order resonant terms and $\mathcal{H}_\Theta$ (Eq. (3.24)) is the total rotational kinetic energy, where $\sigma_2^* = \sigma_2$ only exists for $p = 1$.

Now, we replace e_k and I_k by Eqs. (3.55) and (3.56) and a_k by Eqs. (3.29), (3.47) and (3.48) (see Appendix B) and expand to the first order in Σ_k/Γ_k and Φ_k/Γ_k, that is, to the second order in the eccentricities and the inclinations. We finally obtain the secular Hamiltonian expressed in the resonant canonical coordinates (Eqs. (3.38) to (3.46))

$$\begin{aligned}
\tilde{\mathcal{H}} = &(\mathcal{K}_1 + \mathcal{S}_1)(\Sigma_1 + \Sigma_2 + \Phi_1 + \Phi_2) + \mathcal{K}_2(\Sigma_1 + \Sigma_2 + \Phi_1 + \Phi_2)^2 \\
&+ (\mathcal{O}_1 + \mathcal{S}_2)\Sigma_1 + (\mathcal{O}_2 + \mathcal{S}_3)\Sigma_2 + \mathcal{S}_4 \sqrt{\Sigma_1}\sqrt{\Sigma_2}\cos(\sigma_1 - \sigma_2) \\
&+ (\mathcal{O}_3 + \mathcal{S}_5)\Phi_1 + (\mathcal{O}_4 + \mathcal{S}_6)\Phi_2 + \mathcal{S}_7 \sqrt{\Phi_1}\sqrt{\Phi_2}\cos(\varphi_1 - \varphi_2) \\
&+ \mathcal{R}_1 \Sigma_1 \cos(2\sigma_1) + \mathcal{R}_2 \Sigma_2 \cos(2\sigma_2) + \mathcal{R}_3 \sqrt{\Sigma_1}\sqrt{\Sigma_2}\cos(\sigma_1 + \sigma_2) \\
&+ \mathcal{R}_4 \Phi_1 \cos(2\varphi_1) + \mathcal{R}_5 \Phi_2 \cos(2\varphi_2) + \mathcal{R}_6 \sqrt{\Phi_1}\sqrt{\Phi_2}\cos(\varphi_1 + \varphi_2),
\end{aligned} \tag{3.68}$$

where

$$\mathcal{K}_1 = -\frac{p}{q}\frac{\mu_1^2 \beta_1^3}{\Gamma_1^3} + \frac{p+q}{q}\frac{\mu_2^2 \beta_2^3}{\Gamma_2^3}, \tag{3.69}$$

$$\mathcal{K}_2 = -\frac{3}{2}\left(\frac{p^2}{q^2}\frac{\mu_1^2 \beta_1^3}{\Gamma_1^4} + \frac{(p+q)^2}{q^2}\frac{\mu_2^2 \beta_2^3}{\Gamma_2^4}\right), \tag{3.70}$$

$$\mathcal{O}_1 = \frac{3}{2}J_{2_0}R_0^2\left(-\frac{2p+q}{q}\frac{\mu_1^4 \beta_1^7}{\Gamma_1^7} + \frac{2(p+q)}{q}\frac{\mu_2^4 \beta_2^7}{\Gamma_2^7}\right), \tag{3.71}$$

$$\mathcal{O}_2 = \frac{3}{2}J_{2_0}R_0^2\left(-\frac{2p}{q}\frac{\mu_1^4 \beta_1^7}{\Gamma_1^7} + \frac{2p+q}{q}\frac{\mu_2^4 \beta_2^7}{\Gamma_2^7}\right), \tag{3.72}$$

$$O_3 = \frac{3}{2} J_{2_0} R_0^2 \left(-\frac{(2p-q)}{q} \frac{\mu_1^4 \beta_1^7}{\Gamma_1^7} + \frac{2(p+q)}{q} \frac{\mu_2^4 \beta_2^7}{\Gamma_2^7} \right), \tag{3.73}$$

$$O_4 = \frac{3}{2} J_{2_0} R_0^2 \left(-\frac{2p}{q} \frac{\mu_1^4 \beta_1^7}{\Gamma_1^7} + \frac{2p+3q}{q} \frac{\mu_2^4 \beta_2^7}{\Gamma_2^7} \right), \tag{3.74}$$

$$S_1 = \frac{\mathcal{G}\mu_2 m_1 m_2 \beta_2^2}{\Gamma_2^3} \left[\frac{\mu_2 \beta_2^2}{\mu_1 \beta_1^2} \left(\frac{p+q}{q} \frac{\Gamma_1^2}{\Gamma_2^2} + \frac{p}{q} \frac{\Gamma_1}{\Gamma_2} \right) D + \frac{p+q}{q} \right] b_{\frac{1}{2}}^{(0)}(\alpha_0), \tag{3.75}$$

$$S_2 = -\frac{\mathcal{G}\mu_2 m_1 m_2 \beta_2^2}{2\Gamma_1 \Gamma_2^2} \left[\alpha_0 D + \frac{1}{2} \alpha_0^2 D^2 \right] b_{\frac{1}{2}}^{(0)}(\alpha_0), \tag{3.76}$$

$$S_3 = -\frac{\mathcal{G}\mu_2 m_1 m_2 \beta_2^2}{2\Gamma_2^3} \left[\alpha_0 D + \frac{1}{2} \alpha_0^2 D^2 \right] b_{\frac{1}{2}}^{(0)}(\alpha_0), \tag{3.77}$$

$$S_4 = -\frac{\mathcal{G}\mu_2 m_1 m_2 \beta_2^2}{2\Gamma_2^2 \sqrt{\Gamma_1 \Gamma_2}} \left[2 - 2\alpha_0 D - \alpha_0^2 D^2 \right] b_{\frac{1}{2}}^{(1)}(\alpha_0), \tag{3.78}$$

$$S_5 = \frac{\mathcal{G}\mu_2 m_1 m_2 \beta_2^2}{4\Gamma_1 \Gamma_2^2} \alpha_0 b_{\frac{3}{2}}^{(1)}(\alpha_0), \tag{3.79}$$

$$S_6 = \frac{\mathcal{G}\mu_2 m_1 m_2 \beta_2^2}{4\Gamma_2^3} \alpha_0 b_{\frac{3}{2}}^{(1)}(\alpha_0), \tag{3.80}$$

$$S_7 = -\frac{\mathcal{G}\mu_2 m_1 m_2 \beta_2^2}{2\Gamma_2^2 \sqrt{\Gamma_1 \Gamma_2}} \alpha_0 b_{\frac{3}{2}}^{(1)}(\alpha_0), \tag{3.81}$$

$$\mathcal{R}_1 = -\frac{\mathcal{G}\mu_2 m_1 m_2 \beta_2^2}{2\Gamma_1 \Gamma_2^2} \left[\frac{8p^2 + 11pq + 3q^2}{q^2} + \frac{4p+3q}{q} \alpha_0 D + \frac{\alpha_0^2}{2} D^2 \right] b_{\frac{1}{2}}^{(p+2)}(\alpha_0), \tag{3.82}$$

$$\mathcal{R}_2 = -\frac{\mathcal{G}\mu_2 m_1 m_2 \beta_2^2}{2\Gamma_2^3} \left[\frac{8p^2 + 9pq + 2q^2}{q^2} + \frac{4p+3q}{q} \alpha_0 D + \frac{\alpha_0^2}{2} D^2 \right] b_{\frac{1}{2}}^{(p)}(\alpha_0) + \mathcal{R}_2^*, \tag{3.83}$$

$$\mathcal{R}_2^* = \begin{cases} \frac{9}{4} \frac{\beta_1 \beta_2 \mu_1 \mu_2}{\Gamma_1 \Gamma_2^2} & \text{if} \quad p = 1 \\ 0 & \text{if} \quad p \neq 1 \end{cases}, \tag{3.84}$$

$$\mathcal{R}_3 = -\frac{\mathcal{G}\mu_2 m_1 m_2 \beta_2^2}{\Gamma_2^2 \sqrt{\Gamma_1 \Gamma_2}} \left[\frac{8p^2 + 10pq + 3q^2}{q^2} + \frac{4p+3q}{q} \alpha_0 D + \frac{\alpha_0^2}{2} D^2 \right] b_{\frac{1}{2}}^{(p+1)}(\alpha_0), \tag{3.85}$$

$$\mathcal{R}_4 = -\frac{\mathcal{G}\mu_2 m_1 m_2 \beta_2^2}{4\Gamma_1 \Gamma_2^2} \alpha_0 b_{\frac{3}{2}}^{(p+1)}(\alpha_0), \tag{3.86}$$

$$\mathcal{R}_5 = -\frac{\mathcal{G}\mu_2 m_1 m_2 \beta_2^2}{4\Gamma_2^3} \alpha_0 b_{\frac{3}{2}}^{(p+1)}(\alpha_0), \tag{3.87}$$

$$\mathcal{R}_6 = \frac{\mathcal{G}\mu_2 m_1 m_2 \beta_2^2}{2\Gamma_2^2 \sqrt{\Gamma_1 \Gamma_2}} \alpha_0 b_{\frac{3}{2}}^{(p+1)}(\alpha_0), \tag{3.88}$$

$$\alpha_0 = \frac{\mu_2 \beta_2^2 \Gamma_2^2}{\mu_1 \beta_1^2 \Gamma_1^2}, \tag{3.89}$$

and $q = 2$. The $\mathcal{K}$ stands for the Keplerian terms, O for the oblateness terms, S for the secular terms, and $\mathcal{R}$ for the resonant terms. The Keplerian part needed to be expanded to the second order in Σ_k and Φ_k, because $\mathcal{K}_2$ it is much larger than the remaining terms.

3.5   Cartesian complex coordinates

The secular equations of motion can be easily obtained from the Hamiltonian (3.68) using the Hamilton equations. For instance,

$$
\begin{aligned}
\dot{\sigma}_1 = \frac{\partial \tilde{\mathcal{H}}}{\partial \Sigma_1} &= \mathcal{K}_1 + \mathcal{O}_1 + \mathcal{S}_1 + \mathcal{S}_2 + 2\mathcal{K}_2(\Sigma_1 + \Sigma_2 + \Phi_1 + \Phi_2) \\
&+ \frac{\mathcal{S}_4}{2}\sqrt{\frac{\Sigma_2}{\Sigma_1}}\cos(\sigma_1 - \sigma_2) + \mathcal{R}_1\cos(2\sigma_1) + \frac{\mathcal{R}_3}{2}\sqrt{\frac{\Sigma_2}{\Sigma_1}}\cos(\sigma_1 + \sigma_2).
\end{aligned}
\tag{3.90}
$$

Analysing Eq. (3.90), we note that the terms with the coefficients $\mathcal{S}_4$ and $\mathcal{R}_3$ are not defined when $\Sigma_1 = 0$. The same occurs for $\dot{\sigma}_2$, $\dot{\varphi}_1$, and $\dot{\varphi}_2$, where, for the terms with coefficients $\mathcal{S}_4$, $\mathcal{S}_7$, $\mathcal{R}_3$, and $\mathcal{R}_6$, the equations of motion present singularities for $\Sigma_k = 0$ or $\Phi_k = 0$. This means that, for zero eccentricities or inclinations of either bodies, the equations of motion are not defined.

To overcome this problem, Tittemore and Wisdom (1988) employed a set of rectangular coordinates. In contrast, we choose to introduce a distinct set of coordinates, the complex Cartesian canonical coordinates, denoted as $x_k = \sqrt{\Sigma_k}e^{i\sigma_k}$ and $y_k = \sqrt{\Phi_k}e^{i\varphi_k}$. Since this complex coordinates are composed, that is, they contain a real and an imaginary component, we reduce the number of equations of motion by half, resulting in a more simple formulation for describing the secular problem. Using a type 2 generating function (S_2), which depends on the new canonical moments and the old canonical coordinates, we obtain the new set of rectangular canonical variables by replacing $\Sigma_k = x_k^2\,e^{-2i\sigma_k}$ and $\Phi_k = y_k^2\,e^{-2i\varphi_k}$, yielding to

$$
\begin{aligned}
S_2 &= \int \Sigma_1\,d\sigma_1 + \int \Sigma_2\,d\sigma_2 + \int \Phi_1\,d\varphi_1 + \int \Phi_2\,d\varphi_2 + \Theta_0\vartheta_0 + \Theta_1\vartheta_1 + \Theta_2\vartheta_2 \\
&= i\frac{1}{2}\left(x_1^2\,e^{-2i\sigma_1} + x_2^2\,e^{-2i\sigma_2} + y_1^2\,e^{-2i\varphi_1} + y_2^2\,e^{-2i\varphi_2}\right) + \Theta_0\vartheta_0 + \Theta_1\vartheta_1 + \Theta_2\vartheta_2.
\end{aligned}
\tag{3.91}
$$

The conjugated canonical coordinates are obtained by $\boldsymbol{Q} = \partial S_2/\partial \boldsymbol{P}$, leading to the transformation $(\Sigma_k, \sigma_k, \Phi_k, \varphi_k) \to (x_k, i\overline{x}_k, y_k, i\overline{y}_k)$, where

$$
x_k = \sqrt{\Sigma_k}e^{i\sigma_k}, \qquad i\,\overline{x}_k = i\sqrt{\Sigma_k}e^{-i\sigma_k},
\tag{3.92}
$$

$$
y_k = \sqrt{\Phi_k}e^{i\varphi_k}, \qquad i\,\overline{y}_k = i\sqrt{\Phi_k}e^{-i\varphi_k}.
\tag{3.93}
$$

From Eqs. (3.55) and (3.56) we have

$$
x_k \approx e_k\sqrt{\frac{\Gamma_k}{2}}e^{i\sigma_k},
\tag{3.94}
$$

and

$$
y_k \approx I_k\sqrt{\frac{\Gamma_k}{2}}e^{i\varphi_k},
\tag{3.95}
$$

and so, x_k and y_k are proportional to the eccentricities and the inclinations, respectively. The resonant secular Hamiltonian (Eq. (3.68)) now becomes

$$
\begin{aligned}
\tilde{\mathcal{H}} &= (\mathcal{K}_1 + \mathcal{S}_1)\,(x_1\overline{x}_1 + x_2\overline{x}_2 + y_1\overline{y}_1 + y_2\overline{y}_2) + \mathcal{K}_2\,(x_1\overline{x}_1 + x_2\overline{x}_2 + y_1\overline{y}_1 + y_2\overline{y}_2)^2 \\
&+ (\mathcal{O}_1 + \mathcal{S}_2)x_1\overline{x}_1 + (\mathcal{O}_2 + \mathcal{S}_3)x_2\overline{x}_2 + \frac{\mathcal{S}_4}{2}\,(x_1\overline{x}_2 + \overline{x}_1 x_2) \\
&+ (\mathcal{O}_3 + \mathcal{S}_5)y_1\overline{y}_1 + (\mathcal{O}_4 + \mathcal{S}_6)y_2\overline{y}_2 + \frac{\mathcal{S}_7}{2}\,(y_1\overline{y}_2 + \overline{y}_1 y_2) \\
&+ \frac{\mathcal{R}_1}{2}\left(x_1^2 + \overline{x}_1^2\right) + \frac{\mathcal{R}_2}{2}\left(x_2^2 + \overline{x}_2^2\right) + \frac{\mathcal{R}_3}{2}\,(x_1 x_2 + \overline{x}_1\overline{x}_2) \\
&+ \frac{\mathcal{R}_4}{2}\left(y_1^2 + \overline{y}_1^2\right) + \frac{\mathcal{R}_5}{2}\left(y_2^2 + \overline{y}_2^2\right) + \frac{\mathcal{R}_6}{2}\,(y_1 y_2 + \overline{y}_1\overline{y}_2).
\end{aligned}
\tag{3.96}
$$

In this formulation, the Hamilton equations are simply

$$\frac{dx_k}{dt} = i\frac{\partial \tilde{\mathcal{H}}}{\partial \bar{x}_k} \quad \text{and} \quad \frac{dy_k}{dt} = i\frac{\partial \tilde{\mathcal{H}}}{\partial \bar{y}_k} \,, \tag{3.97}$$

yielding the equations of motion free of singular terms as

$$\dot{x}_1 = i\left[(\mathcal{K}_1 + \mathcal{S}_1)\,x_1 + 2\mathcal{K}_2\,(x_1\bar{x}_1 + x_2\bar{x}_2 + y_1\bar{y}_1 + y_2\bar{y}_2)\,x_1 + (O_1 + \mathcal{S}_2)\,x_1 + \frac{\mathcal{S}_4}{2}x_2 + \mathcal{R}_1\bar{x}_1 + \frac{\mathcal{R}_3}{2}\bar{x}_2\right], \tag{3.98}$$

$$\dot{x}_2 = i\left[(\mathcal{K}_1 + \mathcal{S}_1)\,x_2 + 2\mathcal{K}_2\,(x_1\bar{x}_1 + x_2\bar{x}_2 + y_1\bar{y}_1 + y_2\bar{y}_2)\,x_2 + (O_2 + \mathcal{S}_3)\,x_2 + \frac{\mathcal{S}_4}{2}x_1 + \mathcal{R}_2\bar{x}_2 + \frac{\mathcal{R}_3}{2}\bar{x}_1\right], \tag{3.99}$$

$$\dot{y}_1 = i\left[(\mathcal{K}_1 + \mathcal{S}_1)\,y_1 + 2\mathcal{K}_2\,(x_1\bar{x}_1 + x_2\bar{x}_2 + y_1\bar{y}_1 + y_2\bar{y}_2)\,y_1 + (O_3 + \mathcal{S}_5)\,y_1 + \frac{\mathcal{S}_7}{2}y_2 + \mathcal{R}_4\bar{y}_1 + \frac{\mathcal{R}_6}{2}\bar{y}_2\right], \tag{3.100}$$

and

$$\dot{y}_2 = i\left[(\mathcal{K}_1 + \mathcal{S}_1)\,y_2 + 2\mathcal{K}_2\,(x_1\bar{x}_1 + x_2\bar{x}_2 + y_1\bar{y}_1 + y_2\bar{y}_2)\,y_2 + (O_4 + \mathcal{S}_6)\,y_2 + \frac{\mathcal{S}_7}{2}y_1 + \mathcal{R}_5\bar{y}_2 + \frac{\mathcal{R}_6}{2}\bar{y}_1\right]. \tag{3.101}$$

3.6 Dynamical evolution

The values of m_k, J_{2_0} and R_k are relatively well determined for the Uranian system (Tables 1.1 and 1.2). Therefore, to compute the coefficients $\mathcal{K}$, O, $\mathcal{S}$, and $\mathcal{R}$ appearing in the Hamiltonian (3.96), we only need to know the values of the parameters Γ_1 and Γ_2 (Eqs. (3.69)-(3.88)), which in turn depend on the parameters Γ and Δ (Eqs. (3.49) and (3.50)).

If we neglect the O coefficients (oblateness terms), it is possible to eliminate the dependence in Γ, because we get $\tilde{\mathcal{H}} \propto \Gamma^{-2}$ (Eqs. (3.69)-(3.88), see also Delisle et al. 2012, Sect. 2.1.4). Although here we cannot use this simplification, the conservative dynamics is still not very sensitive to the Γ parameter (e.g. Tittemore and Wisdom 1988, 1989), and so we fix it at the reference value

$$\Gamma = 2.6684 \times 10^{-12}\, \text{M}_\odot\, \text{au}^2\, \text{yr}^{-1} \,, \tag{3.102}$$

obtained by reversing the orbital tidal evolution of the system (Eq. (4.34)) until the nominal resonance (Eq. (5.1)) is achieved and starting with the present semi-major axes (Table 2.2).

The dynamics of a second order MMR essentially depends on the Δ parameter (Eq. (3.51)), which measures the proximity to the resonance. Following Delisle et al. (2012), we write

$$\delta = \frac{\Delta}{\Delta_r} - 1 \,, \tag{3.103}$$

where Δ_r is the value of Δ at the circular and planar ($e_k = 0$ and $I_k = 0$) nominal resonance, that is (Eqs. (3.36) and (3.51)),

$$\Delta_r = (\Lambda_{1,r} + \Lambda_{2,r})/\Gamma_r \tag{3.104}$$

when $n_1/n_2 = (p + 2)/p$, where n_k is the mean motion of the satellite with mass m_k. At the nominal resonance, using Kepler's third law, we have the following relation for the $\Lambda_{k,r}$:

$$\Lambda_{2,r} = \varrho\left(\frac{p+2}{p}\right)^{1/3}\Lambda_{1,r}\,, \quad \text{with} \quad \varrho = \frac{\beta_2\mu_2^{2/3}}{\beta_1\mu_1^{2/3}} \approx \frac{m_2}{m_1}\,. \tag{3.105}$$

From the expression of Γ_r (Eq. (3.39)), we additionally have

$$\Lambda_{2,r} = \Gamma_r - \frac{p+2}{p}\Lambda_{1,r}\,, \tag{3.106}$$

which can be combined with Eq. (3.105) to give

$$\Lambda_{1,r} = \left(\frac{p+2}{p} + \varrho \left(\frac{p+2}{p} \right)^{1/3} \right)^{-1} \Gamma_r \tag{3.107}$$

$$\Lambda_{2,r} = \left(1 + \varrho^{-1} \left(\frac{p+2}{p} \right)^{2/3} \right)^{-1} \Gamma_r \,, \tag{3.108}$$

and finally (Eq. (3.104))

$$\Delta_r = \left(1 + \varrho \left(\frac{p+2}{p} \right)^{1/3} \right) \left(\frac{p+2}{p} + \varrho \left(\frac{p+2}{p} \right)^{1/3} \right)^{-1} \,. \tag{3.109}$$

3.7 Equilibrium points

The equilibrium points correspond to stationary solutions of the Hamiltonian. They can be found by solving

$$\frac{\partial \tilde{\mathcal{H}}}{\partial x_1} = 0 \quad , \quad \frac{\partial \tilde{\mathcal{H}}}{\partial x_2} = 0 \quad , \quad \frac{\partial \tilde{\mathcal{H}}}{\partial y_1} = 0 \quad \text{and} \quad \frac{\partial \tilde{\mathcal{H}}}{\partial y_2} = 0 \,, \tag{3.110}$$

that is, finding the roots of Eqs. (3.98), (3.99), (3.100), and (3.101). Splitting these equations in their real and imaginary parts, $x_k = x_{k,r} + i x_{k,i}$ and $y_k = y_{k,r} + i y_{k,i}$, we get

$$x_{2,r} = -2 \frac{\mathcal{K}_1 + 2\mathcal{K}_2 \left(\Sigma_1 + \Sigma_2 + \Phi_1 + \Phi_2 \right) + O_1 + S_1 + S_2 + \mathcal{R}_1}{S_4 + \mathcal{R}_3} x_{1,r} \,, \tag{3.111}$$

$$x_{1,r} = -2 \frac{\mathcal{K}_1 + 2\mathcal{K}_2 \left(\Sigma_1 + \Sigma_2 + \Phi_1 + \Phi_2 \right) + O_2 + S_1 + S_3 + \mathcal{R}_2}{S_4 + \mathcal{R}_3} x_{2,r} \,, \tag{3.112}$$

$$x_{2,i} = -2 \frac{\mathcal{K}_1 + 2\mathcal{K}_2 \left(\Sigma_1 + \Sigma_2 + \Phi_1 + \Phi_2 \right) + O_1 + S_1 + S_2 - \mathcal{R}_1}{S_4 - \mathcal{R}_3} x_{1,i} \,, \tag{3.113}$$

$$x_{1,i} = -2 \frac{\mathcal{K}_1 + 2\mathcal{K}_2 \left(\Sigma_1 + \Sigma_2 + \Phi_1 + \Phi_2 \right) + O_2 + S_1 + S_3 - \mathcal{R}_2}{S_4 - \mathcal{R}_3} x_{2,i} \,. \tag{3.114}$$

$$y_{2,r} = -2 \frac{\mathcal{K}_1 + 2\mathcal{K}_2 \left(\Sigma_1 + \Sigma_2 + \Phi_1 + \Phi_2 \right) + O_3 + S_1 + S_5 + \mathcal{R}_4}{S_7 + \mathcal{R}_6} y_{1,r} \,, \tag{3.115}$$

$$y_{1,r} = -2 \frac{\mathcal{K}_1 + 2\mathcal{K}_2 \left(\Sigma_1 + \Sigma_2 + \Phi_1 + \Phi_2 \right) + O_4 + S_1 + S_6 + \mathcal{R}_5}{S_7 + \mathcal{R}_6} y_{2,r} \,, \tag{3.116}$$

$$y_{2,i} = -2 \frac{\mathcal{K}_1 + 2\mathcal{K}_2 \left(\Sigma_1 + \Sigma_2 + \Phi_1 + \Phi_2 \right) + O_3 + S_1 + S_5 - \mathcal{R}_4}{S_7 - \mathcal{R}_6} y_{1,i} \,, \tag{3.117}$$

$$y_{1,i} = -2 \frac{\mathcal{K}_1 + 2\mathcal{K}_2 \left(\Sigma_1 + \Sigma_2 + \Phi_1 + \Phi_2 \right) + O_4 + S_1 + S_6 - \mathcal{R}_5}{S_7 - \mathcal{R}_6} y_{2,i} \,. \tag{3.118}$$

Solving the equation system, yields that equilibria arise for

$$\begin{aligned}
x_{1,r} = x_{2,r} = 0 \quad &\text{and} \quad y_{1,r} = y_{2,r} = 0 \,, \quad \text{or} \\
x_{1,r} = x_{2,r} = 0 \quad &\text{and} \quad y_{1,i} = y_{2,i} = 0 \,, \quad \text{or} \\
x_{1,i} = x_{2,i} = 0 \quad &\text{and} \quad y_{1,r} = y_{2,r} = 0 \,, \quad \text{or} \\
x_{1,i} = x_{2,i} = 0 \quad &\text{and} \quad y_{1,i} = y_{2,i} = 0 \,.
\end{aligned} \tag{3.119}$$

A more deep analysis of the second derivatives of $\tilde{\mathcal{H}}$ shows that the imaginary roots can be stable, while the real roots are always unstable. We then focus on the imaginary roots to determine the exact position of the stable equilibria. Since $x_{1,r} = x_{2,r} = 0$ and $y_{1,r} = y_{2,r} = 0$, we have (Eqs. (3.92) and (3.93))

$$x_{1,i} = \pm \sqrt{\Sigma_1} \quad , \quad x_{2,i} = \pm \sqrt{\Sigma_2} \,, \tag{3.120}$$

and

$$y_{1,i} = \pm \sqrt{\Phi_1} \quad \text{and} \quad y_{2,i} = \pm \sqrt{\Phi_2} \,, \tag{3.121}$$

that we replace in Eqs. (3.113), (3.114), (3.117), and (3.118) to determine the possible values of Σ_1 and Σ_2:

$$\Sigma_1 = \Sigma_2 = 0 \,, \tag{3.122}$$

or

$$\Sigma_1 = \frac{(\mathcal{R}_3 - \mathcal{S}_4)\varepsilon_{x\pm} - 2(\mathcal{K}_1 + O_1 + \mathcal{S}_1 + \mathcal{S}_2 - \mathcal{R}_1)}{4\mathcal{K}_2(1 + \varepsilon_{x\pm}^2)} - \frac{1 + \varepsilon_{y\pm}^2}{1 + \varepsilon_{x\pm}^2}\Phi_1 \,, \tag{3.123}$$

$$\Sigma_2 = \varepsilon_{x\pm}^2 \Sigma_1 \,, \tag{3.124}$$

and Φ_1, Φ_2,

$$\Phi_1 = \Phi_2 = 0 \,, \tag{3.125}$$

or

$$\Phi_1 = \frac{(\mathcal{R}_6 - \mathcal{S}_7)\varepsilon_{y\pm} - 2(\mathcal{K}_1 + O_3 + \mathcal{S}_1 + \mathcal{S}_5 - \mathcal{R}_4)}{4\mathcal{K}_2(1 + \varepsilon_{y\pm}^2)} - \frac{1 + \varepsilon_{x\pm}^2}{1 + \varepsilon_{y\pm}^2}\Sigma_1 \,, \tag{3.126}$$

$$\Phi_2 = \varepsilon_{y\pm}^2 \Phi_1 \,, \tag{3.127}$$

where

$$\varepsilon_{x\pm} = \frac{O_1 - O_2 - \mathcal{R}_1 + \mathcal{R}_2 + \mathcal{S}_2 - \mathcal{S}_3}{\mathcal{R}_3 - \mathcal{S}_4} \pm \frac{\sqrt{(O_1 - O_2 - \mathcal{R}_1 + \mathcal{R}_2 + \mathcal{S}_2 - \mathcal{S}_3)^2 + (\mathcal{R}_3 - \mathcal{S}_4)^2}}{\mathcal{R}_3 - \mathcal{S}_4} \,, \tag{3.128}$$

and

$$\varepsilon_{y\pm} = \frac{O_3 - O_4 - \mathcal{R}_4 + \mathcal{R}_5 + \mathcal{S}_5 - \mathcal{S}_6}{\mathcal{R}_6 - \mathcal{S}_7} \pm \frac{\sqrt{(O_3 - O_4 - \mathcal{R}_4 + \mathcal{R}_5 + \mathcal{S}_5 - \mathcal{S}_6)^2 + (\mathcal{R}_6 - \mathcal{S}_7)^2}}{\mathcal{R}_6 - \mathcal{S}_7} \,. \tag{3.129}$$

We note that the solutions of Eqs. (3.123) and (3.126) are only defined when $\Phi_1 = 0$ and $\Sigma_1 = 0$, respectively. That is, the equilibrium points can only be obtained in the planar ($I_k = 0$) or circular ($e_k = 0$) approximation. The equilibrium points at $\Sigma_1 = \Sigma_2 = 0$ and $\Phi_1 = \Phi_2 = 0$ are always present, although they can be stable or unstable. The remaining equilibria only exist for some δ-values.

We now apply these results to the 5/3 MMR between Ariel and Umbriel. In Fig. 3.1, we show the evolution of the equilibrium points as a function of δ. We rescale $x_{k,i}$ and $y_{k,i}$ by $\sqrt{\Gamma_k/2}$, such that we can translate the different equilibria in terms of eccentricity and inclination values (Eqs. (3.94) and (3.95)).

For positive δ values far from zero, there is only one equilibrium point at $e_k = 0$ and $I_k = 0$, which is stable (in blue colour). For $\delta = 2.07 \times 10^{-6}$, there is a first bifurcation in the equilibria of the inclination: two new stable equilibrium appear at non-zero inclination (in green colour), while the point at $I_k = 0$ becomes unstable. Later, the same occurs for the eccentricity equilibria, at $\delta = 1.20 \times 10^{-6}$. For $\delta = -2.54 \times 10^{-7}$, which is close to the resonance nominal value $\delta = 0$ (Eq. (3.104)), a second bifurcation arises for the inclination: two additional unstable equilibrium points appear at non-zero inclination (in red colour), while the point at $I_k = 0$ becomes stable again. Once more, the same behaviour is observed for the eccentricity, but for $\delta = -3.7 \times 10^{-6}$.

3.8 Energy levels

For a better understanding of the dynamics, we can look at the energy levels of the resonant secular Hamiltonian (3.96) for different values of δ (Eq. (3.109)). Since our problem has four degrees of freedom, and thus eight dimensions, we need to adopt the planar or circular approximations. In order to all stable equilibria become visible, we need to plot these levels on section planes. We choose the plane $(x_{1,i}, x_{2,i})$ with $x_{1,r} = x_{2,r} = 0$ (Eqs. (3.120) (3.121)) for the planar case, and the plane $(y_{1,i}, y_{2,i})$ with $y_{1,r} = y_{2,r} = 0$ (Eqs. (3.120) and (3.121)) for the circular case. Once more, we apply the study of the energy levels to the 5/3 MMR between Ariel and Umbriel.
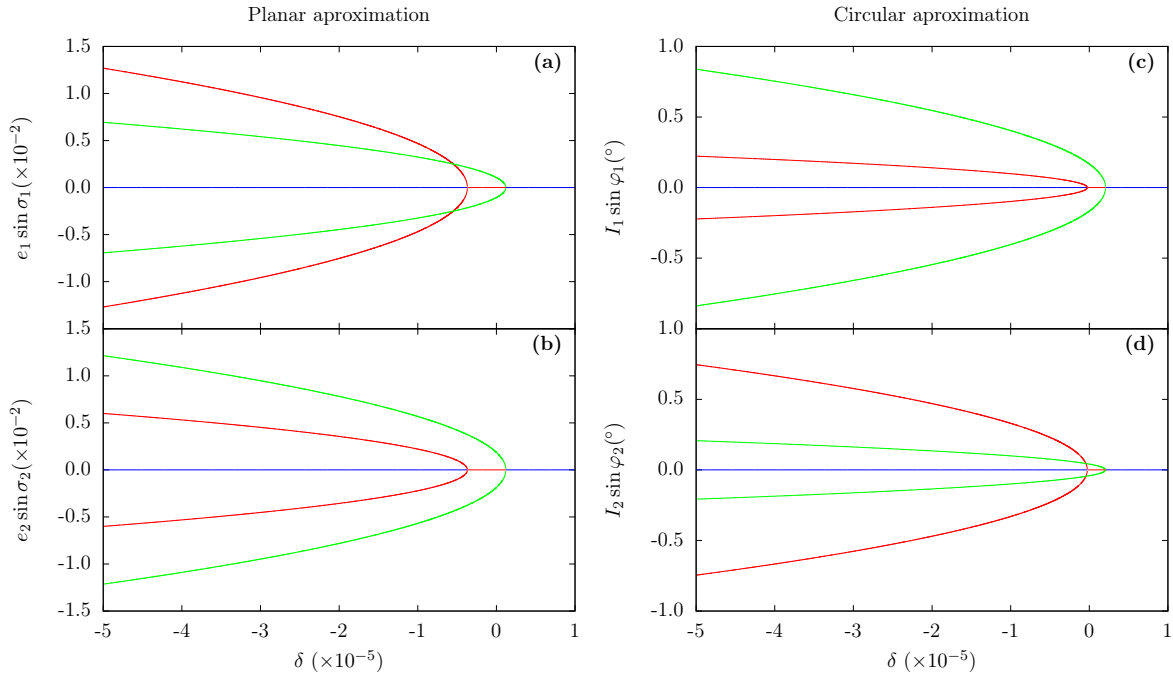
Figure 3.1: Evolution of the equilibrium points as function of δ. The green lines represent stable points inside the resonance (in a libration region), the red lines represent hyperbolic points (unstable), and the blue line represent stable fixed points (in a circulation region).

In Fig. 3.2, we show the energy levels for three values of δ, which are representative of the three different equilibrium possibilities appearing in Fig. 3.1. Again, we rescale $x_{k,i}$ and $y_{k,i}$ by $\sqrt{\Gamma_k/2}$, and so we actually show the energy levels in the plane $(e_1 \sin \sigma_1, e_2 \sin \sigma_2)$ with $\cos \sigma_1 = \cos \sigma_2 = 0$ for the planar approximation, and the plane $(I_1 \sin \varphi_1, I_2 \sin \varphi_2)$ with $\cos \varphi_1 = \cos \varphi_2 = 0$ for the circular approximation. The analysis and results for both approximations are very similar.

For $\delta = 5 \times 10^{-6} > 0$ (Fig. 3.2 a,d) there is a single equilibrium point $(x_{1,i} = 0, x_{2,i} = 0)$ and $(y_{1,i} = 0, y_{2,i} = 0)$ at the centre (in blue). It corresponds to a fixed point of the Hamiltonian (3.96), which is surrounded by a circulation region. Therefore, in this case (and for higher δ-values), all trajectories are outside the 5/3 MMR.

For $\delta = 0$ (Fig. 3.2 b,e), the system is at the nominal resonance (Eq. (3.103)). In this case, the equilibrium points at the centre $(x_{1,i} = 0, x_{2,i} = 0)$ and $(y_{1,i} = 0, y_{2,i} = 0)$ are still present (in red), but they are now unstable. Indeed, there is a separatrix (that is, a boundary between the circulation and the libration regions) in a tilted 8-shape emerging from these points that surrounds two additional equilibrium stable points (in green). Trajectories inside the separatrix that encircle the stable points are in libration and correspond to orbits inside the 5/3 MMR. Trajectories outside the separatrix are in circulation.

Finally, for $\delta = -4 \times 10^{-6} < 0$ (Fig. 3.2 c,f), several equilibria exist. There are two hyperbolic points (in red) from which emerges a separatrix with two "banana" shapes. This separatrix delimits the phase space in libration and circulation regions. There are two stable points (in green), one inside each banana island. Trajectories that move around these points are in libration and correspond to orbits inside the 5/3 MMR. The points $(x_{1,i} = 0, x_{2,i} = 0)$ and $(y_{1,i} = 0, y_{2,i} = 0)$ at the centre (in blue) are again stable and inside a small circulation region. Trajectories outside the separatrix are also in circulation. This kind of phase space persists for smaller δ-values, but the central circulation region becomes larger, while the resonant islands become thinner. Note that, for the planar case, the separatrix is tilted $\sim 45°$ angle relatively to the axis (Fig. 3.2 b,c). Thus, if the system follows one of the resonance islands, the eccentricities of Ariel and Umbriel will increase more or less evenly. As for the circular approximation, the separatrix is more inclined towards the $y_{2,i}$ axis (Fig. 3.2 e,f). Therefore, following the resonance islands, the inclination of Ariel will be more excited than the inclination of Umbriel.
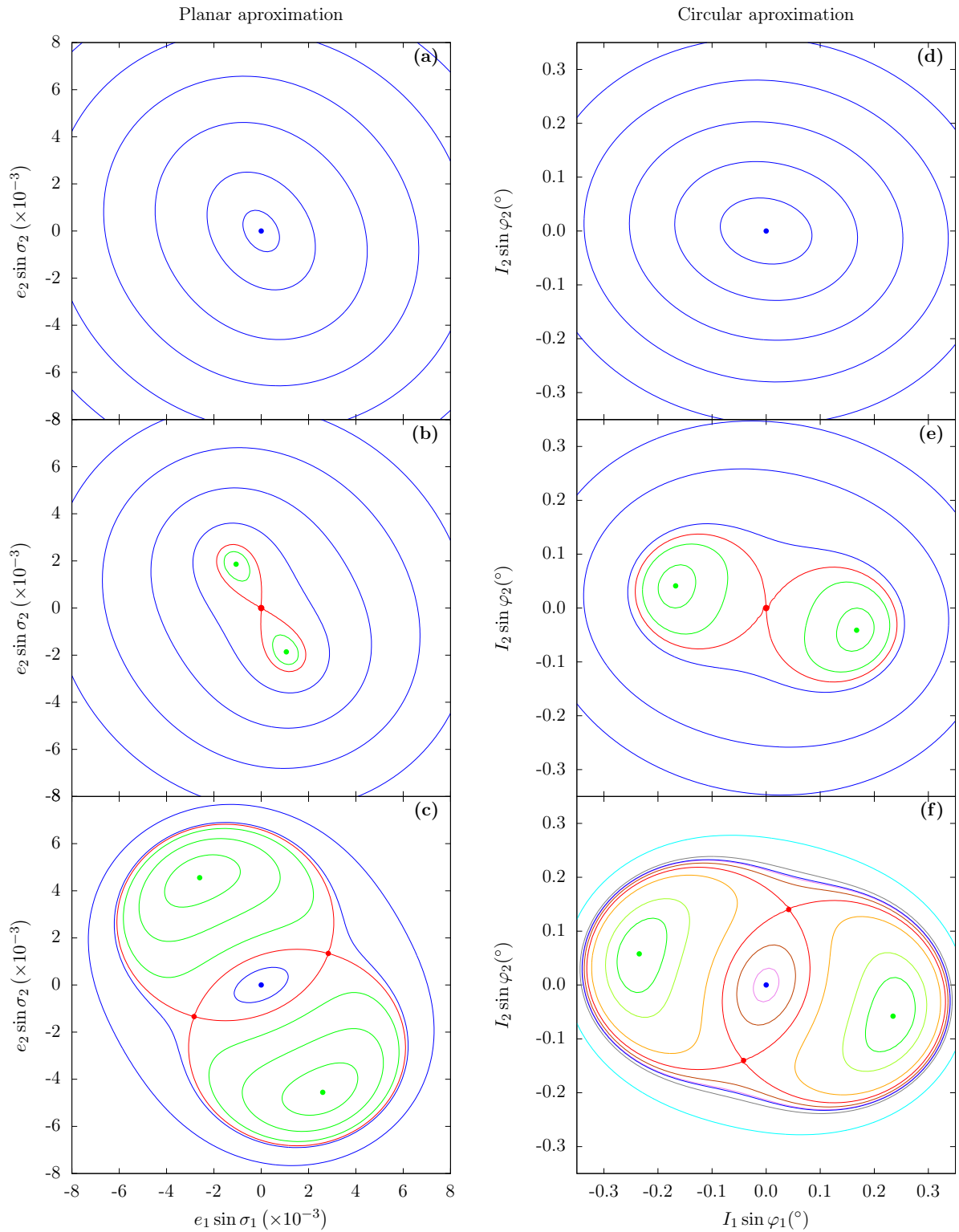
Figure 3.2: Energy level curves in the planes: $(e_1 \sin \sigma_1, e_2 \sin \sigma_2)$ with $\cos \sigma_1 = \cos \sigma_2 = 0$ (left); $(I_1 \sin \varphi_1, I_2 \sin \varphi_2)$ with $\cos \varphi_1 = \cos \varphi_2 = 0$ (rigth), for $\delta = 5 \times 10^{-6}$ (top), $\delta = 0$ (middle), and $\delta = -5 \times 10^{-6}$ (bottom). Stable equilibria are coloured in green (resonance) and blue, while unstable equilibria are coloured in red, as well as the level curves that correspond to the separatrix.

3.9 Surface sections

Using the conservative Hamiltonian (Eq. (3.96)), the energy levels from the previous Sect. (3.8) allowed us to identify the different regions of the phase space, but a priori they do not correspond to trajectories followed by the system. Indeed, since our restricted problem has eight dimensions, they show the trajectories when they cross the section plane with $x_{1,r} = x_{2,r} = 0$ or $y_{1,r} = y_{2,r} = 0$, which only remain constant for the equilibrium points. An alternative projection consists on fixing only $y_{1,r} = 0$ (or $y_{2,r} = 0$) together with a constant energy, that is, to draw Poincaré surface sections. This projection is less restrictive, and therefore allows us to distinguish between periodic (fixed points), quasi-periodic (closed curves), and chaotic trajectories. For that purpose, we used the modified Hénon method (Henon and Heiles 1964; Palaniyandi 2009).

In Fig. 3.2, we observe that, during the 5/3 Ariel-Umbriel MMR passage, the more diverse dynamics occurs for $\delta = -2 \times 10^{-6}$. We thus adopted this value to draw the surface sections for the circular approximation ($x_k = 0$). Since, in this approximation, the Hamiltonian (3.96) is a four-degree function of y_k, the intersection of the constant energy manifold by a plane may have up to four roots (families). Each family corresponds to a different dynamical behaviour, and so we must plot one of them at a time. However, the families are symmetric and actually we only need to show two of them. We chose to represent the families with the positive roots (that we dub 1 and 2).

In Fig. 3.3, we show a set of surface sections for the motion of Ariel in the plane $(y_{1,i}, y_{1,r})$ with $y_{2,r} = 0$. We rescaled y_1 again by $\sqrt{\Gamma_1/2}$, and so we actually show the surface sections in the plane $(I_1 \sin\varphi_1, I_1 \cos\varphi_1)$ with $\cos\varphi_2 = 0$. Each panel corresponds to a different energy value, which coincides with the energy levels that are shown in Fig. 3.2c (we adopted the same colour code). The lowest energies occur in the circulation regions, $\tilde{\mathcal{H}} < \mathcal{H}_0$, the separatrix corresponds to a transition level, $\tilde{\mathcal{H}} = \mathcal{H}_0$, while the largest energies occur in the libration region, $\tilde{\mathcal{H}} > \mathcal{H}_0$. The inner circulation region is delimited by the levels $0 < \tilde{\mathcal{H}} < \mathcal{H}_0$, where $\tilde{\mathcal{H}} = 0$ corresponds to the energy of the equilibrium point with $y_1 = y_2 = 0$ (blue point in Fig. 3.2c). For this energy range, there are four families, while for the remaining energies only two families exist.

For $\tilde{\mathcal{H}} \ll 0$ (Fig. 3.3a), only family 1 exists, and we observe that the system is always quasi-periodic, corresponding to trajectories in the outer circulation region. As the energy increases, two islands appear, corresponding to trajectories that are in the libration region (in resonance). Initially, the motion in these new regions is also quasi-periodic. However, as the energy approaches the threshold $\tilde{\mathcal{H}} = 0$ (Fig. 3.3b,c), some chaotic regions appear in the transition between the circulation and libration regions. For $0 < \tilde{\mathcal{H}} < \mathcal{H}_0$ (family 1), the chaotic regions increase, while the resonant islands shrink (Fig. 3.3d,e), until they completely disappear for $\tilde{\mathcal{H}} = \mathcal{H}_0$ (Fig. 3.3f). For this specific energy range, we also needed to plot family 2. Close to $\tilde{\mathcal{H}} = 0$, we observe quasi-periodic motion in the inner circulation region, but, as we approach $\tilde{\mathcal{H}} = \mathcal{H}_0$, this area is also completely replaced by a chaotic region (Fig. 3.3j,k,l). Finally, for $\tilde{\mathcal{H}} > \mathcal{H}_0$, we observe that the chaotic region progressively vanishes, and it is replaced by quasi-periodic motion in the libration region (Fig. 3.3g,h,i). In this energy range, we only have family 1 and trajectories in the outer circulation region also do not exist. Moreover, there is also a forbidden region at the centre of each panel that grows with the energy value while the libration areas shrink.

In Fig. 3.4, we show the analogous set of surface sections for the motion of Umbriel in the plane $(y_{2,i}, y_{2,r})$ with $y_{1,r} = 0$. Again, we rescaled y_2 by $\sqrt{\Gamma_2/2}$, therefore showing the surface sections in the plane $(I_2 \sin\varphi_2, I_2 \cos\varphi_2)$ with $\cos\varphi_1 = 0$, and preserve the same colour scheme as in Figs. 3.2 and 3.3. We note that, for the case of Umbriel, the circulation and libration regions are inverted relatively to the case of Ariel. This can also be seen in Fig. 3.1, where the stable equilibrium points are always larger than the unstable equilibrium points. Whereas for Umbriel, the stable equilibrium points quickly become smaller than the unstable equilibrium points. As expected, the stable and chaotic regions appear for the same $\tilde{\mathcal{H}}/\mathcal{H}_0$ values. For $\tilde{\mathcal{H}} \ll 0$ (Fig. 3.4a) the system is always quasi-periodic, and, as the energy approaches the threshold $\tilde{\mathcal{H}} = 0$ (Fig. 3.4b,c), some chaotic regions appear in the transition between the circulation and libration regions. For $0 < \tilde{\mathcal{H}} < \mathcal{H}_0$ (family 1), the chaotic regions increase, while the resonant islands shrink (Fig. 3.4d,e), until they completely disappear for $\tilde{\mathcal{H}} = \mathcal{H}_0$ (Fig. 3.4f). Again, for this specific energy range, we also have the family 2. Close to $\tilde{\mathcal{H}} = 0$, we observe quasi-periodic

Figure 3.3: Poincaré surfaces of section for Ariel in the plane $(I_1 \sin\varphi_1, I_1 \cos\varphi_1)$ with $\cos\varphi_2 = 0$ and $\delta = -2\times10^{-6}$. Each panel was obtained with a different energy value, corresponding to the energy levels shown in Fig. 3.2c (we adopted the same colour code), and $\mathcal{H}_0 = 1.06 \times 10^{-19}$ M$_\odot$ au^2 yr^{-2}.

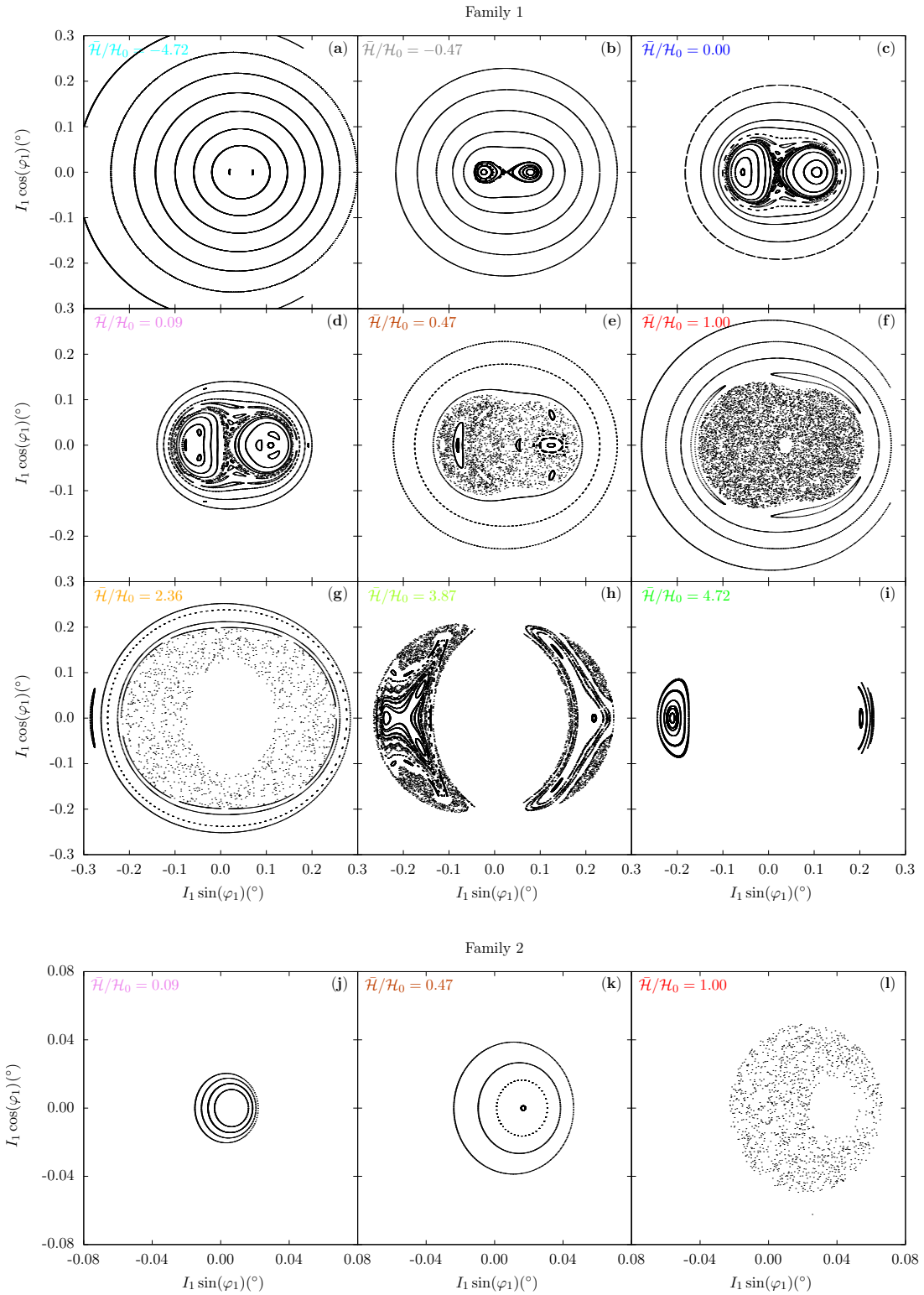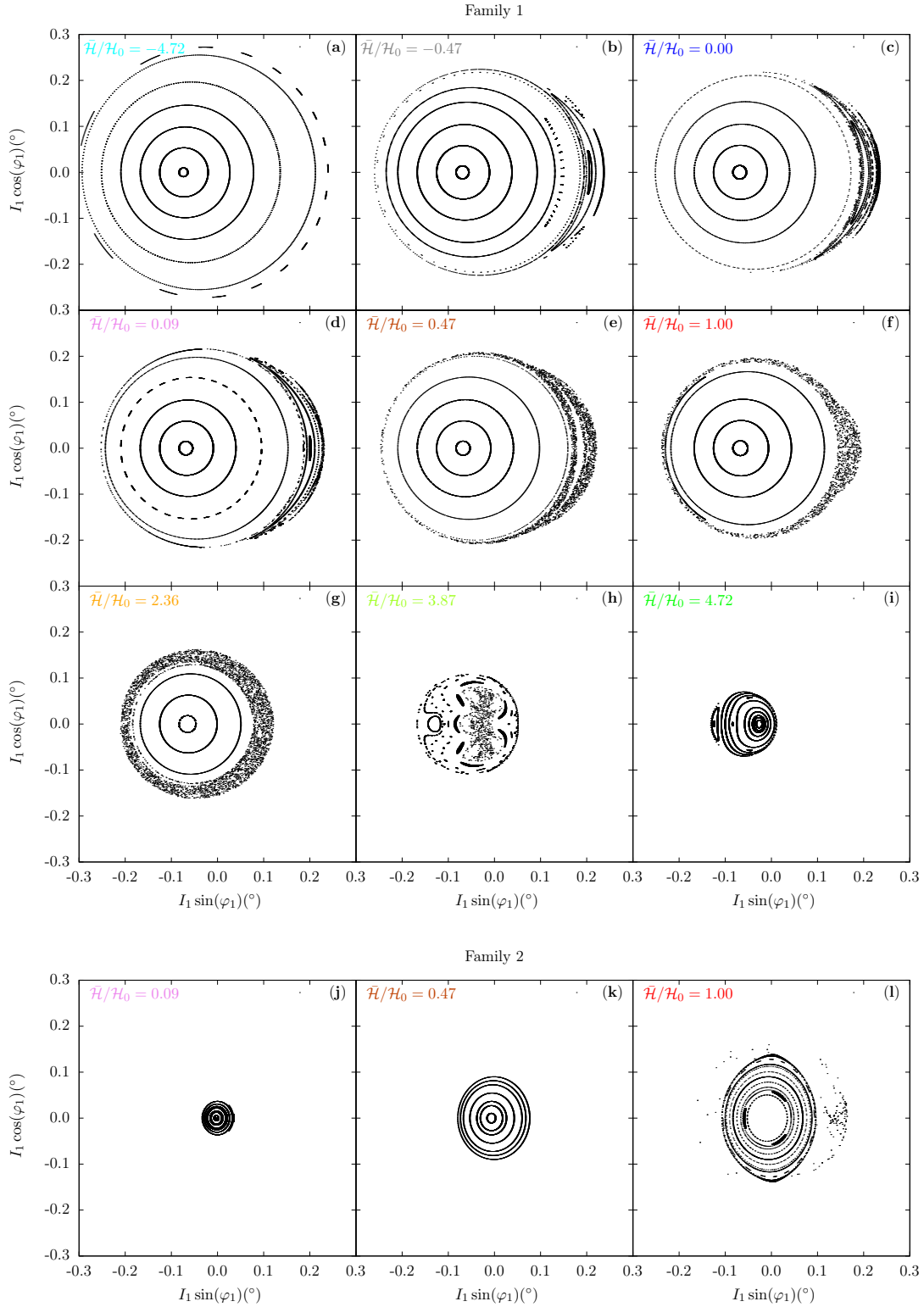Figure 3.4: Poincaré surfaces of section for Umbriel in the plane $(I_2 \sin \varphi_2, I_2 \cos \varphi_2)$ with $\cos \varphi_1 = 0$ and $\delta = -2 \times 10^{-6}$. Each panel was obtained with a different energy value, corresponding to the energy levels shown in Fig. 3.2c (we adopted the same colour code), and $\mathcal{H}_0 = 1.06 \times 10^{-19} \, \mathrm{M}_\odot \, \mathrm{au}^2 \, \mathrm{yr}^{-2}$.

motion in the inner circulation region. However, contrary to the case of Ariel, as we approach $\tilde{\mathcal{H}} = \mathcal{H}_0$, the chaotic region does not replace entirely the quasi-periodic region, and the inner circulation region is preserved (Fig. 3.4j,k,l). Finally, for $\tilde{\mathcal{H}} > \mathcal{H}_0$, we only have family 1 and trajectories in the outer circulation region also do not exist. We observe that the chaotic region progressively vanishes, and it is replaced by quasi-periodic motion in the libration region (Fig. 3.4g,h,i).

From the analysis of the surface sections, we conclude that the dynamics of the 5/3 MMR between Ariel and Umbriel is very rich and depends on the energy of the system. In fact, the energy depends on the value of the inclinations (Eq. (3.96)), given by the variables y_1 and y_2 (Eq. (3.95)). Therefore, the value of the inclinations of Ariel and Umbriel when the system encounters the resonance can trigger completely different behaviours. For $\tilde{\mathcal{H}} < 0$, the motion is quasi-periodic, either in circulation or libration. Near the separatrix, $\tilde{\mathcal{H}} \sim \mathcal{H}_0$, the motion is mainly chaotic. Finally, for $\tilde{\mathcal{H}} \gg \mathcal{H}_0$, the motion is again quasi-periodic, but only possible in libration with a small amplitude around the high inclination stable equilibrium points (Fig. 3.1).

3.10 Stability maps

In the previous section we analysed the behaviour of Ariel and Umbriel in the circular approximation at different stages of the crossing of the 5/3 MMR resorting to Poincaré surface sections. Here, we analyse the global dynamics of this resonance using stability maps. To this end, we adopt the frequency analysis method (Laskar 1990, 1993) to map the diffusion of the orbits. These results were partially presented in Gomes and Correia (2023b).

For coherence, we fix $\delta = -2 \times 10^{-6}$ (Eq. (3.103)) as for the surface sections (Sect. 3.9), for which the most diverse dynamics can be found, and adopt the physical properties of the system from Tables 1.1 and 1.2. For each energy value, we build a grid of 200×200 equally distributed initial conditions in the plane $(y_{1,i}, y_{1,r})$ for Ariel and in the plane $(y_{2,i}, y_{2,r})$ for Umbriel. We fix $y_{2,r} = 0$ (for Ariel) or $y_{1,r} = 0$ (for Umbriel) for all initial conditions and compute $y_{2,i}$ (for Ariel) or $y_{1,i}$ (for Umbriel) for each family from the total energy (Eq. (3.96)). We then numerically integrate the equations of motion (3.100) and (3.101) for a time T. Finally, we perform a frequency analysis of y_1 or y_2, using the software TRIP (Gastineau and Laskar 2011) over the time intervals $[0, T/2]$ and $[T/2, T]$, and determine the main frequency in each interval, f_{in} and f_{out}, respectively. The stability of the orbit is measured by the index

$$D \equiv \left| 1 - \frac{f_{\text{out}}}{f_{\text{in}}} \right| , \tag{3.130}$$

which estimates the stability of the orbital long-distance diffusion (Dumas and Laskar 1993). The larger D, the more orbital diffusion exists. For stable motion, we have $D \sim 0$, while $D \ll 1$ if the motion is weakly perturbed, and $D \sim 1$ when the motion is irregular. It is difficult to determine the precise value of D for which the motion is stable or unstable, but a threshold of stability D_s can be estimated such that most of the trajectories with $D < D_s$ are stable (Couetdic et al. 2010).

The diffusion index depends on the considered time interval. Here, we integrate the equations of motion for $T = 10^4$ yr, because this interval is able to capture the main characteristics of the dynamics regarding the resonant frequency, which lies within the range ~ 60 yr. With this time interval, we estimate that $D_s \sim 10^{-4}$. The diffusion index D is represented by a logarithmic colour scale calibrated such that blue and green correspond to stable trajectories ($D \ll D_s$), while orange and red correspond to chaotic motion ($D \gg D_s$).

In Fig. 3.5, we show the stability maps for Ariel. We rescale y_1 by $\sqrt{\Gamma_1/2}$, and so we actually plot the maps in the plane $(I_1 \sin \varphi_1, I_1 \cos \varphi_1)$ with $\cos \varphi_2 = 0$ (Eqs. (3.92) and (3.93)), as already done for the Poincaré surface section (Fig. 3.3). Each panel corresponds to a different energy value $\tilde{\mathcal{H}}/\mathcal{H}_0$, where $\mathcal{H}_0 = 1.06 \times 10^{-19}$ $M_\odot$ au^2 yr^{-2} is the energy of the transition between the circulation and libration regions, i.e., the energy of the separatrix. The lowest energies occur in the circulation regions, $\tilde{\mathcal{H}} < \mathcal{H}_0$, while the largest energies occur in the libration region, $\tilde{\mathcal{H}} > \mathcal{H}_0$. The inner circulation region is delimited

by $0 < \tilde{\mathcal{H}} < \mathcal{H}_0$, where $\tilde{\mathcal{H}} = 0$ corresponds to the energy of the equilibrium point with $y_1 = y_2 = 0$. For this energy range, there are four families, while for the remaining energies only two families exist.

For $\tilde{\mathcal{H}} \ll 0$ (Fig. 3.5 a), only family 1 exists, and we observe that the system is always stable, corresponding to trajectories in the outer circulation region. As the energy increases, two islands appear, corresponding to trajectories that are in the libration region (in resonance). Initially, the motion in these new regions is also stable, but the separatrix and some localized concentric regions outside the separatrix are chaotic. As the energy approaches the threshold $\tilde{\mathcal{H}} = 0$ (Figs. 3.5 b,c), the chaotic regions expand for the vicinities of the separatrix. For $0 < \tilde{\mathcal{H}} < \mathcal{H}_0$ (family 1), the chaotic regions increase even further, while the resonant islands shrink (Figs. 3.5 d,e), until they completely disappear for $\tilde{\mathcal{H}} = \mathcal{H}_0$ (Fig. 3.5 f). We note that up to these energies, outside the chaotic regions, the circulation region remains stable. For this specific energy range, we also need to plot family 2. Close to $\tilde{\mathcal{H}} = 0$, we observe stable motion in the inner circulation region (Figs. 3.5 j,k). However, as we approach $\tilde{\mathcal{H}} = \mathcal{H}_0$, this area is replaced by a chaotic region (Fig. 3.5 l). Finally, for $\tilde{\mathcal{H}} > \mathcal{H}_0$, we observe that the stable region progressively vanishes, and chaotic motion dominates the phase-space, where only small libration regions remain stable (Figs. 3.5 g,h,i). In this energy range, we only have family 1 and trajectories in the outer circulation region also do not exist. Moreover, there is also a forbidden region at the centre of each panel that grows with the energy value, while the libration areas shrink.

In Fig. 3.6, we show the analogous stability maps for Umbriel, that is, in the plane $(I_2 \sin \varphi_2, I_2 \cos \varphi_2)$ with $\cos \varphi_1 = 0$ (Eqs. (3.92) and (3.93)). As mentioned in Sect. 3.9, the libration and circulation regions are inverted, relatively to the case of Ariel. Therefore, the circulation region is close to center of the phase-space ($y_k = 0$), and the libration region is located at the outer regions, surrounded by the chaotic regions. Again, the stable and chaotic regions appear for the same energy values $\tilde{\mathcal{H}}/\mathcal{H}_0$, and family 2 only appear within the range $0 < \tilde{\mathcal{H}} < \mathcal{H}_0$. In addition, the forbidden regions are at the center of each panel, but at the outer regions.

The results in Figs. 3.5 and 3.6 are in good agreement with those shown in Figs. 3.3 and 3.4, respectively. They show that chaos has a strong presence in the passage through the 5/3 MMR between Ariel and Umbriel. The analysis of this resonance with stability maps allows to quantify the chaos for each region. For $\tilde{\mathcal{H}} < 0$, the phase-space is dominated by stable orbits. As we approach the separatrix energy, $\tilde{\mathcal{H}} \sim \mathcal{H}_0$, the chaotic motion engorges the low inclination regions, while the outer circulation regions remain stable. Finally, for $\tilde{\mathcal{H}} \gg \mathcal{H}_0$, only small libration regions remain stable, surrounded by large chaotic areas. This contrasts with the results from Sect. 3.9, since surface sections appeared to have exclusive quasi-periodic motion for energies near the equilibrium resonance points.

Figure 3.5: Stability maps for Ariel in the plane $(I_1 \sin \varphi_1, I_1 \cos \varphi_1)$ with $\cos \varphi_2 = 0$ and $\delta = -2 \times 10^{-6}$. The colour scale corresponds to the relative frequency diffusion index in logarithmic scale (Eq. (3.130)). Each panel was obtained with a different energy value and $\mathcal{H}_0 = 1.06 \times 10^{-19}$ $M_\odot$ au^2 yr^{-2}.
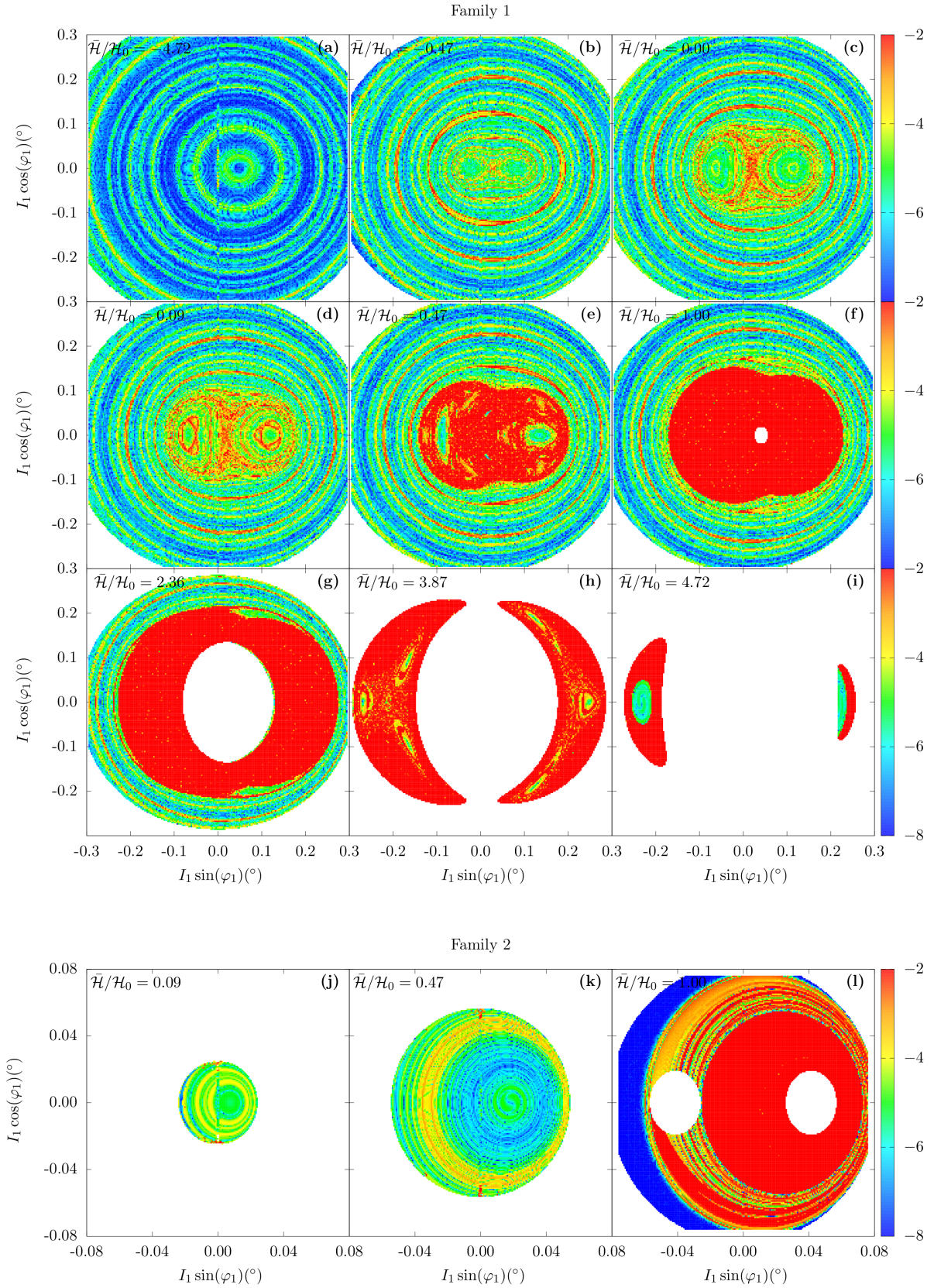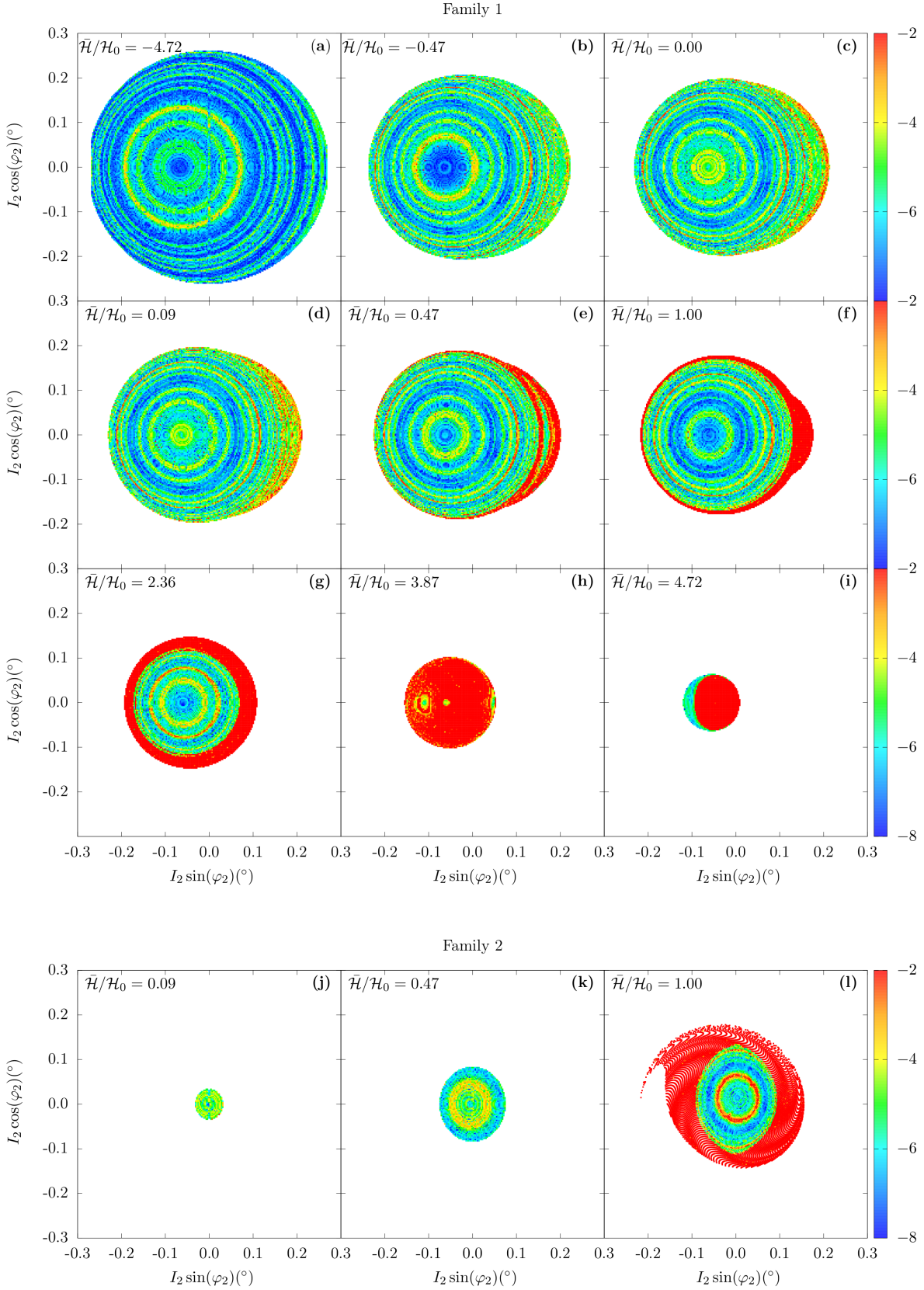
Figure 3.6: Stability maps for Umbriel in the plane $(I_2 \sin\varphi_2, I_2 \cos\varphi_2)$ with $\cos\varphi_1 = 0$ and $\delta = -2\times 10^{-6}$. The colour scale corresponds to the relative frequency diffusion index in logarithmic scale (Eq. (3.130)). Each panel was obtained with a different energy value and $\mathcal{H}_0 = 1.06 \times 10^{-19}$ M$_\odot$ au^2 yr^{-2}.

Chapter 4

Secular tidal evolution

The resonant dynamics presented in Sect. 3 is conservative and thus the average semi-major axes remain constant. However, the orbits of the Uranian system are expected to evolve because of dissipative tidal interactions (Sect. 2.3.2).

Tittemore and Wisdom (1988, 1989, 1990) introduced the tidal effects in the system by artificially evolving the first Keplerian term ($\mathcal{K}_1$). With this approximation, the authors only consider the evolution of the semi-major axes, thus neglecting the tidal effects on the eccentricities, inclinations, and rotations. In this chapter, we develop a more comprehensive model that takes into account tidal effects on all coordinates of the system. The tidal contributions to the orbital and spin evolution can be obtained by adding the contribution of the tidal potential (Eq. (2.33)) to the average conservative Hamiltonian (Eq. (3.63)) (Darwin 1880; Kaula 1964; Mignard 1979).

4.1   Tidal potential energy

Tides arise from differential and inelastic deformations of an extended body (e.g. planet) owing to the gravitational effect of a perturber (e.g. satellite). The resulting distortion gives rise to a tidal bulge, which modifies the gravitational potential of the extended body. The dissipation of the mechanical energy of tides inside the extended body introduces a time delay, τ, between the initial perturbation and the maximal deformation. As the perturber interacts with the additional potential field, the amount of tidal potential energy is given by (Eq. (2.33))

$$U_{i,j} = -k_{2_j} \frac{\mathcal{G}m_i^2}{2R_j} \left(\frac{R_j}{r_{i,j}}\right)^3 \left(\frac{R_j}{r'_{i,j}}\right)^3 \left(3\left(\hat{\mathbf{r}}_{i,j} \cdot \hat{\mathbf{r}}'_{i,j}\right)^2 - 1\right), \tag{4.1}$$

where k_{2_j} is the second Love number for the potential of the deformed body, $\mathbf{r}_{i,j} = \mathbf{r}_{i,j}(t) = \mathbf{r}_i - \mathbf{r}_j$ is the position of the perturber at a time t, and $\mathbf{r}'_{i,j} = \mathbf{r}_{i,j}(t - \tau_j)$ is its position when it exerts the perturbation. Although tidal effects do not preserve the mechanical energy, it is possible to extend the Hamiltonian formalism from Sect. 3, by considering the primed quantities, $\mathbf{r}'_{i,j}$, as parameters (Mignard 1979). We note that, for $i, j \neq 0$,

$$\frac{U_{0,j}}{U_{i,j}} \sim \left(\frac{m_0}{m_j}\right)^2 \gg 1 \quad \text{and} \quad \frac{U_{i,0}}{U_{i,j}} \sim \left(\frac{R_0}{R_j}\right)^5 \gg 1. \tag{4.2}$$

That is, the tidal interactions between the planet and the satellites are much stronger than the mutual tidal interactions between the satellites, thus we neglect $U_{1,2}$ and $U_{2,1}$. The tidal Hamiltonian then reads (Eqs. (3.23) and (4.1))

$$\mathcal{H}_t = \mathcal{H} + U_{0,1} + U_{1,0} + U_{0,2} + U_{2,0}. \tag{4.3}$$

For the considered terms, we note that $r_{0,k} = r_{k,0} = r_k$. Therefore, in the following expressions of $U_{i,j}$ (Eq. (4.1)) we assume the subscript $k = i + j$.

As in Sect. 3.1, we initially expand $U_{i,j}$ in elliptical elements. First, one must express the vectors $\mathbf{r}_k$ and $\mathbf{r}'_k$ in a body centred reference of frame ($\mathbf{I}, \mathbf{J}, \mathbf{K}$), instead of the generic inertial frame ($\boldsymbol{i}, \boldsymbol{j}, \boldsymbol{k}$) (see
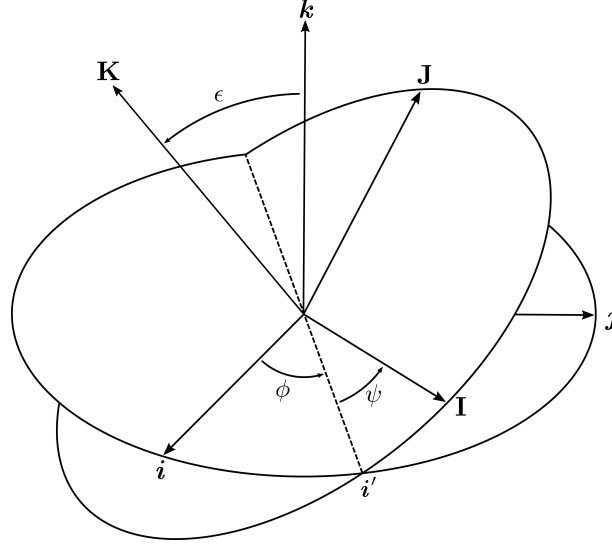
Figure 4.1: Geometrical representation of the Euler angles. We depart from the initial frame (i, j, k) and, through three rotations, end up in the frame $(\mathbf{I}, \mathbf{J}, \mathbf{K})$. The first rotation is through an angle ϕ around the k axis. The second rotation is through an angle ϵ around the i' axis, where $i' = k \times \mathbf{K} / \sin \epsilon$. The last rotation is through an angle ψ around the $\mathbf{K}$ axis.

Fig. 4.1). Using the Euler angles (ψ, ϵ, ϕ), this is achieved by performing a simple set of rotations around the main axes, that is

$$\mathbf{r}_{(i,j,k)} = \mathcal{R}_3(\psi)\,\mathcal{R}_1(\epsilon)\,\mathcal{R}_3(\phi)\,\mathbf{r}_{(\mathrm{I,J,K})} = \mathcal{R}(\psi, \epsilon, \phi)\,\mathbf{r}_{(\mathrm{I,J,K})} \tag{4.4}$$

where $\mathcal{R}_1$ and $\mathcal{R}_3$ are the rotation matrices around the x-axis and z-axis, respectively (Eq. (A.24)). Using the previous expression, we can express the positions of the satellite on the planet frame $(\mathbf{I}, \mathbf{J}, \mathbf{K})$:

$$\hat{\mathbf{r}}_k = \mathcal{R}^{\mathrm{T}}(\psi_j, \epsilon_j, \phi_j)\,\mathcal{R}(\Omega_k, I_k, \nu_k + \omega_k)\,i\,, \tag{4.5}$$

$$\hat{\mathbf{r}}'_k = \mathcal{R}^{\mathrm{T}}(\psi'_j, \epsilon'_j, \phi'_j)\,\mathcal{R}(\Omega'_k, I'_k, \nu'_k + \omega'_k)\,i\,. \tag{4.6}$$

Using Eqs. (4.5) and (4.6), and considering that the obliquity is null ($\epsilon_j = \epsilon'_j = 0$), we can take $\theta_j = \psi_j + \phi_j$ and $\theta'_j = \psi'_j + \phi'_j$ (see Fig. 4.1), and the inner product $\hat{\mathbf{r}}_k \cdot \hat{\mathbf{r}}'_k$ can be written as

$$\hat{\mathbf{r}}_k \cdot \hat{\mathbf{r}}'_k = \hat{\mathbf{r}}_k^{\mathrm{T}}\,\hat{\mathbf{r}}'_k = i^{\mathrm{T}}\,\mathcal{R}^T(\Omega_k, I_k, \nu_k + \omega_k)\,\mathcal{R}_3(\theta_j)\,\mathcal{R}_3^T(\theta'_j)\,\mathcal{R}(\Omega'_k, I'_k, \nu'_k + \omega'_k)\,i\,. \tag{4.7}$$

Expanding Eq. (4.7) to first order in the mass ratios, second order in the eccentricities and in the inclinations, we have

$$\begin{aligned}
\hat{\mathbf{r}}_k \cdot \hat{\mathbf{r}}'_k = {} & \left(1 - e_k^2 - e_k'^2 - \frac{1}{4}I_k^2 - \frac{1}{4}I_k'^2\right)\cos\left(\lambda_k - \lambda'_k - \theta_j + \theta'_j\right) \\
& + \frac{9}{8}e_k^2\cos\left(3\lambda_k - \lambda'_k - 2\varpi_k - \theta_j + \theta'_j\right) + \frac{9}{8}e_k'^2\cos\left(\lambda_k - 3\lambda'_k + 2\varpi'_k - \theta_j + \theta'_j\right) \\
& - \frac{1}{8}e_k^2\cos\left(\lambda_k + \lambda'_k - 2\varpi_k + \theta_j - \theta'_j\right) - \frac{1}{8}e_k'^2\cos\left(\lambda_k + \lambda'_k - 2\varpi'_k - \theta_j + \theta'_j\right) \\
& + e_k e'_k\cos\left(\varpi_k - \varpi'_k - \theta_j + \theta'_j\right) + e_k e'_k\cos\left(2\lambda_k - 2\lambda'_k - \varpi_k + \varpi'_k - \theta_j + \theta'_j\right) \\
& - e_k e'_k\cos\left(2\lambda_k - \varpi_k - \varpi'_k - \theta_j + \theta'_j\right) - e_k e'_k\cos\left(2\lambda'_k - \varpi_k - \varpi'_k + \theta_j - \theta'_j\right) \\
& - e_k\cos\left(\lambda'_k - \varpi_k + \theta_j - \theta'_j\right) + e_k\cos\left(2\lambda_k - \lambda'_k - \varpi_k - \theta_j + \theta'_j\right) \\
& - e'_k\cos\left(\lambda_k - \varpi'_k - \theta_j + \theta'_j\right) + e'_k\cos\left(\lambda_k - 2\lambda'_k + \varpi'_k - \theta_j + \theta'_j\right) \\
& + \frac{1}{4}I_k^2\cos\left(\lambda_k + \lambda'_k - 2\Omega_k + \theta_j - \theta'_j\right) + \frac{1}{4}I_k'^2\cos\left(\lambda_k + \lambda'_k - 2\Omega'_k - \theta_j + \theta'_j\right) \\
& + \frac{1}{2}I_k I'_k\cos\left(\lambda_k - \lambda'_k - \Omega_k + \Omega'_k\right) - \frac{1}{2}I_k I'_k\cos\left(\lambda_k + \lambda'_k - \Omega_k - \Omega'_k\right)\,.
\end{aligned} \tag{4.8}$$

Then, inserting Eq. (4.8) in the Eq. (4.1), we finally get:

$$
\begin{aligned}
U_{i,j} = -k_{2_j} \frac{\mathcal{G} m_i^2 R_j^5}{4 a_k^3 a_k'^3} &\Bigg[1 + 3\cos(2\lambda_k - 2\lambda_k' - 2\theta_j + 2\theta_j') \\
&+ \frac{3}{2} e_k \Big(2\cos(\lambda_k - \varpi_k) - \cos\big(\lambda_k - 2\lambda_k' + \varpi_k - 2\theta_j + 2\theta_j'\big) + 7\cos\big(3\lambda_k - 2\lambda_k' - \varpi_k - 2\theta_j + 2\theta_j'\big) \Big) \\
&+ \frac{3}{2} e_k' \Big(2\cos\big(\lambda_k' - \varpi_k'\big) - \cos\big(2\lambda_k - \lambda_k' - \varpi_k' - 2\theta_j + 2\theta_j'\big) + 7\cos\big(2\lambda_k - 3\lambda_k' + \varpi_k' - 2\theta_j + 2\theta_j'\big) \Big) \\
&+ \frac{3}{2} e_k^2 \Big(1 + 3\cos\big(2\lambda_k - 2\varpi_k\big) - 5\cos\big(2\lambda_k - 2\lambda_k' - 2\theta_j + 2\theta_j'\big) + 17\cos\big(4\lambda_k - 2\lambda_k' - 2\varpi_k - 2\theta_j + 2\theta_j'\big) \Big) \\
&+ \frac{3}{2} e_k'^2 \Big(1 + 3\cos\big(2\lambda_k' - 2\varpi_k'\big) - 5\cos\big(2\lambda_k - 2\lambda_k' - 2\theta_j + 2\theta_j'\big) + 17\cos\big(2\lambda_k - 4\lambda_k' + 2\varpi_k' - 2\theta_j + 2\theta_j'\big) \Big) \\
&+ \frac{3}{4} e_k e_k' \Big(6\cos\big(\lambda_k - \lambda_k' - \varpi_k + \varpi_k'\big) + 6\cos\big(\lambda_k + \lambda_k' - \varpi_k - \varpi_k'\big) + \cos\big(\lambda_l - \lambda_k' + \varpi_k - \varpi_k' - 2\theta_j + 2\theta_j'\big) \\
&\qquad - 9\cos\big(\lambda_l - 3\lambda_k' + \varpi_k + \varpi_k' - 2\theta_j + 2\theta_j'\big) - 9\cos\big(3\lambda_l - \lambda_k' - \varpi_k - \varpi_k' - 2\theta_j + 2\theta_j'\big) \\
&\qquad + 47\cos\big(3\lambda_l - 3\lambda_k' - \varpi_k + \varpi_k' - 2\theta_j + 2\theta_j'\big) \Big) \\
&- \frac{3}{2} I_k^2 \Big(1 - \cos\big(2\lambda_k - 2\Omega_k\big) + \cos\big(2\lambda_k - 2\lambda_k' - 2\theta_j + 2\theta_j'\big) - \cos\big(2\lambda_k' - 2\Omega_k + 2\theta_j - 2\theta_j'\big) \Big) \\
&- \frac{3}{2} I_k'^2 \Big(1 - \cos\big(2\lambda_k' - 2\Omega_k'\big) + \cos\big(2\lambda_k - 2\lambda_k' - 2\theta_j + 2\theta_j'\big) - \cos\big(2\lambda_k - 2\Omega_k' - 2\theta_j + 2\theta_j'\big) \Big) \\
&+ 3 I_k I_k' \Big(\cos\big(2\lambda_k - 2\lambda_k' - \Omega_k + \Omega_k' - \theta_j + \theta_j'\big) + \cos\big(\Omega_k - \Omega_k' - \theta_j + \theta_j'\big) \\
&\qquad - \cos\big(2\lambda_k - \Omega_k - \Omega_k' - \theta_j + \theta_j'\big) \;\; - \cos\big(2\lambda_k' - \Omega_k - \Omega_k' + \theta_j - \theta_j'\big) \Big) \Bigg].
\end{aligned}
$$

$$(4.9)$$

As in the conservative case, we now perform a canonical change of variables that uses the resonant angles (Eqs. (3.38)-(3.46)), then followed by the change to the complex Cartesian coordinates (Eqs. (3.92) and (3.93)), leading to

$$
\begin{aligned}
U_{i,j} = -k_{2_j} \frac{\mathcal{G} m_i^2 R_j^5 \beta_k^{12} \mu_k^6}{16 \Gamma_k^7 \Gamma_k'^7} &\Bigg[4\Gamma_k \Gamma_k' + 12\Gamma_k' x_k \bar{x}_k + 12\Gamma_k x_k' \bar{x}_k' - 12\Gamma_k' y_k \bar{y}_k - 12\Gamma_k y_k' \bar{y}_k' \\
&- 24 p_k \Big(\Gamma_k'(x_1 \bar{x}_1 + x_2 \bar{x}_2 + y_1 \bar{y}_1 + y_2 \bar{y}_2) \Big) - 24 p_k \Big(\Gamma_k(x_1' \bar{x}_1' + x_2' \bar{x}_2' + y_1' \bar{y}_1' + y_2' \bar{y}_2') \Big) \\
&+ 12 \Big(\Gamma_k \Gamma_k' - \Gamma_k'(5 x_k \bar{x}_k - y_k \bar{y}_k) - \Gamma_k(5 x_k' \bar{x}_k' - y_k' \bar{y}_k') \\
&\qquad - 6 p_k \Big(\Gamma_k'(x_1 \bar{x}_1 + x_2 \bar{x}_2 + y_1 \bar{y}_1 + y_2 \bar{y}_2) + \Gamma_k(x_1' \bar{x}_1' + x_2' \bar{x}_2' + y_1' \bar{y}_1' + y_2' \bar{y}_2') \Big) \Big) \\
&\qquad \times \cos(2(\vartheta_j - \vartheta_j' - q_k(\gamma - \gamma'))) \\
&+ 6\sqrt{2}\,(x_k + \bar{x}_k)\sqrt{\Gamma_k}\Gamma_k' \cos(q_k \gamma) + 6\sqrt{2}\,(x_k' + \bar{x}_k')\Gamma_k \sqrt{\Gamma_k'} \cos(q_k \gamma') \\
&- 3\sqrt{2}\,(x_k + \bar{x}_k)\sqrt{\Gamma_k}\Gamma_k' \cos\big(q_k(\gamma - 2\gamma') - 2\vartheta_j + 2\vartheta_j'\big) \\
&- 3\sqrt{2}\,(x_k' + \bar{x}_k')\Gamma_k \sqrt{\Gamma_k'} \cos\big(q_k(2\gamma - \gamma') - 2\vartheta_j + 2\vartheta_j'\big) \\
&+ 21\sqrt{2}\,(x_k + \bar{x}_k)\sqrt{\Gamma_k}\Gamma_k' \cos\big(q_k(3\gamma - 2\gamma') - 2\vartheta_j + 2\vartheta_j'\big) \\
&+ 21\sqrt{2}\,(x_k' + \bar{x}_k')\Gamma_k \sqrt{\Gamma_k'} \cos\big(q_k(2\gamma - 3\gamma') - 2\vartheta_j + 2\vartheta_j'\big)
\end{aligned}
$$

...(continues on next page)

...(continuation)

$$+ 6\,\Gamma'_k\left(3x_k^2 + 3\overline{x}_k^2 + y_k^2 + \overline{y}_k^2\right)\cos(2q_k\gamma) + 6\,\Gamma_k\left(3x_k'^2 + 3\overline{x}_k'^2 + y_k'^2 + \overline{y}_k'^2\right)\cos(2q_k\gamma')$$

$$+ 18\left(x_k\overline{x}_k' + x_k'\overline{x}_k\right)\sqrt{\Gamma_k\Gamma'_k}\cos\left(q_k(\gamma - \gamma')\right) + 18\left(x_kx_k' + \overline{x}_k\overline{x}_k'\right)\sqrt{\Gamma_k\Gamma'_k}\cos\left(q_k(\gamma + \gamma')\right)$$

$$+ 102\,\Gamma'_k\left(x_k^2 + \overline{x}_k^2\right)\cos\left(2(2q_k\gamma - q_k\gamma' - \vartheta_j + \vartheta_j')\right)$$

$$+ 102\,\Gamma_k\left(x_k'^2 + \overline{x}_k'^2\right)\cos\left(2(q_k\gamma - 2q_k\gamma' - \vartheta_j + \vartheta_j')\right)$$

$$+ 3\,\sqrt{\Gamma_k\Gamma'_k}\left(x_k\overline{x}_k' + x_k'\overline{x}_k\right)\cos\left(q_k(\gamma - \gamma') - 2\vartheta_j + 2\vartheta_j'\right)$$

$$+ 147\,\sqrt{\Gamma_k\Gamma'_k}\left(x_k\overline{x}_k' + x_k'\overline{x}_k\right)\cos\left(3q_k(\gamma - \gamma') - 2\vartheta_j + 2\vartheta_j'\right)$$

$$- 21\,\sqrt{\Gamma_k\Gamma'_k}\left(x_kx_k' + \overline{x}_k\overline{x}_k'\right)\cos\left(q_k(\gamma - 3\gamma') - 2\vartheta_j + 2\vartheta_j'\right)$$

$$- 21\,\sqrt{\Gamma_k\Gamma'_k}\left(x_kx_k' + \overline{x}_k\overline{x}_k'\right)\cos\left(q_k(3\gamma - \gamma') - 2\vartheta_j + 2\vartheta_j'\right)$$

$$+ 6\,\Gamma_k\left(y_k'^2 + \overline{y}_k'^2\right)\cos\left(2(q_k\gamma - \vartheta_j + \vartheta_j')\right) + 6\,\Gamma'_k\left(y_k^2 + \overline{y}_k^2\right)\cos\left(2(q_k\gamma' + \vartheta_j - \vartheta_j')\right)$$

$$+ 12\,\sqrt{\Gamma_k\Gamma'_k}\left(y_k\overline{y}_k' + y_k'\overline{y}_k\right)\cos\left(\vartheta_j - \vartheta_j'\right) + 12\,\sqrt{\Gamma_k\Gamma'_k}\left(y_k\overline{y}_k' + y_k'\overline{y}_k\right)\cos\left(2q_k(\gamma - \gamma') - \vartheta_j + \vartheta_j'\right)$$

$$- 12\,\sqrt{\Gamma_k\Gamma'_k}\left(y_ky_k' + \overline{y}_k\overline{y}_k'\right)\cos(2q_k\gamma - \vartheta_j + \vartheta_j') - 12\,\sqrt{\Gamma_k\Gamma'_k}\left(y_ky_k' + \overline{y}_k\overline{y}_k'\right)\cos(2q_k\gamma' + \vartheta_j - \vartheta_j')$$

$$+ 6\sqrt{2}\,\mathrm{i}\,(x_k - \overline{x}_k)\sqrt{\Gamma_k}\Gamma'_k\sin\left(q_k\gamma\right) + 6\sqrt{2}\,\mathrm{i}\,(x_k' - \overline{x}_k')\Gamma_k\sqrt{\Gamma'_k}\sin\left(q_k\gamma'\right)$$

$$+ 3\sqrt{2}\,\mathrm{i}\,(x_k - \overline{x}_k)\sqrt{\Gamma_k}\Gamma'_k\sin\left(q_k(\gamma - 2\gamma') - 2\vartheta_j + 2\vartheta_j'\right)$$

$$- 3\sqrt{2}\,\mathrm{i}\,(x_k' - \overline{x}_k')\Gamma_k\sqrt{\Gamma'_k}\sin\left(q_k(2\gamma - \gamma') - 2\vartheta_j + 2\vartheta_j'\right)$$

$$+ 21\sqrt{2}\,\mathrm{i}\,(x_k - \overline{x}_k)\sqrt{\Gamma_k}\Gamma'_k\sin\left(q_k(3\gamma - 2\gamma') - 2\vartheta_j + 2\vartheta_j'\right)$$

$$- 21\sqrt{2}\,\mathrm{i}\,(x_k' - \overline{x}_k')\Gamma_k\sqrt{\Gamma'_k}\sin\left(q_k(2\gamma - 3\gamma') - 2\vartheta_j + 2\vartheta_j'\right)$$

$$+ 102\,\mathrm{i}\,\Gamma'_k\left(x_k^2 - \overline{x}_k^2\right)\sin\left(2(2q_k\gamma - q_k\gamma' - \vartheta_j + \vartheta_j')\right)$$

$$- 102\,\mathrm{i}\,\Gamma_k\left(x_k'^2 - \overline{x}_k'^2\right)\sin\left(2(q_k\gamma - 2q_k\gamma' - \vartheta_j + \vartheta_j')\right)$$

$$+ 18\,\mathrm{i}\left(x_k\overline{x}_k' + x_k'\overline{x}_k\right)\sqrt{\Gamma_k\Gamma'_k}\sin\left(q_k(\gamma - \gamma')\right) + 18\,\mathrm{i}\left(x_kx_k' + \overline{x}_k\overline{x}_k'\right)\sqrt{\Gamma_k\Gamma'_k}\sin\left(q_k(\gamma + \gamma')\right)$$

$$- 3\,\mathrm{i}\,\sqrt{\Gamma_k\Gamma'_k}\left(x_k\overline{x}_k' - x_k'\overline{x}_k\right)\sin\left(q_k(\gamma - \gamma') - 2\vartheta_j + 2\vartheta_j'\right)$$

$$+ 147\,\mathrm{i}\,\sqrt{\Gamma_k\Gamma'_k}\left(x_k\overline{x}_k' - x_k'\overline{x}_k\right)\sin\left(3q_k(\gamma - \gamma') - 2\vartheta_j + 2\vartheta_j'\right)$$

$$+ 21\,\mathrm{i}\,\sqrt{\Gamma_k\Gamma'_k}\left(x_kx_k' - \overline{x}_k\overline{x}_k'\right)\sin\left(q_k(\gamma - 3\gamma') - 2\vartheta_j + 2\vartheta_j'\right)$$

$$- 21\,\mathrm{i}\,\sqrt{\Gamma_k\Gamma'_k}\left(x_kx_k' - \overline{x}_k\overline{x}_k'\right)\sin\left(q_k(3\gamma - \gamma') - 2\vartheta_j + 2\vartheta_j'\right)$$

$$+ 6\,\mathrm{i}\,\Gamma'_k\left(3x_k^2 - 3\overline{x}_k^2 + y_k^2 - \overline{y}_k^2\right)\sin\left(2q_k\gamma\right) + 6\,\mathrm{i}\,\Gamma_k\left(3x_k'^2 - 3\overline{x}_k'^2 + y_k'^2 - \overline{y}_k'^2\right)\sin\left(2q_k\gamma'\right)$$

$$+ 6\,\mathrm{i}\,\Gamma'_k\left(y_k^2 - \overline{y}_k^2\right)\sin\left(2(q_k\gamma' + \vartheta_j - \vartheta_j')\right) + 6\,\mathrm{i}\,\Gamma_k\left(y_k'^2 - \overline{y}_k'^2\right)\sin\left(2(q_k\gamma - \vartheta_j + \vartheta_j')\right)$$

$$+ 12\,\mathrm{i}\,\sqrt{\Gamma_k\Gamma'_k}\left(y_k\overline{y}_k' - y_k'\overline{y}_k\right)\sin\left(\vartheta_j - \vartheta_j'\right) + 12\,\mathrm{i}\,\sqrt{\Gamma_k\Gamma'_k}\left(y_k\overline{y}_k' - y_k'\overline{y}_k\right)\sin\left(2q_k(\gamma - \gamma') - \vartheta_j + \vartheta_j'\right)$$

$$- 12\,\mathrm{i}\,\sqrt{\Gamma_k\Gamma'_k}\left(y_ky_k' - \overline{y}_k\overline{y}_k'\right)\sin(2q_k\gamma - \vartheta_j + \vartheta_j')$$

$$- 12\,\mathrm{i}\,\sqrt{\Gamma_k\Gamma'_k}\left(y_ky_k' - \overline{y}_k\overline{y}_k'\right)\sin(2q_k\gamma' + \vartheta_j - \vartheta_j')\bigg],$$

(4.10)

where $p_1 = -p/2$, $p_2 = 1 + p/2$, $q_1 = 1 + 2/p$, and $q_2 = 1$.

Note that σ does not appear in the expression of tidal potential. Therefore, in presence of tides, the parameter Σ (Eq. (3.36)) is still conserved (total angular momentum). The fast angle γ is still present in the expression of $U_{i,j}$, but at this stage we cannot perform an average as in Sect. 3.4, because γ' is considered as a parameter that can later cancel with γ (see Eq. (4.19)).

4.2 Tidal equations of motion

The equations of motion are obtained from Eq. (4.10) using the Hamilton equations. The additional contribution from tides derive only from the $U_{i,j}$ (Eq. (4.1)), and are thus given by

$$\dot{x}_k = i\frac{\partial U_{0,k}}{\partial \overline{x}_k} + i\frac{\partial U_{k,0}}{\partial \overline{x}_k} \,, \tag{4.11}$$

$$\dot{y}_k = i\frac{\partial U_{0,k}}{\partial \overline{y}_k} + i\frac{\partial U_{k,0}}{\partial \overline{y}_k} \,, \tag{4.12}$$

$$\dot{\Gamma} = -\frac{\partial U_{0,1}}{\partial \gamma} - \frac{\partial U_{0,2}}{\partial \gamma} - \frac{\partial U_{1,0}}{\partial \gamma} - \frac{\partial U_{2,0}}{\partial \gamma} \,, \tag{4.13}$$

$$\dot{\Theta}_0 = -\frac{\partial U_{1,0}}{\partial \vartheta_0} - \frac{\partial U_{2,0}}{\partial \vartheta_0} \,, \tag{4.14}$$

$$\dot{\Theta}_k = -\frac{\partial U_{0,k}}{\partial \vartheta_k} \,. \tag{4.15}$$

In principle, we should also write the equations for $\dot{\gamma}$ and $\dot{\vartheta}_k$, but these angles disappear from the equations of motion with some of the following simplifications, and so we do not need them to get a closed set for the secular evolution of the system.

To handle the expression of the primed quantities, we need to use a tidal model. For continuity, we adopt again the weak friction model (Sect. 2.3), which assumes a constant and small time delay, τ_j, between the tidal potential and the perturbing potentials. This model provides very simple expressions for the tidal interactions, because it can be made linear (e.g. Mignard 1979),

$$\lambda'_k \approx \lambda_k - n_k \tau_j \,, \quad \text{and} \quad \theta'_j \approx \theta_j - \omega_j \tau_j \,. \tag{4.16}$$

Substituting Eq. (4.16) into Eqs. (3.38)-(3.46) and (3.92)-(3.93), and expanding up to first order in τ_j, it follows for the remaining primed quantities,

$$x'_k \approx x_k - ix_k (p_2\overline{n}_2 + p_1\overline{n}_1) \tau_j \,, \tag{4.17}$$

$$y'_k \approx y_k - iy_k (p_2\overline{n}_2 + p_1\overline{n}_1) \tau_j \,, \tag{4.18}$$

$$\gamma' \approx \gamma - p_1 (\overline{n}_2 - \overline{n}_1) \tau_j \,, \tag{4.19}$$

$$\vartheta'_j \approx \vartheta_j + \left(p_2\overline{n}_2 + p_1\overline{n}_1 - \omega_j\right)\tau_j \,, \tag{4.20}$$

with

$$\overline{n}_k = \beta_k^3 \mu_k^2 / \Gamma_k^3 \,. \tag{4.21}$$

We then substitute expressions (4.18) to (4.20) into the equations of motion (4.11)-(4.15) and average over the fast angle γ (as in Eq. (3.62)) to finally get the secular equations for the tidal evolution

$$\dot{x}_1 = -\frac{3}{2}\frac{\mathcal{D}_{1,0}}{\Gamma_1^{13}}\left(i(2p + 5) + (19\overline{n}_1 - 12\omega_0)\tau_0\right)x_1 + 3i(p + 2)\frac{\mathcal{D}_{2,0}}{\Gamma_2^{13}} x_1$$
$$-\frac{3}{2}\frac{\mathcal{D}_{0,1}}{\Gamma_1^{13}}\left(i(2p + 5) + (19\overline{n}_1 - 12\omega_1)\tau_1\right)x_1 + 3i(p + 2)\frac{\mathcal{D}_{0,2}}{\Gamma_2^{13}} x_1 \,, \tag{4.22}$$

$$\dot{x}_2 = -3\mathrm{i}p\frac{\mathcal{D}_{1,0}}{\Gamma_1^{13}}\,x_2 - \frac{3}{2}\frac{\mathcal{D}_{2,0}}{\Gamma_2^{13}}\big(\mathrm{i}(1-2p)+(19\bar{n}_2-12\omega_0)\tau_0\big)x_2$$
$$-3\mathrm{i}p\frac{\mathcal{D}_{0,1}}{\Gamma_1^{13}}\,x_2 - \frac{3}{2}\frac{\mathcal{D}_{0,2}}{\Gamma_2^{13}}\big(\mathrm{i}(1-2p)+(19\bar{n}_2-12\omega_2)\tau_2\big)x_2 \,, \tag{4.23}$$

$$\dot{y}_1 = -\frac{3}{2}\frac{\mathcal{D}_{1,0}}{\Gamma_1^{13}}\,(2\mathrm{i}p+\bar{n}_1\tau_0)\,y_1 + 3\mathrm{i}(p+2)\frac{\mathcal{D}_{2,0}}{\Gamma_2^{13}}\,y_1 - \frac{3}{2}\frac{\mathcal{D}_{0,1}}{\Gamma_1^{13}}\,(2\mathrm{i}p+\bar{n}_1\tau_1)\,y_1 + 3\mathrm{i}(p+2)\frac{\mathcal{D}_{0,2}}{\Gamma_2^{13}}\,y_1 \,, \tag{4.24}$$

$$\dot{y}_2 = -3\mathrm{i}p\frac{\mathcal{D}_{1,0}}{\Gamma_1^{13}}\,y_2 + \frac{3}{2}\frac{\mathcal{D}_{2,0}}{\Gamma_2^{13}}\,(2\mathrm{i}(p+2)-\bar{n}_2\tau_0)y_2 - 3\mathrm{i}p\frac{\mathcal{D}_{0,1}}{\Gamma_1^{13}}\,y_2 + \frac{3}{2}\frac{\mathcal{D}_{0,2}}{\Gamma_2^{13}}\,(2\mathrm{i}(p+2)-\bar{n}_2\tau_2)y_2 \,, \tag{4.25}$$

$$\dot{\Gamma} = 3\frac{\mathcal{D}_{1,0}}{\Gamma_1^{13}}\left(1+\frac{2}{p}\right)\Big[\big(27x_1\bar{x}_1 - y_1\bar{y}_1 + 6p(x_1\bar{x}_1 + x_2\bar{x}_2 + y_1\bar{y}_1 + y_2\bar{y}_2) + \Gamma_1\big)\omega_0$$
$$-\big(46x_1\bar{x}_1 + 6p(x_1\bar{x}_1 + x_2\bar{x}_2 + y_1\bar{y}_1 + y_2\bar{y}_2) + \Gamma_1\big)\bar{n}_1\Big]\tau_0$$
$$+3\frac{\mathcal{D}_{0,1}}{\Gamma_1^{13}}\left(1+\frac{2}{p}\right)\Big[\big(27x_1\bar{x}_1 - y_1\bar{y}_1 + 6p(x_1\bar{x}_1 + x_2\bar{x}_2 + y_1\bar{y}_1 + y_2\bar{y}_2) + \Gamma_1\big)\omega_1$$
$$-\big(46x_1\bar{x}_1 + 6p(x_1\bar{x}_1 + x_2\bar{x}_2 + y_1\bar{y}_1 + y_2\bar{y}_2) + \Gamma_1\big)\bar{n}_1\Big]\tau_1$$
$$+3\frac{\mathcal{D}_{2,0}}{\Gamma_2^{13}}\left(1+\frac{2}{p}\right)\Big[\big(27x_2\bar{x}_2 - y_2\bar{y}_2 - 6(p+2)(x_1\bar{x}_1 + x_2\bar{x}_2 + y_1\bar{y}_1 + y_2\bar{y}_2) + \Gamma_2\big)\omega_0$$
$$-\big(46x_2\bar{x}_2 - 6(p+2)(x_1\bar{x}_1 + x_2\bar{x}_2 + y_1\bar{y}_1 + y_2\bar{y}_2) + \Gamma_1\big)\bar{n}_2\Big]\tau_0$$
$$+3\frac{\mathcal{D}_{0,2}}{\Gamma_2^{13}}\left(1+\frac{2}{p}\right)\Big[\big(27x_2\bar{x}_2 - y_2\bar{y}_2 - 6(p+2)(x_1\bar{x}_1 + x_2\bar{x}_2 + y_1\bar{y}_1 + y_2\bar{y}_2) + \Gamma_2\big)\omega_2$$
$$-\big(46x_2\bar{x}_2 - 6(p+2)(x_1\bar{x}_1 + x_2\bar{x}_2 + y_1\bar{y}_1 + y_2\bar{y}_2) + \Gamma_1\big)\bar{n}_2\Big]\tau_2 \,, \tag{4.26}$$

$$\dot{\Theta}_0 = -3\frac{\mathcal{D}_{1,0}}{\Gamma_1^{13}}\Big[\big(15x_1\bar{x}_1 - y_1\bar{y}_1 + 6p(x_1\bar{x}_1 + x_2\bar{x}_2 + y_1\bar{y}_1 + y_2\bar{y}_2) + \Gamma_1\big)\omega_0$$
$$-\big(27x_1\bar{x}_1 - y_1\bar{y}_1 + 6p(x_1\bar{x}_1 + x_2\bar{x}_2 + y_1\bar{y}_1 + y_2\bar{y}_2) + \Gamma_1\big)\bar{n}_1\Big]\tau_0$$
$$-3\frac{\mathcal{D}_{2,0}}{\Gamma_2^{13}}\Big[\big(15x_2\bar{x}_2 - y_2\bar{y}_2 - 6(p+2)(x_1\bar{x}_1 + x_2\bar{x}_2 + y_1\bar{y}_1 + y_2\bar{y}_2) + \Gamma_2\big)\omega_0$$
$$-\big(27x_2\bar{x}_2 - y_2\bar{y}_2 - 6(p+2)(x_1\bar{x}_1 + x_2\bar{x}_2 + y_1\bar{y}_1 + y_2\bar{y}_2) + \Gamma_2\big)\bar{n}_2\Big]\tau_0 \,, \tag{4.27}$$

$$\dot{\Theta}_1 = -3\frac{\mathcal{D}_{0,1}}{\Gamma_1^{13}}\Big[\big(15x_1\bar{x}_1 - y_1\bar{y}_1 + 6p(x_1\bar{x}_1 + x_2\bar{x}_2 + y_1\bar{y}_1 + y_2\bar{y}_2) + \Gamma_1\big)\omega_1$$
$$-\big(27x_1\bar{x}_1 - y_1\bar{y}_1 + 6p(x_1\bar{x}_1 + x_2\bar{x}_2 + y_1\bar{y}_1 + y_2\bar{y}_2) + \Gamma_1\big)\bar{n}_1\Big]\tau_1 \,, \tag{4.28}$$

$$\dot{\Theta}_2 = -3\frac{\mathcal{D}_{0,2}}{\Gamma_2^{13}}\Big[\big(15x_2\bar{x}_2 - y_2\bar{y}_2 - 6(p+2)(x_1\bar{x}_1 + x_2\bar{x}_2 + y_1\bar{y}_1 + y_2\bar{y}_2) + \Gamma_2\big)\omega_2$$
$$-\big(27x_2\bar{x}_2 - y_2\bar{y}_2 - 6(p+2)(x_1\bar{x}_1 + x_2\bar{x}_2 + y_1\bar{y}_1 + y_2\bar{y}_2) + \Gamma_2\big)\bar{n}_2\Big]\tau_2 \tag{4.29}$$

where

$$\mathcal{D}_{i,j} = k_{2_j}\mathcal{G}m_i^2\beta_k^{12}\mu_k^6 R_j^5 \,, \quad \text{with} \quad k = i + j \,, \tag{4.30}$$

and τ_0, τ_1, and τ_2 are the tidal lags of the bodies with masses m_0, m_1, and m_2, respectively (see Sect. 2.4.3).

We note that in the expressions of $\dot{x}_k$ (Eqs. (4.22) and (4.23)) and $\dot{y}_k$ (Eq. (4.24) and (4.25)), we have a conservative contribution (imaginary terms) and a dissipative contribution (real terms in τ_j). The conservative contributions result from a permanent tidal deformation and only slightly modify the fundamental frequencies of the system, while the dissipative contributions modify the secular evolution.

4.3 Orbital evolution

Although very useful mathematically and numerically, the tidal equations of motion presented in complex rectangular coordinates are not intuitive. Nevertheless, we can also obtain their contributions to the elliptical elements. Combining Eqs. (3.29), (3.47)-(3.51) with Eqs. (3.92) and (3.93), we can express the semi-major axes as a function of the rectangular complex coordinates, that is, $a_k(x_1, \overline{x}_1, x_2, \overline{x}_2, y_1, \overline{y}_1, y_2, \overline{y}_2, \Sigma, \Gamma, \Theta_0, \Theta_1, \Theta_2)$. Thus, the time derivatives can be obtained as

$$\dot{a}_k = \frac{\partial a_k}{\partial x_1} \dot{x}_1 + \frac{\partial a_k}{\partial \overline{x}_1} \dot{\overline{x}}_1 + \frac{\partial a_k}{\partial x_2} \dot{x}_2 + \frac{\partial a_k}{\partial \overline{x}_2} \dot{\overline{x}}_2 + \frac{\partial a_k}{\partial y_1} \dot{y}_1 + \frac{\partial a_k}{\partial \overline{y}_1} \dot{\overline{y}}_1 + \frac{\partial a_k}{\partial y_2} \dot{y}_2 + \frac{\partial a_k}{\partial \overline{y}_2} \dot{\overline{y}}_2$$
$$+ \frac{\partial a_k}{\partial \Gamma} \dot{\Gamma} + \frac{\partial a_k}{\partial \Theta_0} \dot{\Theta}_0 + \frac{\partial a_k}{\partial \Theta_1} \dot{\Theta}_1 + \frac{\partial a_k}{\partial \Theta_2} \dot{\Theta}_2 \, . \tag{4.31}$$

As for the eccentricities and the inclinations, since they only depend on $e_k(x_k, \overline{x}_k, \Sigma, \Gamma, \Theta_0, \Theta_1, \Theta_2)$ and $I_k(y_k, \overline{y}_k, \Sigma, \Gamma, \Theta_0, \Theta_1, \Theta_2)$ (Eqs. (3.49)-(3.51), (3.55), (3.56), (3.92) and (3.93)), the time evolutions are obtained as

$$\dot{e}_k = \frac{\partial e_k}{\partial x_k} \dot{x}_k + \frac{\partial e_k}{\partial \overline{x}_k} \dot{\overline{x}}_k + \frac{\partial e_k}{\partial \Gamma} \dot{\Gamma} + \frac{\partial e_k}{\partial \Theta_0} \dot{\Theta}_0 + \frac{\partial e_k}{\partial \Theta_1} \dot{\Theta}_1 + \frac{\partial e_k}{\partial \Theta_2} \dot{\Theta}_2 \, , \tag{4.32}$$

$$\dot{I}_k = \frac{\partial I_k}{\partial y_k} \dot{y}_k + \frac{\partial I_k}{\partial \overline{y}_k} \dot{\overline{y}}_k + \frac{\partial I_k}{\partial \Gamma} \dot{\Gamma} + \frac{\partial I_k}{\partial \Theta_0} \dot{\Theta}_0 + \frac{\partial I_k}{\partial \Theta_1} \dot{\Theta}_1 + \frac{\partial I_k}{\partial \Theta_2} \dot{\Theta}_2 \, . \tag{4.33}$$

Computing Eqs. (4.31)-(4.33) we obtain for the tidal evolution of a_k, e_k, and I_k,

$$\frac{\dot{a}_k}{a_k} \approx \frac{3 \mathcal{G} m_k^2 R_0^5}{\beta_k a_k^8} k_{2_0} \tau_0 \left(\left(2 + 27 e_k^2 - I_k^2 \right) \frac{\omega_0}{n_k} - \left(2 + 46 e_k^2 \right) \right) - \frac{3 \mathcal{G} m_0^2 R_k^5}{\beta_k a_k^8} k_{2_k} \tau_k \left(19 e_k^2 + I_k^2 \right) \, , \tag{4.34}$$

$$\frac{\dot{e}_k}{e_k} \approx \frac{3 \mathcal{G} m_k^2 R_0^5}{2 \beta_k a_k^8} k_{2_0} \tau_0 \left(11 \frac{\omega_0}{n_k} - 18 \right) + \frac{3 \mathcal{G} m_0^2 R_k^5}{2 \beta_k a_k^8} k_{2_k} \tau_k \left(11 \frac{\omega_k}{n_k} - 18 \right) \, , \tag{4.35}$$

$$\frac{\dot{I}_k}{I_k} \approx - \frac{3 \mathcal{G} m_k^2 R_0^5}{2 \beta_k a_k^8} k_{2_0} \tau_0 \frac{\omega_0}{n_k} - \frac{3 \mathcal{G} m_0^2 R_k^5}{2 \beta_k a_k^8} k_{2_k} \tau_k \left(\frac{\omega_k}{n_k} - 1 \right) \, . \tag{4.36}$$

4.4 Evolution timescale

The orbital evolution timescale depends on the tidal lag, τ, which is related to the specific dissipation factor, Q (Eq. (2.69)).

Using Eq. (4.36) we can estimate the inclination damping timescale, $\tau_{\rm inc}$. Assuming the satellites as synchronous, that is, $\omega_k = n_k$, we have

$$\tau_{\rm inc} \approx \frac{4 \beta_k a_k^8 n_k}{3 \mathcal{G} m_k^2 R_0^5} \left(\frac{Q_0}{k_{2_0}} \right) \, . \tag{4.37}$$

This expression only depends on tides raised in Uranus (Eq. (2.70)), and yields an inclination damping timescale of about 290 Gyr for Miranda, 180 Gyr for Ariel, 1 500 Gyr for Umbriel, 14 000 Gyr for Titania and 105 000 Gyr for Oberon. These timescales are much longer than the age of the Solar System. Thus, we conclude that the presently observed inclination values are likely unchanged since the system crossed the 5/3 MMR, and confirm the numerical results obtained in Sect. 2.4.6.

Using Eq. (4.35), we can also estimate the damping timescale for the eccentricities of the satellites. Assuming again $\omega_k = n_k$, we have that, contrarily to the inclination, for the eccentricity the tides raised

by the planet on the satellites have a much higher contribution than the tides raised by the satellites on the planet, that is,

$$\left| \frac{m_k^2 R_0^5 k_{2_0} \tau_0 \left(11 \frac{\omega_0}{n_k} - 18 \right)}{7 m_0^2 R_k^5 k_{2_k} \tau_k} \right| \ll 1 \, . \tag{4.38}$$

Thus, the expression for the eccentricity tidal damping, τ_{ecc}, can then be estimated as

$$\tau_{\text{ecc}} \approx \frac{2 \beta_k a_k^8 n_k}{21 \, \mathcal{G} m_0^2 R_k^5} \left(\frac{Q_k}{k_{2_k}} \right) \, . \tag{4.39}$$

Assuming $Q = 100$ for the satellites, Eq. (4.39) leads to an τ_{ecc} of approximately 250 Myr for Miranda, 50 Myr for Ariel, 690 Myr for Umbriel, 3 700 Myr for Titania, and 23 000 Myr for Oberon. These results are once more in agreement with the numerical results from Sect. 2.4.6, and show that tides are very efficient to damp the eccentricities of Ariel and Miranda.

4.5   Capture/escape probability

The behaviour of the system when it crosses a MMR is not straightforward, since the problem has four degrees of freedom. In order to get an idea of the critical eccentricities and inclinations that tend to trap the system in resonance or skip it, we can nevertheless attempt to build a simplified one degree-of-freedom model (e.g. Goldreich and Peale 1966; Henrard 1982; Batygin 2015).

The system can either be in resonance with the angle σ_1, σ_2, φ_1, or φ_2. Following Tittemore and Wisdom (1988), we retained only the terms associated with each angle and obtained their associated one degree-of-freedom simplified Hamiltonian (Eq. (3.96)). For the planar problem we have

$$\mathcal{H}_k = \mathcal{A}_k \, x_k \bar{x}_k + \mathcal{K}_2 \, (x_k \bar{x}_k)^2 + \frac{\mathcal{B}_k}{2} \, (x_k^2 + \bar{x}_k^2) \, , \tag{4.40}$$

with

$$\mathcal{A}_1 = \mathcal{K}_1 + O_1 + S_1 + S_2 \, , \quad \mathcal{B}_1 = \mathcal{R}_1 \, , \tag{4.41}$$

$$\mathcal{A}_2 = \mathcal{K}_1 + O_2 + S_1 + S_3 \, , \quad \mathcal{B}_2 = \mathcal{R}_2 \, . \tag{4.42}$$

Whereas for the circular problem we have

$$\mathcal{H}_k = \mathcal{A}_k \, y_k \bar{y}_k + \mathcal{K}_2 \, (y_k \bar{y}_k)^2 + \frac{\mathcal{B}_k}{2} \, (y_k^2 + \bar{y}_k^2) \, , \tag{4.43}$$

with

$$\mathcal{A}_1 = \mathcal{K}_1 + O_3 + S_1 + S_5 \, , \quad \mathcal{B}_1 = \mathcal{R}_4 \, , \tag{4.44}$$

$$\mathcal{A}_2 = \mathcal{K}_1 + O_4 + S_1 + S_6 \, , \quad \mathcal{B}_2 = \mathcal{R}_5 \, . \tag{4.45}$$

In this simplified case, we can directly apply the theory of the adiabatic invariant for resonance capture (Henrard 1982; Henrard and Lemaître 1983). In general, the phase space of a given resonance presents three different regions delimited by the separatrix (see Fig. 4.2): a libration region, with area $\mathcal{J}_k^R$ (green region of Fig. 4.2), and two circulation regions, one outside the libration region (white region in Fig. 4.2) and another encircled by the separatrix, with an area $\mathcal{J}_k^C$ (blue region of Fig. 4.2). Consider an initial trajectory with some energy $\mathcal{H}_k$, smaller than the energy of the separatrix (see Eq. 4.48), that is, $\mathcal{H}_k < \mathcal{H}_0$. As the system evolves due to tides, the phase space and the areas of each region also change. When the trajectory encounters the resonance, depending on the exact place where the separatrix is crossed, the system can either evolve into the libration region (resonance) or into the inner circulation region. We can compute the capture probability analytically, provided that the evolution is adiabatic, that is, the tidal induced variations are much slower than the conservative eccentricity and inclination
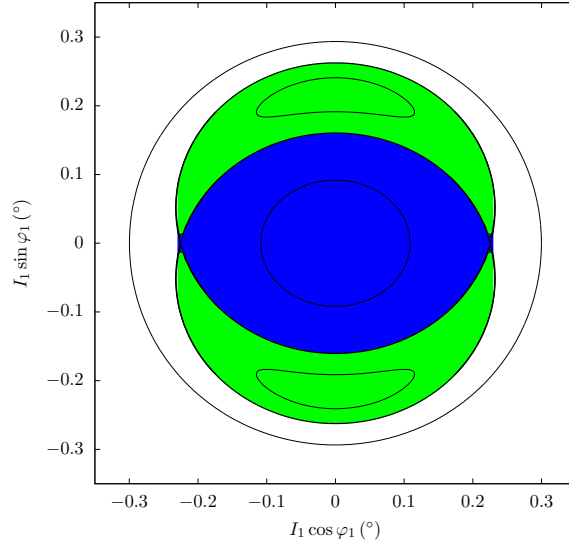
Figure 4.2: Energy level curves in the circular approximation for the single resonance Hamiltonian (4.43), with $\mathcal{A}_1$, $\mathcal{B}_1$ (that is, for Ariel) and $\delta = -2.0 \times 10^{-6}$. The libration regions are coloured in green and have an area $\mathcal{J}_k^R$, the inner circulation region is coloured in blue and has an area $\mathcal{J}_k^C$.

variations. The capture probability can then be obtained by the modification of the phase space with time, that is, by the change in the areas encircled by the separatrix (e.g. Yoder 1979; Henrard 1982):

$$P_{\text{cap}} = \frac{\dot{\mathcal{J}}_k^R}{\dot{\mathcal{J}}_k^R + \dot{\mathcal{J}}_k^C} \, . \tag{4.46}$$

The area of the resonance region is obtained by integrating over the separatrix,

$$\mathcal{J}_k^R = \mathrm{i} \oint x_k \, d\overline{x}_k \quad \text{or} \quad \mathcal{J}_k^R = \mathrm{i} \oint y_k \, d\overline{y}_k \, . \tag{4.47}$$

The energy of the separatrix ($\mathcal{H}_0$) can be found by finding the hyperbolic points (see Sect. 3.7) and computing the Hamiltonians (4.40) and (4.43) at these points,

$$\mathcal{H}_0 = -\frac{(\mathcal{A}_k + \mathcal{B}_k)^2}{4\mathcal{K}_2} \, . \tag{4.48}$$

Replacing $\mathcal{H}_0$ into Eq. (4.40), we find that, for the separatrix points in the planar approximation,

$$x_k = -\frac{2\mathcal{A}_k \overline{x}_k \pm \sqrt{-2\mathcal{B}_k \left(\mathcal{A}_k + 2\overline{x}_k^2 \mathcal{K}_2 + \mathcal{B}_k\right)^2 / \mathcal{K}_2}}{4\overline{x}_k^2 \mathcal{K}_2 + 2\mathcal{B}_k} \, , \tag{4.49}$$

and replacing $\mathcal{H}_0$ into Eq. (4.43), we find that, for the separatrix points in the circular approximation

$$y_k = -\frac{2\mathcal{A}_k \overline{y}_k \pm \sqrt{-2\mathcal{B}_k \left(\mathcal{A}_k + 2\overline{y}_k^2 \mathcal{K}_2 + \mathcal{B}_k\right)^2 / \mathcal{K}_2}}{4\overline{y}_k^2 \mathcal{K}_2 + 2\mathcal{B}_k} \, . \tag{4.50}$$

There are two solutions, the $+$ corresponding to the branch between the libration and the outer circulation region ($\mathcal{J}_k^+$), and the $-$ corresponding to the branch between the libration and the inner circulation region ($\mathcal{J}_k^-$). Therefore, we have $\mathcal{J}_k^R = \mathcal{J}_k^+ + \mathcal{J}_k^-$ and $\mathcal{J}_k^C = -\mathcal{J}_k^-$, which gives (Eq. (4.46))

$$P_{\text{cap}} = \frac{\dot{\mathcal{J}}_k^+ + \dot{\mathcal{J}}_k^-}{\dot{\mathcal{J}}_k^+} = 1 + \frac{\partial \mathcal{J}_k^-}{\partial \Gamma} \bigg/ \frac{\partial \mathcal{J}_k^+}{\partial \Gamma} \,, \tag{4.51}$$

where,

$$\frac{\partial \mathcal{J}_k^-}{\partial \Gamma} = \frac{1}{\mathcal{K}_2^2} \left(\arcsin\left(\sqrt{-\frac{\mathcal{B}_k}{\mathcal{A}_k}} \right) + \frac{\pi}{2} \right) (\mathcal{K}_2 \mathcal{A}_k' - \mathcal{A}_k \mathcal{K}_2') + \frac{1}{\mathcal{K}_2^2} \sqrt{-\frac{\mathcal{B}_k + \mathcal{A}_k}{\mathcal{B}_k}} (\mathcal{K}_2 \mathcal{B}_k' - \mathcal{B}_k \mathcal{K}_2') \,, \tag{4.52}$$

$$\frac{\partial \mathcal{J}_k^+}{\partial \Gamma} = \frac{1}{\mathcal{K}_2^2} \left(\arcsin\left(\sqrt{-\frac{\mathcal{B}_k}{\mathcal{A}_k}} \right) - \frac{\pi}{2} \right) (\mathcal{K}_2 \mathcal{A}_k' - \mathcal{A}_k \mathcal{K}_2') + \frac{1}{\mathcal{K}_2^2} \sqrt{-\frac{\mathcal{B}_k + \mathcal{A}_k}{\mathcal{B}_k}} (\mathcal{K}_2 \mathcal{B}_k' - \mathcal{B}_k \mathcal{K}_2') \,, \tag{4.53}$$

and $\mathcal{A}_k' = \partial \mathcal{A}_k / \partial \Gamma$, $\mathcal{K}_2' = \partial \mathcal{K}_2 / \partial \Gamma$, and $\mathcal{B}_k' = \partial \mathcal{B}_k / \partial \Gamma$. We note that since Γ is the only time-dependent quantity in the expressions of $\mathcal{A}_k$, $\mathcal{K}_2$, and $\mathcal{B}_k$ (Eqs. (3.69) to (3.88)), $\dot{\mathcal{J}}_k = \dot{\Gamma} \partial \mathcal{J}_k / \partial \Gamma$ (we neglected the small changes in Θ from the oblateness coefficients, O_k).

In Fig. 4.3, we show the probability of capture in the σ_1 (top left) and σ_2 (bottom left) resonances in the planar approximation, and in the φ_1 (top right) and φ_2 (bottom right) resonances in the circular approximation, obtained with Eq. (4.51). For some eccentricity and inclination values, we also show the results obtained with numerical integrations of the equations of motion derived from the simplified Hamiltonians (4.40) and (4.43) together with the secular tidal equations (Eqs. (4.22)–(4.27)). For each initial eccentricity and inclination, we ran 100 simulations where the initial angles σ_k or φ_k were uniformly sampled. The amount of simulations captured in resonance at the end of the simulation are marked with a dot. The statistical fluctuation, represented as error bars, were estimated using binomial statistics, with the expression

$$\Delta P = \sqrt{\frac{P_{\text{cap}}}{N} \left(1 - P_{\text{cap}} \right)}, \tag{4.54}$$

where $N = 100$ is the number of simulations (e.g. Tittemore and Wisdom 1988). We observe that there is a good agreement between the theoretical curve (Eq. (4.51)) and the output of the numerical simulations, that is, the adiabatic approximation holds.

In Fig. 4.3, we observe that, in the planar approximation, for initial eccentricities lower than 5.0×10^{-3}, the system is always captured in resonance. However, as we increase the initial eccentricity, the capture probability quickly decreases, it becomes $\sim 50\%$ for $e_k = 7.0 \times 10^{-3}$, and drops to $\sim 30\%$ for $e_k = 1.2 \times 10^{-2}$. These results suggest that a system with nearly circular orbits cannot escape the 5/3 MMR, but for eccentricities higher than about 7.0×10^{-3}, it may be able to evade it.

As for the circular approximation, we observe that for initial inclinations lower than $0.05°$, the system is always captured in resonance. However, as we increase the initial inclination, the capture probability quickly decreases, it becomes $\sim 50\%$ for $I_k = 0.1°$, and drops to $\sim 30\%$ for $I_k = 0.2°$. These results suggest that a system with nearly coplanar orbits cannot escape the 5/3 MMR, but for inclinations higher than about $0.1°$, it may be able to evade it.

We cannot completely rely on the conclusions obtained with the simplified Hamiltonian, mainly for two reasons. One is because the average secular Hamiltonian (Eq. (3.96)) depends on the eccentricities and inclinations of the other body. When we simplified the Hamiltonian (4.40), for example, for x_1, we dropped all terms in x_2 (and vice versa), which is equivalent to setting $x_2 = 0$. However, if we set $x_2 \neq 0$, more terms appear in the Hamiltonian, leading to a different distribution in the capture probabilities. The other reason is that the complete Hamiltonian has four degrees of freedom, and so for some combinations of the eccentricity or inclination values, the system can be chaotic (see Tittemore and Wisdom (1988) and Sects. 3.9 and 3.10). For the trajectories crossing the chaotic regions, the final outcome is unpredictable.
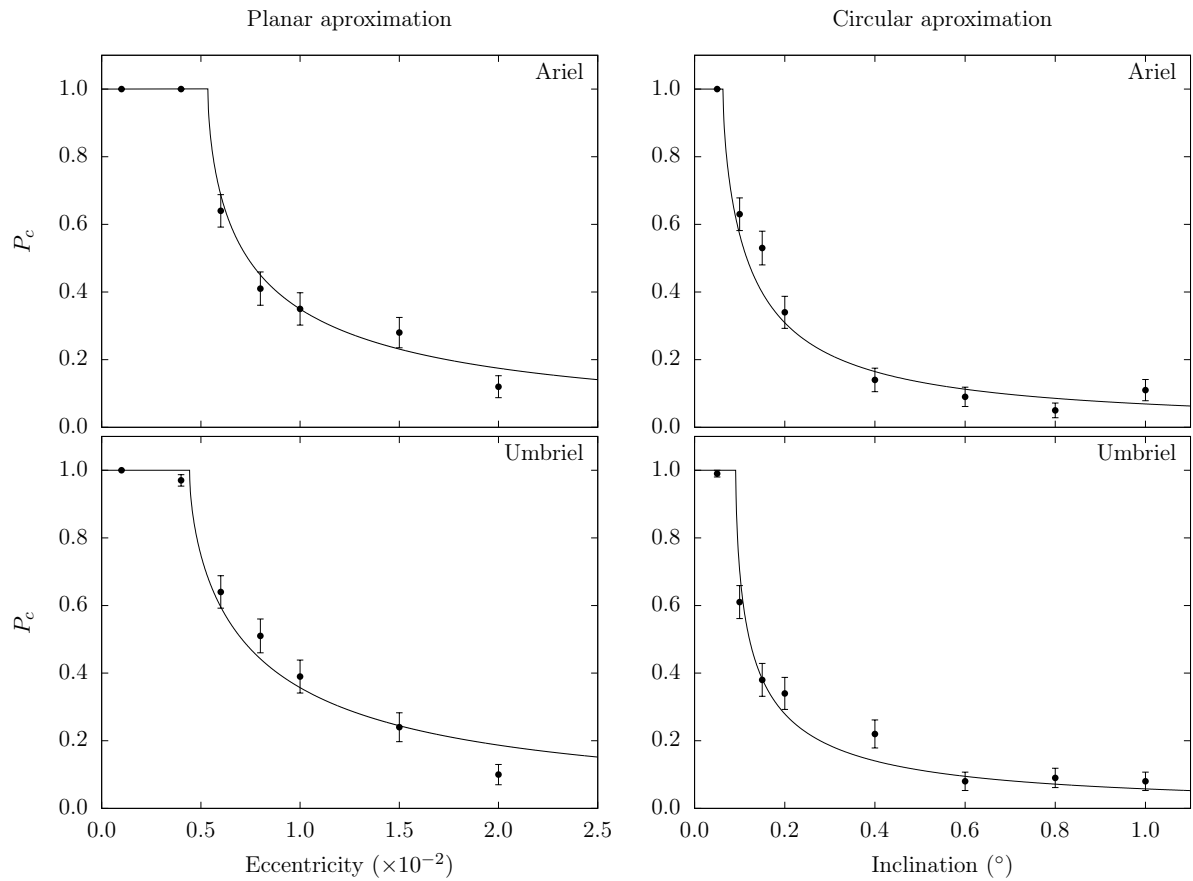
Figure 4.3: Capture probabilities for the planar approximation (left) and circular approximation (right). At the top are the σ_1 and the φ_1 resonances, and the σ_2 and φ_2 resonances are at the bottom. The solid line gives the theoretical approximation given by Eq. (4.51), while the dots give the results of numerical simulations. We ran 100 initial conditions with σ_k and φ_k differing by 1.8°.

Chapter 5

Numerical application to the 5/3 Ariel-Umbriel MMR

Ariel and Umbriel almost certainly encountered the 5/3 MMR at some time in the past. Depending on the initial conditions of these satellites, the system may experience rather different behaviours. Near circular and coplanar orbits are expected to become trapped in resonance, while some eccentricity or inclination can lead to alternative evolution scenarios (Fig. 4.3). In order to get a global view of the resonant dynamics with tides, in this chapter, we start by integrating the differential equations obtained with the secular model (Chaps. 3 and 4). We then validate the results with the N-body model (Chap. 2).

5.1 Circular approximation

Since the inclination appears to play an important role in the passage through the 5/3 MMR between Ariel and Umbriel, we begin by looking at this problem with a different perspective from previous studies (Sect. 1.4). Instead of assuming a coplanar model ($I_1 = I_2 = 0°$) with low initial eccentricities for Ariel and Umbriel as in Tittemore and Wisdom (1988), we assume a circular model ($e_1 = e_2 = 0$) with low inclinations using a similar approach to Tittemore and Wisdom (1989) for the study of the 3/1 MMR between Miranda and Umbriel. With this approximation, we require none of Eqs. (3.98), (3.99), (4.22), and (4.23), and the terms that depend on x_1, $\bar{x}_1$, x_2, or $\bar{x}_2$ can be removed from the equations of motion (3.100), (3.101), and (4.24) to (4.29). For simplicity, in this section we assume the satellites as point masses and solely consider tidal deformations raised on the planet.

The results in this section were published in Gomes and Correia (2023a).

5.1.1 Numerical setup

In Sect. 2.4.3, we have shown that $Q_0 = 8000$ is a suitable value for the tidal dissipation within Uranus. This value leads to $\tau_0 \approx 0.62$ s (Eq. (2.69)) and $k_{2_0}\tau_0 = 0.064$ s (Eq. (2.70)) and places the 5/3 Ariel-Umbriel MMR encounter about 640 Myr in the past (Fig. 1.4). The physical properties of Uranus, Ariel, and Umbriel can be found in Tables 1.1 and 1.2.

When a resonance is crossed, we cannot perform a backwards integration because we have a stochastic evolution. Therefore, we need to place the system slightly before the nominal resonance encounter (Eq. (3.105)),

$$a_2/a_1 \approx (5/3)^{2/3} \approx 1.4057 \,, \tag{5.1}$$

and then integrate it forwards. We estimate that the 5/3 MMR was crossed about 640 Myr ago, with

$$a_1/R_0 = 7.39054 \,, \quad a_2/R_0 = 10.38909 \,, \tag{5.2}$$

where the total angular momentum of the system composed by Uranus, Ariel, and Umbriel is obtained from the present system,

$$\Sigma = 9.367\,247 \times 10^{-10} \, \text{M}_\odot \, \text{au}^2 \, \text{yr}^{-1} \,. \tag{5.3}$$

It is not possible to determine the exact semi-major axes prior to resonance crossing, but if the system does not spend much time in resonance, the semi-major axes should not differ much from the estimation given by Eq. (5.2). We still need to slightly decrease a_1 (or increase a_2) to move the system out of the nominal resonance. Since tides are stronger in Ariel, we opted to shift a_1 and kept a_2 constant:

$$a_1/R_0 = 7.3892 \,, \quad a_2/R_0 = 10.3891 \,. \tag{5.4}$$

For some given initial inclination values, we compute the initial value of Δ (Eq. (3.51)), which translates into an initial $\delta > 0$ (Eq. (3.103)).

Considering the satellites as synchronous, we determine the initial angular velocity of Uranus through (Eqs. (3.49), (3.50), and (3.51)) using

$$\omega_0 = \frac{1}{C_0} \left(\Sigma - \Gamma_1 - \Gamma_2 - \Theta_1 - \Theta_2 \right) \,, \tag{5.5}$$

so that the total angular momentum is conserved.

5.1.2 Comparison with analytical estimations

In general, tidal effects are weak and only correspond to small perturbations of the conservative dynamics (adiabatic approximation). To verify that the numerical integrations do follow the theoretical predictions from Sects. 3.7 and 4.3, we initially ran a few simulations and then superimposed the output in the equilibria map as a function of δ (Fig. 3.1). Since $\omega_0 > n_k$, tidal effects are expected to increase the value of Γ (Eq. (4.26)) and thus decrease the value of δ (Eq. (3.103)). Therefore, the results of the simulations as a function of time must be read from the right to the left in the Figs. 5.1 and 5.2.

In Fig. 5.1, we show the results of a first experiment with very small initial inclinations for both satellites, $I_1 = I_2 = 0.01°$. Initially, when $\delta > 0$, the system is in circulation with a small amplitude around the equilibrium point at zero ($y_1 = 0, y_2 = 0$). The system encounters the resonance when $\delta \approx 0$. However, just before $\delta = 0$, two stable equilibrium points emerge (corresponding to the 5/3 MMR), and the equilibrium point at zero becomes unstable. The system is thus forced to follow one of the two resonance branches. As the system evolves and $\delta < 0$, the equilibrium point at zero becomes stable again. However, because the amplitude of oscillation is small, the system closely follows the resonant branch, which corresponds to an increase in the inclinations. We thus confirm that for initially near coplanar orbits, the system cannot avoid capture in the 5/3 MMR (Sect. 4.5).

In Fig. 5.2, we show the results of a second experiment with higher initial inclinations for both satellites, $I_1 = I_2 = 0.1°$. The initial evolution for $\delta > 0$ is similar to the case with lower initial inclinations (Fig. 5.1), except that the amplitude of oscillation is ten times larger in this case (corresponding to a system with a higher energy). As the system encounters the resonance at $\delta \approx 0$, it is not able to follow one of the resonant equilibria and it remains in a chaotic region around the separatrix (Fig. 3.3f). In the example on the left (Fig. 5.2a), after some time in the chaotic region with $\delta < 0$, the system finds a way into the libration region and follows one of the resonant branches in a quasi-periodic orbit (Fig. 3.3i). On the other hand, in the example on the right (Fig. 5.2b), the system finds an alternative path back into the circulation region around the equilibrium point at zero in a quasi-periodic orbit (Fig. 3.3k). We thus confirm that for initial orbits with some inclination, the system experiences a chaotic regime for some time (Sect. 3.9), after which it can either be captured in the 5/3 MMR, or escape it with some probability (Sect. 4.5).

5.1.3 Capture probability

The present mean inclinations of Ariel and Umbriel (Table 1.2) are likely unchanged after the system quits the 5/3 MMR (Eq. (4.37)). However, they may have been rather different before this encounter, as the inclinations undergo some excitations while crossing the resonance (Chap. 3). The fact that the system is not trapped in resonance at present, implies that the separatrix was crossed at some point and

Figure 5.1: Tidal evolution of the system as function of δ for initial inclinations $I_1 = I_2 = 0.01°$. The results of the numerical simulation (in black) are superimposed in the equilibria map (Fig. 3.1). We show the evolution for the resonant angle φ_1 (top) and φ_2 (bottom).
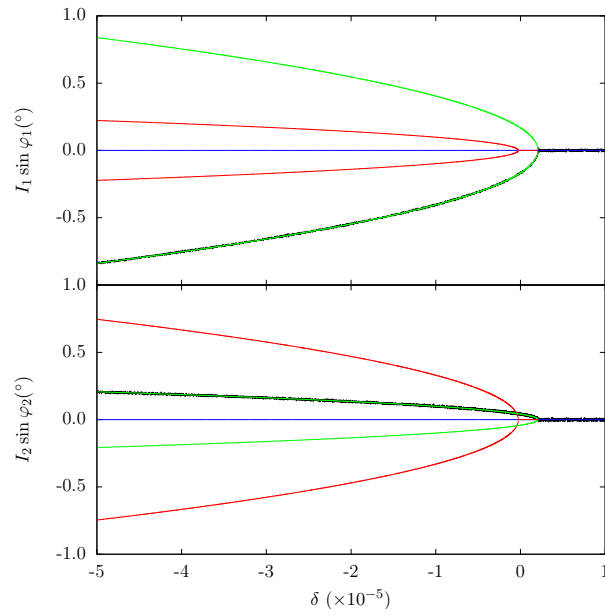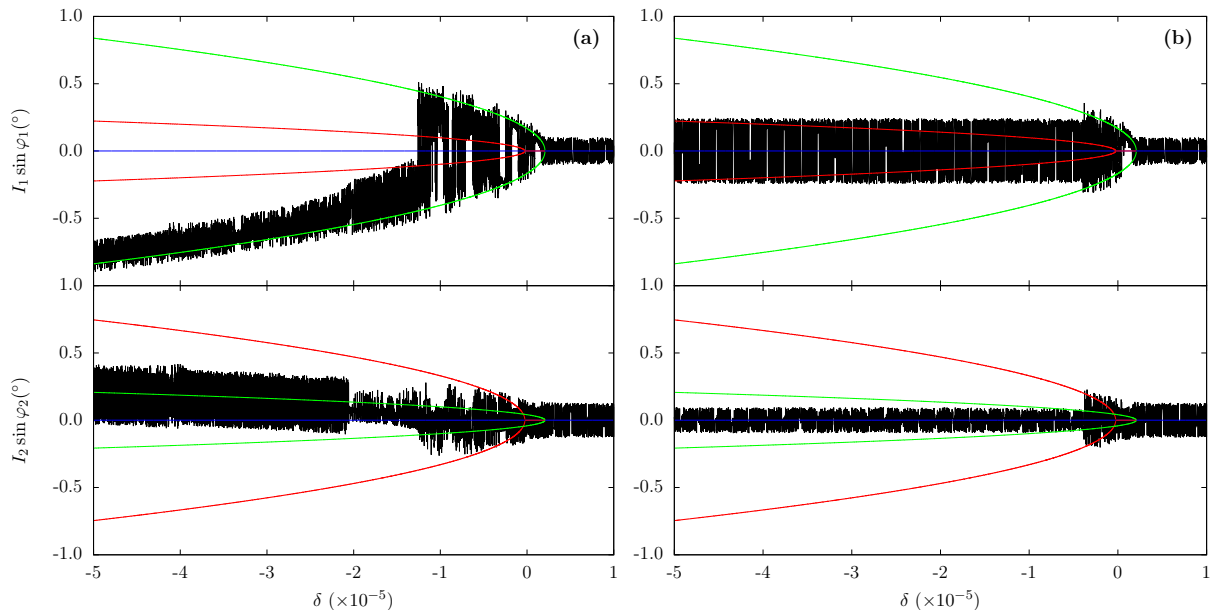

Figure 5.2: Two examples of tidal evolution of the system as a function of δ for initial inclinations $I_1 = I_2 = 0.1°$. The results of the numerical simulation (in black) are superimposed in the equilibria map (Fig. 3.1). We show the evolution for the resonant angle φ_1 (top) and φ_2 (bottom).

the inclinations had to experience some chaotic oscillations (Fig. 5.2b). Therefore, it is impossible to simply integrate backwards and determine the exact inclination values prior to the resonance encounter. To have a more clear idea of what the system may have been, we need to perform a statistical study of its past evolution, starting with arbitrary initial inclinations for both Ariel and Umbriel and then reject those that are not coherent with the present observations.

For that purpose, we explored a mesh of initial inclinations ranging between $0.001°$ and $0.2°$ with a stepsize of $0.05°$. For each pair (I_1, I_2), we ran $1\,000$ simulations evenly sampled over the angle σ (Eq. (3.38)) for 100 Myr, in a total of $25\,000$ experiments. In Table 5.1, we list the complete set of initial conditions together with a summary of the outcome of the resonance crossing. The results of the simulations are presented in percentage because they can be seen as a statistical distribution of a given final evolution possibility. The total number of events of each kind can be simply obtained multiplying the percent by ten.

For each run, we first evaluated whether capture in resonance occurred or not. Capture takes place whenever at least one resonant angle, φ_k (Eqs. (3.42) and (3.43)), switches from circulation to libration, and the mean motion ratio becomes approximately constant ($n_1/n_2 \approx 5/3$). The mean motion ratio criterion is usually more useful to automatically detect captures because inside chaotic regions the behaviour of the resonant angles can be quite erratic. Conversely, capture does not occur when all resonant angles remain in circulation, which introduces only a small jump in the mean motion ratios. For this last case, we consider that the resonance is skipped. In Table 5.1, the relative number of these events is dubbed as P_s (skip probability).

The capture probability can be simply evaluated as $1 - P_s$. However, when a capture occurs, we still have to distinguish between trajectories that remain captured for long periods of time from those that are able to escape shortly after. Indeed, in many resonant lockings, the inclinations remain chaotic and the system is able to evade the resonance after some time. In theory, all trajectories evading the resonance could lead to the present system. In practice, that is not possible, because the longer the system stays in resonance, the higher the final inclinations become (Fig. 5.1), and they cannot be conciliated with the presently observed values (Table 1.2). Moreover, Ćuk et al. (2020) have shown that as long as Ariel and Umbriel stay in resonance, the inclinations of the three other large satellites of Uranus also grow, in particular that of Miranda. After only 10 Myr in resonance, is it impossible to explain the observed values since tides are unable to efficiently damp the inclinations (Eq. (4.37)). Therefore, in our analysis, we split the capture events into those that stay in resonance for more than 10 Myr and those that are able to evade it before that time. In Table 5.1, the relative number of escapes is dubbed as P_e (escape probability) and the relative number of long-term entrapments is referred to as P_c (capture for more than 10 Myr probability).

In most sets of the simulations shown in Table 5.1, all three scenarios described above (capture, escape, and skip) are simultaneously present. To better illustrate the different possibilities, in Fig. 5.3, we show one example of each case, corresponding to set #17 (with an initial $I_1 = 0.05°$ and $I_2 = 0.15°$).

In Fig. 5.3a, the system is permanently captured in resonance. Prior to the resonance encounter, the semi-major axes ratio follows the asymptotic evolution predicted by Eq. (4.34). When the system comes across the resonance (at $t \approx 11$ Myr), the semi-major axes ratio becomes constant (since $n_1/n_2 \approx 5/3$), deviating considerably from the asymptotic line. Indeed, when capture occurs, instead of following the black curve, the system follows the dashed line, corresponding to the nominal resonance (Eq. (5.1)). Shortly after being captured, the system enters into the chaotic region. The inclinations of both satellites are excited and grow steadily on average, in particular that of Ariel, which oscillates between the two resonant branches (green lines in Fig. 3.1). For a time $t \approx 40$ Myr, the system finds a way into the libration region and becomes quasi-periodic, as in the example shown in Fig. 5.2a.

In Fig. 5.3b, the system is temporarily captured in resonance for less than 10 Myr. As in the previous example, the semi-major axes ratio initially follows the asymptotic evolution predicted by Eq. (4.34), but it switches to a constant ratio as soon as capture in resonance occurs (at $t \approx 11$ Myr). As before, during the resonant entrapment, the system enters into the chaotic region and the inclinations of both satellites start to grow. However, for a time around $t \approx 18$ Myr (that is, just 7 Myr after being captured),

#	I_1 (°)	I_2 (°)	P_c(%)	P_e(%)	P_s(%)	$\langle I_1 \rangle$ (°)	ΔI_1 (°)	$\langle I_2 \rangle$ (°)	ΔI_2 (°)
1	0.001	0.001	100.0	–	–				
2	0.05	0.001	100.0	–	–				
3	0.10	0.001	99.2	0.8	–				
4	0.15	0.001	100.0	–	–				
5	0.20	0.001	100.0	–	–				
6	0.001	0.05	100.0	–	–				
7	0.05	0.05	100.0	–	–				
8	0.10	0.05	97.3	2.5	0.2				
9	0.15	0.05	82.4	10.5	7.1	0.149	0.062	0.056	0.023
10	0.20	0.05	80.9	9.3	9.8	0.187	0.054	0.047	0.019
11	0.001	0.10	90.1	9.2	0.7	0.170	0.041	0.047	0.016
12	0.05	0.10	83.1	13.6	3.3	0.167	0.050	0.041	0.022
13	0.10	0.10	50.6	28.5	20.9	0.145	0.059	0.049	0.020
14	0.15	0.10	38.8	19.2	42.0	0.119	0.068	0.068	0.020
15	0.20	0.10	36.2	15.8	48.0	0.141	0.066	0.081	0.023
16	0.001	0.15	39.6	26.5	33.9	0.112	0.068	0.083	0.019
17	0.05	0.15	38.6	25.8	35.6	0.114	0.069	0.095	0.024
18	0.10	0.15	35.1	25.1	39.8	0.088	0.081	0.109	0.017
19	0.15	0.15	31.0	23.2	45.8	0.099	0.082	0.127	0.023
20	0.20	0.15	30.0	15.9	54.1	0.104	0.085	0.136	0.021
21	0.001	0.20	32.7	26.2	41.1	0.107	0.073	0.144	0.018
22	0.05	0.20	31.9	28.6	39.5	0.116	0.070	0.152	0.018
23	0.10	0.20	30.1	23.9	46.0	0.109	0.072	0.162	0.015
24	0.15	0.20	27.1	22.1	50.8	0.117	0.075	0.173	0.013
25	0.20	0.20	27.0	15.2	57.8	0.119	0.076	0.182	0.014

Table 5.1: Initial conditions and summary of the numerical simulations's results of the 5/3 MMR crossing. I_k is the initial inclination of each satellite; P_c is the percentage of simulations trapped in resonance more than 10 Myr; P_e is the percentage of simulations that were captured in resonance, but escaped in less than 10 Myr; P_s is the percentage of simulations that skipped the resonance; and $\langle I_k \rangle$ and ΔI_k are the mean and the standard deviation, respectively, of a Rice distribution adjusted to the final results.

the system finds a way outside the chaotic region that breaks the resonant locking and returns into the circulation region around the equilibrium point at zero (blue line in Fig. 3.1). From that point on, the semi-major axes ratio again follows the asymptotic evolution predicted by Eq. (4.34), though restarting with a slightly higher ratio, and the inclinations of both satellites stabilise around a given constant mean value. The final inclination of Ariel is always higher than its initial value because of the forcing during the resonant phase. The final inclination of Umbriel is less impacted by this mechanism and it does not have a systematic trend because it oscillates around the initial value with a large amplitude during the resonance crossing.

Finally, in Fig. 5.3c, the system shortly skips the resonance. As usual, the semi-major axes ratio initially follows the asymptotic evolution predicted by Eq. (4.34), and it undergoes some perturbations during the resonance crossing. However, it quickly returns to the asymptotic evolution, though restarting with a slightly lower ratio. In this case, there is almost no chaotic evolution for the inclinations because, just after crossing the separatrix, the system directly goes into the circulation region around the equilibrium point at zero (blue line in Fig. 3.1). The inclination of Ariel initially briefly grows since, owing to the topology of the 5/3 MMR (Fig. 3.2), it is not possible to reach the inner circulation region without moving around the resonant equilibrium for a short time (less than 1 Myr). Since in the example #17 the initial inclination of Ariel is indeed relatively small, for a short moment the inclination of Ariel follows
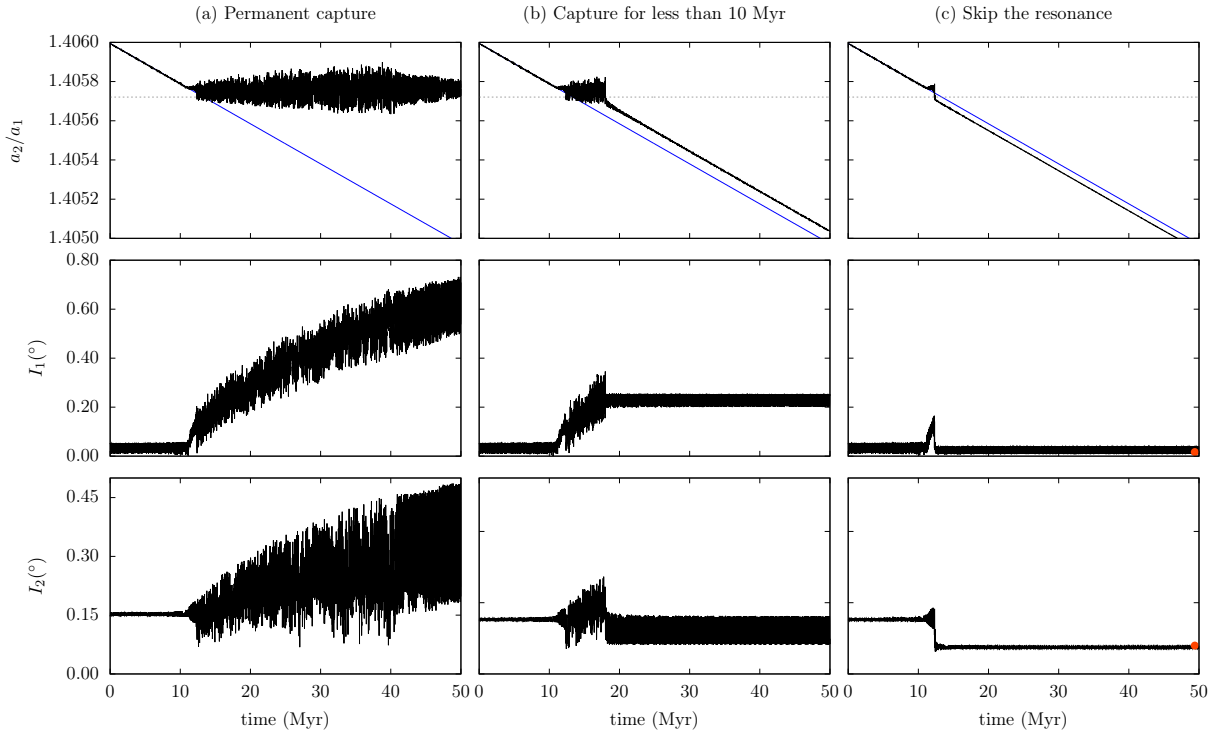
Figure 5.3: Three examples of a system crossing the 5/3 MMR with initial $I_1 = 0.05°$ and $I_2 = 0.15°$ (set #17 in Table 5.1). We show the ratio between the semi-major axes (top), the inclination of Ariel (middle), and the inclination of Umbriel (bottom) as a function of time. Each column corresponds to a different simulation. We show an example of a system that is permanently caught in resonance (a), one that is captured but evades the resonance in less than 10 Myr (b), and another that skips the resonance without capture (c). The blue line gives the asymptotic evolution predicted by Eq. (4.34), while the dashed line gives the position of the nominal resonance (Eq. (5.1)). The red dots mark the present mean inclinations (Table 1.2).

the resonant branch and has to increase (green line in Fig. 3.1). Nevertheless, as soon as the equilibrium point at zero becomes stable, the system moves back into the circulation region and the inclination of Ariel drops. In the example shown in Fig. 5.3c, the inclination of Ariel decreases to a mean value smaller than the initial one, but actually in other examples it can be anything between zero and the maximum previously attained. The brief resonant excitation only involves the angle φ_1, and so it does not impact the inclination of Umbriel much. Its amplitude grows due to the mutual interactions with Ariel, but the mean value remains constant. However, as the resonance is skipped, the mean value of Umbriel inclination suddenly drops to a lower level. This reduction is always observed because the inner circulation region is confined within a region of low inclination for Umbriel, in particular for δ values very close to zero (Fig. 3.2c).

Fig. 5.3c also provides an example of a simulation where the system crosses the 5/3 MMR and subsequently evolves into the presently observed configuration (red dots, taken from Table 1.2). Not all simulations #17 that skip the resonance end in the present system, though a significant number is consistent with it. On the other hand, some simulations starting with different initial conditions (Table 5.1) can also evolve into the present state. Therefore, only a more refined analysis of the final distribution of the inclinations of both Ariel and Umbriel can provide more insight into the occurrence likelihood of the currently observed system.

5.1.4 Statistics

For the set of simulations #1 − #8 (Table 5.1), that is to say those with initial $I_2 \leq 0.05°$, the system is captured in resonance nearly in 100% of the cases. For the initial inclination of Umbriel, these results are thus in agreement with the predictions of the simplified model presented in Sect. 4.5. Since capture in the 5/3 MMR is not observed today, we can immediately exclude this range of initial conditions. We hence conclude that, regardless of the initial inclination of Ariel, the system requires some moderate initial inclination for Umbriel ($I_2 \gtrsim 0.1°$) to evolve into the present state.

The resonance crossing is a stochastic process and therefore the same initial inclinations with a slightly different initial resonant angle may end up in a completely different final state. In all of the other sets of simulations that we performed (#9 − #25), the system can either remain captured for a long time, escape the resonance in less than 10 Myr, or simply skip it. In general, as we increase the initial inclinations of both satellites, the probability of capture in resonance decreases, in conformity with the analysis from Sect. 4.5. Interestingly, the number of trajectories temporarily captured for less than 10 Myr does not change much with the initial conditions, they occur around 20% − 25% of the time. This suggests that the chaotic diffusion, which characterizes this transient regime, is not very sensitive to the initial inclinations. Finally, as a result of the previous two outcomes, as we increase the initial inclinations of both satellites, the number of simulations that simply skip the resonance also increases.

For those systems that skip or escape the 5/3 MMR, one can ask if the final inclinations are in agreement with the present observations. However, there is not an easy answer because of the chaotic diffusion. Indeed, the final inclinations of Ariel and Umbriel never end exactly with the same values, but they rather follow some kind of statistical distribution. Considering only the trajectories that quickly evade or skip the resonance (P_e and P_s), we can build a histogram to better understand how they are distributed for each set of simulations #9 − #25 (i.e. we only consider simulations with less than 95% of capture probability).

In Fig. 5.4, we show three examples of histograms for the sets #9 ($I_1 = 0.15°, I_2 = 0.05°$), #17 ($I_1 = 0.05°, I_2 = 0.15°$), and #19 ($I_1 = 0.15°, I_2 = 0.15°$). The final inclinations of Ariel and Umbriel are distributed in classes with a size of $0.015°$ and the number of events in each class is normalised by the total number of trajectories that quickly evaded or skipped the resonance. We observe that for Ariel, the final inclinations are more or less evenly distributed between $0.01°$ and $0.25°$, while for Umbriel the final inclinations closely pile up around some mean value.

To better analyse the results in a systematic way, and since $I_k \propto |y_k|$ (Eq. (3.95)), we fitted a Rice distribution to each data set (Rice 1945), which describes the modulus of a random walk variable in two dimensions. This function has the form

$$f(I) = \frac{I}{\Delta I^2} B_0 \left(\frac{I \langle I \rangle}{\Delta I^2} \right) \exp \left(-\frac{I^2 + \langle I \rangle^2}{2 \Delta I^2} \right) , \tag{5.6}$$

where $\langle I \rangle$ is the mean inclination, ΔI is the standard deviation, and $B_0(x)$ is the modified Bessel function, given by

$$B_0(x) = \sum_{n=0}^{\infty} \frac{x^{2n}}{n!^2} . \tag{5.7}$$

In Fig. 5.4, for each histogram we also show the curve of the Rice distribution corresponding to the best fit parameters $\langle I \rangle$ and ΔI. We verified there is a reasonably good agreement between the histogram and the derived distribution, in particular for the final inclination of Umbriel. We hence adopted the best fit parameters obtained in this way to characterise each data set.

The statistical results obtained are listed in Table 5.1. From a detailed analysis, for the trajectories that are not trapped in resonance, we observe the following: for Ariel, regardless of the its initial inclination value, the final inclinations are always more or less uniformly distributed[1] in the interval

---

[1] We note that by construction, the Rice distribution must be zero when the inclination is zero and it has to peak around the mean value (Eq. (5.6)). As the final inclinations of Ariel are more or less uniformly distributed, a step function would provide a better adjustment. Nevertheless, we kept the Rice distribution for Ariel for simplicity since it is able to correctly capture the mean value and the dispersion around it.
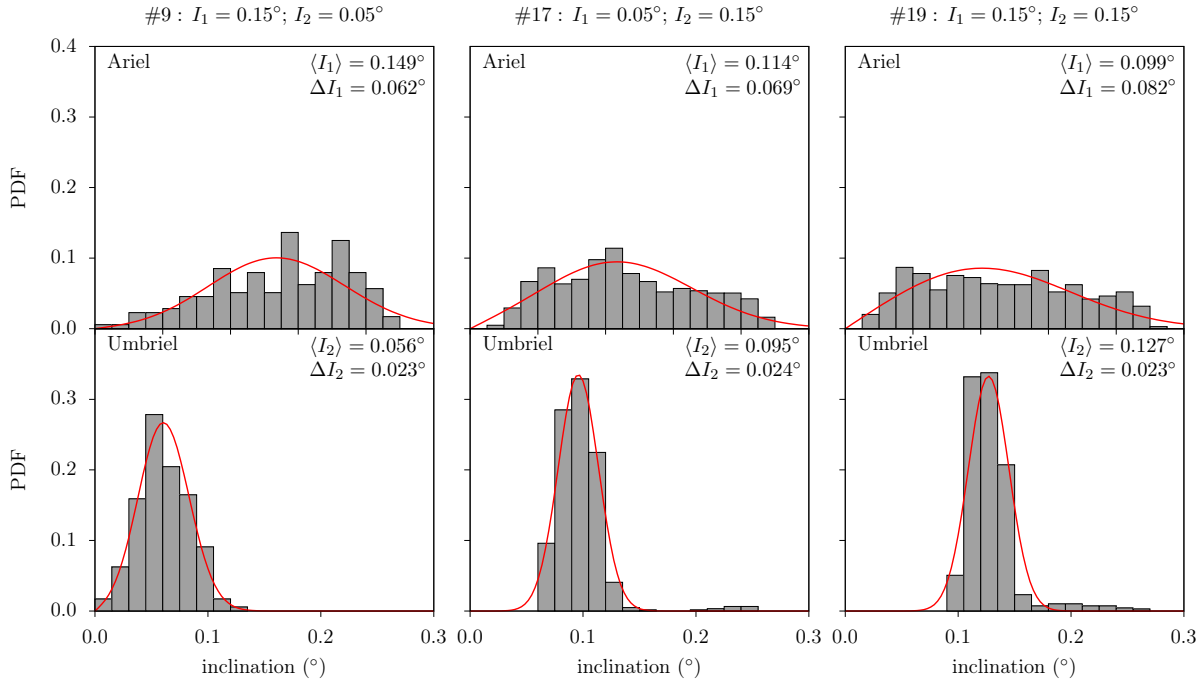
Figure 5.4: Histograms for the final distribution of the inclinations of Ariel (top) and Umbriel (bottom) for different sets of initial conditions. We also plotted the best fit Rice distribution (Eq. (5.6)) to each histogram (red curve) and the corresponding mean inclination, $\langle I_k \rangle$, and standard deviation, ΔI_k. We used the sets #9 (left), #17 (centre), and #19 (right) from Table 5.1.

$I_1 \in [0.01°, 0.25°]$; and for Umbriel, the final inclinations are gathered around the mean value with a standard deviation $\Delta I_2 \approx 0.02°$, and the mean value for the final inclination of Umbriel increases with the initial inclinations of both satellites. A more subtle analysis additionally shows that the average final inclination of Umbriel is always lower than its initial value and it also depends on the initial inclination of Ariel. It is approximately given by (see Fig. 5.5)

$$\langle I_2 \rangle - I_2 \approx -0.06° + 0.22 \, I_1 \, , \tag{5.8}$$

that is, to say the lower the initial inclination of Ariel is, the larger the decrease observed in the initial inclination of Umbriel.

The present average inclinations of Ariel and Umbriel are $I_1 \approx 0.02°$ and $I_2 \approx 0.08°$, respectively (Table 1.2). After crossing the 5/3 MMR, the inclination of Ariel is always approximately uniformly distributed and not very sensitive to the initial conditions. The presently observed value is thus compatible with near zero or moderate initial inclinations of both satellites ($I_k < 0.2°$), but no additional constraints can be derived. However, the final inclination of Umbriel strongly depends on the initial inclination of both satellites (Eq. (5.8)). We hence conclude that the best configuration that reproduces the present data was obtained for initial $I_1 \approx 0.20°$ and $I_2 \approx 0.10°$ (#15, Table 5.1) or initial $I_1 \lesssim 0.05°$ and $I_2 \approx 0.15°$ (#16 and #17, Table 5.1).

The satellites of Uranus were likely formed in a circumplanetary disk (e.g. Pollack et al. 1991; Szulágyi et al. 2018; Ishizawa et al. 2019; Inderbitzi et al. 2020), and so the initial inclinations should have been extremely small. Therefore, initial inclinations of 0.15° or higher are very difficult to explain. However, Umbriel was most likely previously involved in a 3/1 MMR with Miranda (Tittemore and Wisdom 1989, 1990), which can excite the inclination of Umbriel to 0.15° prior to the encounter with the 5/3 MMR. We hence conclude that, neglecting the effects of the eccentricities, the most likely scenario for the initial inclinations of Ariel and Umbriel is $I_1 \lesssim 0.05°$ and $I_2 \approx 0.15°$ (#16 and #17, Table 5.1).
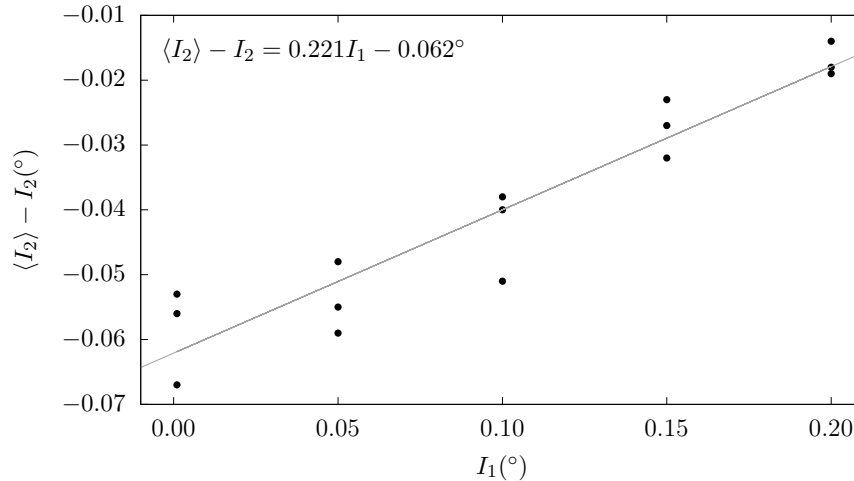
Figure 5.5: Variation in the average inclination of Umbriel after crossing the 5/3 MMR as a function of the initial inclination of Ariel. The points are taken from the simulations #11 to #25 in Table 5.1, and the line gives the adjustment of a linear regression.

5.2 Planar approximation

The planar approximation ($I_1 = I_2 = 0°$) was previously analysed in the work of Tittemore and Wisdom (1988), which involved both analytical and numerical studies. Still, the lack of computational power in the 1980's as compared to today, did not allow the authors to perform the same systematic numerical analysis applied in Sect. 5.1 for the circular approximation. Thus, in this section we adopted the same grid method used in Sect. 5.1 to replicate the results from Tittemore and Wisdom (1988) and determine which is the best configuration of initial eccentricities that allow to reproduce the current architecture of the satellite system for a planar model.

5.2.1 Numerical setup

As done for the circular approximation, we departed from the semi-major axes at nominal resonance (Eq. (5.2)), and slightly decreased a_1 to move the system out of the nominal resonance (Eq. (5.1)):

$$a_1/R_0 = 7.3889 , \quad a_2/R_0 = 10.3891 . \tag{5.9}$$

The physical properties of Uranus and the satellites can be found in Tables 1.1 and 1.2. The total angular momentum was obtained from the present system (Eq. (5.3)). The initial rotational rate of Uranus, ω_0, is obtained from the conservation of Σ using Eq. (5.5) with the pre-resonance semi-major axes (Eq. (5.9)), and considering that the satellites' rotation are synchronous with their orbital period ($n_k = \omega_k$). For the tidal dissipation, we adopted again $k_{2_0}\tau_0 = 0.064$ s (Eq. (2.70)). To prevent that tidal dissipation on the satellites damp the eccentricity of the satellites, resulting in a lower eccentricity at the resonance encounter than the intended, we neglected again the tidal effects acting on the satellites, i.e., $\tau_S = 0$ s. We note that, in the planar approximation, $I_1 = I_2 = 0°$, thus the x_x and y_k coordinates on the equations of motion are decoupled and we can disregard the evolution of y_k (Eqs. (3.100), (3.101), (4.24), and (4.25)). We numerically integrated Eqs. (3.98), (3.99), (4.22), (4.23), (4.26), (4.27), (4.28), and (4.29).

5.2.2 Impact of the initial eccentricity

Adopting the same approach used for the study on the impact of the inclination (Sect. 5.1), we explored a mesh of initial eccentricities ranging between 1×10^{-5} up to 2×10^{-2}, with a stepsize of 5×10^{-3}. For each combination (e_1, e_2), we integrated a set of 1 000 simulations evenly sampled over the resonance

#	e_1	e_2	P_c(%)	P_e(%)	P_s(%)	$\langle e_1 \rangle$ $(\times 10^{-3})$	Δe_1 $(\times 10^{-3})$	$\langle e_2 \rangle$ $(\times 10^{-3})$	Δe_2 $(\times 10^{-3})$
1	1.0×10^{-5}	1.0×10^{-5}	100.0	–	–				
2	5.0×10^{-3}	1.0×10^{-5}	100.0	–	–				
3	1.0×10^{-2}	1.0×10^{-5}	78.5	11.9	9.6	3.2	0.41	3.4	1.4
4	1.5×10^{-2}	1.0×10^{-5}	54.8	30.9	14.3	7.5	1.3	5.4	1.5
5	2.0×10^{-2}	1.0×10^{-5}	40.1	20.2	39.7	12.0	1.2	6.8	1.3
6	1.0×10^{-5}	5.0×10^{-3}	100.0	–	–				
7	5.0×10^{-3}	5.0×10^{-3}	99.9	0.0	0.1				
8	1.0×10^{-2}	5.0×10^{-3}	70.5	15.9	13.6	4.0	0.56	3.9	1.4
9	1.5×10^{-2}	5.0×10^{-3}	48.6	19.4	32.0	8.5	1.3	5.4	1.4
10	2.0×10^{-2}	5.0×10^{-3}	34.2	19.2	46.6	13.4	1.2	7.0	1.4
11	1.0×10^{-5}	1.0×10^{-2}	100.0	–	–				
12	5.0×10^{-3}	1.0×10^{-2}	99.5	0.0	0.5				
13	1.0×10^{-2}	1.0×10^{-2}	79.0	12.4	8.6	5.3	1.3	7.7	1.3
14	1.5×10^{-2}	1.0×10^{-2}	61.9	19.4	18.7	9.4	2.0	8.5	1.4
15	2.0×10^{-2}	1.0×10^{-2}	50.1	21.8	28.1	14.0	2.0	10.4	1.1
16	1.0×10^{-5}	1.5×10^{-2}	100	–	–				
17	5.0×10^{-3}	1.5×10^{-2}	99.8	0.0	0.2				
18	1.0×10^{-2}	1.5×10^{-2}	89.2	7.6	3.2	7.0	1.9	11.7	1.2
19	1.5×10^{-2}	1.5×10^{-2}	72.3	15.9	11.8	10.6	3.2	12.0	1.7
20	2.0×10^{-2}	1.5×10^{-2}	54.3	25.9	19.8	15.2	3.1	13.4	2.2
21	1.0×10^{-5}	2.0×10^{-2}	98.2	1.2	0.6				
22	5.0×10^{-3}	2.0×10^{-2}	99.9	0.1	0.0				
23	1.0×10^{-2}	2.0×10^{-2}	93.0	3.3	3.7	10.3	3.3	14.8	2.3
24	1.5×10^{-2}	2.0×10^{-2}	78.0	11.1	10.9	11.7	4.2	14.7	2.9
25	2.0×10^{-2}	2.0×10^{-2}	65.0	20.2	14.8	15.8	4.2	16.3	2.8

Table 5.2: Initial conditions and summary of the numerical simulations's results of the 5/3 MMR crossing in the planar approximation ($I_1 = I_2 = 0°$). e_k is the initial inclination of each satellite; P_c is the percentage of simulations trapped in resonance more than 10 Myr; P_e is the percentage of simulations that were captured in resonance, but escaped in less than 10 Myr; P_s is the percentage of simulations that skipped the resonance; and $\langle e_k \rangle$ and Δe_k are the mode and the variance, respectively, of a Lognormal distribution adjusted to the final results.

angle σ, for 100 Myr. In Table 5.2, we display the 25 different combinations of (e_1, e_2) studied, as well as the percentage of simulations that were permanently captured in the 5/3 Ariel-Umbriel MMR (P_c), captured for less than 10 Myrs (P_e) or skipped the resonance (P_s).

We note that, for initial $e_1 < 0.005$, the eccentricity of Umbriel does not affect the outcome of the resonance crossing, and capture is almost certain, independently of the initial e_2 value. However, for initial $e_1 \geq 0.010$, increasing the initial e_2 promotes an increase in the probability of capture. Thus, the highest probabilities of escaping/skipping the resonance, $1-P_c$, are achieved with simulations combining a high eccentricity of Ariel and a low eccentricity of Umbriel. This is a configuration particularly difficult to explain, since, as seen in Sect. 4.4, tides are more effective to damp e_1 than e_2, with Umbriel's eccentricity damping timescale being one order of magnitude larger than Ariel's.

In the planar approximation, the mechanism of capture in resonance is similar to the one for the circular approximation. However, here it takes place whenever at least one of the resonant angles, σ_k (Eqs. (3.42), (3.43)), switches from circulation to libration. For each simulation, we evaluated whether capture in resonance occurred by analysing if the semi-major axes ratio a_2/a_1 becomes constant, close to the nominal resonance value (Eq.5.1).
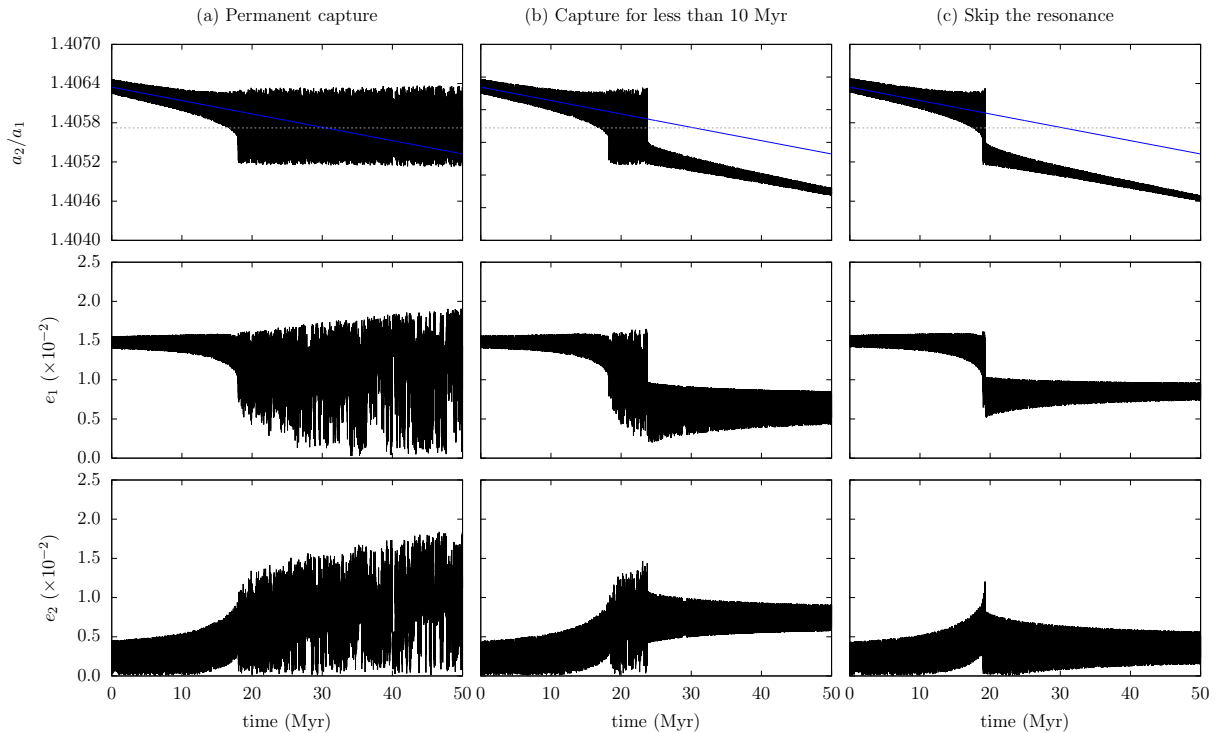
Figure 5.6: Three examples of a system crossing the 5/3 MMR with initial $e_1 = 1.5 \times 10^{-2}$ and $e_2 = 5.0 \times 10^{-3}$ (set #9 in Table 5.2). We show the ratio between the semi-major axes (top), the eccentricity of Ariel (middle), and the eccentricity of Umbriel (bottom) as a function of time. Each column corresponds to a different simulation. We show an example of a system that is permanently caught in resonance (a), one that is captured but evades the resonance in less than 10 Myr (b), and another that skips the resonance without capture (c). The blue line gives the asymptotic evolution predicted by Eq. (4.34), while the dashed line gives the position of the nominal resonance (Eq. (5.1)).

In Fig. 5.6, we provide examples from the set #9 (with initial $e_1 = 1.5 \times 10^{-2}$ and $e_2 = 5.0 \times 10^{-3}$) of the three possible outcomes into which we grouped the results. If the system is captured for more than 10 Myr, we consider that it is permanently captured (Fig. 5.6a). In Fig. 5.6a, up to $t \approx 18$ Myr, that is, before the resonance encounter, the semi-major axes ratio a_2/a_1 follows the asymptotic evolution predicted by Eq. (4.34), represented as a blue line. Since we only consider dissipation in the planet, the eccentricities remain nearly unchanged until the resonance encounter (Eq. (4.35)). However, as the system approaches the resonance, at $t \approx 10$ Myr, the oscillation amplitude of a_2/a_1 and e_1 grow, together with the average value of e_2. When the resonance is crossed, the semi-major axes ratio becomes constant ($a_2/a_1 \approx 1.4057$). Shortly after resonance capture, the system starts to evolve chaotically, considerably increasing the oscillation amplitude of the eccentricities of both satellites. The eccentricity of Ariel ranges between $5.0 \times 10^{-3} < e_1 < 1.5 \times 10^{-2}$, and the eccentricity of Umbriel between $0 < e_2 < 10^{-2}$. During the resonance entrapment, the eccentricities of both satellites continuously grow, in particular for Umbriel.

In Fig. 5.6b, the system, evades the 5/3 MMR in less than 10 Myr after being captured. Up to the break of the resonance, at $t \approx 24$ Myr, the evolution of the system is similar to the case of permanent capture (Fig. 5.6a). Only now, after the system escapes the resonance, the semi-major axes ratio a_2/a_1 follows once more the predicted asymptotic evolution (Eq. (4.34)). The large amplitude of libration of the eccentricity enables Ariel to escape the resonance with an eccentricity value smaller than the initial value previous to the resonance encounter. As for Umbriel, the increase of the average value near the resonance and during resonant entrapment, excites the eccentricity to a higher value than the initial one.

In Fig. 5.6c, we show an example of a simulation where the system shortly escapes the resonance. Once more, until the resonance encounter, the semi-major axes ratio follows the asymptotic evolution

predicted by Eq. (4.34), with the eccentricity of Umbriel increasing in the vicinity of the resonance. In this case, the system avoids entrapment and skips the nominal resonance. After the resonance crossing, a_2/a_1 drops abruptly and returns to the asymptotic evolution. The same step decrease is observed for the eccentricities of Ariel and Umbriel. Note that, despite the final post resonance eccentricity of Ariel is lower than the initial one, the eccentricity of Umbriel skips the MMR with a higher value than the initial one, due to an increase in its average value during the resonance approach.

To properly analyse the final distribution of the eccentricities of Ariel and Umbriel, we built histograms with the final values of e_1 and e_2 of the simulations that either escaped or skipped the resonance. In order to ensure statistical significance, we only consider sets of simulations with less than 95% of capture probability, that is, for initial $e_1 > 5.0 \times 10^{-3}$.

In Fig.5.7, we show three examples of histograms for the sets #4 ($e_1 = 1.5 \times 10^{-2}, e_2 = 10^{-5}$), #9 ($e_1 = 1.5 \times 10^{-2}, e_2 = 5.0 \times 10^{-3}$), and #20 ($e_1 = 2.0 \times 10^{-2}, e_2 = 1.5 \times 10^{-2}$). The final eccentricities of Ariel and Umbriel are distributed in classes with a size 1.5×10^{-3}, and the number of events in each class is normalized by the total number of trajectories that quickly escaped or skipped the resonance. We noticed that the distribution of eccentricities of both Ariel and Umbriel are piled-up around a mean value. However, the distribution of Ariel displays a smaller group in the vicinity of the class with higher counts, that grows with the initial e_2.

To analyse the results systematically, we fitted a distribution to each data set. We observe that the shape of the final eccentricity distribution differs from that of the final inclination distribution in the circular approximation (Sect. 5.2). In the circular approximation, the final inclination distribution gradually increases, reaching the mean value. Conversely, in the planar approximation, the final eccentricities can quickly accumulate around the mean value. Thus, the Rice distribution is no longer suitable to evaluate the planar approximation. After trying several distributions, we have found that the Lognormal distribution is the most suitable. The probability density function (PDF) of the Lognormal distribution is given by

$$f(e) = \frac{1}{e \, \eta \, \sqrt{2\pi}} \exp\left(-\frac{(\ln e - \upsilon)^2}{2 \, \upsilon^2}\right), \tag{5.10}$$

where υ and η are the parameters that define the distribution. The most likely value, that is, the peak of the PDF, is given by

$$\langle e \rangle = \exp\left(\upsilon - \eta^2\right), \tag{5.11}$$

and the variance is given by

$$\Delta e = \left(\exp\left(\eta^2\right) - 1\right)\left(\exp\left(2\upsilon + \eta^2\right)\right). \tag{5.12}$$

The statistical results obtained are listed in Table 5.2. The final eccentricities of Umbriel are gathered around the mean value with a variation $\Delta e_2 \approx 2 \times 10^{-3}$. The same is also observed for Ariel when e_2 is small. However, in addition to the cluster around the mean value (main cluster), we also observe a smaller cluster to the right of the main cluster, that is, around a slightly larger mean value (secondary cluster). As e_2 increases, the secondary cluster also grows, resulting in the most likely value of the distribution lying at an intermediate value between the two clusters. Nevertheless, for $e_1 \leq 2.0 \times 10^{-2}$ the Lognormal provides a good description of the distribution, and we observe that the mean final eccentricity of Ariel and Umbriel increase with the initial eccentricities of both satellites.

Tidal forces most likely damp the eccentricity of Ariel to a value closer to the currently observed $e_1 = 1.22 \times 10^{-3}$ (Table 1.2) if the eccentricity just after the 5/3 passage is about $\sim 10^{-2}$ (Sect. 4.4). On the other hand, the eccentricity tidal damping in the Umbriel is less effective than in Ariel. Therefore, the final eccentricity of Umbriel after the resonance cross must be close to the currently observed $e_2 = 3.94 \times 10^{-3}$ (Table 1.2). We hence conclude that, in the planar secular approximation, the best configurations that reproduce the present data were obtained for $1.5 \times 10^{-2} < e_1 < 2.0 \times 10^{-2}$ and $e_2 < 5.0 \times 10^{-3}$ (#4, #5, #9 and #10, Table 5.2). This configuration is difficult to explain when we account for tidal forces, that efficiently damp the eccentricity of Ariel. The theoretical asymptotic evolution displayed in Fig.1.4 shows that there are none previous low order two-body resonance for some Gyr.
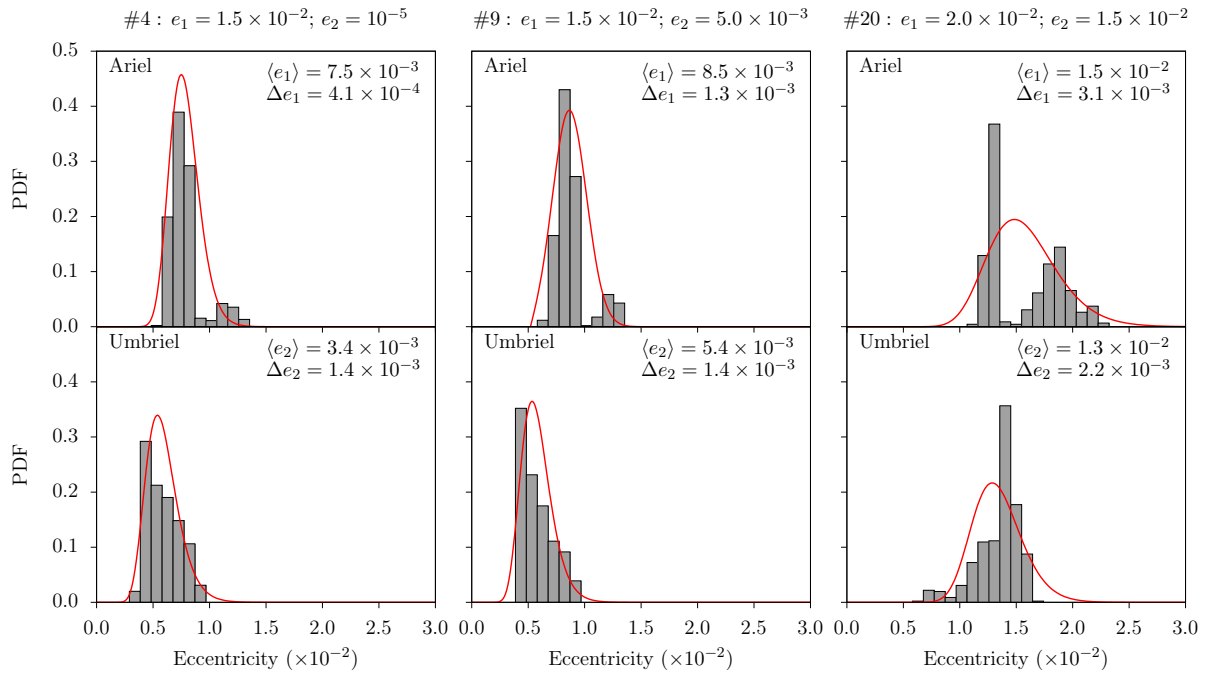
Figure 5.7: Histograms for the final distribution of the eccentricities of Ariel (top) and Umbriel (bottom) for different sets of initial conditions. We also plotted the best fit Lognormal distribution (Eq. (5.10)) to each histogram (red curve) and the corresponding mean eccentricities, $\langle e_k \rangle$, and standard deviation, Δe_k. We used the sets #4 (left), #9 (centre), and #20 (right) from Table 5.2.

5.3 Eccentric-inclined case

The study of the circular and planar approximations allowed us to gain important insights regarding the individual role of the inclinations and the eccentricities for the outcome of the passage through the 5/3 MMR between Ariel and Umbriel. Yet, in a real system, the evolution of the eccentricities and the inclinations are coupled, and mutually perturb each other. Therefore, for a comprehensive study of the evolution of Ariel and Umbriel during the resonance crossing, we must take into account the case where both eccentricities and inclinations are involved. As seen in Chaps. 3 and 4, this problem has 4 degrees of freedom for the conservative motion, and 8 degrees of freedom for the dissipative motion (rotation of the two satellites), rendering analytical studies very difficult. As a result, here we build on the analytical results obtained for the approximated cases and perform numerical integrations, using the same methods used to study circular and planar cases (Sect. 5.1 and 5.2). In this section, we integrate the complete set of equations of motion, that is, Eqs. (3.98) to (3.101) for the conservative motion and (4.22) to (4.29) for the tidal evolution.

5.3.1 Numerical setup

Up to now, we disregarded the tidal effects of Uranus acting on the satellites, that is, we considered $\tau_S = 0$. However, we note that the tidal evolution of the eccentricity (Eq. (4.39)) mainly depends on the tidal strength of the satellites (Q_S / k_{2_k}). Therefore, for completeness, from now on we also take into account the tidal effects acting on the satellites.

It is common to choose a tidal strength $Q_S = 100$ for the satellites (e.g. Murray and Dermott 1999; Ćuk et al. 2020). With this value, we obtain τ_{ecc} of about ~ 60 Myr for Ariel and ~ 660 Myr for Umbriel. Considering the results from Sect. 5.2 (see also Tittemore and Wisdom 1988; Ćuk et al. 2020), the satellites can leave the 5/3 MMR with eccentricities of about ~ 0.01. This means that, during the 640 Myr of tidal evolution from the resonance passage to the present, Ariel's eccentricity should have eroded to values smaller than the ones currently observed. In order to reproduce the current eccentricity

of Ariel, we need to adjust Q_S to reproduce the current $e_1 = 1.22 \times 10^{-3}$. By setting $Q_S = 500$, the τ_{ecc} of Ariel increases to 290 Myr, which places e_1 close to the currently observed value after leaving the 5/3 MMR with $e_1 \approx 0.01$. Although Umbriel's τ_{ecc} is one order of magnitude higher than Ariel's, for coherence, we adopt the same Q_S, resulting in an eccentricity damping timescale of 3300 Myr.

As done for the previous cases, we slightly decreased the semi-major axis of Ariel (a_1), while keeping a_2 constant, in order to place the system just before resonance at the beginning of the simulation (Eq. (5.2)). However, to ensure that $\delta > 0$ (Eq. (3.103)) for a wide range of combinations of eccentricities and inclinations, here we need to shift a_1 slightly more than in the previous sections:

$$a_1/R_0 = 7.3868, \quad a_2/R_0 = 10.3891. \tag{5.13}$$

The total angular momentum was again estimated from the present configuration (Eq. (5.3)), the satellites were initially considered as synchronous, and the initial ω_0 estimated using Eq. (5.5).

5.3.2 Capture probability

Once again, we start by exploring a mesh of initial eccentricities ranging between 10^{-5} and 2.0×10^{-2}, with a stepsize of 5.0×10^{-3}, and initial inclinations ranging between $0.001°$ and $0.2°$, with a stepsize of $0.05°$, totalling 625 different initial combinations of e_1, e_2, I_1, and I_2. For each initial combination, we ran 1 000 simulations for 100 Myr, evenly sampled over the resonance angle σ (Eq. (3.32)). In Table 5.3, the complete set of initial combinations is listed. For each run, we determine if the system is captured in resonance, by analysing if the semi-major axes ratio a_2/a_1 becomes constant. We distinguish between simulations that were captured for more than 10 Myr (P_c), and simulations that either skipped the resonance or escaped in less than 10 Myr ($P_e = 1 - P_c$). In Table 5.3, we display P_e for each initial combination of eccentricities and inclinations.

When capture takes place, at least one of the resonant angles σ_k and φ_k switches from circulation to libration, that is, $d\sigma_k/dt \approx 0$ or $d\varphi_k/dt \approx 0$. The exact mean motion ratio at the resonance encounter is given by

$$\frac{n_1}{n_2} = \frac{5}{3} - \frac{2}{3}\frac{\upsilon}{n_2} \tag{5.14}$$

where $\upsilon = g_k \simeq d\varpi_k/dt$ for σ_k and $\upsilon = s_k \simeq d\Omega_k/dt$ for φ_k. In other words, υ is the frequency of the secular modes (Sect. 2.4.2). From Table 2.3, we observe that $g_2 > g_3 > s_3 > s_2$. Since the exact $n_2/n_1 = 5/3$ is approached from above ($(d/dt(n_1/n_2) < 0$), φ_1 is the first resonant argument that the systems encounters. This can be seen in Fig. 5.8a, with initial $e_1 = 10^{-5}$, $e_2 = 10^{-5}$, $I_1 = 0.001°$, and $I_2 = 0.001°$. Before the resonance encounter, the semi-major axes ratio follows the asymptotic evolution predicted by Eq. (4.34), and the resonant arguments σ_k and φ_k circulate. At $t \sim 30$ Myr, the semi-major axes ratio locks with a value slightly higher than 5/3. Simultaneously, the resonance angles φ_1 and φ_2 start to librate around $90°$ and $-90°$, respectively, while the angles σ_k continue to circulate. Just after the capture into resonance, the inclinations of both satellites start to grow steadily on average.

In Fig. 5.8b, with initial $e_1 = 10^{-5}$, $e_2 = 5 \times 10^{-3}$, $I_1 = 0.001°$, and $I_2 = 0.001°$, up to $t \approx 40$ Myr, the initial evolution is similar to the evolution observed in Fig. 5.8a, where capture occurs at $t \approx 32$ Myr. However, at $t \approx 40$ Myr, φ_k leaves the libration region, and the eccentricities and the inclinations start to evolve chaotically. After ~ 7 Myr in this regime, the resonance angles σ_k start to librate, and the eccentricities grow, while the inclinations become constant. Note that, between $t \approx 40$ Myr and $t \approx 47$ Myr, there is a decrease in the mean motion ratio constant value, resulting from the switch between the resonance arguments, from φ_k to σ_k (Eqs. (3.40), (3.41), (3.42), and (3.43)).

For higher initial inclinations, the system can evade capture into the resonance arguments φ_k, and becomes directly trapped into the arguments σ_k. In Fig. 5.9c, with initial $e_1 = 10^{-5}$, $e_2 = 10^{-2}$, $I_1 = 0.15°$, and $I_2 = 0.20°$, the system is captured inside the chaotic region at $t \approx 32$ Myr, with both eccentricities and inclinations evolving chaotically. Shortly after, at $t \approx 36$ Myr, σ_1 and σ_2 start to librate around $90°$ and $-90°$, respectively, and the eccentricities enters the libration region, while the inclinations become constant. Despite different evolutionary paths for entrapment in the 5/3 MMR are observed in

e_1	I_1 (°)	$e_2 = 1\times10^{-5}$					$e_2 = 5\times10^{-3}$					$e_2 = 1\times10^{-2}$					$e_2 = 1.5\times10^{-2}$					$e_2 = 2\times10^{-2}$				
	I_2 (°)	0.001	0.05	0.10	0.15	0.20	0.001	0.05	0.10	0.15	0.20	0.001	0.05	0.10	0.15	0.20	0.001	0.05	0.10	0.15	0.20	0.001	0.05	0.10	0.15	0.20
$e_1 = 1\times10^{-5}$	0.001	0.0	0.0	0.0	0.0	0.0	0.0	0.0	0.0	0.0	0.0	5.4	4.6	4.2	5.2	5.2	9.8	13.9	13.2	15.0	14.2	5.8	11.8	13.4	15.8	14.9
	0.05	0.0	0.0	0.0	0.0	0.0	0.0	0.0	0.0	0.0	0.0	6.2	4.8	4.7	4.5	4.8	13.9	14.1	15.7	16.2	14.2	13.9	14.3	13.2	14.4	15.2
	0.10	0.0	0.0	0.0	0.0	0.0	0.0	0.0	0.0	0.0	0.0	5.8	5.6	5.5	5.9	5.7	15.8	14.2	14.2	15.3	12.9	12.8	15.6	15.4	16.0	14.6
	0.15	0.0	0.0	0.0	0.0	0.0	0.0	0.0	0.0	0.0	0.0	4.8	4.8	5.7	5.6	5.1	13.9	15.6	16.7	13.3	13.5	16.1	16.0	14.3	15.1	17.5
	0.20	0.0	0.0	0.0	0.0	0.0	0.0	0.0	0.0	0.0	0.0	5.3	5.2	5.0	4.2	4.6	14.0	15.0	14.4	13.3	14.9	16.1	17.1	16.9	13.8	17.2
$e_1 = 5\times10^{-3}$	0.001	0.0	0.0	0.0	0.0	0.0	0.0	0.0	0.0	0.0	0.0	13.0	10.7	10.3	11.7	10.8	10.3	14.3	16.8	13.5	15.4	4.5	12.7	13.2	13.3	12.0
	0.05	0.0	0.0	0.0	0.0	0.0	0.0	0.0	0.0	0.0	0.0	11.9	10.3	11.6	11.3	8.5	16.5	17.6	16.2	15.6	14.7	9.8	11.5	11.9	12.3	13.0
	0.10	0.0	0.0	0.0	0.0	0.0	0.0	0.0	0.0	0.1	0.0	11.0	13.2	12.4	12.5	10.9	14.0	15.2	16.6	16.6	15.5	12.9	12.8	11.9	12.4	13.5
	0.15	0.0	0.0	0.0	0.0	0.0	0.0	0.0	0.0	0.0	0.1	11.3	11.1	11.6	10.4	9.6	17.6	15.4	15.1	15.5	16.7	11.7	14.6	14.5	12.4	14.4
	0.20	0.0	0.0	0.0	0.0	0.0	0.0	0.0	0.0	0.2	0.0	10.2	11.6	11.3	11.4	10.7	15.9	15.0	14.4	15.5	14.5	13.0	14.0	12.8	13.5	13.8
$e_1 = 1\times10^{-2}$	0.001	21.9	20.9	18.7	17.6	20.2	38.5	36.5	33.3	33.6	31.9	23.3	32.8	34.4	36.6	34.5	12.1	19.5	20.5	26.3	22.4	6.2	9.6	12.4	12.9	14.1
	0.05	19.0	20.8	19.7	18.3	17.5	31.1	32.2	32.7	32.0	29.1	33.5	33.5	34.3	36.3	34.2	22.8	23.4	21.4	25.8	25.7	11.3	12.2	12.7	10.3	14.7
	0.10	18.0	22.5	19.2	20.2	15.3	30.0	33.8	34.1	34.5	31.1	36.3	34.7	33.9	36.3	32.7	23.3	22.6	23.8	25.6	25.1	12.4	14.1	13.6	14.6	12.4
	0.15	14.8	18.7	18.4	18.0	13.4	30.4	32.0	31.9	32.1	26.6	33.5	35.7	35.6	33.0	32.4	24.9	26.4	25.8	27.3	24.6	18.6	14.8	16.0	15.2	15.2
	0.20	10.6	11.3	13.3	12.4	13.6	26.9	26.9	25.2	26.3	24.8	33.1	35.6	30.1	34.9	30.3	25.6	25.5	24.3	27.3	26.6	15.3	17.4	17.4	17.1	14.5
$e_1 = 1.5\times10^{-2}$	0.001	48.7	54.8	61.1	63.3	58.8	58.5	67.3	69.3	68.3	71.7	37.2	42.3	45.0	49.7	47.7	24.6	25.4	25.6	26.4	28.9	15.5	15.6	16.0	17.7	19.1
	0.05	61.7	62.8	63.1	62.4	61.6	68.8	69.3	68.4	70.4	69.0	43.3	42.9	44.6	48.6	49.9	25.6	23.7	25.3	24.1	29.1	15.8	16.4	16.0	17.7	17.3
	0.10	60.7	59.3	58.8	59.3	59.1	68.1	68.2	68.8	67.7	64.9	49.3	49.6	51.3	46.7	51.4	25.4	26.7	28.9	31.2	29.2	16.8	17.1	17.9	17.4	16.2
	0.15	58.8	57.9	55.5	55.3	55.1	63.5	61.3	63.1	63.6	61.1	50.5	50.8	49.6	50.6	53.5	29.6	32.6	37.8	29.4	29.7	17.2	19.1	17.3	19.5	17.2
	0.20	50.9	53.8	52.7	48.6	51.4	60.9	58.4	59.3	55.8	57.1	50.5	49.6	51.1	50.9	51.0	32.5	31.3	29.2	30.4	33.1	19.7	20.4	21.0	18.2	19.4
$e_1 = 2\times10^{-2}$	0.001	60.4	66.1	72.0	74.4	73.9	74.0	74.9	77.3	77.7	79.4	44.1	48.5	47.8	52.7	53.2	36.0	40.0	35.9	36.7	36.4	24.7	24.5	24.5	24.8	24.5
	0.05	68.8	68.3	68.5	76.2	77.4	77.7	79.0	78.7	79.1	80.2	50.0	48.6	58.8	49.4	51.4	39.4	36.9	37.9	40.0	36.3	25.5	25.0	26.6	25.8	25.9
	0.10	76.7	76.2	75.7	78.3	76.6	81.5	78.5	82.1	78.9	80.5	52.2	47.8	51.0	49.7	51.9	39.7	39.3	40.4	40.9	37.0	27.1	23.8	27.6	23.0	26.6
	0.15	77.8	75.3	75.3	75.0	73.1	78.8	80.3	80.2	77.5	81.0	50.6	55.7	52.9	54.7	54.8	38.0	38.6	38.5	42.7	39.0	24.7	25.9	23.7	27.0	24.0
	0.20	74.8	73.5	73.9	70.7	71.1	75.4	75.0	79.1	76.9	76.4	57.0	58.5	55.0	53.3	52.4	37.2	39.3	38.6	38.5	38.8	24.0	24.9	25.9	24.5	25.9

Table 5.3: Probability to escape the 5/3 Ariel-Umbriel MMR (P_e) for a mesh of 625 initial (e_1, e_2, I_1, I_2). Each set encompass a total 1 000 runs equally distributed over the resonance angle σ (Eq. (3.32)).
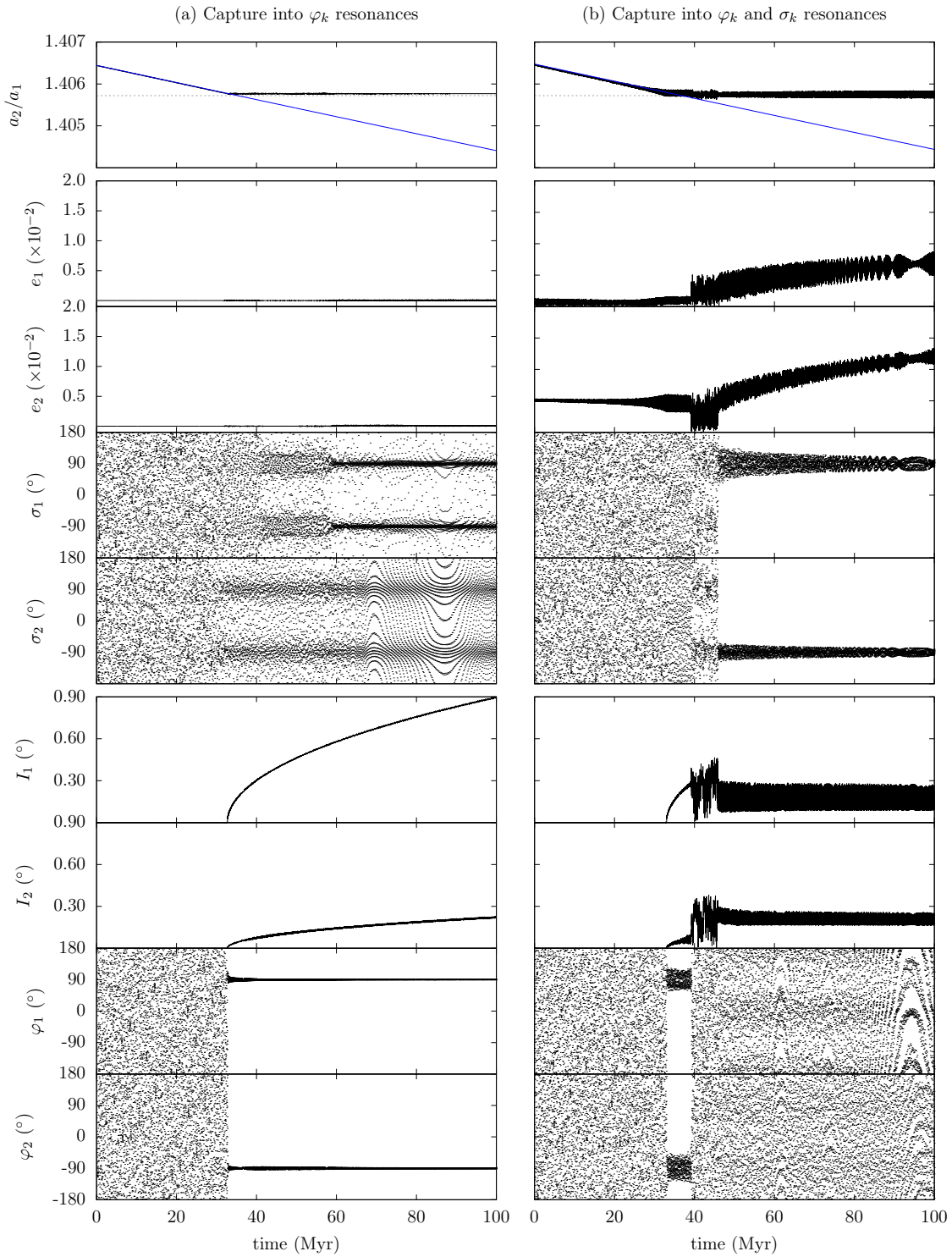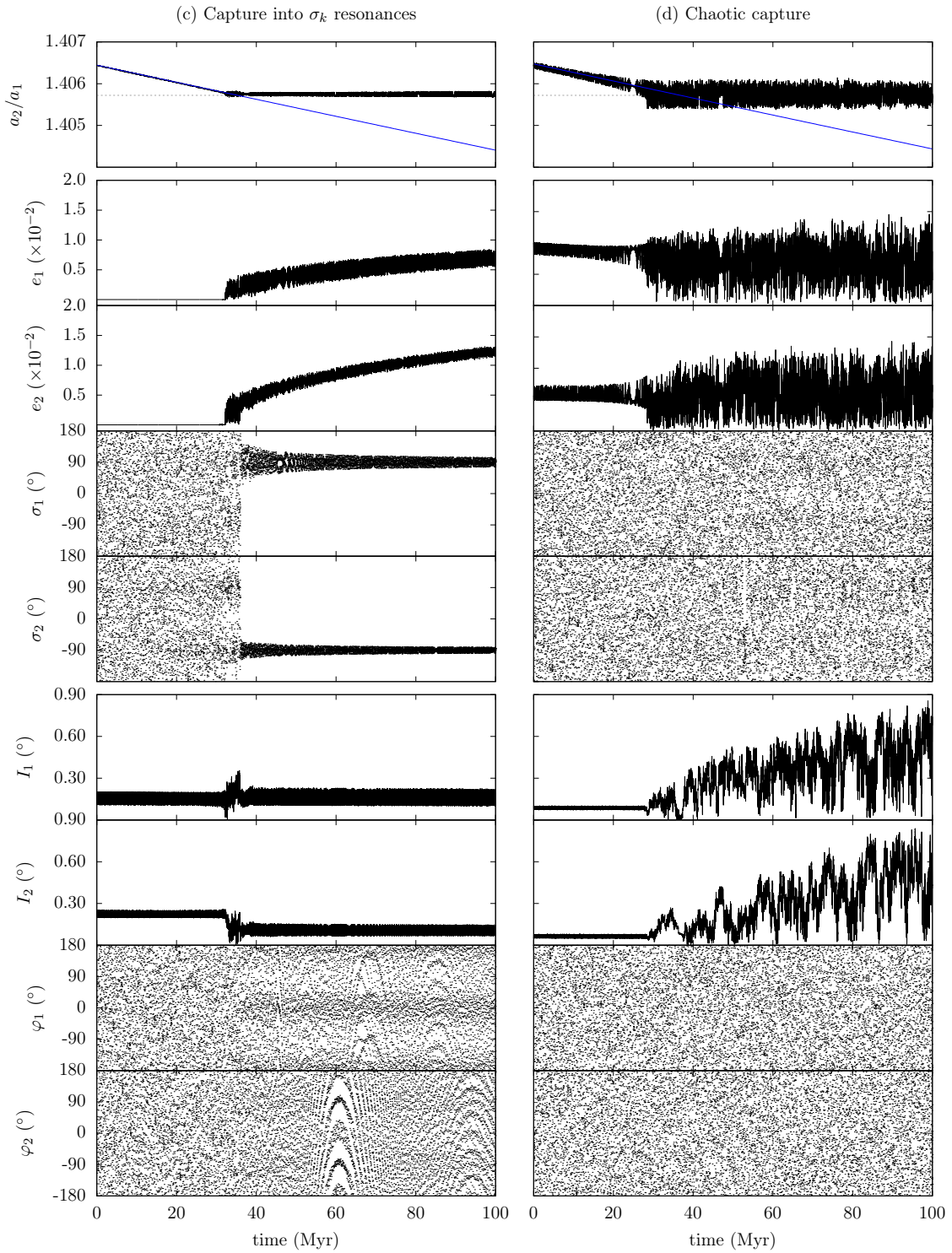
Figure 5.8: Two examples of a system crossing the 5/3 Ariel-Umbriel MMR with the secular model and initial: (a) $e_1 = e_2 = 10^{-5}$ and $I_1 = I_2 = 0.001°$; (b) $e_1 = 10^{-5}$, $e_2 = 5.0 \times 10^{-3}$ and $I_1 = I_2 = 0.001°$. (a) represents an example of permanent capture within the resonance arguments σ_1 and σ_2 and (b) represents capture within the resonant arguments σ_1 and σ_2, followed by resonance entrapment within φ_1 and φ_2. From the top to the bottom figures, we show the semi-major axes ratio a_2/a_1; the eccentricities of Ariel and Umbriel, respectively; the resonant arguments σ_1 and σ_2; the inclinations of Ariel and Umbriel, respectively; and the resonance arguments φ_1 and φ_2. The blue line gives the asymptotic evolution predicted by Eq. (4.34), while the dashed line gives the position of the nominal resonance (Eq. (5.1)).

Figure 5.9: Two examples of a system crossing the 5/3 Ariel-Umbriel MMR with the secular model and initial: (c) $e_1 = e_2 = 10^{-5}$ and $I_1 = I_2 = 0.2°$; (d) $e_1 = 10^{-2}$, $e_2 = 5.0 \times 10^{-3}$, $I_1 = 0.1°$, and $I_2 = 0.05°$. (c) represents an example of permanent capture within the resonance arguments σ_1 and σ_2 and (d) represents permanent chaotic capture. From the top to the bottom figures, we show the semi-major axes ratio a_2/a_1; the eccentricities of Ariel and Umbriel, respectively; the resonant arguments σ_1 and σ_2; the inclinations of Ariel and Umbriel, respectively; and the resonant arguments φ_1 and φ_2. The blue line gives the asymptotic evolution predicted by Eq. (4.34), while the dashed line gives the position of the nominal resonance (Eq. (5.1)).

Figs. 5.8 and 5.9c, the vast majority of the captured simulations evolve chaotically, as exemplified in Fig. 5.9d, with initial $e_1 = 10^{-2}$, $e_2 = 5.0 \times 10^{-3}$, $I_1 = 0.10°$, and $I_2 = 0.005°$. Within this regime, the resonant arguments are constantly switching between the resonant branches (Sect.3.7), and no explicit libration around $\pm 90°$ is observed.

Finally, in Fig. 5.10, we show two examples of non long term capture inside the 5/3 Ariel-Umbriel MMR. Fig. 5.10e provides an example of a simulation that, after being captured, break the resonance after a short period of time, that is, in less than 10 Myr. During the resonance entrapment, both eccentricities and inclinations evolve in the chaotic region, with the inclinations growing on average. In this case, the system leaves the resonance with a high I_1, but with an I_2 similar to the currently observed. Furthermore, after the resonance is broken, the eccentricity of Ariel is quickly damped, while the eccentricity of Umbriel and the inclinations of both satellites remain constant on average.

In Fig. 5.10f, the resonance is shortly skipped. The eccentricity of Umbriel grows as the commensurability is approached, and skip the resonance with a higher value than the initial one. After the resonance passage, the eccentricity of Ariel decreases, together with the inclination of Umbriel. Owing to the topology of the 5/3 MMR (Fig. 3.1), the inclination of Ariel, I_1, initially small, increases slightly as it approaches the nominal resonance ($\delta = 0$). However, after the resonance passage, I_1 quickly returns close to its initial value. In both cases, capture and skip, after the resonance is crossed, the system returns to the predicted asymptotic evolution.

From the analysis of Table 5.3, we observe that for initial eccentricities smaller than 5.0×10^{-3}, long term capture is certain, independently of the choice of the initial inclinations. Actually, this very reduced dependency on the initial inclinations is observed through the whole mesh of initial conditions. That is, for the same pair of initial eccentricities (e_1, e_2), the escape probability is not very sensitive to changes in the initial pair of inclinations (I_1, I_2). This result opposes to the conclusion obtained studying the circular case (Sect. 5.1), where we observed that the initial inclination of Umbriel, I_2, was very important for the outcome of the resonance passage.

For a better analysis of the impact of the eccentricities on the escape probability of the 5/3 MMR, we can condense Table 5.3 by, for each initial pair of (e_1, e_2), add the P_e of the 25 combinations of initial pairs (I_1, I_2) (Table 5.4).

e_1 \ e_2	1.0×10^{-5}	5.0×10^{-3}	1.0×10^{-2}	1.5×10^{-2}	2.0×10^{-2}
1.0×10^{-5}	0.0	0.0	5.1	14.3	14.7
5.0×10^{-3}	0.0	0.1	11.2	15.4	12.5
1.0×10^{-2}	17.4	31.1	33.7	23.9	13.8
1.5×10^{-2}	59.9	64.9	48.3	28.2	17.7
2.0×10^{-2}	75.9	78.8	51.7	38.5	25.2

Table 5.4: Escape probabilities (P_e) of the 5/3 Ariel-Umbriel MMR for a mesh of 25 initial pairs of (e_1, e_2), combining all sets of initial inclination pairs (I_1, I_2), computed from Table 5.3.

Comparing Table 5.4 with the escape and skip probabilities from the planar approximation (Table 5.2), we notice that there is a good agreement between the two results. As for the planar approximation (Sect. 5.2), the capture probability is more sensitive to variations in e_1 than in e_2. Furthermore, the capture probability reaches a maximum for high values of e_1 and $e_2 = 5.0 \times 10^{-3}$. Beyond these eccentricity values, the capture probability decreases slightly with e_2, when compared with the same e_1 value. Yet, it is noticeable that, by combining the effects of the inclination and eccentricity, the probability of escape for $e_1 \leq 5.0 \times 10^{-3}$ and $e_2 > 10^{-2}$ becomes non-negligible, whereas for the planar approximation (Sect. 5.2), capture was observed in almost 100% of the simulations for $e_1 \leq 5.0 \times 10^{-3}$ (Table 5.2). Still, the initial eccentricities dominate the outcome of the capture probability of the 5/3 Ariel-Umbriel MMR.
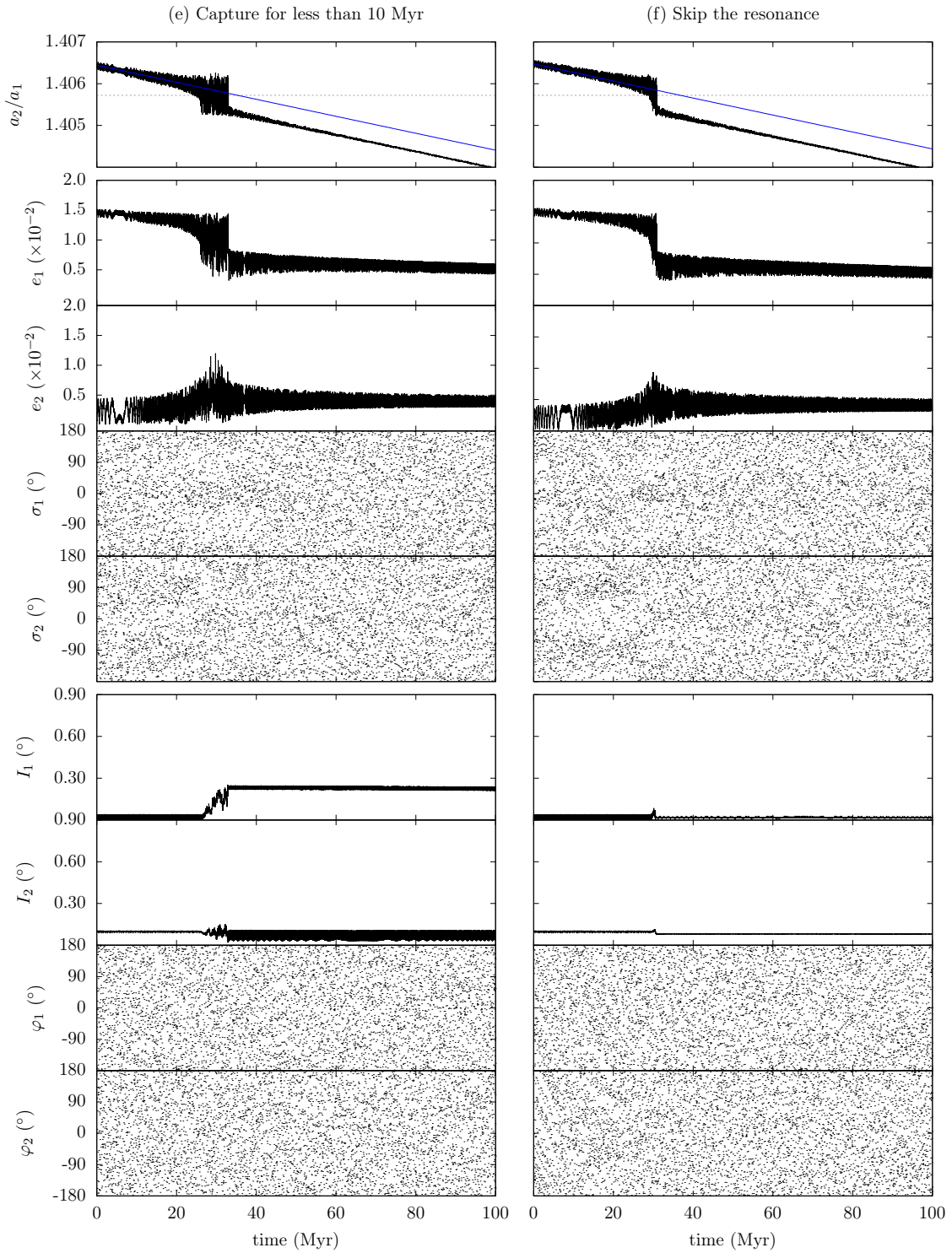
Figure 5.10: Two examples of a system crossing the 5/3 Ariel-Umbriel MMR with the secular model and initial $e_1 = 1.5 \times 10^{-2}$, $e_2 = 10^{-5}$, $I_1 = 0.001°$, and $I_2 = 0.10°$. (e) represents a system that is initially captured, but escapes the MMR in less than 10 Myr and (f) represents a system that evades resonant entrapment. From the top to the bottom figures, we show the semi-major axes ratio a_2/a_1; the eccentricities of Ariel and Umbriel, respectively; the resonant arguments σ_1 and σ_2; the inclinations of Ariel and Umbriel, respectively; and the resonant arguments φ_1 and φ_2. The blue line gives the asymptotic evolution predicted by Eq. (4.34), while the dashed line gives the position of the nominal resonance (Eq. (5.1)).

5.3.3   Final orbital elements

To achieve the current orbital configuration of Ariel and Umbriel after the passage through the 5/3 resonance, we must not only be able to evade this the resonance, but also to replicate the current eccentricities and inclinations of the system. To analyse how the resonance crossing impacts the eccentricities and inclinations of Ariel and Umbriel, we created plots depicting the final distributions of the eccentricities (Fig. 5.11a) and inclinations (Fig. 5.11b) for the 170 430 simulations that were not captured in resonance beyond 10 Myr. Each pair of initial eccentricities and inclinations was assigned a distinct colour. Consequently, in Fig. 5.11a, each colour represents the total of simulations with the same initial values (e_1, e_2), and in Fig. 5.11b, each colour represents the total of simulations with the same initial values (I_1, I_2).

We observe that the final eccentricities are disposed along one line, while the inclinations cluster around some final values. We also observe that both distributions of final eccentricities and inclinations are constrained within a cone[2], whose vertex is located at the origin of the distribution, that is, at $(e_1, e_2) = (0, 0)$ and $(I_1, I_2) = (0°, 0°)$, and widens as the values of eccentricity and inclination increase. However, the underlying reason for this constraint on eccentricity and inclination values is still uncertain, and additional studies must be conducted to determine its origin.

A closer look at the region in the vicinity of the currently observed inclinations (Fig. 5.12), shows a pattern relation between the initial inclinations and the distribution of the final inclinations, where each pair of initial (I_1, I_2) (represented using the same colours used in Fig. 5.11b) clusters around a mean value. In Fig. 5.12 we superimposed straight dashed lines, where, when following a particular line, the clusters of points along that same line represent the same initial inclination, $I_{k,0}$.

For near zero initial inclinations ($I_{k,0} = 0.001°$), the final inclination trend line remains close to the boundary of the distribution. However, by increasing the initial $I_{k,0} \geq 0.05°$, the trend line detaches from the boundary and form an equally spaced, well-defined grid, correlating the initial and mean final inclinations distributions. This grid is approximately described by

$$\begin{bmatrix} \langle I_1 \rangle \\ \langle I_2 \rangle \end{bmatrix} \approx \begin{bmatrix} 0.8112 & 0.0448 \\ 0.3292 & 0.7802 \end{bmatrix} \begin{bmatrix} I_{1,0} \\ I_{2,0} \end{bmatrix}. \tag{5.15}$$

The solutions from Eq. (5.15) must be considered with caution, since they are only valid if two conditions are met: the initial inclinations must be $I_{k,0} \geq 0.05°$; and the final mean inclinations ($\langle I_1 \rangle, \langle I_2 \rangle$) must fall within the boundary cone. Indeed, the solutions of Eq. (5.15) that lay outside the permitted region, appear to shift inward, moving to the nearest position inside the boundary cone. This can be seen, for instance, for the dark green cluster of points located around $(0.04°, 0.15°)$, which, according to Eq. (5.15), should be situated outside the allowed cone region at $(0.03°, 0.15°)$.

The damping timescale of the inclinations is several orders of magnitude larger than the age of the satellite system (Sect. 2.4.3). Thus, the current inclinations of Ariel and Umbriel most likely remained unchanged since the 5/3 MMR crossing. By inverting Eq. (5.15), we estimate that, in order to obtain the current observed inclination of ($\langle I_1 \rangle, \langle I_2 \rangle$) = $(0.0167°, 0.0796°)$ (Table 1.2), the system should have an initial inclination of $(I_{1,0}, I_{2,0}) = (0.036°, 0.082°)$ prior to the resonant encounter. Also, the current inclinations of Ariel and Umbriel lay slightly inside the boundary cone (see Fig. 5.12). Therefore, in addition to the prediction from Eq. (5.15), the current inclinations can also be achieved by taking the initial I_2 obtained by Eq. (5.15), and a small initial I_1, i.e., $(I_{1,0}, I_{2,0}) = (0.001°, 0.082°)$.

To investigate whether these two sets of initial inclinations can effectively replicate the present inclinations of Ariel and Umbriel, we employed the same methodology used for the circular, planar, and eccentric-inclined statistics. We fixed the initial (I_1, I_2), and explored a mesh of initial eccentricities ranging between 10^{-5} and 2.0×10^{-2}, with a step size of 5.0×10^{-3}. For each set of initial (e_1, e_2, I_1, I_2), we ran 1 000 simulations for 100 Myr, equally distributed over the resonance angle σ. As carried so far, we evaluated for each run if the resonance was escaped in less than 10 Myr or if it was captured.

---

[2]Although in reality the geometric shape corresponds to an hyperbolic conic section crossing the vertex of the cone, for simplicity we refer to it as a cone.
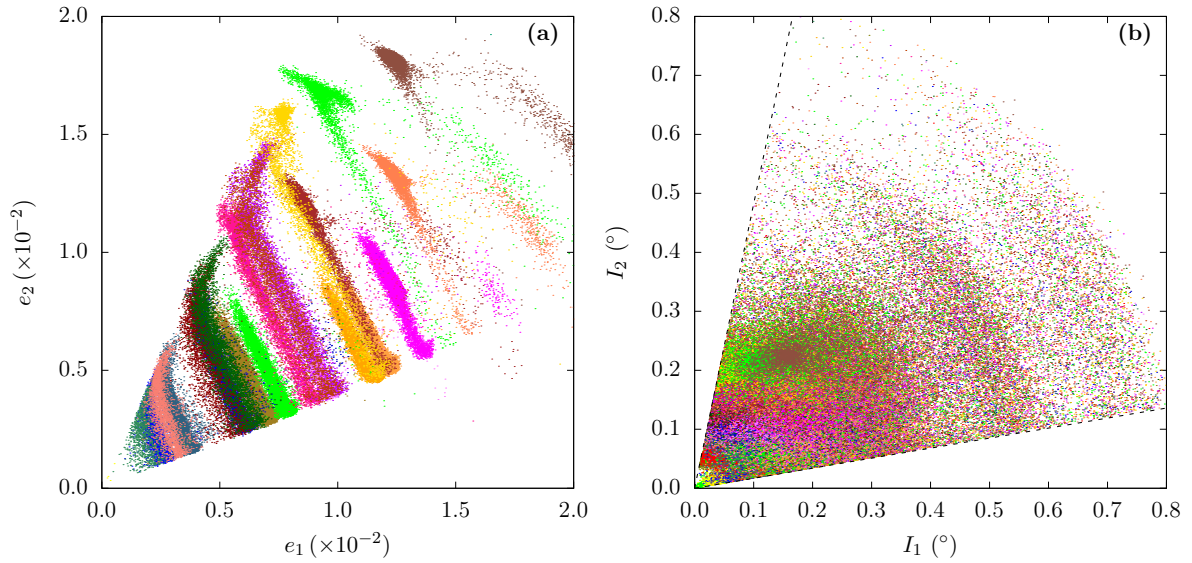
Figure 5.11: Distribution of the final eccentricities (a) and inclinations (b) after the 5/3 Ariel-Umbriel MMR passage. Both figures encompass 170 430 simulations that were not captured, where different colours represent different pairs of initial (e_1, e_2) or (I_1, I_2). The black dashed lines at (b) are the boundaries of the distribution of final inclinations, given by $I_2 = 0.170 \, I_1$ and $I_2 = 4.817 \, I_1$.
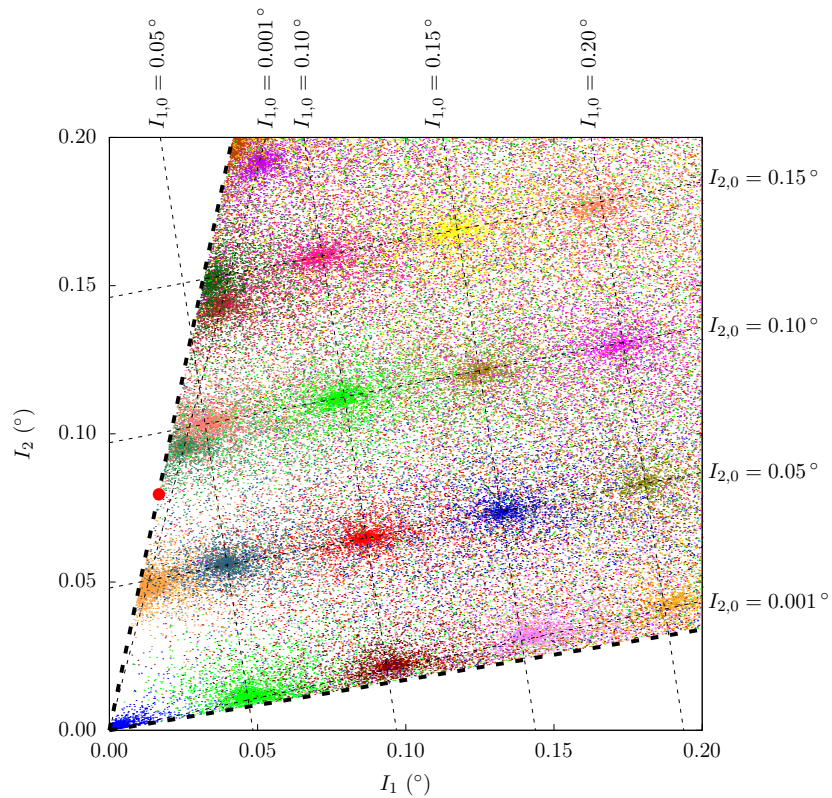

Figure 5.12: Zoom of distribution of the final inclinations after the 5/3 Ariel-Umbriel MMR passage. Different colours represent different pairs of initial conditions (I_1, I_2). The thick dashed lines are the boundaries of the distribution of final inclinations. The thin dashed lines represent regions with the same initial inclinations. The near horizontal lines correspond to regions with the same initial I_1, and the near vertical lines correspond to regions with the same initial I_2. The red dot mark the current mean inclinations of Ariel and Umbriel.

In Fig. 5.13, we show the histograms with the final inclinations of the two pairs of initial inclinations, distributed over 51 classes ranging between 0.0° and 0.3°, with a stepsize of 0.006°. We only considered the final inclinations from the simulations that escaped the MMR, totalizing 5923 simulations for initial $(I_1, I_2) = (0.001°, 0.082°)$, and 6685 simulations for initial $(I_1, I_2) = (0.036°, 0.082°)$. For each pair of initial (I_1, I_2), we combined the results from the 25 combinations of initial (e_1, e_2). Both histograms display very similar distributions, with prominent peaks for the final inclinations of Ariel and Umbriel around a well-defined mean value.
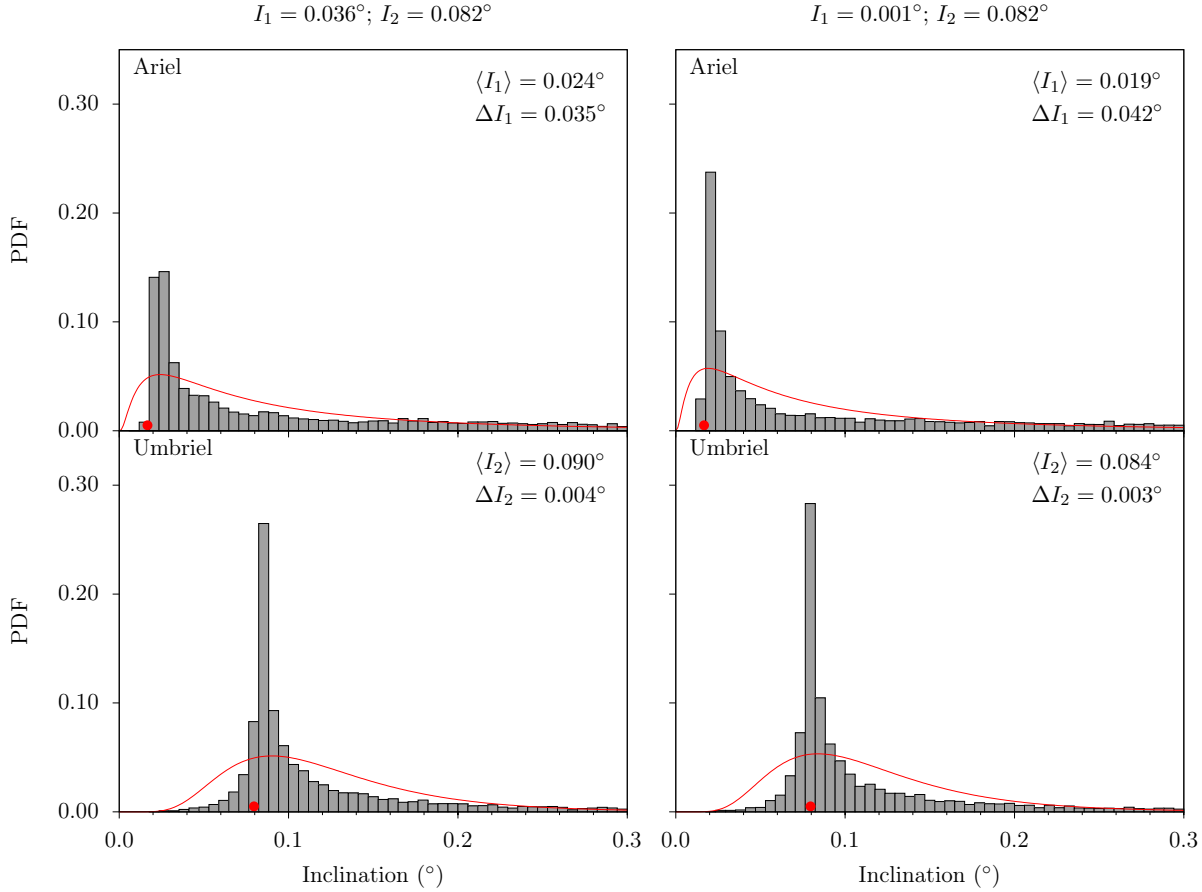
Figure 5.13: Histograms for the final distribution of the inclinations of Ariel (top) and Umbriel (bottom) for two sets of initial inclinations: (a) $(I_1 = 0.036°, I_2 = 0.082°)$; (b) $(I_1 = 0.001°, I_2 = 0.082°)$. We also plotted the best fit Lognormal distribution (Eq. (5.10)) to each histogram (red curve) and the corresponding inclination mode, $\langle I \rangle$, and variance, ΔI. The presently observed inclinations are marked as red dots.

We fitted a Lognormal curve to each histogram (Eq. (5.10)), and calculated the mode (Eq. (5.11)) and the variance (Eq. (5.12)) of each PDF. As anticipated by Eq. (5.15) and the trend line corresponding to $I_1 = 0.001°$, both distributions exhibit peaks in close proximity to the intended current inclinations, $(0.01697°, 0.0796°)$, with $(\langle I_1 \rangle, \langle I_2 \rangle) = (0.024°, 0.090°) \pm (0.035°, 0.004°)$ for the initial conditions extracted solely from Eq. (5.15), and $(\langle I_1 \rangle, \langle I_2 \rangle) = (0.019°, 0.084°) \pm (0.042°, 0.003°)$ for the initial conditions obtained from the Eq. (5.15) and the trend line of initial $I_1 = 0.01°$.

Finally, we determined the escape probability for each pair of initial (e_1, e_2), for both sets of initial inclinations (Table 5.5). The results obtained for both sets are very similar. Also, in accordance with the results from Table 5.4, for $e_k \leq 0.05$, resonance capture always occurs. The best statistics for the system to avoid resonance capture, are obtained when $e_1 \geq 0.015$ and $e_k \leq 0.1$, where $P_e > 50\%$.

e_1 \ e_2	10^{-5}	0.005	0.010	0.015	0.020
		$I_1 = 0.001°; I_2 = 0.082°$			
10^{-5}	0.0	0.0	7.3	12.4	11.4
0.005	0.0	0.0	13.5	14.6	9.5
0.010	33.1	43.3	31.6	19.3	8.3
0.015	56.5	67.4	37.7	20.9	16.4
0.020	51.1	58.9	38.8	28.9	18.7

e_1 \ e_2	10^{-5}	0.005	0.010	0.015	0.020
		$I_1 = 0.036°; I_2 = 0.082°$			
10^{-5}	0.0	0.0	7.4	15.3	11.2
0.005	0.0	0.0	15.5	14.3	10.8
0.010	32.5	42.2	35.7	15.1	10.3
0.015	57.0	61.0	35.7	24.7	14.5
0.020	51.2	59.5	43.7	30.8	14.3

Table 5.5: Escape probabilities of the 5/3 Ariel-Umbriel MMR (P_e) for a mesh of 25 initial pairs of (e_1, e_2). At the left table, P_e for initial (I_1, I_2) = (0.001°, 0.082°) and at the right table P_e for initial (I_1, I_2) = (0.036°, 0.082°).

5.3.4 Monte Carlo method

So far, we have established that the initial eccentricities and inclinations have distinct roles in shaping the outcome of the resonance passage. By employing a discrete distribution of eccentricities and inclinations, we have been able to calculate the capture probability for each set of initial conditions. Moreover, we managed to retrieve two sets of initial conditions which are likely able to reproduce the current eccentricities and inclinations of the system. However, the discrete nature of the distribution may conceal some of the initial conditions that can also reproduce the current configuration of the system. To ensure that all potential combinations of initial conditions are thoroughly examined, we employ the Monte Carlo method to encompass the entire range of initial combinations.

To ensure statistical significant meaning, we conducted one million simulations in which, for each run, we randomly selected an eccentricity within the range of 0 and 0.02, a random inclination within the range of 0 and 0.2°, and random σ_k and φ_k. The initial semi-major axes were the same used for the discrete distribution (Eq. (5.13)). In each simulation, the initial ω_0 was adjusted using Eq. (5.5), while conserving Σ (Eq. (5.3)). Subsequently, for each simulation, we assessed whether the system becomes captured in the resonance, escapes within 10 Myr, or skips the resonance. Overall, we find that 29.5% of the simulations successfully avoided capture.

We first analysed the distribution of the initial eccentricities and inclinations that avoided captured into resonance. In Fig. 5.14, we divided the range of initial eccentricities (0.00, 0.02) and initial inclinations (0.00°, 0.2°) into a grid of 50×50 equally spaced intervals, and evaluated the probability of escape (P_e) for each bin. This provides a more in-depth examination of the escape probability distribution under various initial conditions. Rather than relying on a fixed discrete set of initial conditions, we can now analyse a more continuous dataset, and pinpoint the values where behavioural changes occur in the initial conditions.

From the analysis of the eccentricity distribution (Fig. 5.14a), there are two distinct features that stand out: for initial $\sqrt{e_1^2 + e_2^2} < 0.007$, all simulations were captured into resonance ($P_e = 0$); there is a clear bias for Ariel's high initial eccentricities, where, for $e_1 < 0.01$ and $e_2 > 0.01$, the escape probability is around $\sim 30\%$, whereas for the inverse case, that is, for $e_1 > 0.01$ and $e_2 < 0.01$, the probability of escape reaches $\sim 80\%$. Concerning the initial inclinations (Fig. 5.14b), the distribution of points exhibited an uniform spread across the phase space, devoid of any discernible trends, with escapes probabilities around $\sim 35\%$.

In Figs. 5.15a and 5.15b, we plotted the distribution of the final eccentricities and inclinations, respectively. We observe a similar distribution as the one in Fig. 5.11. However, now there is an even spread of the inclinations over the phase-space. This allow us to confirm the confinement of the final inclinations within the same cone described for the discrete distribution. Furthermore, we observe a similar confinement for the final eccentricities, which was not very clear in the discrete distribution. It
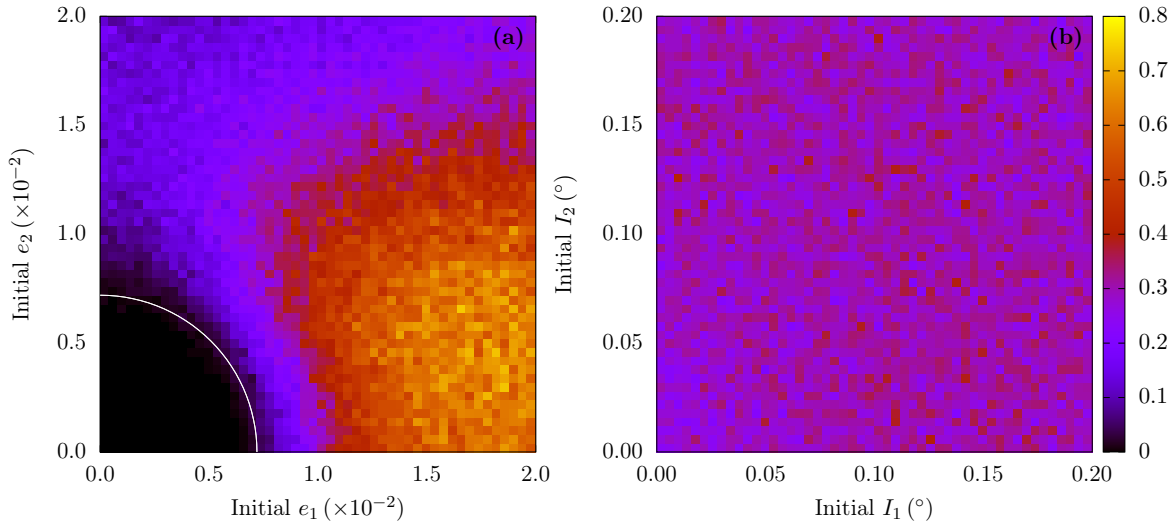
Figure 5.14: Probability of escape of the 5/3 MMR between Ariel and Umbriel for a grid of 50×50 intervals, equally spaced between: (a) 0 and 0.02 for the initial eccentricities; (b) 0 and 0.2° for the initial inclinations. We also plotted a white circle, corresponding to $\sqrt{e_1^2 + e_2^2} = 0.0072$.

is noticeable that there is a more dense concentration of results at the lower edge of the confinement cone, that is, for higher final e_1 and lower final e_2. In addition, there is a clear void of results for final eccentricities below 0.001. Both observations are perfectly related with the results shown in Fig. 5.14. The impossibility of escaping the resonance with low eccentricities means that the initial eccentricity must be high. Therefore, it is more challenging to obtain near zero eccentricities when the system escapes the resonance. Similarly, the clustering of points in the region where $e_1 > e_2$ can be attributed to the higher probability of escape associated with higher eccentricities of Ariel ($e_1 > 0.01$) combined with lower inclinations of Umbriel ($e_2 < 0.015$).

From the distribution of the final inclinations, we can easily identify the simulations that closely match the presently observed I_1 and I_2 (orange dot in Fig. 5.15b). For that, we established a circular region around the current (I_1, I_2) point, with a radius equivalent to 10% of the smallest of the two current inclinations, namely, I_1. These points were coloured as red in Fig. 5.15.

We observe that the final eccentricities of the selected points are scattered across the confinement cone (Fig. 5.15a), lacking any noticeable pattern that influences the resonance passage's outcome. As for the distribution of the initial eccentricities (Fig. 5.15c), we observe that the selected points are evenly distributed over the interval where $e_1 > 0.005$. In contrast, the initial inclinations of the selected points (Fig. 5.15d) are well constrained within the interval $(0.01°, 0.05°)$ for I_1, and $(0.06°, 0.09°)$ for I_2.

The results of the Monte Carlo method not only validate the observations made by the discrete distribution of initial conditions, but also provide more precise constraints on the necessary initial conditions to replicate the current architecture of Ariel and Umbriel. In particular, they show that the initial inclinations have a minimal impact on the likelihood of the resonance capture. The pivotal factor are the initial eccentricities. For low initial eccentricities, capture in the 5/3 MMR is certain. However, we have now determined that a combination of $\sqrt{e_1^2 + e_2^2} > 0.007$ is required to get a measurable number of simulations that escape the resonance. This result was already predicted by the simplified one degree-of-freedom model, used to infer analytically the capture probability (Sect. 4.5). Furthermore, e_1 plays a predominant role for the capture probability statistics, with $e_1 > 0.01$ favouring resonance escape. In order to achieve the current inclinations of the satellites, the initial inclinations must be $0.01° < I_1 < 0.05°$ and $0.06° < I_2 < 0.09°$. Finally, the simulations that reproduce the current inclinations of the satellites leave the resonance with $e_1 > 0.005$. The low eccentricity damping timescale of Ariel quickly erodes

e_1, and places the eccentricity close the current ~ 0.001 value. As for e_2, the much longer damping timescale when compared with the one from Ariel, leads to a smaller decrease in e_2, possibly explaining the current larger eccentricity of Umbriel ($e_2 \approx 0.004$).
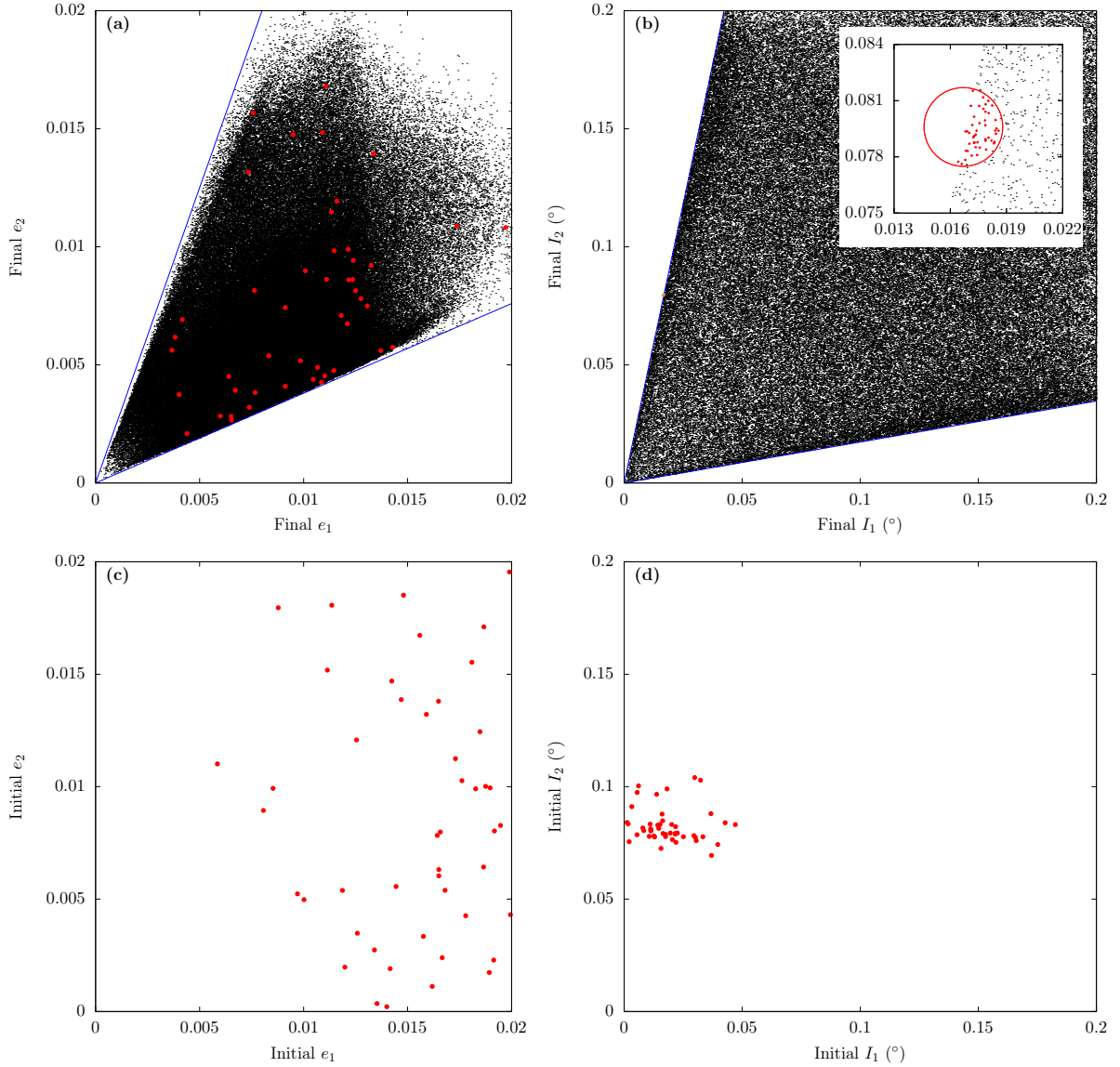

Figure 5.15: Distribution of the final eccentricities (a) and inclinations (b) after the 5/3 Ariel-Umbriel MMR passage. The figures encompass 295 953 runs with random initial (e_1, e_2, I_1, I_2) that avoid resonance capture. From (b), we selected the points that lay inside a circle centred at the current inclinations of Ariel and Umbriel and a radius with 10% of I_1. The selected points were coloured in red, and their corresponding initial eccentricities and inclinations are plotted in (c) and (d).

5.4   N-body simulations

The results from the previous sections were obtained using a two-satellite secular model. In this section, we attempt to validate those results by adopting a more complete and general model, namely, by using the full N-body model described in Chap. 2. For that purpose, we numerically integrate the Eqs. (2.8), (2.9), (2.27), (2.37), and (2.39).

5.4.1 Two-satellite simulations

We first compare the results obtained with the secular model with the full three-body problem (Uranus and two satellites). This allow us to determine whether the secular model provides a good description of the system, or if the high-frequency terms, which were averaged over one orbital revolution, introduce some unexpected features in the long term evolution of the system.

As for the secular model numerical integrations (Sects. 5.1, 5.2, and 5.3), we integrated a system with Ariel and Umbriel orbiting a central massive planet, Uranus, with the physical properties given in Tables 1.1 and 1.2. The initial semi-major axes were obtained by Eq. (4.34), with a_1 being slightly decreased to move the system away from the nominal resonance, leading to $a_1/R_0 = 7.3868$ and $a_2/R_0 = 10.3891$ (Eq. (5.13)). The tidal parameters also have the same values as in the eccentric-inclined secular study (Sect. 5.3), with $Q_U = 8000$ and $Q_S = 500$. In the circular approximation (Sect. 5.1), we saw that the initial inclination of Umbriel has a stronger impact to the capture probability in the 5/3 MMR than the inclination of Ariel. In the planar approximation (Sect.5.2), we observed that Ariel's initial eccentricity is more important for the capture probability. Furthermore, from the eccentric-inclined study (Sect. 5.3), when we combine the effects from both eccentricities and inclinations, the inclinations no longer seem to impact significantly the capture probability, which is mostly affected by the initial e_1. Thus, to verify if the low impact of the inclinations remains for the three-body model, we choose to fix the initial $I_1 = 0.001°$, and vary I_2 between $0.001°$ and $0.20°$, with a step size of $0.05°$. To confirm the role of e_1 to the capture probability, we fix the initial $e_2 = 10^{-5}$ and vary e_1 between 10^{-5} and 0.02, with a step size of 0.005. This totalizes 25 initial combinations of (e_1, I_2). Finally, the satellites were considered to be synchronous at the beginning of the simulations, and the rotation of Uranus was calculated taking into account the conservation of the total angular momentum of the system (Eq. (5.3) and (5.5)).

The computation time to integrate these initial conditions for the same time spam (100 Myr) with the three-body model is 10^4 longer than with the secular model. Therefore, it is not feasibly to compute 1 000 runs equally distributed over the resonance angle σ for every pair of initial (e_1, I_2). We thus reduced the number of simulations per initial condition by a factor of ten, to 100 runs for each pair, which gives a total number of 2 500 simulations. Then, for each run, we determined again if the system was captured into the 5/3 MMR or evaded the resonance by evaluating the semi-major axes ratio a_2/a_1.

In Table 5.6, we show the probability of escape and skip of the 5/3 Ariel-Umbriel MMR for the 25 pairs of initial (e_1, I_2) obtained with the three-body model (right table) and the secular model (left table)[3]. For $e_1 \leq 0.005$, both models show that capture into resonance is certain, independently of the initial I_2. For $I_2 = 0.10°$, we notice a small increase in the escape probability for the three-body model, when compared with the results from the secular model. For $I_2 \geq 0.15°$, the escape probabilities of the two models agree quite well.

Secular model						Two-satellite model				
e_1 $\diagdown$ I_2	10^{-5}	0.005	0.010	0.015	0.020	e_1 $\diagdown$ I_2	10^{-5}	0.005	0.010	0.015	0.020
0.001°	0	0	22	49	60	0.001°	0	0	37	46	59
0.05°	0	0	21	55	66	0.05°	0	0	37	54	48
0.10°	0	0	19	61	72	0.10°	0	0	27	55	54
0.15°	0	0	18	63	74	0.15°	0	0	16	62	56
0.20°	0	0	20	59	74	0.20°	0	0	36	67	48

Table 5.6: Escape probabilities of the 5/3 Ariel-Umbriel MMR (P_e) for a mesh of 25 initial pairs of (e_1, I_2), with $e_2 = 10^{-5}$ and $I_1 = 0.001°$. In the left table, the escape probabilities were obtained with the secular model (Sect. 5.3), while in the right table, the escape probabilities were obtained with a two-satellite model.

---

[3]The results from the secular model were obtained in Sect. 5.3 and displayed here again for a more convenient comparison between the two sets of results.

The escape probabilities obtained with the two models are in good agreement, despite some small local variations that likely arise from the smaller data set of the three-body model. In particular, we note that the same tendency for the eccentricity of Ariel to dominate the escape probability, with very low impact from the inclination of Umbriel, prevails outside the secular approximation.

From the secular study, we determined that, prior to the resonance encounter, the inclinations should be $(I_1, I_2) \simeq (0.001°, 0.085°)$ in order to replicate the currently observed values. In Fig. 5.16, we show one example of a simulation with the three-body model, where the system skips the 5/3 Ariel-Umbriel MMR. The initial eccentricities were $(e_1, e_2) = (1.5 \times 10^{-2}, 5.0 \times 10^{-3})$. Prior to the commensurability, the average semi-major axes (top figures) follow the asymptotic tidal evolution (blue line), with the eccentricities and inclinations (middle and bottom figures, respectively) librating around a mean value close to the initial ones. As the system approaches the nominal resonance, the amplitude of libration of the eccentricities increases. Then, a quick variation of the semi-major axes shifts the mean motion ratio from the nominal resonance, returning to the asymptotic evolution. Simultaneously, the e_1 and e_2 drop to lower average values, while the amplitudes of I_1 and I_2 decrease. In this example of resonance passage, chaos does not significantly impact the system's evolution. Note that, after resonance passage, both Ariel and Umbriel are left with inclinations close to the current values, as well as the eccentricity of Umbriel (red dot).

Using the pair of initial inclinations $(I_1, I_2) = (0.001°, 0.082°)$ obtained in Sect. 5.3, we integrated 100 simulations evenly distributed across σ for 100 million years. To ensure a low capture probability, we chose $(e_1, e_2) = (1.5 \times 10^{-2}, 5.0 \times 10^{-3})$. With these results, we built an histogram of the final distribution of the eccentricities and inclinations (middle column of Fig. 5.17). For each distribution, we overlaid the Lognormal curve obtained with the secular case (Eq. (5.10)). We observe a good agreement between the distribution obtained with the three-body model and the distribution obtained with the secular model (left column of Fig. 5.17). The eccentricities of Ariel and Umbriel are piled around a mean value, very close to the mean value of the secular model. The distribution of the inclinations display the same diffusion observed for the secular model. The only difference is in the mode of the distribution, which exhibits a less pronounced peak. Nevertheless, the Lognormal curve obtained for the secular model presents a remarkable adjustment to the results obtained with the three-body model.

The agreement observed in this section between the two models demonstrates that the secular model provides a good description of the two-satellite system composed of Ariel and Umbriel and Uranus. Therefore, we conclude that the high-frequency gravitational interaction terms are indeed dominated by the secular terms in the long-term evolution of the system, as expected.

5.4.2 Five-satellite simulations

Up to this point, we isolated the two satellites directly involved in the 5/3 Ariel-Umbriel MMR. However, mutual interactions between the remaining satellites may also influence the architecture of the entire system during the resonance passage (Ćuk et al. 2020). Therefore, as in the previous Sect. 5.4.1, here we adopt again the N-body model (Chap. 2), but now we add Miranda, Titania, and Oberon to the system (five-satellite problem).

The physical properties of the five satellites are given in Table 1.2. The semi-major axes of the satellites at nominal resonances were calculated using Eq. (4.34), assuming that the satellites are synchronous, the orbits are circular and in the equatorial plane of Uranus, and the angular velocity of Uranus corrected (Eq. (5.5)) such that the current total angular momentum of the system,

$$\Sigma = 9.446\,072 \times 10^{-10} \text{ M}_\odot \text{ au}^2 \text{ yr}^{-1}, \tag{5.16}$$

is conserved. The semi-major axis of Ariel was slightly decreased to move the system from the nominal resonance, leading to

$$a_1/R_0 = 5.0794, \quad a_2/R_0 = 7.3868, \quad a_3/R_0 = 10.3891,$$
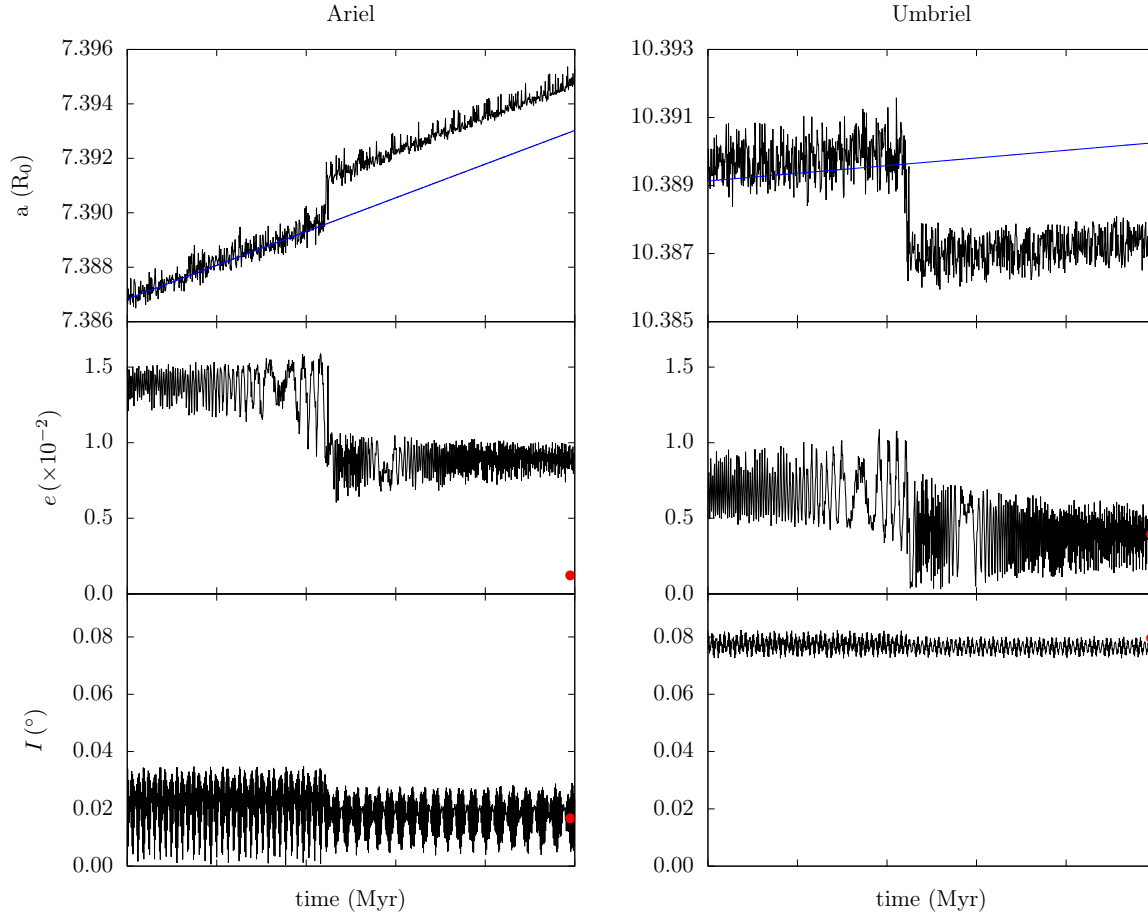$$a_4/R_0 = 10.3892, \quad a_5/R_0 = 22.8239. \tag{5.17}$$

Figure 5.16: Simulation with the three-body model for the passage through the 5/3 MMR between Ariel and Umbriel. At the top, the semi-major axes, at the middle the eccentricities and at the bottom the inclinations. The system evolved from initial $e_1 = 1.5 \times 10^{-2}$, $e_2 = 5.0 \times 10^{-3}$, $I_1 = 0.001°$, and $I_2 = 0.082°$. The asymptotic tidal evolution of the semi-major axis (Eq. (4.34)) is represented as a blue line, and the present mean eccentricities and inclinations (Table 1.2) marked as red dots.

As in the previous two-satellite simulation, we use $Q_U = 8000$ and $Q_S = 500$ (Sects. 5.3 and 5.4.1).

When we increase the number of bodies in the system, the computation time inevitably increases again. As a result, the five-satellite simulations require four times more time for integration compared to the two-satellite system simulations (Sect. 5.4.1). Consequently, we needed to limit the total number of simulations. We start by reproducing the Table 5.6, where we fix $e_2 = 10^{-5}$ and $I_1 = 0.001°$, by integrating 100 simulations equally distributed over σ for each initial pair (e_1, I_2), over 100 Myr. The initial eccentricities and inclinations for Miranda, Titania, and Oberon were kept at the currently observed values (Table 1.2). For each simulation, we verified if the system was captured within the resonance for more than 10 Myr. The results can be found in Table 5.7.

Although for initial $e_1 \leq 0.005$ resonance entrapment is certain, we observe that for $e_1 = 0.01$ the escape probability is lower than when compared with the secular model and the three-body model (Table 5.6). Contrariwise, for higher values of initial e_1, the presence of the five satellites privileges resonance escape. Again, the inclination of Umbriel does not impact the capture probability of the 5/3 MMR.

In another experiment, we integrated the set of 100 simulations equally distributed over σ with the best suited initial eccentricities and inclinations obtained from the eccentric and inclined secular study (Sect.5.3), that is, $e_1 = 1.5 \times 10^{-2}$, $e_2 = 5.0 \times 10^{-3}$, $I_1 = 0.001°$ and $I_1 = 0.082°$. The initial eccentricities and inclinations for Miranda, Titania, and Oberon were kept at the currently observed values (Table 1.2), and the semi-major axis from Eq. (5.17).

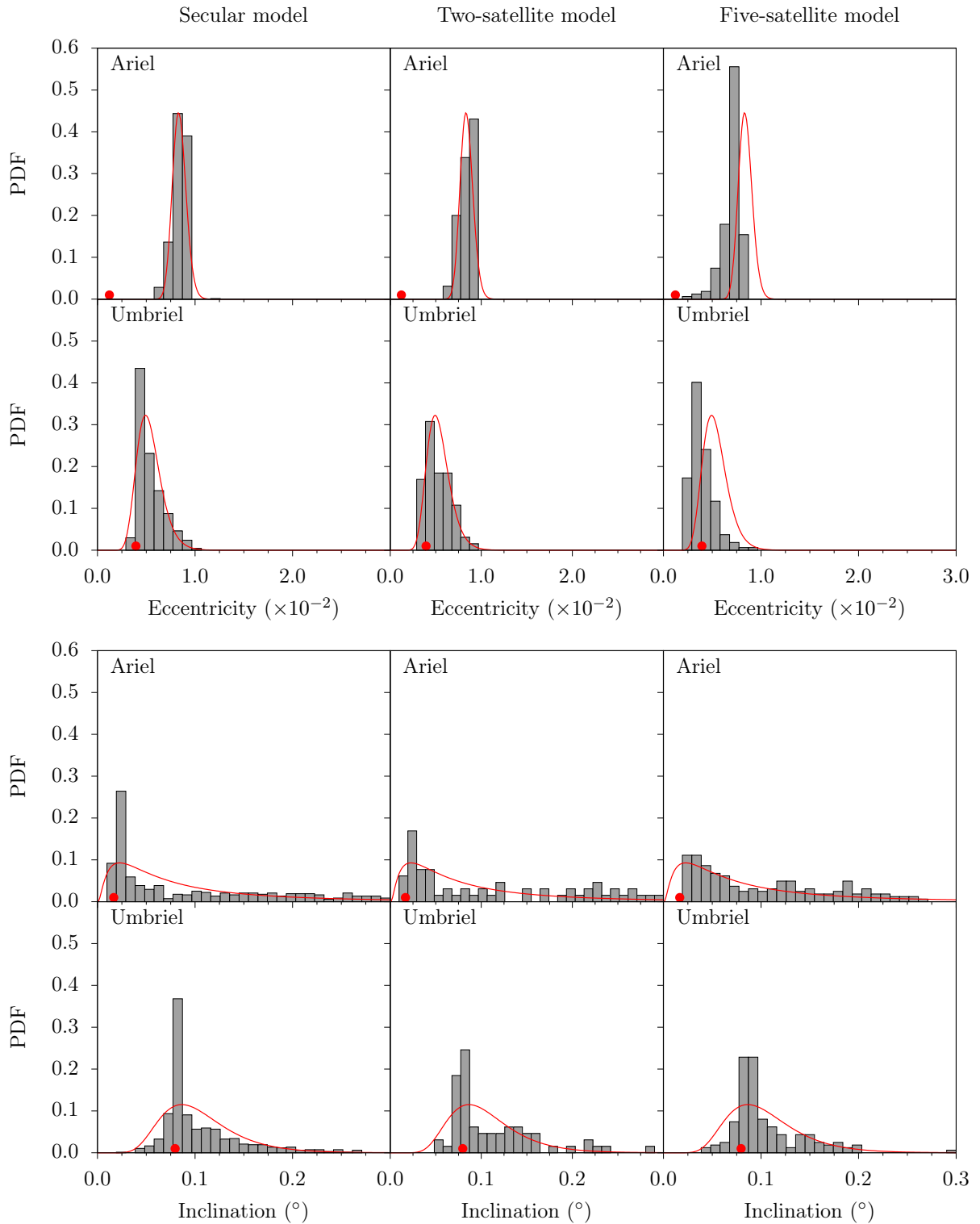In Figs. 5.18, 5.19, and 5.20, we show three examples of the passage through the 5/3 MMR with

Figure 5.17: Histograms for the final distribution of the eccentricities of Ariel (top) and Umbriel (bottom) and the inclinations of Ariel (top) and Umbriel (bottom) for three different models. In the left column we have the secular model; in the middle column the two-satellite model; and the right column the five-satellite model, with initial $e_1 = 1.5 \times 10^{-2}$, $e_2 = 5.0 \times 10^{-3}$, $I_1 = 0.001°$ and $I_2 = 0.082°$. We also plotted the best fit Lognormal distribution (Eq. (5.10)) to the histogram of the secular model (red curve), and overlap this curve to the histograms of the two-satellite problem and five-satellite problem. The presently observed eccentricities and inclinations are marked as red dots.

Five-satellite model					
I_2 \ e_1	10^{-5}	0.005	0.010	0.015	0.020
0.001	0	0	4	62	82
0.05	0	0	13	72	77
0.10	0	0	7	67	85
0.15	0	0	15	70	86
0.20	0	0	10	65	90

Table 5.7: Escape probabilities of the 5/3 Ariel-Umbriel MMR (P_e) for a distribution of 25 initial pairs of (e_1, I_2), with $e_2 = 10^{-5}$ and $I_1 = 0.001°$, with the five-satellite model, where 1 denotes Ariel and 2 denotes Umbriel.

all the regular Uranian moons. In Fig. 5.18, the system is permanently captured in resonance. Prior to the 5/3 Ariel-Umbriel MMR, the semi-major axis of all the satellites (top figures) follow the asymptotic line of tidal evolution (Eq. (4.34)). The eccentricities (middle figures) and inclinations (bottom figures) remain nearly constant on average, oscillating around a mean value close to the initial ones. At $t \approx 15$ Myr, Ariel and Umbriel are captured into the 5/3 MMR. The semi-major axes of Ariel and Umbriel depart from the asymptotic evolution, and the evolution of the eccentricities of all satellites in the system becomes chaotic. The eccentricities of Ariel and Umbriel remain nearly constant on average, but the chaotic regime increases the amplitude of the oscillations. Despite not being directly involved in the resonance, the eccentricity of Miranda is also significantly affected, where, during the resonance entrapment, it increases by a factor of 20. We note that the tidal evolution of the semi-major axes (Eq. (4.34)) has a dependency on the eccentricity and the inclination. If one of these elements reach a critical value, the negative term of the expression becomes dominant (Eq. (4.34)), and the satellite starts to migrate inwards. This can be observed in this example, where, at $t \approx 35$ Myr, the eccentricity of Miranda reaches a critical value of about 0.02, and the semi-major axis undergoes an inflection and starts decreasing. Although in a smaller scale, the eccentricities of the remaining four satellites also grow on average. During the resonance capture, the evolution of the inclinations of Miranda, Ariel, and Umbriel are also chaotic, and, on average, the inclinations of these three innermost satellites grow. However, large oscillations are observed, with moments of overall increase and others of overall decrease. The inclinations of Titania and Oberon do not initially present changes in their evolution. Yet, around $t \approx 30$ Myr they also enter in the chaotic regime.

The excitation of all satellite's orbits when Ariel and Umbriel are captured into the 5/3 MMR was previously reported by Ćuk et al. (2020), with all eccentricities and inclinations increasing to values much higher than the pre-encounter ones. However, the authors begin with Miranda having a near zero inclination and show that the 5/3 MMR could be responsible for Miranda's current 4.4° inclination. We do not entertain this hypothesis and demonstrate that capture in the resonance can reconfigure the whole system, making the current configuration unattainable.

In Fig. 5.19, we shown an example of a simulation that was captured in resonance, and then escaped within 10 Myrs. Prior to the resonance encounter, the system evolves due to tidal interactions between the planet and the satellites. The semi-major axes follow the asymptotic tidal evolution, and the eccentricities and inclinations oscillate around a mean value. Then, at $t \approx 15$ Myr, Ariel and Umbriel becomes trapped in the 5/3 MMR. During resonance entrapment, the semi-major axes of Ariel and Umbriel deviate from the asymptotic evolution, and the evolution of the eccentricities become chaotic. Simultaneously, the eccentricity of Miranda starts to grow steadily on average, and the eccentricities of Titania and Oberon are slightly perturbed, with an increase of the amplitude of oscillation. The inclination of Ariel also grows during the capture, to a value one order of magnitude larger than the currently observed. The inclination of Miranda starts to evolve chaotically, while the inclinations of the remaining satellites do not show a general change of behaviour. After ~ 6 Myr of entrapment, the system escapes the MMR. The semi-major axes of Ariel and Umbriel return to the asymptotic evolution. The eccentricity of Umbriel drops

to a slightly lower level, while the inclination remains nearly unchanged. Ariel leaves the resonance with an eccentricity smaller than the one previous to the MMR encounter, but with a higher inclination. As for Miranda, due to the proximity to Uranus, the large eccentricity acquired during the resonance passage is quickly damped, while the inclination stabilises in a value close to the initial one. Both Titania and Oberon are not much affected by the short entrapment, preserving the initial eccentricities and inclinations.

Finally, in Fig. 5.20, we show an example of a simulation that skips the resonance. Until the resonance encounter, the evolution of the five satellites is identical to the previous cases (Figs. 5.18 and 5.19). However, as the system approaches the nominal resonance, the semi-major axes of Ariel and Umbriel quickly shift, placing the mean-motion ratio below the nominal resonance, and thus avoiding resonance entrapment. Due to the conservation of the total angular momentum, the eccentricity of Ariel quickly drops, while the eccentricity of Miranda grows. The eccentricity of Umbriel, Titania, and Oberon, as well as the inclinations of all the satellites, appear to be unaffected by the resonance crossing. After the resonance passage, tidal effects damp the eccentricities of Miranda and Ariel, and the system evolves to the present configuration.

Note that, in this example, the inclinations of the system subsequently evolve into the presently observed configuration (red dots). This is only achieved if the system avoids resonance entrapment, which requires $e_1 > 0.01$ and $e_2 < 0.015$, and if the inclinations before the resonance encounter were $I_1 > 0.05°$ and $I_2 \approx 0.082°$.

In order to observe the effects of considering the five satellites on the final distribution of eccentricities and inclinations of Ariel and Umbriel, we constructed a histogram with their distributions, at the right column of Fig. 5.17. In each distribution, we overlaid the Lognormal curve obtained for the secular case. Comparing the results with the histograms obtained with the secular (left column) and the two-satellite models (central column), we can observe a very good agreement between the three sets of simulations. This is particularly visible for the distribution of the eccentricities of Ariel and Umbriel, with the final e_1 and e_2 piling around 7.2×10^{-3} and 3.3×10^{-3} respectively. The inclination distribution of Ariel is more diffuse than the previous cases and do not present a clear peak. Nevertheless, the distribution shows a significant number of simulations within the class of the present inclination. The distribution of I_2 for the five-satellite model is also more diffuse than the previous studies. Still, there is a clear peak above the present inclination of Umbriel.

The comparison between the secular, the two-satellite and the five-satellite models shows a good agreement between the results obtained with the three different methods. Therefore, we conclude that the results obtained from the approximated secular model can be extrapolated for the complete, five-satellite case. With initial $e_1 = 1.5 \times 10^{-2}$, $e_2 = 5.0 \times 10^{-3}$, $I_1 = 0.001°$, and $I_2 = 0.082°$ we were able to reproduce the current eccentricities and inclinations of the five major satellites of Uranus (Fig. 5.20). If the 5/3 Ariel-Umbriel MMR is shortly skipped, Titania and Oberon are insensitive to the resonance crossing. As for Miranda, tides quickly erode the acquired eccentricity. To accomplish the high eccentricity of Ariel and inclination of Umbriel, some past dynamical event must have occurred, and excited both values. Since tides are very inefficient on damp the inclination, Umbriel's value can be attributed to the possible passage through the past 3/1 MMR between Miranda and Umbriel (Tittemore and Wisdom 1989). As for the Ariel's eccentricity, the small eccentricity damping timescale (Sect. 5.3.1) requires that the excitation must have occurred nearly until the encounter with the 5/3 MMR.
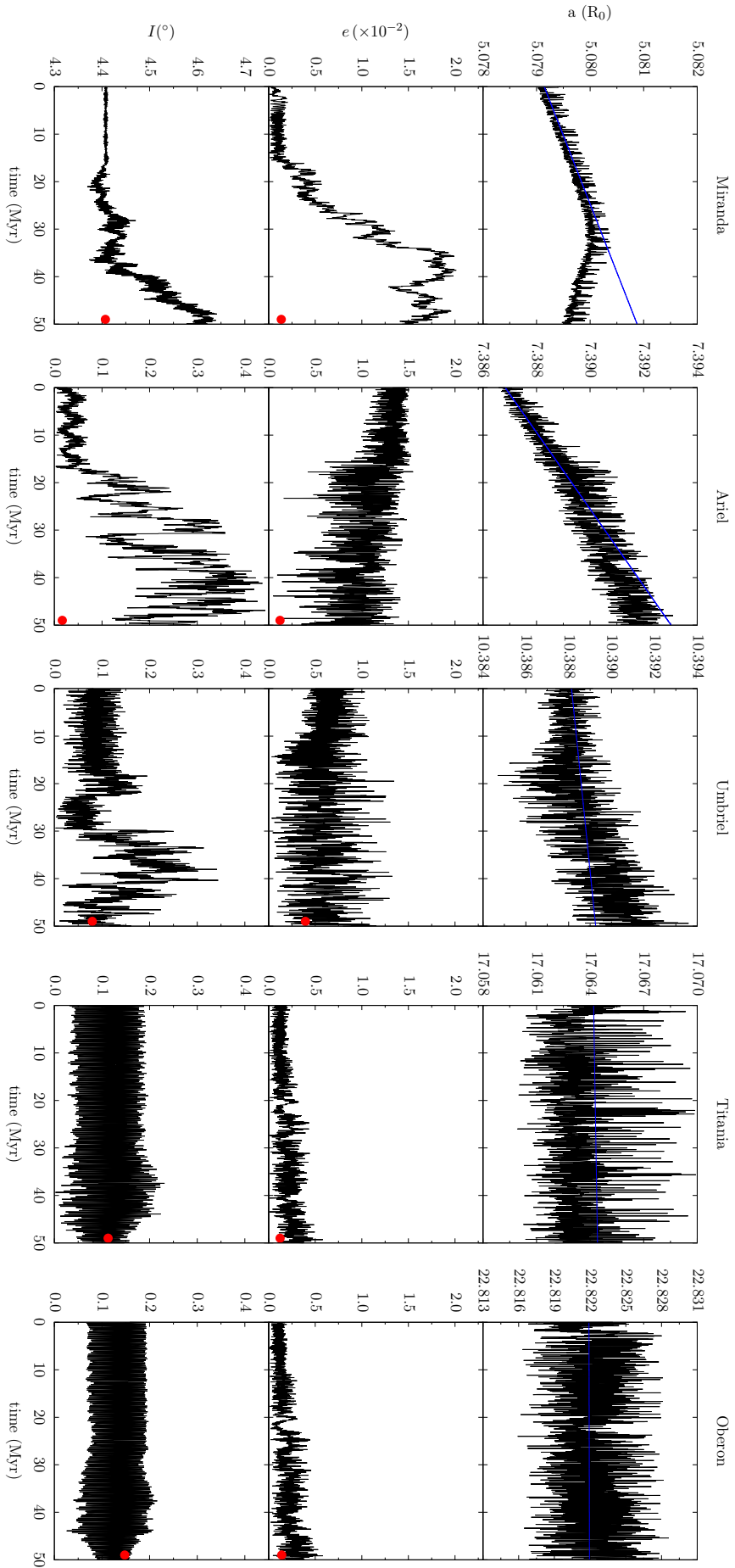
Figure 5.18: Capture in the 5/3 Ariel-Umbriel MMR for the five-satellite system composed by Miranda, Ariel, Umbriel, Titania, and Oberon. The initial eccentricities and inclinations of Ariel and Umbriel are: $e_1 = 1.5 \times 10^{-2}$, $e_2 = 5.0 \times 10^{-3}$, $I_1 = 0.001°$, and $I_2 = 0.082°$, respectively. The initial eccentricities and inclinations of Miranda, Titania, and Oberon correspond to their current mean values (Table 1.2). The blue lines are the the asymptotic tidal evolution of the semi-major axes predicted by Eq. (4.34), and the red dots are the presently observed eccentricities and inclinations.
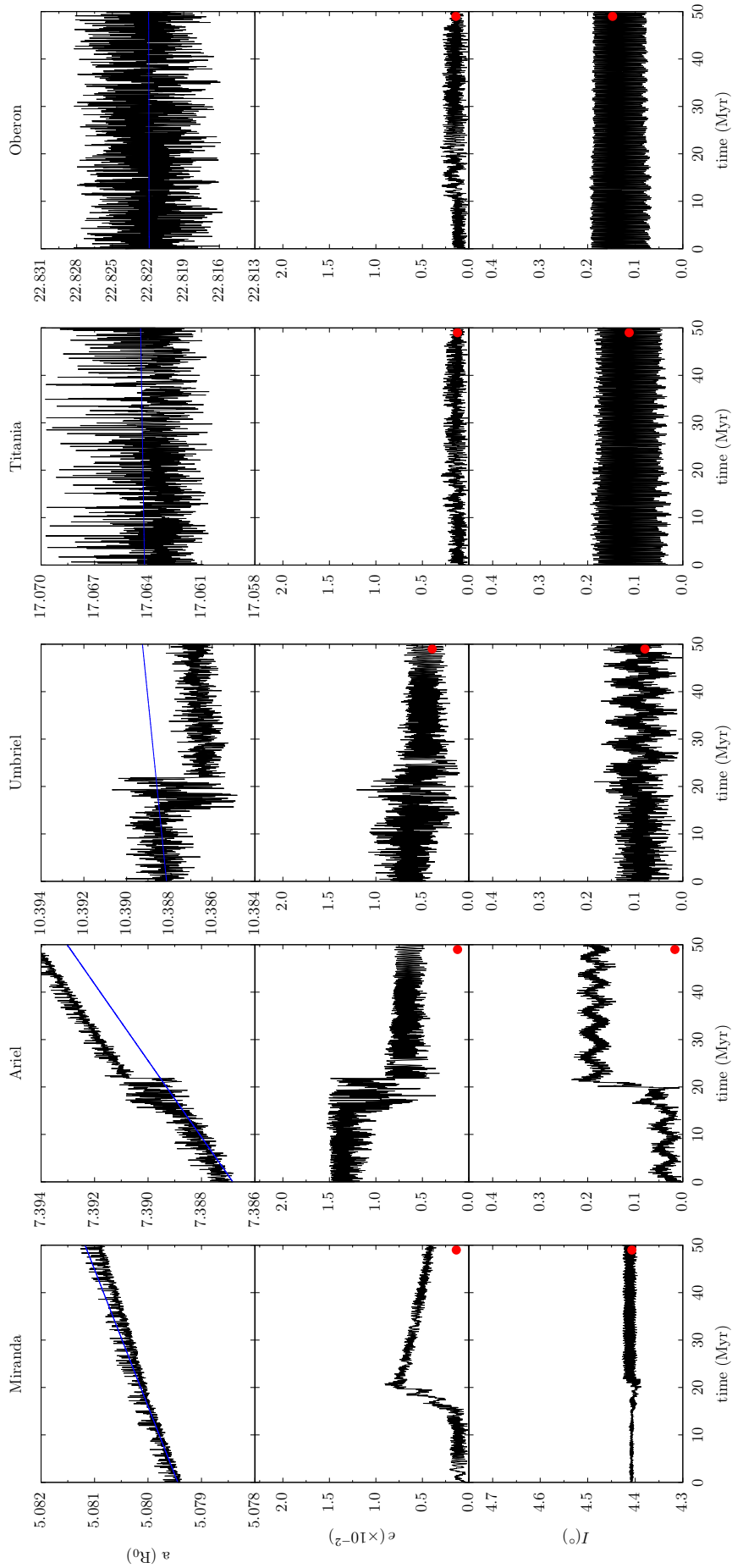
Figure 5.19: Capture in the 5/3 Ariel-Umbriel MMR, followed by escape in less than 10 Myrs for the five-satellite system composed by Miranda, Ariel, Umbriel, Titania, and Oberon. The initial eccentricities and inclinations of Ariel and Umbriel were set to be: $e_1 = 1.5 \times 10^{-2}$, $e_2 = 5.0 \times 10^{-3}$, $I_1 = 0.001°$, and $I_1 = 0.082°$, respectively. The initial eccentricities and inclinations of Miranda, Titania, and Oberon correspond to their current mean values (Table 1.2). The blue lines are the the asymptotic tidal evolution of the semi-major axes, predicted from Eq. (4.34), and the red dots are the presently observed eccentricities and inclinations.

Figure 5.20: Passage through 5/3 Ariel-Umbriel MMR without resonant entrapment for the five-satellite system composed by Miranda, Ariel, Umbriel, Titania, and Oberon. The initial eccentricities and inclinations of Ariel and Umbriel were set to be: $e_1 = 1.5 \times 10^{-2}$, $e_2 = 5.0 \times 10^{-3}$, $I_1 = 0.001°$, and $I_1 = 0.082°$, respectively. The initial eccentricities and inclinations of Miranda, Titania, and Oberon correspond to their current mean values (Table 1.2). The blue lines are the asymptotic tidal evolution of the semi-major axes, predicted from Eq. (4.34), and the red dots are the presently observed eccentricities and inclinations.

Chapter 6

Conclusion

6.1 Overview

In this thesis manuscript, we have studied the dynamical and tidal evolution of the five major Uranian moons, namely, Miranda, Ariel, Umbriel, Titania, and Oberon. The geological traces of global surface melting in Miranda, Ariel, and Titania (Sect. 1.3), the relatively high $\sim 4.4°$ inclination of Miranda (Sect. 1.4), and the fact that the current free eccentricities of the system are higher than expected (Sect. 2.4.4), strongly suggest that the system experienced significant dynamical interactions across its past history.

We initiate our study of the Uranian system by adopting an N-body model that takes into account the tidal evolution of the orbits and the spins of all bodies (Chap. 2). After deriving the equations of motion (Sects. 2.1, 2.2, and 2.3), we estimated the tidal dissipation within Uranus and its satellites (Sect. 2.3.2). We also determined the free and forced orbital elements of the satellites (Sect. 2.4.4), and evaluated the possibility of spin-orbit resonances in the system (Sect. 2.4.5). Subsequently, we conducted numerical simulations of the long-term evolution of the system over a time span of 4.5 Gyr, using the initial semi-major axes values predicted by an asymptotic tidal evolution (Sect. 2.4.6). We observed a series of MMRs crossings, with capture in several cases, that could have shaped the evolution of the system. During the resonance entrapment, the evolution of the semi-major axes deviate from the asymptotic prediction obtained through tidal effects (Eq. (2.68)), causing the final orbits to significantly differ from the presently observed ones.

The inability to reproduce the current architecture of the Uranian system (Table 1.2), prompted us to adopt a *step-by-step* approach, and study each dynamical event individually. The most recent MMR to have occurred in the Uranian system was the 5/3 MMR between Ariel and Umbriel (see Fig. 1.4). Thus, we integrated the system from just after the resonance passage until the present days (Sect. 2.4.7). We did not observe any dynamical mechanism that excite the orbits of the satellites during that time.

The extensive computation time required for the N-body model, makes this model unsuitable for a detailed analysis of the passage through the 5/3 MMR with a large number of simulations. Thus, in Chap. 3, we developed the conservative equations for a secular two-satellite model using a similar approach to Tittemore and Wisdom (1988, 1989, 1990). However, in our model we introduce the spin evolution of the planet and the satellites, and we adopted the total angular momentum of the system as a canonical variable, which is conserved and naturally removes one degree of freedom from the problem. We thus only need to perform one average over a fast angle, instead of the widely used average over two fast angles (e.g. Tittemore and Wisdom 1989; Michtchenko and Ferraz-Mello 2001; Alves et al. 2016). We also introduced a new set of complex rectangular coordinates (Sect. 3.5), that allow us to remove some singularities and reduce by half the number of equations of motion.

Applying the conservative secular equations to the passage through the 5/3 Ariel-Umbriel MMR for the circular approximation (i.e. $e_1 = e_2 = 0$) and for the planar approximation (i.e. $I_1 = I_2 = 0°$), we have shown that, prior to the 5/3 MMR encounter, Ariel and Umbriel are in circulation around an equilibrium point at the origin of the coordinates ($x_k = y_k = 0$). As the system approaches the resonance, this equilibrium becomes unstable, while two other stable symmetrical equilibria appear, corresponding

to libration in resonance. Shortly after, the equilibrium at the origin becomes again stable, corresponding to a new circulation region (see Fig. 3.1). For initial very low eccentricity and inclination values (low energy), the system is thus forced to follow one of the resonant equilibria (capture) (see Fig. 5.1). However, for moderate eccentricities or inclinations (higher energy), the system may encounter the resonance when all the stable equilibrium possibilities are already available and directly go to the circulation region (skip). Alternatively, the system enters in a chaotic regime and can subsequently evade into the circulation (escape) or the libration regions (capture) (see Fig. 5.2). The chaotic nature of the system as a function of the energy is clearly portrayed in a sequence of Poincaré surface sections obtained with the modified Hénon method (Sect. 3.9) and in the stability maps obtained with the frequency analysis method (Sect.3.10).

In Chap. 4, we developed a Hamiltonian extension to include tides based on the constant time-lag model, which provides the tidal evolution for all variables in the problem. This is again an improvement relative to the model of Tittemore and Wisdom (1988, 1989, 1990), where tides are artificially introduced through the variation of the distance to the resonance, using the δ-parameter (Sect. (3.6)), thus neglecting the tidal evolution on the orbits and spins. We then resorted to the simplified single resonance model to estimate the capture probabilities on the 5/3 Ariel-Umbriel MMR, as a function of the individual eccentricities and inclinations of each satellite.

In Chap. 5, we numerically studied in detail the passage through the 5/3 MMR between Ariel and Umbriel. First, we studied the effect of the inclination to the outcome of the resonance crossing, by adopting the circular approximation ($e_1 = e_2 = 0$) (Sect. 5.1). The crossing of the 5/3 MMR is a stochastic process, and so we performed a large number of numerical simulations covering many different combinations for the initial inclinations of Ariel and Umbriel. Then, we revisited the passage through the 5/3 Ariel-Umbriel MMR in the planar approximation ($I_1 = I_2 = 0°$) with our secular model (Sect. 5.2). Again, we conducted an extensive set of numerical simulations encompassing a wide range of different combinations for the initial eccentricities for both Ariel and Umbriel. We then continued our study with the more general case, encompassing the effects of both eccentricity and inclination (Sect. 5.3). Once more, we performed a large number of numerical simulations across a mesh of discrete combinations of initial eccentricities and inclinations of Ariel and Umbriel. The discrete nature of the previous analysis compelled us to adopt a Monte Carlo methodology, and perform one million simulations with random initial eccentricities, inclinations, mean anomaly, longitude of the pericentre, and argument of the pericentre (Sect. 5.3.4). The results obtained with the two-satellite secular model were then validated using the N-body model presented in Chap. 2. First, we used a three-body model with Uranus, Ariel, and Umbriel (Sect. 5.4.1). Finally, we studied the general case with a six-body model, with Uranus and the five major satellites, and re-evaluated the results obtained from the secular model and the three-body problem (Sect. 5.4.2).

6.2   Results and discussion

In this work, we re-estimated the specific dissipation factor of Uranus and constrain it to be $5\,800 < Q_0 < 11\,500$ (Sect. 2.4.3). These values clearly extend beyond the previously established range outlined by Tittemore and Wisdom (1990). This is a consequence of the improvement in the determination of the physical parameters of the satellites, namely, in the radii and masses (Jacobson 2014).

Tittemore and Wisdom (1989) atribute the high inclination of Miranda to the crossing of the 3/1 Miranda-Umbriel MMR, while Ćuk et al. (2020) suggest that this could have been due to the 5/3 Ariel-Umbriel MMR. The excitation of the satellites' orbits not involved in this resonance, that is, Miranda, Titania, and Oberon, requires some additional mechanism to reduce the high inclinations of these satellites. In this work, we did not see the spin-orbit resonances invoked by Ćuk et al. (2020), and have shown that currently there are not any spin-orbit resonance within the Uranian major satellites, even if Cassini-state forced obliquities are considered (Sect. 2.4.5). Thus, we are led to conclude that the 5/3 MMR between Ariel and Umbriel must have been skipped or captured within a short interval of time, and the 3/1 MMR between Miranda and Umbriel is the most likely responsible for the 4.4° inclination

value of Miranda.

With the N-body model, we have shown that, since the formation, $\sim$ 4.5 Gyr ago, the Uranian satellites could have encountered many different MMRs (Sect. 2.4.6). As a consequence, it is difficult to reconstruct the entire evolution of the Uranian system. However, we have shown that after the passage through the 5/3 Ariel-Umbriel MMR, the evolution of the system is not disturbed (Sect. 2.4.7). We were thus able to reconstruct the evolution of the semi-major axes of the satellites from the resonance passage (see Fig. 2.13), until the present days. Since tides are not very effective on damping the inclinations of the satellites, with damping timescales of at least 180 Gyr (assuming $Q_0 = 8\,000$), we have shown that the inclinations most likely remained unchanged since then (Sect. 4.4). Yet, tides quickly erode the eccentricities of Miranda, Ariel, and Umbriel, with damping timescales of 250 Myr, 60 Myr, and 690 Myr, respectively (assuming $Q_S = 500$). Therefore, the eccentricities of the three innermost satellites must have been higher just after the resonance passage.

The statistical results from the secular two-satellite model show that, in the circular approximation (Sect. 5.1), the initial inclination of Ariel must have been higher than about 0.05°, and the initial inclination of Umbriel higher than about 0.1° to avoid a permanent capture. Moreover, we showed that the final inclination distributions of Umbriel tend to cluster around a mean value, whereas the final inclination distributions of Ariel spread between 0.01° and 0.25° with a nearly equal probability. As for the planar approximation (Sect. 5.2), our results are in agreement with those obtained by Tittemore and Wisdom (1988). Namely, we showed that the eccentricity of at least one of the satellites must be higher than 0.01 in order to avoid resonance capture. However, we have shown that, for the planar approximation, the eccentricity of Ariel plays a key role in the 5/3 MMR capture probability. On the other hand, the eccentricity of Umbriel does not appear to play a significant role in the probability of escape.

When adopting the more realistic eccentric-inclined case with the secular two-satellite model (Sect. 5.3), later validated with the N-body model, we have confirmed that Ariel's eccentricity is the primary factor influencing the capture probability in the 5/3 Ariel-Umbriel MMR. We also established that if the initial $\sqrt{e_1^2 + e_2^2} \leq 0.007$, long-term capture within the resonance is certain. Moreover, the optimal configuration to enhance the escape probability is achieved when the initial $e_1 \geq 0.01$ and $e_2 \leq 0.015$. In contrast, the initial inclinations of both satellites do not significantly impact this statistical outcome of the capture probability. Nonetheless, the pre-encounter inclinations determine the final inclinations after the resonance passage. In fact, we have found a linear relation between the initial and final inclinations (Eq. (5.15)), which allows us to estimate initial pairs of inclinations required to achieve the presently observed inclinations. However, the distribution of the eccentricities and inclinations lie within a cone, with its origin at $e_k = I_k = 0$, that widens with the eccentricity and inclination values (Figs. 5.11 and 5.15). Therefore, the results obtained with Eq. (5.15) must be taken with caution, as they are not valid for final $I_k \leq 0.05°$, and for final inclination values that lay outside the restriction cone. Still, from Monte-Carlo simulations (Sect. 5.3.4), we conclude that the initial inclination of Ariel should have been $I_1 \leq 0.05°$, and the initial inclination of Umbriel $I_2 \approx 0.082°$, so that the final inclinations after the resonance passage match the current inclinations of the system (Table 1.2). Following the resonance passage, the eccentricities of the satellites are higher than the currently observed ones (Table 1.2). However, these eccentricities should be quickly eroded, particularly for Ariel, as tidal forces exert a stronger influence compared to Umbriel.

When comparing the results from the secular model with the three-body model (Sect. 5.4.1), we observed that both models present a very good agreement, with no substantial differences to be noted between them. This shows that the long-term evolution through the 5/3 Ariel-Umbriel MMR is ruled by secular interactions within the two satellites and the planet, and that high frequency terms can be averaged.

Finally, no significant differences between the secular, the two-satellite, and the five-satellite models were found for the evolution of Ariel and Umbriel (Sect. 5.4.2). We confirm the results from Ćuk et al. (2020), and observe that Miranda, although not involved in the 5/3 resonance, is severely excited by the resonance entrapment, increasing both eccentricities and inclinations by several times the initial values. Nevertheless, we also observed that, in several cases, the increase in eccentricity lead to an inward

migration of the satellite, and the eccentricities and inclinations of Titania and Oberon, after some time of resonance entrapment, are also affected by the resonance and display chaotic motion.

The satellites of Uranus were presumably formed in a circumplanetary disk, and so the primordial eccentricities and inclinations should have been extremely small. Before the encounter with the 5/3 MMR, the Uranian satellites may have crossed other MMRs (e.g. Peale 1988; Ćuk et al. 2020). In general, these resonances excite the eccentricities and the inclinations of the bodies involved in the commensurabilities. Tides are very efficient at damping the eccentricities, but not the inclinations. Therefore, while the remnant eccentricities are quickly eroded, the inclinations are fossilized until the next resonant encounter. The hypothesis that the present inclination of Miranda can be explained by the passage through the 3/1 MMR between Miranda and Umbriel that could have occurred several billion years ago is captivating. This resonance also involves Umbriel, whose inclination can therefore also be excited, though to a much lower value than that of Miranda (Tittemore and Wisdom 1989). As a consequence, prior to the encounter with the 5/3 MMR, it is reasonable to assume a near zero inclination for Ariel and an inclination around 0.082° for Umbriel. Yet, a high eccentricity of Ariel is difficult to explain. Tidal evolution of the semi-major axes does not predict any two-body MMR close to the 5/3 MMR between Ariel and Umbriel (see Fig. 1.4). Thus, some other event must be found to excite the eccentricity of Ariel. According to the Eq. (2.68), we have determined that ~ 300 Myr prior to the 5/3 MMR, Miranda, Ariel, and Oberon could have encountered a first order three-body MMR described as $3n_1 - 8n_2 + 4n_3$. Also, Miranda, Ariel, and Umbriel could have crossed the $-4n_1 - 10n_2 - 5n_3$, approximately 250 Myr before the 5/3 MMR. Note that, contrarily to zeroth order three-body MMR, first order three-body MMR can excite the eccentricities and inclinations of the bodies (Petit 2021). Therefore, a preceding three-body MMR prior to the two-body MMR scenario appears to be a compelling explanation, especially when we take into account that the most recent geological features on Ariel's surface are estimated to be ~ 1 Gyr old (Zahnle et al. 2003).

6.3   Perspectives

The work conducted in this thesis enables the reconstruction of the orbital evolution of the five major Uranian satellites from their passage through the 5/3 Ariel-Umbriel MMR until the present day. However, the exact past evolution of the system, since the formation, about 4.5 Gyr ago, until the 5/3 MMR between Ariel and Umbriel remains unknown.

In this work, we assume that the 5/3 Ariel-Umbriel MMR was most likely skipped. Therefore, we did not take into account the energy dissipated during resonance entrapment due to the orbital excitation of the satellites. However, the signs of geological resurfacing observed at Miranda, Ariel, and Titania are indicators that during the satellites' evolution, large amounts of energy had to be dissipated for their surfaces to melt. Then, future studies to the passage through resonances within the Uranian system should account for the energy dissipation on the system. The tidal energy dissipated by a synchronous satellite orbiting in the equatorial plane of the planet is given by (e.g. Peterson et al. 2015)

$$\dot{E}_t = -\frac{21}{2}\frac{k_{2_k}}{Q_k}\frac{n_k^5 R_k^5}{G}e_k^2\,. \tag{6.1}$$

In Fig. 6.1, we estimated $\dot{E}_t$ per unit of area for the five major Uranian satellites, in the example of Fig. 2.12. For Miranda, Ariel, and Titania, we also plotted the minimum energy required to form the geological features observed in their surfaces, 31 mW/m^2 (Beddingfield et al. 2015), 28 mW/m^2 (Peterson et al. 2015), and 5 mW/m^2 (Beddingfield et al. 2023), respectively. For the remaining satellites, we did not found estimations of these energies in the literature. As can be seen, there are several periods of time where the energy dissipation surpass the minimum energy required to melt the surface of the satellite. Combined with the estimation of the ages of the geological features given by Zahnle et al. (2003), this could pinpoint the precise temporal location of each MMR.

Our model can be directly applied to the passage through the 3/1 MMR between Miranda and Umbriel. Such would allow us to study with an unprecedented detail the influence of this resonance on

the inclination of Miranda, and possible to ascertain the origin of its high value (Tittemore and Wisdom 1989; Ćuk et al. 2020). Moreover, our model is also valid for any second order MMR with low inclinations and eccentricities, and thus not restricted to the Uranian satellites. Thus, it can also be used to study a large number of planetary systems near second order resonances, such as the 3/1 MMR for HD 60532 (Laskar and Correia 2009), the 5/3 MMR for HD 33844 (Wittenmyer et al. 2016), the 7/5 MMR for HD 41248 (Jenkins et al. 2013), or the 9/7 MMR for Kepler-29 (Vissapragada et al. 2020), as long as we keep the low eccentricity and inclination approximation. We could also generalize our model to higher eccentricities and inclinations, by developing the model up to higher orders of eccentricity and inclinations.

In our secular model, we restricted ourselves to second-order two-body MMRs. However, we can also easily apply our methodology to first-order two-body MMRs, by preserving the linear eccentricity and inclination terms in Eq. (3.57), (3.58), and (4.9), and developing the resulting Hamiltonian. We could also study, for instance, the 2/1 Ganymede-Europa and the 2/1 Europa-Io MMRs on the Jovian system(Sinclair 1975), or the 2/1 Dione-Enceladus (Sinclair 1972) and the 4/3 Hyperion-Titan MMRs (Colombo et al. 1974) on the Saturnian system.

The mechanism that excites the eccentricity of Ariel prior to the 5/3 MMR still needs to be explained. As already proposed, three-body MMRs could provide such a mechanism. In addition, in Sect. 2.4, we have noticed the presence of several of these resonances in the Uranian system, especially first order three-body MMR. Thus, we could apply the methodologies developed in this work, and build a secular model with tides to study the influence of these resonances into shaping the Uranian system.
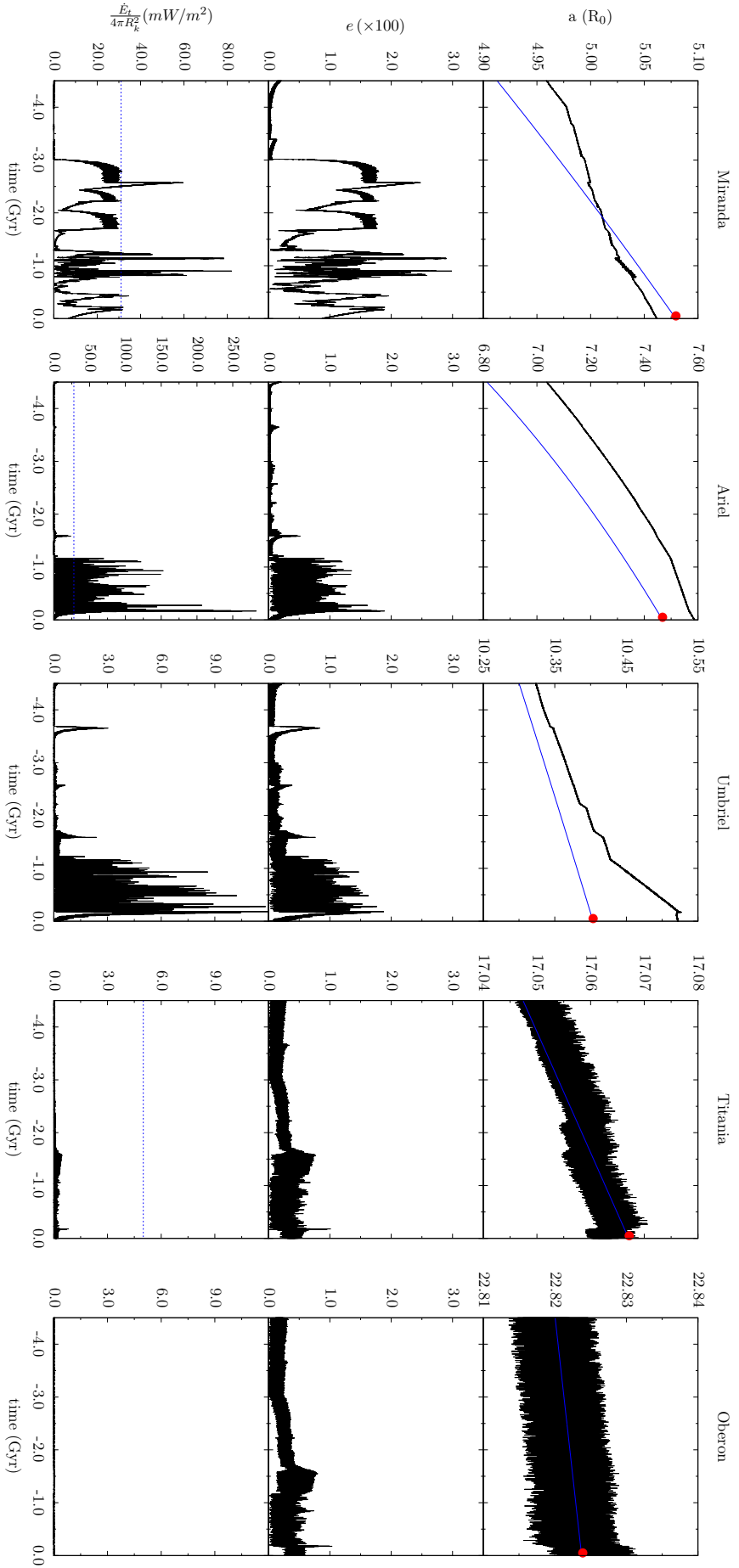
Figure 6.1: Energy dissipated in all major Uranian satellites for several MMR crossings. The semi-major axes were extrapolated using Eq. (2.68), with small changes on the asymptotic initial values for Miranda, Ariel, and Umbriel, so that the 3/1 Miranda-Umbriel MMR ($t \approx -4.0$ Gyr) and the 5/3 Ariel-Umbriel MMR ($t \approx -1.1$ Gyr) are crossed. The eccentricities were initially set to $e = 2 \times 10^{-3}$ and the inclinations to the current mean value, except for Miranda, with $I = 0.1°$. The first row gives the semi-major axes of the five satellites, the middle row shows the eccentricities, and the bottom one gives the tidal energy dissipated per unit of area. The asymptotic semi-major axes evolution were superimposed as a blue solid line and the minimum required energy to melt the surfaces of Miranda, Ariel, and Titania as a blue dashed line (Peterson et al. 2015; Beddingfield et al. 2015, 2023). The red dots are the presently observed semi-major axes and eccentricities.

Appendix A

Elliptical elements

Gravitational forces drive almost all the dynamics of the celestial bodies. Isaac Newton provided a simple set of relations that allow us to describe and explain these dynamics. These relations are simple to solve for systems with only two bodies. Let us consider two point-like masses, m_1 and m_2. The gravitational force acting on each body due to the mass of the other is given by Newton's universal law of gravitation:

$$\mathbf{F}_1 = \mathcal{G}\frac{m_1 m_2}{r^3}\mathbf{r} = m_1 \ddot{\mathbf{R}}_1 , \tag{A.1}$$

$$\mathbf{F}_2 = -\mathcal{G}\frac{m_1 m_2}{r^3}\mathbf{r} = m_2 \ddot{\mathbf{R}}_2 , \tag{A.2}$$

where $\mathbf{R}_1$ and $\mathbf{R}_2$ are the position vectors of m_1 and m_2, respectively, $\mathbf{r} = \mathbf{R}_2 - \mathbf{R}_1$, r the norm of $\mathbf{r}$, and $\mathcal{G} = 4\pi^2 \, \text{au} \, M_\odot^{-1} \, \text{yr}^{-2}$ is the universal gravitational constant. Using Eqs. (A.1) and (A.2), and since the sum of the forces must be zero, we can write the equation of relative motion

$$\ddot{\mathbf{r}} + \mu\frac{\mathbf{r}}{r^3} = 0 , \tag{A.3}$$

where $\mu = \mathcal{G}(m_1 + m_2)$.

Taking the vector product of $\mathbf{r}$ with Eq. (A.3) we have $\mathbf{r} \times \ddot{\mathbf{r}} = 0$, which integrating leads to

$$\mathbf{r} \times \dot{\mathbf{r}} = \mathbf{h} , \tag{A.4}$$

where $\mathbf{h}$ is a constant vector normal to the orbital motion, the specific angular momentum. Since the motion is constrained to a plan, polar coordinates (r, f) are more suitable to express the motion of the system, where $\hat{\mathbf{r}} = (\cos f, \sin f)$ and $\hat{\boldsymbol{f}} = (-\sin f, \cos f)$. Then

$$\mathbf{r} = r\hat{\mathbf{r}} , \tag{A.5}$$

$$\dot{\mathbf{r}} = \dot{r}\hat{\mathbf{r}} + r\dot{f}\,\hat{\boldsymbol{f}} , \tag{A.6}$$

$$\ddot{\mathbf{r}} = (\ddot{r} - r\dot{f}^2)\hat{\mathbf{r}} + \left(\frac{1}{r}\frac{d}{dt}(r^2\dot{f})\right)\hat{\boldsymbol{f}} . \tag{A.7}$$

Substituting Eq. (A.6) in Eq. (A.4), yields to

$$|\mathbf{h}| = \text{h} = r^2\dot{f} \qquad (\text{Kepler's second law}) . \tag{A.8}$$

Comparing the radial terms of Eq. (A.3) and Eq. (A.7) we get that

$$\ddot{r} - r\dot{f}^2 = -\frac{\mu}{r^2} . \tag{A.9}$$

Now, performing the change of variable $u = 1/r$, and replacing Eq. (A.8) in Eq. (A.9), we obtain

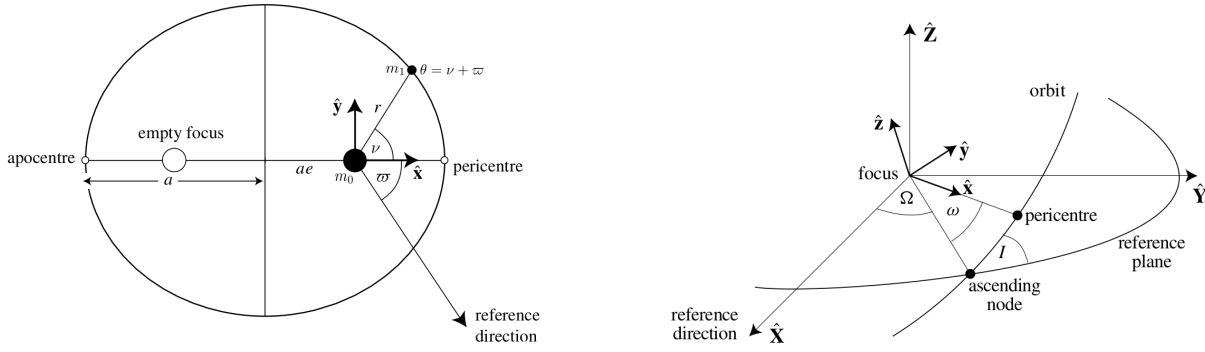$$\frac{d^2u}{df^2} + u = \frac{\mu}{\text{h}^2} . \tag{A.10}$$

Figure A.1: Geometric representation of the elliptical elements. Left: the geometry of the ellipse of semi-major axis a, eccentricity e and longitude of pericentre ϖ. Right: orbital motion with respect to the reference plane with inclination. Figures from Murray and Dermott (1999).

This is a second-order linear differential equation, with solution

$$u = \frac{\mu}{h^2}(1 + e \cos(f - \varpi)),$$ (A.11)

where e is the amplitude and ϖ the phase. Substituting back to r in Eq. (A.11), we obtain the general equation of a conic in polar coordinates, that is,

$$r = \frac{a(1 - e^2)}{1 + e \cos(f - \varpi)} \qquad \text{(Kepler's first law)},$$ (A.12)

where a is known as the semi-major axis, e the eccentricity, f the true longitude, ϖ the longitude of the pericentre (see Fig. A.1), and

$$h = \sqrt{\mu a(1 - e^2)}.$$ (A.13)

This equation describes Kepler's first law of planetary motion, which states that planets move in ellipses with the Sun at one focus.

The angle inside the cosine is often substituted by the true anomaly $\nu = f - \varpi$. This angle has a period of 2π, but it is only a linear function of time for circular orbits, that is, when $e = 0$. Hence, let's define the commonly used mean anomaly, M, and the mean longitude, λ, as

$$M(t) = n(t - \tau),$$ (A.14)

$$\lambda = M + \omega + \Omega = M + \varpi,$$ (A.15)

where

$$n = 2\pi/T,$$ (A.16)

is the mean motion, T the orbital period, τ is the time of pericentre passage, and

$$\varpi = \omega + \Omega.$$ (A.17)

The relation between the true anomaly and the mean anomaly is given by (Murray and Dermott 1999)

$$\nu = M + 2e \sin M + \frac{5}{4}e^2 \sin 2M + e^3 \left(\frac{13}{12} \sin 3M - \frac{1}{4} \sin M\right) + O(e^4).$$ (A.18)

In addition, it will be important for the following sections to have a relation between the mean motion (n) and semi-major axis (a). The area of the ellipse defined by the orbit is given by

$$A = \frac{1}{2} \int_0^{2\pi} r \, d\nu.$$ (A.19)

Substituting Eq. (A.12) into the equation, we obtain

$$A = \pi a \left(1 - e^2\right). \tag{A.20}$$

We can also compute the area by replacing Eqs. (A.8) and (A.13) in Eq. (A.19), yielding to

$$A = \frac{1}{2}hT = \frac{1}{n}\sqrt{\mu a(1 - e^2)}. \tag{A.21}$$

Combining Eqs. (A.20) and (A.21), we obtain

$$n^2 a^3 = \mu \qquad \text{(Kepler's third law)}, \tag{A.22}$$

which states that the square of the orbital period (T) of a planet is proportional to the cube of its semi-major axis.

So far, we only describe the orbit of a mass on the orbital plane. To describe the motion in a general plane, e.g., the orbits of the objects of the Solar System with respect to the ecliptic plane, an additional set of parameters is required. Let's take $(\hat{\mathbf{x}}, \hat{\mathbf{y}}, \hat{\mathbf{z}})$ as an orthogonal referential, where $\hat{\mathbf{z}}$ is perpendicular to the orbital plane and $\hat{\mathbf{x}}$ is taken to lie along the major axis of the ellipse (Fig. A.1). To represent the orbit with respect to a general Cartesian reference frame $(\hat{\mathbf{X}}, \hat{\mathbf{Y}}, \hat{\mathbf{Z}})$, we need to perform a change of referential. First, a rotation around the $\hat{\mathbf{z}}$ axis through an angle ω, followed by a rotation of I around $\hat{\mathbf{x}}$, and finally a rotation about $\hat{\mathbf{z}}$ through an angle Ω. The line where both planes cross is the ascending node, ω the argument of pericentre, I the inclination, and Ω the longitude of the ascending node. Mathematically, this can be described as

$$\begin{bmatrix} X \\ Y \\ Z \end{bmatrix} = \mathcal{R}_3(\Omega)\,\mathcal{R}_1(I)\,\mathcal{R}_3(\omega) \begin{bmatrix} r\cos v \\ r\sin v \\ 0 \end{bmatrix}, \tag{A.23}$$

where (X, Y, Z) are the coordinates of the body in the reference plane, and $\mathcal{R}_1$ and $\mathcal{R}_3$ are the rotation matrices around the x-axis and z-axis, respectively, given by

$$\mathcal{R}_1(x) = \begin{bmatrix} 1 & 0 & 0 \\ 0 & \cos(x) & -\sin(x) \\ 0 & \sin(x) & \cos(x) \end{bmatrix} \quad \text{and} \quad \mathcal{R}_3(x) = \begin{bmatrix} \cos(x) & -\sin(x) & 0 \\ \sin(x) & \cos(x) & 0 \\ 0 & 0 & 1 \end{bmatrix}. \tag{A.24}$$

Performing the matrix products we reach the relation between the coordinates of a body in a reference plane and the orbital elements

$$X = r\left[\cos\Omega\cos(\omega + v) - \sin\Omega\sin(\omega + v)\cos I\right], \tag{A.25}$$

$$Y = r\left[\sin\Omega\cos(\omega + v) + \cos\Omega\sin(\omega + v)\cos I\right], \tag{A.26}$$

$$Z = r\left[\sin(\omega + v)\sin I\right]. \tag{A.27}$$

Appendix B

Secular and resonance Hamiltonian expansion in resonant variables

Departing from the conservative secular Hamiltonian written in elliptical elements (Eq. (3.63)), one can replace the semi-major axis (a_k), the eccentricity (e_k) and the inclinations (I_k) by the momenta Σ_1, Σ_2, Φ_1 and Φ_2 (Eqs. (3.29)-(3.31)) and the constants Γ_1 and Γ_2 (Eqs. (3.49) and (3.50)). Furthermore, we can isolate the contributions from each individual terms from the momenta. The secular Hamiltonian (3.65) then writes as

$$\mathcal{H}_{S_1} = -\frac{\mathcal{G}\mu_2 m_1 m_2 \beta_2^2}{2\Gamma_2^2} \frac{1}{\left[1 + \frac{(p+q)}{q}\left(\frac{\Sigma_1}{\Gamma_1}\frac{\Gamma_1}{\Gamma_2} + \frac{\Sigma_2}{\Gamma_2} + \frac{\Phi_1}{\Gamma_1}\frac{\Gamma_1}{\Gamma_2} + \frac{\Phi_2}{\Gamma_2}\right)\right]^2} b_{\frac{1}{2}}^{(0)}\left(\alpha\left(\frac{\Sigma_1}{\Gamma_1}, \frac{\Sigma_2}{\Gamma_2}, \frac{\Phi_1}{\Gamma_1}, \frac{\Phi_2}{\Gamma_2}\right)\right), \tag{B.1}$$

$$\mathcal{H}_{S_2} = -\frac{\mathcal{G}\mu_2 m_1 m_2 \beta_2^2}{2\Gamma_2^2}\left(\frac{\mu_2\beta_2^2}{\mu_1\beta_1^2}\frac{\Gamma_1^2\left[1 - \frac{p}{q}\left(\frac{\Sigma_1}{\Gamma_1} + \frac{\Sigma_2}{\Gamma_2}\frac{\Gamma_2}{\Gamma_1} + \frac{\Phi_1}{\Gamma_1} + \frac{\Phi_2}{\Gamma_2}\frac{\Gamma_2}{\Gamma_1}\right)\right]}{\Gamma_2^2\left[1 + \frac{(p+q)}{q}\left(\frac{\Sigma_1}{\Gamma_1}\frac{\Gamma_1}{\Gamma_2} + \frac{\Sigma_2}{\Gamma_2} + \frac{\Phi_1}{\Gamma_1}\frac{\Gamma_1}{\Gamma_2} + \frac{\Phi_2}{\Gamma_2}\right)\right]^4}D\right.$$
$$\left.+\frac{\mu_2^2\beta_2^4}{2\mu_1^2\beta_1^4}\frac{\Gamma_1^4\left[1 - \frac{p}{q}\left(\frac{\Sigma_1}{\Gamma_1} + \frac{\Sigma_2}{\Gamma_2}\frac{\Gamma_2}{\Gamma_1} + \frac{\Phi_1}{\Gamma_1} + \frac{\Phi_2}{\Gamma_2}\frac{\Gamma_2}{\Gamma_1}\right)\right]^3}{\Gamma_2^4\left[1 + \frac{(p+q)}{q}\left(\frac{\Sigma_1}{\Gamma_1}\frac{\Gamma_1}{\Gamma_2} + \frac{\Sigma_2}{\Gamma_2} + \frac{\Phi_1}{\Gamma_1}\frac{\Gamma_1}{\Gamma_2} + \frac{\Phi_2}{\Gamma_2}\right)\right]^4}D^2\right)b_{\frac{1}{2}}^{(0)}\left(\alpha\left(\frac{\Sigma_1}{\Gamma_1}, \frac{\Sigma_2}{\Gamma_2}, \frac{\Phi_1}{\Gamma_1}, \frac{\Phi_2}{\Gamma_2}\right)\right)\frac{\Sigma_1}{\Gamma_1}, \tag{B.2}$$

$$\mathcal{H}_{S_3} = -\frac{\mathcal{G}\mu_2 m_1 m_2 \beta_2^2}{2\Gamma_2^2}\left(\frac{\mu_2\beta_2^2}{\mu_1\beta_1^2}\frac{\Gamma_1^2\left[1 - \frac{p}{q}\left(\frac{\Sigma_1}{\Gamma_1} + \frac{\Sigma_2}{\Gamma_2}\frac{\Gamma_2}{\Gamma_1} + \frac{\Phi_1}{\Gamma_1} + \frac{\Phi_2}{\Gamma_2}\frac{\Gamma_2}{\Gamma_1}\right)\right]^2}{\Gamma_2^2\left[1 + \frac{(p+q)}{q}\left(\frac{\Sigma_1}{\Gamma_1}\frac{\Gamma_1}{\Gamma_2} + \frac{\Sigma_2}{\Gamma_2} + \frac{\Phi_1}{\Gamma_1}\frac{\Gamma_1}{\Gamma_2} + \frac{\Phi_2}{\Gamma_2}\right)\right]^5}D\right.$$
$$\left.+\frac{\mu_2^2\beta_2^4}{2\mu_1^2\beta_1^4}\frac{\Gamma_1^4\left[1 - \frac{p}{q}\left(\frac{\Sigma_1}{\Gamma_1} + \frac{\Sigma_2}{\Gamma_2}\frac{\Gamma_2}{\Gamma_1} + \frac{\Phi_1}{\Gamma_1} + \frac{\Phi_2}{\Gamma_2}\frac{\Gamma_2}{\Gamma_1}\right)\right]^4}{\Gamma_2^4\left[1 + \frac{(p+q)}{q}\left(\frac{\Sigma_1}{\Gamma_1}\frac{\Gamma_1}{\Gamma_2} + \frac{\Sigma_2}{\Gamma_2} + \frac{\Phi_1}{\Gamma_1}\frac{\Gamma_1}{\Gamma_2} + \frac{\Phi_2}{\Gamma_2}\right)\right]^7}D^2\right)b_{\frac{1}{2}}^{(0)}\left(\alpha\left(\frac{\Sigma_1}{\Gamma_1}, \frac{\Sigma_2}{\Gamma_2}, \frac{\Phi_1}{\Gamma_1}, \frac{\Phi_2}{\Gamma_2}\right)\right)\frac{\Sigma_2}{\Gamma_2}, \tag{B.3}$$

$$\mathcal{H}_{S_4} = -\frac{\mathcal{G}\mu_2 m_1 m_2 \beta_2^2}{\Gamma_2^2}2\left(\frac{2}{\left[1 + \frac{(p+q)}{q}\left(\frac{\Sigma_1}{\Gamma_1}\frac{\Gamma_1}{\Gamma_2} + \frac{\Sigma_2}{\Gamma_2} + \frac{\Phi_1}{\Gamma_1}\frac{\Gamma_1}{\Gamma_2} + \frac{\Phi_2}{\Gamma_2}\right)\right]^{5/2}\left[1 - \frac{p}{q}\left(\frac{\Sigma_1}{\Gamma_1} + \frac{\Sigma_2}{\Gamma_2}\frac{\Gamma_2}{\Gamma_1} + \frac{\Phi_1}{\Gamma_1} + \frac{\Phi_2}{\Gamma_2}\frac{\Gamma_2}{\Gamma_1}\right)\right]^{1/2}}\right.$$
$$\left.-2\frac{\mu_2\beta_2^2}{\mu_1\beta_1^2}\frac{\Gamma_1^2\left[1 - \frac{p}{q}\left(\frac{\Sigma_1}{\Gamma_1} + \frac{\Sigma_2}{\Gamma_2}\frac{\Gamma_2}{\Gamma_1} + \frac{\Phi_1}{\Gamma_1} + \frac{\Phi_2}{\Gamma_2}\frac{\Gamma_2}{\Gamma_1}\right)\right]^{3/2}}{\Gamma_2^2\left[1 + \frac{(p+q)}{q}\left(\frac{\Sigma_1}{\Gamma_1}\frac{\Gamma_1}{\Gamma_2} + \frac{\Sigma_2}{\Gamma_2} + \frac{\Phi_1}{\Gamma_1}\frac{\Gamma_1}{\Gamma_2} + \frac{\Phi_2}{\Gamma_2}\right)\right]^{9/2}}D\right.$$
$$\left.-\frac{\mu_2^2\beta_2^4}{\mu_1^2\beta_1^4}\frac{\Gamma_1^4\left[1 - \frac{p}{q}\left(\frac{\Sigma_1}{\Gamma_1} + \frac{\Sigma_2}{\Gamma_2}\frac{\Gamma_2}{\Gamma_1} + \frac{\Phi_1}{\Gamma_1} + \frac{\Phi_2}{\Gamma_2}\frac{\Gamma_2}{\Gamma_1}\right)\right]^{7/2}}{\Gamma_2^4\left[1 + \frac{(p+q)}{q}\left(\frac{\Sigma_1}{\Gamma_1}\frac{\Gamma_1}{\Gamma_2} + \frac{\Sigma_2}{\Gamma_2} + \frac{\Phi_1}{\Gamma_1}\frac{\Gamma_1}{\Gamma_2} + \frac{\Phi_2}{\Gamma_2}\right)\right]^{13/2}}D^2\right)$$
$$b_{\frac{1}{2}}^{(1)}\left(\alpha\left(\frac{\Sigma_1}{\Gamma_1}, \frac{\Sigma_2}{\Gamma_2}, \frac{\Phi_1}{\Gamma_1}, \frac{\Phi_2}{\Gamma_2}\right)\right)\sqrt{\frac{\Sigma_1}{\Gamma_1}}\sqrt{\frac{\Sigma_2}{\Gamma_2}}\cos\left(\sigma_1 - \sigma_2\right), \tag{B.4}$$

$$\mathcal{H}_{S_5} = \frac{\mathcal{G}\mu_2 m_1 m_2 \beta_2^2}{4\Gamma_2^2} \frac{\mu_2 \beta_2^2}{\mu_1 \beta_1^2} \frac{\Gamma_1^2 \left[1 - \frac{p}{q}\left(\frac{\Sigma_1}{\Gamma_1} + \frac{\Sigma_2}{\Gamma_2}\frac{\Gamma_2}{\Gamma_1} + \frac{\Phi_1}{\Gamma_1} + \frac{\Phi_2}{\Gamma_2}\frac{\Gamma_2}{\Gamma_1}\right)\right]}{\Gamma_2^2 \left[1 + \frac{(p+q)}{q}\left(\frac{\Sigma_1}{\Gamma_1}\frac{\Gamma_1}{\Gamma_2} + \frac{\Sigma_2}{\Gamma_2} + \frac{\Phi_1}{\Gamma_1}\frac{\Gamma_1}{\Gamma_2} + \frac{\Phi_2}{\Gamma_2}\right)\right]^4} b_{\frac{3}{2}}^{(1)}\left(\alpha\left(\frac{\Phi_1}{\Gamma_1}, \frac{\Phi_2}{\Gamma_2}\right)\right) \frac{\Phi_1}{\Gamma_1}, \tag{B.5}$$

$$\mathcal{H}_{S_6} = \frac{\mathcal{G}\mu_2 m_1 m_2 \beta_2^2}{4\Gamma_2^2} \frac{\mu_2 \beta_2^2}{\mu_1 \beta_1^2} \frac{\Gamma_1^2 \left[1 - \frac{p}{q}\left(\frac{\Sigma_1}{\Gamma_1} + \frac{\Sigma_2}{\Gamma_2}\frac{\Gamma_2}{\Gamma_1} + \frac{\Phi_1}{\Gamma_1} + \frac{\Phi_2}{\Gamma_2}\frac{\Gamma_2}{\Gamma_1}\right)\right]^2}{\Gamma_2^2 \left[1 + \frac{(p+q)}{q}\left(\frac{\Sigma_1}{\Gamma_1}\frac{\Gamma_1}{\Gamma_2} + \frac{\Sigma_2}{\Gamma_2} + \frac{\Phi_1}{\Gamma_1}\frac{\Gamma_1}{\Gamma_2} + \frac{\Phi_2}{\Gamma_2}\right)\right]^5} b_{\frac{3}{2}}^{(1)}\left(\alpha\left(\frac{\Phi_1}{\Gamma_1}, \frac{\Phi_2}{\Gamma_2}\right)\right) \frac{\Phi_2}{\Gamma_2}, \tag{B.6}$$

$$\mathcal{H}_{S_7} = -\frac{\mathcal{G}\mu_2 m_1 m_2 \beta_2^2}{2\Gamma_2^2} \frac{\mu_2 \beta_2^2}{\mu_1 \beta_1^2} \frac{\Gamma_1^2 \left[1 - \frac{p}{q}\left(\frac{\Sigma_1}{\Gamma_1} + \frac{\Sigma_2}{\Gamma_2}\frac{\Gamma_2}{\Gamma_1} + \frac{\Phi_1}{\Gamma_1} + \frac{\Phi_2}{\Gamma_2}\frac{\Gamma_2}{\Gamma_1}\right)\right]^{\frac{3}{2}}}{\Gamma_2^4 \left[1 + \frac{(p+q)}{q}\left(\frac{\Sigma_1}{\Gamma_1}\frac{\Gamma_1}{\Gamma_2} + \frac{\Sigma_2}{\Gamma_2} + \frac{\Phi_1}{\Gamma_1}\frac{\Gamma_1}{\Gamma_2} + \frac{\Phi_2}{\Gamma_2}\right)\right]^{\frac{9}{2}}}$$
$$b_{\frac{3}{2}}^{(1)}\left(\alpha\left(\frac{\Phi_1}{\Gamma_1}, \frac{\Phi_2}{\Gamma_2}\right)\right) \sqrt{\frac{\Phi_1}{\Gamma_1}} \sqrt{\frac{\Phi_2}{\Gamma_2}} \cos\left(\varphi_2 - \varphi_1\right), \tag{B.7}$$

and the resonant and indirect Hamiltonian (Eqs. (3.66) and (3.67)) writes as

$$\mathcal{H}_{R_1} = -\frac{\mathcal{G}\mu_2 m_1 m_2 \beta_2^2}{4\Gamma_2^2}$$
$$\Bigg(\frac{-\frac{10(p+q)}{q} + \frac{16(p+q)^2}{q^2}}{\left[1 - \frac{p}{q}\left(\frac{\Sigma_1}{\Gamma_1} + \frac{\Sigma_2}{\Gamma_2}\frac{\Gamma_2}{\Gamma_1} + \frac{\Phi_1}{\Gamma_1} + \frac{\Phi_2}{\Gamma_2}\frac{\Gamma_2}{\Gamma_1}\right)\right]\left[1 + \frac{(p+q)}{q}\left(\frac{\Sigma_1}{\Gamma_1}\frac{\Gamma_1}{\Gamma_2} + \frac{\Sigma_2}{\Gamma_2} + \frac{\Phi_1}{\Gamma_1}\frac{\Gamma_1}{\Gamma_2} + \frac{\Phi_2}{\Gamma_2}\right)\right]^2} b_{\frac{1}{2}}^{\left(2\frac{p}{q}+2\right)}\left(\alpha\left(\frac{\Sigma_1}{\Gamma_1}, \frac{\Sigma_2}{\Gamma_2}\right)\right)$$
$$\left(2 - \frac{8(p+q)}{q}\right)\frac{\left[1 - \frac{p}{q}\left(\frac{\Sigma_1}{\Gamma_1} + \frac{\Sigma_2}{\Gamma_2}\frac{\Gamma_2}{\Gamma_1} + \frac{\Phi_1}{\Gamma_1} + \frac{\Phi_2}{\Gamma_2}\frac{\Gamma_2}{\Gamma_1}\right)\right]}{\left[1 + \frac{(p+q)}{q}\left(\frac{\Sigma_1}{\Gamma_1}\frac{\Gamma_1}{\Gamma_2} + \frac{\Sigma_2}{\Gamma_2} + \frac{\Phi_1}{\Gamma_1}\frac{\Gamma_1}{\Gamma_2} + \frac{\Phi_2}{\Gamma_2}\right)\right]^4}\alpha_0 D b_{\frac{1}{2}}^{\left(2\frac{p}{q}+2\right)}\left(\alpha\left(\frac{\Sigma_1}{\Gamma_1}, \frac{\Sigma_2}{\Gamma_2}\right)\right)$$
$$\frac{\left[1 - \frac{p}{q}\left(\frac{\Sigma_1}{\Gamma_1} + \frac{\Sigma_2}{\Gamma_2}\frac{\Gamma_2}{\Gamma_1} + \frac{\Phi_1}{\Gamma_1} + \frac{\Phi_2}{\Gamma_2}\frac{\Gamma_2}{\Gamma_1}\right)\right]^3}{\left[1 + \frac{(p+q)}{q}\left(\frac{\Sigma_1}{\Gamma_1}\frac{\Gamma_1}{\Gamma_2} + \frac{\Sigma_2}{\Gamma_2} + \frac{\Phi_1}{\Gamma_1}\frac{\Gamma_1}{\Gamma_2} + \frac{\Phi_2}{\Gamma_2}\right)\right]^6}\alpha_0^2 D^2 b_{\frac{1}{2}}^{\left(2\frac{p}{q}+2\right)}\left(\alpha\left(\frac{\Sigma_1}{\Gamma_1}, \frac{\Sigma_2}{\Gamma_2}\right)\right)\Bigg)\frac{\Sigma_1}{\Gamma_1}\cos\left(2\sigma_1\right),$$
$$\tag{B.8}$$

$$\mathcal{H}_{R_2} = -\frac{\mathcal{G}\mu_2 m_1 m_2 \beta_2^2}{4\Gamma_2^2}\Bigg[\frac{2 - \frac{14(p+q)}{q} + \frac{16(p+q)^2}{q^2}}{\left[1 + \frac{(p+q)}{q}\left(\frac{\Sigma_1}{\Gamma_1}\frac{\Gamma_1}{\Gamma_2} + \frac{\Sigma_2}{\Gamma_2} + \frac{\Phi_1}{\Gamma_1}\frac{\Gamma_1}{\Gamma_2} + \frac{\Phi_2}{\Gamma_2}\right)\right]^3} b_{\frac{1}{2}}^{\left(2\frac{p}{q}\right)}\left(\alpha\left(\frac{\Sigma_1}{\Gamma_1}, \frac{\Sigma_2}{\Gamma_2}\right)\right)$$
$$-\left(2 - \frac{8(p+q)}{q}\right)\frac{\left[1 - \frac{p}{q}\left(\frac{\Sigma_1}{\Gamma_1} + \frac{\Sigma_2}{\Gamma_2}\frac{\Gamma_2}{\Gamma_1} + \frac{\Phi_1}{\Gamma_1} + \frac{\Phi_2}{\Gamma_2}\frac{\Gamma_2}{\Gamma_1}\right)\right]^2}{\left[1 + \frac{(p+q)}{q}\left(\frac{\Sigma_1}{\Gamma_1}\frac{\Gamma_1}{\Gamma_2} + \frac{\Sigma_2}{\Gamma_2} + \frac{\Phi_1}{\Gamma_1}\frac{\Gamma_1}{\Gamma_2} + \frac{\Phi_2}{\Gamma_2}\right)\right]^5}\alpha_0 D b_{\frac{1}{2}}^{\left(2\frac{p}{q}\right)}\left(\alpha\left(\frac{\Sigma_1}{\Gamma_1}, \frac{\Sigma_2}{\Gamma_2}\right)\right)$$
$$+\frac{\left[1 - \frac{p}{q}\left(\frac{\Sigma_1}{\Gamma_1} + \frac{\Sigma_2}{\Gamma_2}\frac{\Gamma_2}{\Gamma_1} + \frac{\Phi_1}{\Gamma_1} + \frac{\Phi_2}{\Gamma_2}\frac{\Gamma_2}{\Gamma_1}\right)\right]^4}{\left[1 + \frac{(p+q)}{q}\left(\frac{\Sigma_1}{\Gamma_1}\frac{\Gamma_1}{\Gamma_2} + \frac{\Sigma_2}{\Gamma_2} + \frac{\Phi_1}{\Gamma_1}\frac{\Gamma_1}{\Gamma_2} + \frac{\Phi_2}{\Gamma_2}\right)\right]^7}\alpha_0^2 D^2 b_{\frac{1}{2}}^{\left(2\frac{p}{q}\right)}\left(\alpha\left(\frac{\Sigma_1}{\Gamma_1}, \frac{\Sigma_2}{\Gamma_2}\right)\right)\Bigg]\frac{\Sigma_2}{\Gamma_2}\cos\left(2\sigma_2\right), \tag{B.9}$$

$$\mathcal{H}_{R_3} = -\frac{\mathcal{G}\mu_2 m_1 m_2 \beta_2^2}{4\Gamma_2^2}$$

$$\left[\frac{-2 + \frac{12(p+q)}{q} - \frac{16(p+q)^2}{q^2}}{\left[1 - \frac{p}{q}\left(\frac{\Sigma_1}{\Gamma_1} + \frac{\Sigma_2}{\Gamma_2}\frac{\Gamma_2}{\Gamma_1} + \frac{\Phi_1}{\Gamma_1} + \frac{\Phi_2}{\Gamma_2}\frac{\Gamma_2}{\Gamma_1}\right)\right]^{\frac{1}{2}} \left[1 + \frac{(p+q)}{q}\left(\frac{\Sigma_1}{\Gamma_1}\frac{\Gamma_1}{\Gamma_2} + \frac{\Sigma_2}{\Gamma_2} + \frac{\Phi_1}{\Gamma_1}\frac{\Gamma_1}{\Gamma_2} + \frac{\Phi_2}{\Gamma_2}\right)\right]^{5/2}} b_{\frac{1}{2}}^{\left(2\frac{p}{q}+1\right)}\left(\alpha\left(\frac{\Sigma_1}{\Gamma_1}, \frac{\Sigma_2}{\Gamma_2}\right)\right)\right.$$

$$+ \left(2 - \frac{8(p+q)}{q}\right) \frac{\left[1 - \frac{p}{q}\left(\frac{\Sigma_1}{\Gamma_1} + \frac{\Sigma_2}{\Gamma_2}\frac{\Gamma_2}{\Gamma_1} + \frac{\Phi_1}{\Gamma_1} + \frac{\Phi_2}{\Gamma_2}\frac{\Gamma_2}{\Gamma_1}\right)\right]^{\frac{3}{2}}}{\left[1 + \frac{(p+q)}{q}\left(\frac{\Sigma_1}{\Gamma_1}\frac{\Gamma_1}{\Gamma_2} + \frac{\Sigma_2}{\Gamma_2} + \frac{\Phi_1}{\Gamma_1}\frac{\Gamma_1}{\Gamma_2} + \frac{\Phi_2}{\Gamma_2}\right)\right]^{9/2}} \alpha_0 \mathcal{D} b_{\frac{1}{2}}^{\left(2\frac{p}{q}+1\right)}\left(\alpha\left(\frac{\Sigma_1}{\Gamma_1}, \frac{\Sigma_2}{\Gamma_2}\right)\right)$$

$$+ \frac{\left[1 - \frac{p}{q}\left(\frac{\Sigma_1}{\Gamma_1} + \frac{\Sigma_2}{\Gamma_2}\frac{\Gamma_2}{\Gamma_1} + \frac{\Phi_1}{\Gamma_1} + \frac{\Phi_2}{\Gamma_2}\frac{\Gamma_2}{\Gamma_1}\right)\right]^{7/2}}{\left[1 + \frac{(p+q)}{q}\left(\frac{\Sigma_1}{\Gamma_1}\frac{\Gamma_1}{\Gamma_2} + \frac{\Sigma_2}{\Gamma_2} + \frac{\Phi_1}{\Gamma_1}\frac{\Gamma_1}{\Gamma_2} + \frac{\Phi_2}{\Gamma_2}\right)\right]^{\frac{13}{2}}} \alpha_0^2 \mathcal{D}^2 b_{\frac{1}{2}}^{\left(2\frac{p}{q}+1\right)}\left(\alpha\left(\frac{\Sigma_1}{\Gamma_1}, \frac{\Sigma_2}{\Gamma_2}\right)\right)\right] \sqrt{\frac{\Sigma_1}{\Gamma_1}}\sqrt{\frac{\Sigma_2}{\Gamma_2}}\cos\left(\sigma_1 + \sigma_2\right),$$

$$(B.10)$$

$$\mathcal{H}_{R_4} = -\frac{\mathcal{G}\mu_2 m_1 m_2 \beta_2^2}{4\Gamma_2^2} \frac{\mu_2 \beta_2^2}{\mu_1 \beta_1^2} \frac{\Gamma_1^2 \left[1 - \frac{p}{q}\left(\frac{\Sigma_1}{\Gamma_1} + \frac{\Sigma_2}{\Gamma_2}\frac{\Gamma_2}{\Gamma_1} + \frac{\Phi_1}{\Gamma_1} + \frac{\Phi_2}{\Gamma_2}\frac{\Gamma_2}{\Gamma_1}\right)\right]}{\Gamma_2^2 \left[1 + \frac{(p+q)}{q}\left(\frac{\Sigma_1}{\Gamma_1}\frac{\Gamma_1}{\Gamma_2} + \frac{\Sigma_2}{\Gamma_2} + \frac{\Phi_1}{\Gamma_1}\frac{\Gamma_1}{\Gamma_2} + \frac{\Phi_2}{\Gamma_2}\right)\right]^4} b_{\frac{3}{2}}^{\left(2\frac{p}{q}+1\right)}\left(\alpha\left(\frac{\Phi_1}{\Gamma_1}, \frac{\Phi_2}{\Gamma_2}\right)\right) \frac{\Phi_1}{\Gamma_1} \cos\left(2\varphi_1\right),$$

$$(B.11)$$

$$\mathcal{H}_{R_5} = -\frac{\mathcal{G}\mu_2 m_1 m_2 \beta_2^2}{4\Gamma_2^2} \frac{\mu_2 \beta_2^2}{\mu_1 \beta_1^2} \frac{\Gamma_1^2 \left[1 - \frac{p}{q}\left(\frac{\Sigma_1}{\Gamma_1} + \frac{\Sigma_2}{\Gamma_2}\frac{\Gamma_2}{\Gamma_1} + \frac{\Phi_1}{\Gamma_1} + \frac{\Phi_2}{\Gamma_2}\frac{\Gamma_2}{\Gamma_1}\right)\right]^2}{\Gamma_2^2 \left[1 + \frac{(p+q)}{q}\left(\frac{\Sigma_1}{\Gamma_1}\frac{\Gamma_1}{\Gamma_2} + \frac{\Sigma_2}{\Gamma_2} + \frac{\Phi_1}{\Gamma_1}\frac{\Gamma_1}{\Gamma_2} + \frac{\Phi_2}{\Gamma_2}\right)\right]^5} b_{\frac{3}{2}}^{\left(2\frac{p}{q}+1\right)}\left(\alpha\left(\frac{\Phi_1}{\Gamma_1}, \frac{\Phi_2}{\Gamma_2}\right)\right) \frac{\Phi_2}{\Gamma_2} \cos\left(2\varphi_2\right),$$

$$(B.12)$$

$$\mathcal{H}_{R_6} = \frac{\mathcal{G}\mu_2 m_1 m_2 \beta_2^2}{2\Gamma_2^2} \frac{\mu_2 \beta_2^2}{\mu_1 \beta_1^2} \frac{\Gamma_1^2 \left[1 - \frac{p}{q}\left(\frac{\Sigma_1}{\Gamma_1} + \frac{\Sigma_2}{\Gamma_2}\frac{\Gamma_2}{\Gamma_1} + \frac{\Phi_1}{\Gamma_1} + \frac{\Phi_2}{\Gamma_2}\frac{\Gamma_2}{\Gamma_1}\right)\right]^{\frac{3}{2}}}{\Gamma_2^2 \left[1 + \frac{(p+q)}{q}\left(\frac{\Sigma_1}{\Gamma_1}\frac{\Gamma_1}{\Gamma_2} + \frac{\Sigma_2}{\Gamma_2} + \frac{\Phi_1}{\Gamma_1}\frac{\Gamma_1}{\Gamma_2} + \frac{\Phi_2}{\Gamma_2}\right)\right]^{9/2}}$$

$$b_{\frac{3}{2}}^{\left(2\frac{p}{q}+1\right)}\left(\alpha\left(\frac{\Phi_1}{\Gamma_1}, \frac{\Phi_2}{\Gamma_2}\right)\right) \sqrt{\frac{\Phi_1}{\Gamma_1}}\sqrt{\frac{\Phi_2}{\Gamma_2}}\cos\left(\varphi_1 + \varphi_2\right).$$

$$(B.13)$$

Bibliography

Agnor, C. B. and Hamilton, D. P. (2006). Neptune's capture of its moon Triton in a binary-planet gravitational encounter. *Nature*, 441(7090):192–194.

Akins, A., Hofstadter, M., Butler, B., Friedson, A. J., Molter, E., Parisi, M., and de Pater, I. (2023). Evidence of a Polar Cyclone on Uranus From VLA Observations. *Geophysical Research Letters*, 50(10):e2023GL102872.

Alexander, M. E. (1973). The Weak Friction Approximation and Tidal Evolution in Close Binary Systems. *Astrophysics and Space Science*, 23:459–510.

Alves, A. J., Michtchenko, T. A., and Tadeu dos Santos, M. (2016). Dynamics of the 3/1 planetary mean-motion resonance: an application to the HD60532 b-c planetary system. *Celestial Mechanics and Dynamical Astronomy*, 124(3):311–334.

Andoyer, H. (1915). Sur les problèmes fondamenteaux de la mécanique céleste. *Bulletin Astronomique, Serie I*, 32:5–18.

Andoyer, H. (1923). *Cours de mecanique celeste*.

Asphaug, E. (2014). Impact Origin of the Moon? *Annual Review of Earth and Planetary Sciences*, 42:551–578.

Avramchuk, V. V., Rosenbush, V. K., and Bul'Ba, T. P. (2007). Photometric study of the major satellites of Uranus. *Solar System Research*, 41(3):186–202.

Barstow, J. K. and Irwin, P. G. J. (2016). Habitable worlds with JWST: transit spectroscopy of the TRAPPIST-1 system? *Monthly Notices of the Royal Astronomical Society]*, 461(1):L92–L96.

Barton, S. G. (1946). The names of the satellites. *Popular Astronomy*, 54:122.

Batygin, K. (2015). Capture of planets into mean-motion resonances and the origins of extrasolar orbital architectures. *Monthly Notices of the Royal Astronomical Society]*, 451(3):2589–2609.

Beddingfield, C. B., Burr, D. M., and Emery, J. P. (2015). Fault geometries on Uranus' satellite Miranda: Implications for internal structure and heat flow. *Icarus*, 247:35–52.

Beddingfield, C. B. and Cartwright, R. J. (2020). Hidden tectonism on Miranda's Elsinore Corona revealed by polygonal impact craters. *Icarus*, 343:113687.

Beddingfield, C. B., Cartwright, R. J., Leonard, E., Nordheim, T., and Scipioni, F. (2022). Ariel's Elastic Thicknesses and Heat Fluxes. *Plan. Sci. J.*, 3(5):106.

Beddingfield, C. B., Leonard, E. J., Nordheim, T. A., Cartwright, R. J., and Castillo-Rogez, J. C. (2023). Titania's Heat Fluxes Revealed by Messina Chasmata. *Plan. Sci. J.*, 4(11):211.

Bierson, C. J. and Nimmo, F. (2022). A note on the possibility of subsurface oceans on the Uranian satellites. *Icarus*, 373:114776.

Bocanegra-Bahamón, T., Bracken, C., Costa Sitjà, M., Dirkx, D., Gerth, I., Konstantinidis, K., Labrianidis, C., Laneuville, M., Luntzer, A., MacArthur, J. L., Maier, A., Morschhauser, A., Nordheim, T. A., Sallantin, R., and Tlustos, R. (2015). MUSE - Mission to the Uranian system: Unveiling the evolution and formation of ice giants. *Advances in Space Research*, 55(9):2190–2216.

Boué, G. and Laskar, J. (2010). A Collisionless Scenario for Uranus Tilting. *The Astrophysical Journal Letters*, 712(1):L44–L47.

Bourtembourg, R. (2013). Was Uranus Observed by Hipparchus? *Journal for the History of Astronomy*, 44(4):377–388.

Brunini, A. (1995). A possible constraint to Uranus' great collision. *Planetary and Space Science*, 43(8):1019–1021.

Brunini, A., Parisi, M. G., and Tancredi, G. (2002). Constraints to Uranus' Great Collision III: The Origin of the Outer Satellites. *Icarus*, 159(1):166–177.

Canup, R. M. (2005). A Giant Impact Origin of Pluto-Charon. *Science*, 307(5709):546–550.

Canup, R. M. (2012). Forming a Moon with an Earth-like Composition via a Giant Impact. *Science*, 338(6110):1052.

Canup, R. M. and Asphaug, E. (2001). Origin of the Moon in a giant impact near the end of the Earth's formation. *Nature*, 412(6848):708–712.

Canup, R. M. and Ward, W. R. (2006). A common mass scaling for satellite systems of gaseous planets. *Nature*, 441(7095):834–839.

Carpino, M., Milani, A., and Nobili, A. M. (1987). Long-term numerical integrations and synthetic theories for the motion of the outer planets. *Astronomy and Astrophysics*, 181(1):182–194.

Cartwright, R. J., Beddingfield, C. B., Nordheim, T. A., Elder, C. M., Castillo-Rogez, J. C., Neveu, M., Bramson, A. M., Sori, M. M., Buratti, B. J., Pappalardo, R. T., Roser, J. E., Cohen, I. J., Leonard, E. J., Ermakov, A. I., Showalter, M. R., Grundy, W. M., Turtle, E. P., and Hofstadter, M. D. (2021). The Science Case for Spacecraft Exploration of the Uranian Satellites: Candidate Ocean Worlds in an Ice Giant System. *Plan. Sci. J.*, 2(3):120.

Castillo-Rogez, J., Weiss, B., Beddingfield, C., Biersteker, J., Cartwright, R., Goode, A., Melwani Daswani, M., and Neveu, M. (2023). Compositions and interior structures of the large moons of uranus and implications for future spacecraft observations. *Journal of Geophysical Research: Planets*, 128(1):e2022JE007432. e2022JE007432 2022JE007432.

Chen, E. M. A., Nimmo, F., and Glatzmaier, G. A. (2014). Tidal heating in icy satellite oceans. *Icarus*, 229:11–30.

Cochrane, C. J., Vance, S. D., Nordheim, T. A., Styczinski, M. J., Masters, A., and Regoli, L. H. (2021). In Search of Subsurface Oceans Within the Uranian Moons. *Journal of Geophysical Research (Planets)*, 126(12):e06956.

Colombo, G., Franklin, F. A., and Shapiro, I. I. (1974). On the formation of the orbit-orbit resonance of Titan and Hyperion. *The Astronomical Journal*, 79:61.

Correia, A. C. M. (2009). Secular Evolution of a Satellite by Tidal Effect: Application to Triton. *The Astrophysical Journal Letters*, 704(1):L1–L4.

Correia, A. C. M. (2018). Chaotic dynamics in the (47171) Lempo triple system. *Icarus*, 305:250–261.

Correia, A. C. M. and Rodríguez, A. (2013). On the Equilibrium Figure of Close-in Planets and Satellites. *The Astrophysical Journal*, 767(2):128.

Correia, A. C. M. and Valente, E. F. S. (2022). Tidal evolution for any rheological model using a vectorial approach expressed in Hansen coefficients. *Celestial Mechanics and Dynamical Astronomy*, 134(3):24.

Couetdic, J., Laskar, J., Correia, A. C. M., Mayor, M., and Udry, S. (2010). Dynamical stability analysis of the HD 202206 system and constraints to the planetary orbits. *Astronomy and Astrophysics*, 519:A10.

Ćuk, M., El Moutamid, M., and Tiscareno, M. S. (2020). Dynamical History of the Uranian System. *Plan. Sci. J.*, 1(1):22.

Dai, F., Masuda, K., Beard, C., Robertson, P., Goldberg, M., Batygin, K., Bouma, L., Lissauer, J. J., Knudstrup, E., Albrecht, S., Howard, A. W., Knutson, H. A., Petigura, E. A., Weiss, L. M., Isaacson, H., Kristiansen, M. H., Osborn, H., Wang, S., Wang, X.-Y., Behmard, A., Greklek-McKeon, M., Vissapragada, S., Batalha, N. M., Brinkman, C. L., Chontos, A., Crossfield, I., Dressing, C., Fetherolf, T., Fulton, B., Hill, M. L., Huber, D., Kane, S. R., Lubin, J., MacDougall, M., Mayo, A., Močnik, T., Akana Murphy, J. M., Rubenzahl, R. A., Scarsdale, N., Tyler, D., Zandt, J. V., Polanski, A. S., Schwengeler, H. M., Terentev, I. A., Benni, P., Bieryla, A., Ciardi, D., Falk, B., Furlan, E., Girardin, E., Guerra, P., Hesse, K. M., Howell, S. B., Lillo-Box, J., Matthews, E. C., Twicken, J. D., Villaseñor, J., Latham, D. W., Jenkins, J. M., Ricker, G. R., Seager, S., Vanderspek, R., and Winn, J. N. (2023). TOI-1136 is a Young, Coplanar, Aligned Planetary System in a Pristine Resonant Chain. *The Astronomical Journal*, 165(2):33.

Darwin, G. H. (1880). On the Secular Changes in the Elements of the Orbit of a Satellite Revolving about a Tidally Distorted Planet. *Philos. Trans. R. Soc. London*, 171:713–891.

Deienno, R., Yokoyama, T., Nogueira, E. C., Callegari, N., and Santos, M. T. (2011). Effects of the planetary migration on some primordial satellites of the outer planets. I. Uranus' case. *Astronomy and Astrophysics*, 536:A57.

Delisle, J. B., Laskar, J., Correia, A. C. M., and Boué, G. (2012). Dissipation in planar resonant planetary systems. *Astronomy and Astrophysics*, 546:A71.

Dermott, S. F. and Nicholson, P. D. (1986). Masses of the satellites of Uranus. *Nature*, 319(6049):115–120.

Desch, M. D., Connerney, J. E. P., and Kaiser, M. L. (1986). The rotation period of Uranus. *Nature*, 322(6074):42–43.

Dumas, H. S. and Laskar, J. (1993). Global dynamics and long-time stability in Hamiltonian systems via numerical frequency analysis. *Physical Review Letters*, 70(20):2975–2979.

Fabrycky, D. C., Johnson, E. T., and Goodman, J. (2007). Cassini States with Dissipation: Why Obliquity Tides Cannot Inflate Hot Jupiters. *The Astrophysical Journal*, 665(1):754–766.

Gastineau, M. and Laskar, J. (2011). Trip: A computer algebra system dedicated to celestial mechanics and perturbation series. *ACM Commun. Comput. Algebra*, 44(3/4):194–197.

Gavrilov, S. V. and Zharkov, V. N. (1977). Love Numbers of the Giant Planets. *Icarus*, 32(4):443–449.

Goldreich, P. (1965). An explanation of the frequent occurrence of commensurable mean motions in the solar system. *Monthly Notices of the Royal Astronomical Society]*, 130:159.

Goldreich, P. and Peale, S. (1966). Spin-orbit coupling in the solar system. *The Astronomical Journal*, 71:425.

Goldstein, H., Poole, C., and Safko, J. (2002). *Classical mechanics*. Addison Wesley.

Gomes, S. R. A. and Correia, A. C. M. (2023a). Effect of the inclination in the passage through the 5/3 mean motion resonance between Ariel and Umbriel. *Astronomy and Astrophysics*, 674:A111.

Gomes, S. R. A. and Correia, A. C. M. (2023b). Stability maps for the 5/3 mean motion resonance between Ariel and Umbriel with inclination. *arXiv e-prints*, page arXiv:2309.04786.

Grimm, S. L., Demory, B.-O., Gillon, M., Dorn, C., Agol, E., Burdanov, A., Delrez, L., Sestovic, M., Triaud, A. H. M. J., Turbet, M., Bolmont, É., Caldas, A., de Wit, J., Jehin, E., Leconte, J., Raymond, S. N., Van Grootel, V., Burgasser, A. J., Carey, S., Fabrycky, D., Heng, K., Hernandez, D. M., Ingalls, J. G., Lederer, S., Selsis, F., and Queloz, D. (2018). The nature of the TRAPPIST-1 exoplanets. *Astronomy and Astrophysics*, 613:A68.

Hamilton, D. P. and Ward, W. R. (2004). Tilting Saturn. II. Numerical Model. *The Astronomical Journal*, 128(5):2510–2517.

Harris, A. W. and Ward, W. R. (1982). Dynamical Constraints on the Formation and Evolution of Planetary Bodies. *Annual Review of Earth and Planetary Sciences*, 10:61.

Helled, R., Anderson, J. D., Podolak, M., and Schubert, G. (2011). Interior Models of Uranus and Neptune. *The Astrophysical Journal*, 726(1):15.

Helled, R., Anderson, J. D., and Schubert, G. (2010). Uranus and Neptune: Shape and rotation. *Icarus*, 210(1):446–454.

Helled, R. and Bodenheimer, P. (2014). The Formation of Uranus and Neptune: Challenges and Implications for Intermediate-mass Exoplanets. *The Astrophysical Journal*, 789(1):69.

Helled, R. and Fortney, J. J. (2020). The interiors of Uranus and Neptune: current understanding and open questions. *Philosophical Transactions of the Royal Society of London Series A*, 378(2187):20190474.

Henon, M. and Heiles, C. (1964). The applicability of the third integral of motion: Some numerical experiments. *The Astronomical Journal*, 69:73.

Henrard, J. (1982). Capture Into Resonance - an Extension of the Use of Adiabatic Invariants. *Celestial Mechanics*, 27(1):3–22.

Henrard, J. and Lemaître, A. (1983). A second fundamental model for resonance. *Celestial Mechanics*, 30:197–218.

Herschel, W. (1787). An Account of the Discovery of Two Satellites Revolving Round the Georgian Planet. By William Herschel, LLD. F. R. S. *Philosophical Transactions of the Royal Society of London Series I*, 77:125–129.

Herschel, W. and Watson, D. (1781). Account of a Comet. By Mr. Herschel, F. R. S.; Communicated by Dr. Watson, Jun. of Bath, F. R. S. *Philosophical Transactions of the Royal Society of London Series I*, 71:492–501.

Hussmann, H., Sohl, F., and Spohn, T. (2006). Subsurface oceans and deep interiors of medium-sized outer planet satellites and large trans-neptunian objects. *Icarus*, 185(1):258–273.

Hut, P. (1980). Stability of tidal equilibrium. *Astronomy and Astrophysics*, 92(1-2):167–170.

Ida, S., Ueta, S., Sasaki, T., and Ishizawa, Y. (2020). Uranian satellite formation by evolution of a water vapour disk generated by a giant impact. *Nature Astronomy*, 4:880–885.

Inderbitzi, C., Szulágyi, J., Cilibrasi, M., and Mayer, L. (2020). Formation of satellites in circumplanetary discs generated by disc instability. *Monthly Notices of the Royal Astronomical Society]*, 499(1):1023–1036.

Ishizawa, Y., Sasaki, T., and Hosono, N. (2019). Can the Uranian Satellites Form from a Debris Disk Generated by a Giant Impact? *The Astrophysical Journal*, 885(2):132.

Jacobson, R. A. (2014). The Orbits of the Uranian Satellites and Rings, the Gravity Field of the Uranian System, and the Orientation of the Pole of Uranus. *The Astronomical Journal*, 148(5):76.

Jeffreys, H. (1976). *The earth. Its origin, history and physical constitution.*

Jenkins, J. S., Tuomi, M., Brasser, R., Ivanyuk, O., and Murgas, F. (2013). Two Super-Earths Orbiting the Solar Analog HD 41248 on the Edge of a 7:5 Mean Motion Resonance. *The Astrophysical Journal*, 771(1):41.

Jewitt, D. and Haghighipour, N. (2007). Irregular Satellites of the Planets: Products of Capture in the Early Solar System. *Annual Review of Astronomy and Astrophysics*, 45(1):261–295.

Kaula, W. M. (1964). Tidal dissipation by solid friction and the resulting orbital evolution. *Rev. Geophys.* , 2:661–685.

Kegerreis, J. A., Teodoro, L. F. A., Eke, V. R., Massey, R. J., Catling, D. C., Fryer, C. L., Korycansky, D. G., Warren, M. S., and Zahnle, K. J. (2018). Consequences of Giant Impacts on Early Uranus for Rotation, Internal Structure, Debris, and Atmospheric Erosion. *The Astrophysical Journal*, 861(1):52.

Kellermann, C., Becker, A., and Redmer, R. (2018). Interior structure models and fluid Love numbers of exoplanets in the super-Earth regime. *Astronomy and Astrophysics*, 615:A39.

Kenyon, S. J. and Bromley, B. C. (2021). A Pluto-Charon Concerto. II. Formation of a Circumbinary Disk of Debris after the Giant Impact. *The Astronomical Journal*, 161(5):211.

Kepler, J. (1609). *Astronomia nova ..., seu physica coelestis, tradita commentariis de motibus stellae martis.*

Kirchoff, M. R., Dones, L., Singer, K., and Schenk, P. (2022). Crater Distributions of Uranus's Mid-sized Satellites and Implications for Outer Solar System Bombardment. *Plan. Sci. J.*, 3(2):42.

Korycansky, D. G., Bodenheimer, P., Cassen, P., and Pollack, J. B. (1990). One-dimensional calculations of a large impact on Uranus. *Icarus*, 84(2):528–541.

Kubo-Oka, T. and Nakazawa, K. (1995). Gradual increase in the obliquity of Uranus due to tidal interaction with a hypothetical retrograde satellite. *Icarus*, 114(1):21–32.

Kuiper, G. P. (1949). The Fifth Satellite of Uranus. *Publications of the Astronomical Society of the Pacific*, 61(360):129.

Kurosaki, K. and Inutsuka, S.-i. (2019). The Exchange of Mass and Angular Momentum in the Impact Event of Ice Giant Planets: Implications for the Origin of Uranus. *The Astronomical Journal*, 157(1):13.

Laskar, J. (1986). A general theory for the Uranian satellites. *Astronomy and Astrophysics*, 166(1-2):349–358.

Laskar, J. (1990). The chaotic motion of the solar system - A numerical estimate of the size of the chaotic zones. *Icarus*, 88:266–291.

Laskar, J. (1993). Frequency analysis for multi-dimensional systems. Global dynamics and diffusion. *Physica D Nonlinear Phenomena*, 67:257–281.

Laskar, J. and Correia, A. C. M. (2009). HD 60532, a planetary system in a 3:1 mean motion resonance. *Astronomy and Astrophysics*, 496:L5–L8.

Laskar, J. and Jacobson, R. A. (1987). GUST86 - an analytical ephemeris of the Uranian satellites. *Astronomy and Astrophysics*, 188(1):212–224.

Laskar, J. and Robutel, P. (1993). The chaotic obliquity of the planets. *Nature*, 361(6413):608–612.

Laskar, J. and Robutel, P. (1995). Stability of the Planetary Three-Body Problem. I. Expansion of the Planetary Hamiltonian. *Celestial Mechanics and Dynamical Astronomy*, 62(3):193–217.

Leleu, A., Alibert, Y., Hara, N. C., Hooton, M. J., Wilson, T. G., Robutel, P., Delisle, J. B., Laskar, J., Hoyer, S., Lovis, C., Bryant, E. M., Ducrot, E., Cabrera, J., Delrez, L., Acton, J. S., Adibekyan, V., Allart, R., Allende Prieto, C., Alonso, R., Alves, D., Anderson, D. R., Angerhausen, D., Anglada Escudé, G., Asquier, J., Barrado, D., Barros, S. C. C., Baumjohann, W., Bayliss, D., Beck, M., Beck, T., Bekkelien, A., Benz, W., Billot, N., Bonfanti, A., Bonfils, X., Bouchy, F., Bourrier, V., Boué, G., Brandeker, A., Broeg, C., Buder, M., Burdanov, A., Burleigh, M. R., Bárczy, T., Cameron, A. C., Chamberlain, S., Charnoz, S., Cooke, B. F., Corral Van Damme, C., Correia, A. C. M., Cristiani, S., Damasso, M., Davies, M. B., Deleuil, M., Demangeon, O. D. S., Demory, B. O., Di Marcantonio, P., Di Persio, G., Dumusque, X., Ehrenreich, D., Erikson, A., Figueira, P., Fortier, A., Fossati, L., Fridlund, M., Futyan, D., Gandolfi, D., García Muñoz, A., Garcia, L. J., Gill, S., Gillen, E., Gillon, M., Goad, M. R., González Hernández, J. I., Guedel, M., Günther, M. N., Haldemann, J., Henderson, B., Heng, K., Hogan, A. E., Isaak, K., Jehin, E., Jenkins, J. S., Jordán, A., Kiss, L., Kristiansen, M. H., Lam, K., Lavie, B., Lecavelier des Etangs, A., Lendl, M., Lillo-Box, J., Lo Curto, G., Magrin, D., Martins, C. J. A. P., Maxted, P. F. L., McCormac, J., Mehner, A., Micela, G., Molaro, P., Moyano, M., Murray, C. A., Nascimbeni, V., Nunes, N. J., Olofsson, G., Osborn, H. P., Oshagh, M., Ottensamer, R., Pagano, I., Pallé, E., Pedersen, P. P., Pepe, F. A., Persson, C. M., Peter, G., Piotto, G., Polenta, G., Pollacco, D., Poretti, E., Pozuelos, F. J., Queloz, D., Ragazzoni, R., Rando, N., Ratti, F., Rauer, H., Raynard, L., Rebolo, R., Reimers, C., Ribas, I., Santos, N. C., Scandariato, G., Schneider, J., Sebastian, D., Sestovic, M., Simon, A. E., Smith, A. M. S., Sousa, S. G., Sozzetti, A., Steller, M., Suárez Mascareño, A., Szabó, G. M., Ségransan, D., Thomas, N., Thompson, S., Tilbrook, R. H., Triaud, A., Turner, O., Udry, S., Van Grootel, V., Venus, H., Verrecchia, F., Vines, J. I., Walton, N. A., West, R. G., Wheatley, P. J., Wolter, D., and Zapatero Osorio, M. R. (2021). Six transiting planets and a chain of Laplace resonances in TOI-178. *Astronomy and Astrophysics*, 649:A26.

Levrard, B., Correia, A. C. M., Chabrier, G., Baraffe, I., Selsis, F., and Laskar, J. (2007). Tidal dissipation within hot Jupiters: a new appraisal. *Astronomy and Astrophysics*, 462(1):L5–L8.

Lissauer, J. J., Ragozzine, D., Fabrycky, D. C., Steffen, J. H., Ford, E. B., Jenkins, J. M., Shporer, A., Holman, M. J., Rowe, J. F., Quintana, E. V., Batalha, N. M., Borucki, W. J., Bryson, S. T., Caldwell, D. A., Carter, J. A., Ciardi, D., Dunham, E. W., Fortney, J. J., Gautier, Thomas N., I., Howell, S. B., Koch, D. G., Latham, D. W., Marcy, G. W., Morehead, R. C., and Sasselov, D. (2011). Architecture and Dynamics of Kepler's Candidate Multiple Transiting Planet Systems. *The Astrophysical Journal Supplement*, 197(1):8.

Lu, T. and Laughlin, G. (2022). Tilting Uranus via Spin-Orbit Resonance with Planet Nine. *Plan. Sci. J.*, 3(9):221.

Maire, A.-L., Delrez, L., Pozuelos, F. J., Becker, J., Espinoza, N., Lillo-Box, J., Revol, A., Absil, O., Agol, E., Almenara, J. M., Anglada-Escudé, G., Beust, H., Blunt, S., Bolmont, E., Bonavita, M., Brandner, W., Mirek Brandt, G., Brandt, T. D., Brown, G., Cantero Mitjans, C., Charalambous, C., Chauvin, G., Correia, A. C. M., Cranmer, M., Defrère, D., Deleuil, M., Demory, B.-O., De Rosa, R. J., Desidera, S., Dévora-Pajares, M., Díaz, R. F., Do Ó, C., Ducrot, E., Dupuy, T. J., Ferrer-Chávez, R., Fontanive, C., Gillon, M., Giuppone, C., Gkouvelis, L., de Oliveira Gomes, G., Gomes, S. R. A., Günther, M. N., Hadden, S., Han, Y., Hernandez, D. M., Jehin, E., Kane, S. R., Kervella, P., Kiefer, F., Konopacky, Q. M., Langlois, M., Lanssens, B., Lazzoni, C., Lendl, M., Li, Y., Libert, A.-S., Lovos, F., Miculán, R. G., Murray, Z., Pallé, E., Rein, H., Rodet, L., Roisin, A., Sahlmann, J., Siverd, R., Stalport, M., Carlos Suárez, J., Tamayo, D., Teyssandier, J., Thuillier, A., Timmermans, M., Triaud, A. H. M. J., Trifonov, T., Valente, E. F. S., Van Grootel, V., Vasist, M., Wang, J. J., Wyatt, M. C., Xuan, J., Young, S., and Zimmerman, N. T. (2023). Workshop Summary: Exoplanet Orbits and Dynamics. *Publications of the Astronomical Society of the Pacific*, 135(1052):106001.

Malhotra, R., Fox, K., Murray, C. D., and Nicholson, P. D. (1989). Secular perturbations of the Uranian satellites: theory and practice. *Astronomy and Astrophysics*, 221:348–358.

Maxima (2020). Maxima, a computer algebra system. version 5.44.0.

Meyer, K. R. and Hall, G. R. (1992). *Introduction to Hamiltonian Dynamical Systems and the N-Body Problem*. Springer New York, NY.

Michtchenko, T. A. and Ferraz-Mello, S. (2001). Modeling the 5 : 2 Mean-Motion Resonance in the Jupiter-Saturn Planetary System. *Icarus*, 149(2):357–374.

Mignard, F. (1979). The Evolution of the Lunar Orbit Revisited. I. *Moon and Planets*, 20(3):301–315.

Milani, A., Nobili, A. M., and Carpino, M. (1987). Secular variations of the semimajor axes - Theory and experiments. *Astronomy and Astrophysics*, 172(1-2):265–279.

Millholland, S. and Laughlin, G. (2019). Obliquity-driven sculpting of exoplanetary systems. *Nature Astronomy*, 3:424–433.

Morbidelli, A., Tsiganis, K., Batygin, K., Crida, A., and Gomes, R. (2012). Explaining why the uranian satellites have equatorial prograde orbits despite the large planetary obliquity. *Icarus*, 219(2):737–740.

Mosqueira, I. and Estrada, P. R. (2003). Formation of the regular satellites of giant planets in an extended gaseous nebula I: subnebula model and accretion of satellites. *Icarus*, 163(1):198–231.

Mozel, P. (1986). In Search of Sprites - the Discovery of Ariel and Umbriel. *Journal of the Royal Astronomical Society of Canada*, 80:344.

Murray, C. D. and Dermott, S. F. (1999). *Solar system dynamics*.

Nettelmann, N., Wang, K., Fortney, J. J., Hamel, S., Yellamilli, S., Bethkenhagen, M., and Redmer, R. (2016). Uranus evolution models with simple thermal boundary layers. *Icarus*, 275:107–116.

Palaniyandi, P. (2009). On computing Poincaré map by Hénon method. *Chaos Solitons and Fractals*, 39(4):1877–1882.

Parisi, M. G. and Brunini, A. (1997). Constraints to Uranus' Great Collision - II. *Planetary and Space Science*, 45(2):181–187.

Parisi, M. G., Carraro, G., Maris, M., and Brunini, A. (2008). Constraints to Uranus' great collision IV. The origin of Prospero. *Astronomy and Astrophysics*, 482(2):657–664.

Peale, S. J. (1988). Speculative histories of the Uranian satellite system. *Icarus*, 74(2):153–171.

Peale, S. J. (1999). Origin and Evolution of the Natural Satellites. *Annual Review of Astronomy and Astrophysics*, 37:533–602.

Peterson, G., Nimmo, F., and Schenk, P. (2015). Elastic thickness and heat flux estimates for the uranian satellite Ariel. *Icarus*, 250:116–122.

Petit, A. C. (2021). An integrable model for first-order three-planet mean motion resonances. *Celestial Mechanics and Dynamical Astronomy*, 133(8):39.

Plescia, J. B. (1987). Cratering history of the Uranian satellites: Umbriel, Titania, and Oberon. *Journal of Geophysical Research*, 92(A13):14918–14932.

Plescia, J. B. (1988). Cratering history of Miranda: Implications for geologic processes. *Icarus*, 73(3):442–461.

Pollack, J. B., Lunine, J. I., and Tittemore, W. C. (1991). Origin of the Uranian satellites. In Bergstralh, J. T., Miner, E. D., and Matthews, M. S., editors, *Uranus*, pages 469–512.

Prentice, A. J. R. (1986). Uranus after Voyager 2 and the origin of the solar system. *Proceedings of the Astronomical Society of Australia*, 6(4):394–402.

Prockter, L. M., Lopes, R. M. C., Giese, B., Jaumann, R., Lorenz, R. D., Pappalardo, R. T., Patterson, G. W., Thomas, P. C., Turtle, E. P., and Wagner, R. J. (2010). Characteristics of Icy Surfaces. *Space Science Reviews*, 153(1-4):63–111.

Rice, S. O. (1945). Mathematical Analysis of Random Noise-Conclusion. *Bell System Technical Journal*, 24:46–156.

Rogoszinski, Z. and Hamilton, D. P. (2021). Tilting Uranus: Collisions versus Spin-Orbit Resonance. *Plan. Sci. J.*, 2(2):78.

Safronov, V. S. (1966). Sizes of the largest bodies falling onto the planets during their formation. *Soviet Astronomy*, 9:987–991.

Saillenfest, M., Rogoszinski, Z., Lari, G., Baillié, K., Boué, G., Crida, A., and Lainey, V. (2022). Tilting Uranus via the migration of an ancient satellite. *Astronomy and Astrophysics*, 668:A108.

Salmon, J. and Canup, R. M. (2022). Co-accretion + Giant Impact Origin of the Uranus System: Post-impact Evolution. *The Astrophysical Journal*, 924(1):6.

Scheibe, L., Nettelmann, N., and Redmer, R. (2021). Thermal evolution of Uranus and Neptune. II. Deep thermal boundary layer. *Astronomy and Astrophysics*, 650:A200.

Schubert, G. (2015). *Treatise on Geophysics: Second Edition*.

Sinclair, A. T. (1972). On the origin of the commensurabilities amongst the satellites of Saturn. *Monthly Notices of the Royal Astronomical Society]*, 160:169.

Sinclair, A. T. (1975). The orbital resonance amongst the Galilean satellites of Jupiter. *Monthly Notices of the Royal Astronomical Society]*, 171:59–72.

Singer, S. F. (1968). The Origin of the Moon and Geophysical Consequences. *Geophysical Journal International*, 15(1-2):191–204.

Slattery, W. L., Benz, W., and Cameron, A. G. W. (1992). Giant impacts on a primitive Uranus. *Icarus*, 99(1):167–174.

Smart, W. M. and Green, E. b. R. M. (1977). *Textbook on Spherical Astronomy*.

Smith, B. A., Soderblom, L. A., Beebe, R., Bliss, D., Boyce, J. M., Brahic, A., Briggs, G. A., Brown, R. H., Collins, S. A., Cook, A. F., Croft, S. K., Cuzzi, J. N., Danielson, G. E., Davies, M. E., Dowling, T. E., Godfrey, D., Hansen, C. J., Harris, C., Hunt, G. E., Ingersoll, A. P., Johnson, T. V., Krauss, R. J., Masursky, H., Morrison, D., Owen, T., Plescia, J. B., Pollack, J. B., Porco, C. C., Rages, K., Sagan, C., Shoemaker, E. M., Sromovsky, L. A., Stoker, C., Strom, R. G., Suomi, V. E., Synnott, S. P., Terrile, R. J., Thomas, P., Thompson, W. R., and Veverka, J. (1986). Voyager 2 in the Uranian System: Imaging Science Results. *Science*, 233(4759):43–64.

Squyres, S. W., Reynolds, R. T., and Lissauer, J. J. (1985). The enigma of the Uranian satellites' orbital eccentricities. *Icarus*, 61(2):218–223.

Strom, R. G. (1987). The solar system cratering record: Voyager 2 results at Uranus and implications for the origin of impacting objects. *Icarus*, 70(3):517–535.

Szulágyi, J., Cilibrasi, M., and Mayer, L. (2018). In Situ Formation of Icy Moons of Uranus and Neptune. *The Astrophysical Journal Letters*, 868(1):L13.

Thomas, P. C. (1988). Radii, shapes, and topography of the satellites of Uranus from limb coordinates. *Icarus*, 73(3):427–441.

Tittemore, W. C. and Wisdom, J. (1988). Tidal evolution of the Uranian satellites I. Passage of Ariel and Umbriel through the 5:3 mean-motion commensurability. *Icarus*, 74(2):172–230.

Tittemore, W. C. and Wisdom, J. (1989). Tidal evolution of the Uranian satellites II. An explanation of the anomalously high orbital inclination of Miranda. *Icarus*, 78(1):63–89.

Tittemore, W. C. and Wisdom, J. (1990). Tidal evolution of the Uranian satellites III. Evolution through the Miranda-Umbriel 3:1, Miranda-Ariel 5:3, and Ariel-Umbriel 2:1 mean-motion commensurabilities. *Icarus*, 85(2):394–443.

Tsiganis, K., Gomes, R., Morbidelli, A., and Levison, H. F. (2005). Origin of the orbital architecture of the giant planets of the Solar System. *Nature*, 435(7041):459–461.

Vissapragada, S., Jontof-Hutter, D., Shporer, A., Knutson, H. A., Liu, L., Thorngren, D., Lee, E. J., Chachan, Y., Mawet, D., Millar-Blanchaer, M. A., Nilsson, R., Tinyanont, S., Vasisht, G., and Wright, J. T. (2020). Diffuser-assisted Infrared Transit Photometry for Four Dynamically Interacting Kepler Systems. *The Astronomical Journal*, 159(3):108.

Ward, W. R. and Hamilton, D. P. (2004). Tilting Saturn. I. Analytic Model. *The Astronomical Journal*, 128(5):2501–2509.

Wittenmyer, R. A., Johnson, J. A., Butler, R. P., Horner, J., Wang, L., Robertson, P., Jones, M. I., Jenkins, J. S., Brahm, R., Tinney, C. G., Mengel, M. W., and Clark, J. (2016). The Pan-Pacific Planet Search. IV. Two Super-Jupiters in a 3:5 Resonance Orbiting the Giant Star HD 33844. *The Astrophysical Journal*, 818(1):35.

Woo, J. M. Y., Reinhardt, C., Cilibrasi, M., Chau, A., Helled, R., and Stadel, J. (2022). Did Uranus' regular moons form via a rocky giant impactor? *Icarus*, 375:114842.

Wright, D. C. (1987). Uranus in Antiquity. *Quarterly Journal of the Royal Astronomical Society*, 28:79.

Xavier, J., Prado, A. B., Winter, S. G., and Amarante, A. (2022). Mapping Long-Term Natural Orbits about Titania, a Satellite of Uranus. *Symmetry*, 14(4):667.

Yoder, C. F. (1979). Diagrammatic Theory of Transition of Pendulum-like Systems. *Celestial Mechanics*, 19(1):3–29.

Zahnle, K., Schenk, P., Levison, H., and Dones, L. (2003). Cratering rates in the outer Solar System. *Icarus*, 163(2):263–289.

Zhu, W., Petrovich, C., Wu, Y., Dong, S., and Xie, J. (2018). About 30% of Sun-like Stars Have Kepler-like Planetary Systems: A Study of Their Intrinsic Architecture. *The Astrophysical Journal*, 860(2):101.